

**The Q/U Imaging Experiment (QUIET): The
Q-band Receiver Array Instrument and
Observations**

by

Laura Newburgh

Advisor: Professor Amber Miller

Submitted in partial fulfillment of the
requirements for the degree of

Doctor of Philosophy

in the Graduate School of Arts and Sciences

COLUMBIA UNIVERSITY

2010

Abstract

The Q/U Imaging Experiment (QUIET): The Q-band Receiver Array Instrument and Observations

by

Laura Newburgh

Phase I of the Q/U Imaging Experiment (QUIET) measures the Cosmic Microwave Background polarization anisotropy spectrum at angular scales $25 \lesssim \ell \lesssim 1000$. QUIET has deployed two independent receiver arrays. The 40-GHz array took data between October 2008 and June 2009 in the Atacama Desert in northern Chile. The 90-GHz array was deployed in June 2009 and observations are ongoing. Both receivers observe four $15^\circ \times 15^\circ$ regions of the sky in the southern hemisphere that are expected to have low or negligible levels of polarized foreground contamination. This thesis will describe the 40 GHz (Q-band) QUIET Phase I instrument, instrument testing, observations, analysis procedures, and preliminary power spectra.

Contents

1	Cosmology with the Cosmic Microwave Background	1
1.1	The Cosmic Microwave Background	1
1.2	Inflation	2
1.2.1	Single Field Slow Roll Inflation	3
1.2.2	Observables	4
1.3	CMB Anisotropies	6
1.3.1	Temperature	6
1.3.2	Polarization	7
1.3.3	Angular Power Spectrum Decomposition	8
1.4	Foregrounds	14
1.5	CMB Science with QUIET	15
2	The Q/U Imaging Experiment Q-band Instrument	19
2.1	QUIET Q-band Instrument Overview	19
2.2	Optics	23
2.2.1	Introduction	23
2.2.2	Telescope Optics	23
2.2.3	Feedhorns and Interface Plate	27
2.2.4	Ortho-mode Transducer Assemblies	28
2.2.5	Hybrid-Tee Assembly	33
2.2.6	Optics Performance	34
2.3	Polarimeter Modules	49
2.3.1	Introduction	49

2.3.2	Polarimeter Module Components	51
2.3.3	Module Bias Optimization	60
2.3.4	Compression	61
2.3.5	Signal Processing by the QUIET Module	62
2.4	Single Module Testing at the Jet Propulsion Laboratory and Columbia University	77
2.5	Electronics	79
2.5.1	Introduction	79
2.5.2	Electronics Overview	80
2.5.3	Protection Circuitry	84
2.5.4	Bias Boards	88
2.5.5	Monitor and Data Acquisition Boards	90
2.5.6	Timing cards	94
2.5.7	External-Temperature Monitor Boards	94
2.5.8	Software	94
2.6	Cryostat	96
2.6.1	Introduction	96
2.6.2	Description of W- and Q- band Cryostats	96
2.6.3	Mechanical Simulations	99
2.6.4	Expected and Measured Cryostat Temperatures	100
2.6.5	The Cryostat Window	106
3	Q-band Array Integration, Characterization, and Testing	119
3.1	Introduction	119
3.2	Bandpasses	119
3.2.1	Columbia Laboratory Data	121
3.2.2	Site Data	122
3.2.3	Receiver Bandwidths and Central Frequencies	124
3.2.4	Amplifier Bias	128

3.2.5	Central Frequencies and Bandwidths: Weighted by Source Spectrum	131
3.3	Noise Temperature Measurements	133
3.4	Responsivity	135
3.4.1	Total Power	135
3.4.2	Polarized Response	137
3.5	Compression	140
3.6	Noise	142
3.7	Instrument Sensitivity	144
4	Observations and Data Reduction	148
4.1	QUIET Observing Site	148
4.1.1	Observing Conditions	148
4.2	Patch Selection	151
4.3	Scan Strategy	151
4.4	Data Selection and Reduction	151
4.4.1	Nomenclature	152
4.4.2	Standard and Static Cuts	152
4.4.3	Scan Duration	153
4.4.4	Glitching Cut	153
4.4.5	Phase Switch Cut	154
4.4.6	Weather Cut	155
4.4.7	Fourier-Transform Based Cuts and Filtering	166
4.4.8	Side-lobe Cut	171
4.4.9	Coordinate System	171
4.4.10	Cut Development	172
4.4.11	Ground Map	173
4.4.12	Max-Min Removal	177
4.4.13	Source Removal and Edge-Masking	179
4.4.14	Data Selected	179

5	Instrument Calibration and Characterization	180
5.1	Introduction	180
5.1.1	Nomenclature	180
5.2	Calibration Overview	181
5.2.1	Calibration Sources	181
5.3	Responsivity	183
5.3.1	Total Power Responsivity	184
5.3.2	Polarization Responsivity	185
5.3.3	Systematic Error Assessment	185
5.4	Sensitivity	187
5.5	Pointing	188
5.5.1	Systematic Error Assessment	193
5.6	Timing	194
5.7	Polarized Detector Angles	196
5.7.1	Systematic Error Assessment	198
5.8	Leakage	198
5.8.1	Systematic Error Assessment	199
5.9	Beams	201
5.9.1	Polarized Beams	201
5.9.2	Total Power Beams	204
5.9.3	Ghosting	205
5.9.4	Systematic Error Assessment for the Beams	206
5.10	Summary of Calibration and Systematics	207
5.10.1	Summary of Calibration Accuracy and Precision	207
5.10.2	Systematics Summary	208
6	CMB Power Spectrum Analysis and Results With a Maximum Like- likelihood Pipeline	209
6.1	Introduction	209
6.2	Maximum-Likelihood Method Background	209

6.3	Optimal Map Making	210
6.4	Maximum Likelihood Power Spectrum Estimation	212
6.4.1	Overview	212
6.4.2	Gibbs Sampling	214
6.4.3	Null Spectrum Testing	215
6.5	Foreground Estimation	221
6.6	Preliminary Results	224
6.6.1	Galactic Center	224
6.6.2	Null Tests	224
A	Module Signal Processing	242
A.1	Phase Switch Transmission Imbalance	242
A.2	Module Systematics	246
A.3	Signal Processing including systematics	246
A.3.1	No Systematics: OMT input	246
A.3.2	No Systematics: hybrid-Tee input	246
A.3.3	Complex gain: OMT input	246
A.3.4	Complex gain: Hybrid-Tee input	248
A.3.5	Imperfect coupling within the Hybrid-Tee	250
A.3.6	Phase lag in 180° coupler at <i>input</i> : OMT input	252
A.3.7	Phase lag in 180° coupler at input: Hybrid-Tee input	253
A.3.8	Phase lag in the branchline coupler of the 180° coupler: OMT input	253
A.3.9	Phase lag at the output the 180° coupler: OMT input	255
A.4	Correlated Noise	258
A.4.1	No Systematics	260
A.4.2	Complex Gain	264
A.4.3	Phase Lag at the Input to the 180° Coupler	264
A.4.4	Phase Lag in the Branchline Coupler	265
A.4.5	Phase Lag at the Output of the Coupler	266

B	Bandpasses: Site measurements	267
B.1	Bandpasses from Site Measurements	267
B.2	Bandwidths and Central Frequencies for Source Weighted Bandpasses	268
C	Optimizer Signal Derivation	282
D	Sensitivity Calculation	284
D.1	Array Sensitivity Computation	284
D.1.1	Masking Factor	285
D.1.2	Combining Diodes to Find Array Sensitivity	285
D.1.3	Extrapolation for the Chilean Sky	285
D.1.4	Rayleigh-Jeans Correction	286

List of Figures

1-1	Inflationary Potentials	3
1-2	Thomson scattering	8
1-3	Polarization around a potential well	9
1-4	Polarization from a gravity wave	10
1-5	Stokes Q and U vectors definition	11
1-6	E-mode and B-mode definition	12
1-7	TT, EE, and (predicted) BB anisotropy angular power spectra	13
1-8	Foreground and TT anisotropy power with frequency	15
1-9	Foreground emission compared to CMB anisotropy signal power . . .	16
1-10	Predicted QUIET polarization angular power spectrum	18
2-1	Overview of the QUIET Instrument	21
2-2	Q-band Module numbering	22
2-3	Cross-Dragone Telescope Design	25
2-4	Q-band feedhorn array	28
2-5	Measured beam pattern for the Q-band horns compared to an electro- formed horn	29
2-6	A septum polarizer OMT photograph	29
2-7	Septum polarizer OMT schematic	30
2-8	Schematic of the TT assembly	35
2-9	Simulated beam pattern for the feedhorn and mirror system	37
2-10	Predicted ellipticity and cross-polarization for different array sizes . .	38
2-11	Sidelobe coordinate systems	39

2-12	Predicted sidelobe contamination	40
2-13	Physical sidelobe regions corresponding to predicted sidelobes	41
2-14	Telescope beam profile in two dimensions	42
2-15	The measured and predicted beam, including mirror surface irregularities	45
2-16	Sidelobe measurements at the observing site	47
2-17	Location of external temperature thermometers	48
2-18	A schematic of the bandpasses of the amplifiers	51
2-19	Signal processing components in a QUIET Q-band module	52
2-20	A module waveguide probe	53
2-21	QUIET Q-band Low-noise amplifier	54
2-22	QUIET phase-switch	56
2-23	QUIET Q-band phase discriminator	58
2-24	QUIET detector diode	59
2-25	A schematic of diode response	60
2-26	Illustration of amplifier compression	61
2-27	QUIET electronics system	80
2-28	Enclosure temperature during the Q-band observing season	83
2-29	A photograph of the FPCs	84
2-30	The two electronics board backplanes	85
2-31	The QUIET Q-band MABs	86
2-32	Temperature dependence of the amplifier bias board output	88
2-33	Phase switch board output signal, with timing	89
2-34	A QUIET preamplifier board	91
2-35	Illustration of the ADC glitch	93
2-36	The QUIET Cryostats, external components	97
2-37	The QUIET Cryostats, internal components	98
2-38	QUIET Cryostat radiation shielding	99
2-39	Mechanical simulations for the W-band cryostat design	101
2-40	Average cryogenic temperatures during the Q-band observing season	104

2-41	Measurements during cooldown of the horn-dewar interface plate temperatures for the W-band cryostat.	105
2-42	Index of refraction and loss tangent over a range of frequencies for HDPE and teflon	108
2-43	Schematic of the three layers in the window	110
2-44	Schematic of the VNA testing setup	112
2-45	Reflection data from VNA measurements of the W-band window . . .	113
2-46	Predicted transmission properties of the W-band window	114
2-47	Predicted transmission properties of the Q-band window	114
2-48	Noise temperature contribution from the window as a function of HDPE thickness	117
3-1	Schematic of the setup for bandpass measurements in the laboratory .	121
3-2	Schematic of the setup for bandpass measurements on the telescope at the site	123
3-3	Comparison of bandpass quantities between laboratory and site measurements	126
3-4	Amplifier bias current compared to bandpass quantities	130
3-5	Two zotefoam cryogen buckets photograph	134
3-6	Noise temperatures from laboratory measurements	135
3-7	Q-band responsivities from laboratory measurements	136
3-8	The Q-band array optimizer (illustration and photograph)	138
3-9	An example time stream of the signal from an optimizer	140
3-10	A comparison between the total power and polarized gains	141
3-11	Demodulated data time-stream from laboratory measurements	143
3-12	White noise floor values from laboratory measurements	144
3-13	Expected polarimeter sensitivities for the Chilean sky	146
4-1	Atmospheric opacity near the two QUIET frequency bands	149
4-2	PWV, humidity, ambient temperature, and wind speed during scans in the Q-band season	150

4-3	QUIET sky patches	156
4-4	Illustration of de-glitching	157
4-5	Phase switch bias current data cut	158
4-6	Weather data cut criteria	159
4-7	Example time-streams for determining the weather data cut	162
4-8	Example standard deviation of time-streams for determining the weather data cut	163
4-9	The weather cut compared to diode I→Qleakage	165
4-10	Example FFT of a demodulated time stream	168
4-11	Distribution of χ^2 to the FFT noise model	170
4-12	A co-added map for all CESes in a flat projection of the sun-boresight coordinates for RQ02	173
4-13	A ground map	175
4-14	A ground map	176
4-15	An example of a TOD spike	177
4-16	Distribution of extreme TOD outliers	178
5-1	Array sensitivity for the polarization modules	188
5-2	Illustration of the collimation offset parameters	191
5-3	Deck encoder slip through the observing season	193
5-4	Illustration of the timing offset measurements	195
5-5	Timing offset correction	196
5-6	A comparison of detector angles	197
5-7	A comparison of I→Qleakage coefficients	200
5-8	Normalized maps of Tau A for the central polarimeter	202
5-9	Radial beam profile for the central polarimeter	203
5-10	Window function for the polarization modules	204
5-11	Window function for the hybrid-Tee modules	205
5-12	Map of the moon and ghosted moon in RQ04	206
6-1	A schematic of a two-variable posterior	214

6-2	Illustration of quantifying consistency with null for power spectrum null-tests	223
6-3	Galactic Center polarized maps	225
6-4	Null map of the ‘pointside’ null test	226
6-5	The angular power spectrum for the ‘pointside’ null test	227
6-6	P-test for the ‘pointside’ null test	228
B-1	Q1 diode bandpasses measured by site data	268
B-2	Q2 diode bandpasses measured by site data	269
B-3	Q1 diode bandpasses	270
B-4	Q2 diode bandpasses	271

List of Tables

2.1	QUIET Phase I instrument and observations overview	20
2.2	Parameters for the QUIET mirror design	24
2.3	Simulated Q-band beam characteristics	36
2.4	Compression points of the low-noise amplifiers	63
2.5	Module systematics and resulting demodulated and averaged signal .	73
2.6	Summary of correlation coefficients	76
2.7	Summary of electronics boards for the Q- and W-band polarimeter arrays	81
2.8	Dimensions of the external elements of each cryostat	100
2.9	Calculated thermal loading from various sources with 300K and 270K environment temperature	102
2.10	Refrigerator temperatures given loading for the W- and Q-band receivers	103
2.11	Average cryogenic temperatures during the Q-band observing season	103
2.12	Calculated and Measured thermal gradient between modules	106
2.13	Window Testing Results	107
2.14	Window material thicknesses and indices of refraction	113
2.15	Predicted transmission properties of each window	114
2.16	Noise temperature contribution for the W-band and Q-band windows	118
3.1	Q-band polarimeter array central frequencies	127
3.2	Q-band polarimeter array bandwidths	128
3.3	Q-band hybrid-Tee central frequencies	129
3.4	Q-band hybrid-Tee bandwidths	129
3.5	Spectral indices at Q-band for various sources	132

3.6	Expected polarized emission from the optimizer	139
4.1	Description of static and standard data cuts	153
4.2	Weather variable standard deviation criteria for two example time streams	161
4.3	Percentage of data cut by each data cut	179
5.1	QUIET calibration scheme	183
5.2	Responsivity model systematic errors	187
5.3	Beam parameters from calibration observations	202
5.4	Preliminary calibration precision for QUIET Phase I	207
5.5	Maximum systematic errors, expressed as a percentage of the statistical error	208
6.1	Maximum Likelihood null tests	217
6.2	Summary of patch foreground contamination	221
6.3	Summary of expected patch foreground contamination	222
B.1	Q-band array central frequencies for dust foreground.	272
B.2	Q-band array bandwidths for dust emission	273
B.3	Q-band array central frequencies for sychrotron emission	274
B.4	Q-band array bandwidths for sychrotron emission	275
B.5	Q-band array central frequencies for Tau A	276
B.6	Q-band array bandwidths for Tau A	277
B.7	Q-band array bandwidths for 250mm PWV	278
B.8	Q-band array central frequencies for 250mm PWV	279
B.9	Q-band array bandwidths for 5000mm PWV	280
B.10	Q-band array central frequencies for 5000mm PWV	281

Acknowledgments

Thanks first to my advisor and mentor, Amber Miller. You have been generous with your time, have always had your door open, have demanded the best, but always given room to make mistakes.

I have been extremely fortunate to have worked in the Miller lab and be surrounded by smart, knowledgeable, amazing, fun people. I can't possibly list everything I've learned from you all, so I won't try, and instead just say: Ross, thanks for never letting me off the hook and making each day a bit of an adventure. Rob, you keep me laughing even when its (likely) at myself. Jonathan, thanks for leading me through the harrowing world of Bayesian analysis and only making fun of me a fraction of the time you could have. Seth, thank you for always being willing to help, whether it was welding cold-straps or extracting our data. And thank you Michele, because I always have just one last question.

Working on QUIET was an incredible learning experience, for which I would like to thank the entire QUIET collaboration, with a special thanks to our PI, Bruce Winstein. Thanks also to the Q-band deployment team for making the Caltech high-bay and Chilean desert an unforgettable experience: Simon, Michele, Ross, Rob, Ali, Immanuel, Raul, Ricardo, Rodrigo, Cristobal, and Jose. If I have more pictures of flamingos in Chile than the Q-band cryostat, its your fault.

Thank you Mom and Dad because you never once said girls can't do science, and thank you Kate and Maggie, for being awesome, supportive sisters. Thank you Tanya and Malika, for keeping me sane since college. Thank you Mari for keeping me young at heart, and Azfar, whose unconditional support was a great gift.

Chapter 1

Cosmology with the Cosmic Microwave Background

Today, a variety of different data sets have converged to a common model describing the Universe and its constituents: it is expanding at an accelerated rate and its energy density is dominated by dark energy, with smaller contributions from cold dark matter, baryonic matter, photons, and neutrinos. Measurements of the Cosmic Microwave Background (CMB) played a critical role in forming this model. This chapter will discuss the origin of the CMB and how we can use measurements of the CMB to constrain models describing the dynamics of the Universe when it was less than 10^{-30} seconds old.

1.1 The Cosmic Microwave Background

When the Universe was not yet $\simeq 380,000$ years old, photons, baryons, and electrons were tightly coupled, forming a photon-baryon fluid. As the universe expanded and cooled to a temperature of $\simeq 1/4$ eV, the electrons began to bind to protons to form neutral elements, predominantly hydrogen, and the scattering cross section for photons off of electrons dropped dramatically. As a result, the photons were decoupled from the electrons and the CMB was formed by free photons at the surface of last scattering, this era is known as decoupling or recombination. The CMB was emitted

from a uniform, hot plasma such that at decoupling it had a black-body spectrum with a wavelength peak $\simeq 1\mu\text{m}$ (infrared band). As the universe continued to expand and cool, the wavelength of this background radiation stretched such that today it lies in the microwave band and has a Planck spectrum peak at $2.726\text{K}\pm 0.01\text{K}$ (Ref. [65]). Today we know the temperature of this surface is uniform to one part in 10^5 (Refs. [66],[33],[87],[46],[79],[51]).

1.2 Inflation

There are a variety of theories that describe the dynamics of the early universe, none of which are experimentally proven. We will limit ourselves to briefly describing the best-motivated class of these: inflation. Inflation describes a period in which the Universe underwent brief, exponential expansion (Ref. [32],[61]), increasing in size by $\simeq 25$ orders of magnitude in $\lesssim 10^{-34}$ seconds when it was $\simeq 10^{-30}$ seconds old (Ref. [4]). Inflation naturally explains three observations (Ref. [59]):

1. **Lack of Observed Relic Particles:** A variety of stable particles such as magnetic monopoles should be created when symmetry was broken in the early Universe at energies $\simeq 10^{16}$ GeV, however these particles have not been observed. Inflation dilutes their abundance such that they would be too rare to observe today (Ref. [50]).
2. **Super-horizon Fluctuations:** The uniformity of the CMB shows that scales which were causally disconnected during recombination had been in thermal equilibrium. This homogeneity arises naturally from inflationary theory; those regions were causally connected before they were pushed apart by inflationary expansion.
3. **Flatness:** Observations show the universe is very close to spatially flat (Ref. [66]). This is a natural prediction of inflation as it dilutes the curvature of space in

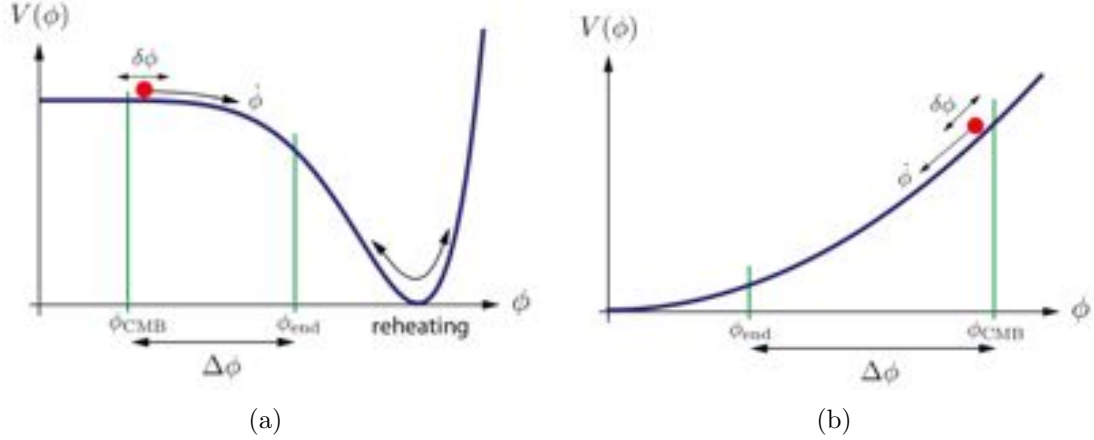


Figure 1-1: Figures from Ref. [4]. An example slow-roll potential $V(\phi)$ for *a*: small field ϕ and *b*: large field ϕ inflationary models. The conditions for small and large field models are discussed in the text. The fluctuations seen in the CMB were imprinted at ϕ_{CMB} and blown to large scales during inflation. Reheating refers to the process by which the inflaton decayed to form standard model particles.

much the same way that it dilutes the relic particles.

1.2.1 Single Field Slow Roll Inflation

Inflationary expansion is sourced by the motion of one or more primordial field/s in a potential. While there are a variety of inflationary models, here we consider only the simplest class: single scalar-field slow-roll inflationary models. Slow-roll inflation requires that the potential is not particularly steep, this condition will provide a natural mechanism for generating the expansion rate necessary for inflation to solve the three problems presented above. Examples of two typical potentials which could give rise to slow-roll inflationary expansion are shown in Figures 1-1(a) and 1-1(b). The slow-roll condition will place constraints on the kinetic terms of the equations of motion (Ref. [60]), which are parametrized by ϵ and η (the ‘slow-roll parameters’):

$$\epsilon = -\frac{\dot{H}}{H} = \frac{M_{\text{pl}}^2}{2} \frac{\dot{\phi}^2}{H^2} \approx \frac{M_{\text{pl}}^2}{2} \left(\frac{V'}{V} \right)^2 \ll 1 \quad (1.1)$$

$$|\eta| = M_{\text{pl}}^2 \left| \frac{V''}{V} \right| \ll 1 \quad (1.2)$$

where $(')$ denotes a derivative with respect to ϕ . The end-point of inflation is model-dependent but will occur when the slow-roll condition is violated: $\epsilon \rightarrow 1$.

1.2.2 Observables

Inflationary models generally predict perturbations in the inflaton field $\delta\phi(t, \mathbf{x})$ and in the metric $\delta g_{\mu\nu}(t, \mathbf{x})$ prior to inflation. These perturbations can be transformed to Fourier space ($\delta\phi(t, \mathbf{x}) \rightarrow \delta\phi(\mathbf{k})$ and $\delta g_{\mu\nu}(t, \mathbf{x}) \rightarrow \delta g_{\mu\nu}(\mathbf{k})$) and then decomposed into scalar and tensor perturbations¹. Computing the two-point correlation of the scalar perturbations will yield a power spectrum of scalar fluctuations, P_s , given by equation 1.3:

$$P_s(k) = A_s(k_*) \left(\frac{k}{k_*} \right)^{n_s(k_*) - 1 + \frac{1}{2}\alpha_s(k_*) \ln(k/k_*)} \quad (1.3)$$

that is dependent on a normalization A_s , a spectral tilt n_s , and a parameter α_s , which gives the slope of the spectral tilt with scale. All are defined at a specific scale k_* , known as the pivot scale (Ref. [4]). $n_s = 1$ would give a scale-invariant spectrum of scalar perturbations, such that the distribution of power is uniform over all scales.

The two-point correlation of tensor perturbations yield a power spectrum of tensor

¹Vector perturbations are also included in this decomposition, but non-negligible amplitudes of these perturbations are unique to predictions from specific models that we are not considering here.

perturbations, P_t , given by 1.4 (Ref. [92], form taken from Ref. [4]):

$$P_t(k) = A_t(k_*) \left(\frac{k}{k_*} \right)^{n_t(k_*)} \quad (1.4)$$

with amplitude A_t and spectral tilt parameter n_t . $n_t = 0$ would give a scale-invariant spectrum of tensor perturbations. The tensor perturbations represent gravitational wave generation, sourcing primordial inflationary gravity waves.

The tensor-to-scalar ratio, $r_k = \frac{P_s(k)}{P_t(k)}$, describes the relative amplitude of the scalar and tensor fluctuations at the end of inflation. For slow-roll inflation, the spectral tilts are directly related to the slow-roll parameters as $n_s - 1 = 2\eta - 6\epsilon$ and $n_t = -2\epsilon$ (Ref. [60]). In these models, the tensor-to-scalar ratio r determines the energy scale of inflation as (Ref. [3]):

$$V^{1/4} = 1.06 \times 10^{16} \text{GeV} \left(\frac{r_*}{0.01} \right)^{1/4} \quad (1.5)$$

where r_* denotes the tensor-to-scalar ratio when perturbations currently seen in the CMB were imprinted (denoted by ϕ_{CMB} in Figures 1-1(a) and 1-1(b)). Consequently r can be used to distinguish between different models with unique predictions of the energy scale of inflation. A class of inflationary models known as ‘large-field’ models are characterized by a relatively large tensor-to-scalar ratio, expressed in relation to the Planck mass:

$$\frac{\Delta\phi}{M_{\text{pl}}} \gtrsim 1.06 \times \left(\frac{r_*}{0.01} \right)^{1/2} \quad (1.6)$$

An example of a large-field potential is given in Figure 1-1(b). A detection of $r_* \gtrsim 0.01$ would yield an energy scale of inflation near the Grand Unified Theory (GUT) scale and shed light on physics at the highest energies, inaccessible to particle accelerators. If $r_* < 0.01$, an entire class of inflationary models would be ruled out and small-field

inflationary models or non-inflationary models would be favored (an example of a small-field potential is given in Figure 1-1(a)). The current lower bound on r is 0.22 (Ref. [51]) and the goal of QUIET Phase II (for which the work in this thesis is a pathfinder experiment) is to probe values of $r \simeq 0.01$.

1.3 CMB Anisotropies

1.3.1 Temperature

Scalar perturbations give rise to over- and under-dense regions which will leave an imprint in the CMB during decoupling. Over-dense regions represent potential wells which will aggregate matter over time through gravitational collapse. Together, the over- and under-dense regions source the large scale structure in the Universe.

Prior to decoupling, photons and baryons were tightly coupled. In the presence of a potential well, the photons and baryons form an oscillatory system in which the driving forces are gravitational collapse and photon pressure. The temperature of the photon-baryon fluid near the potential well from a given oscillatory mode is expressed as a fraction of the average temperature ($\frac{\Delta T}{T}$) and is a combination of the depth of the potential well Ψ and the baryon density (expressed as a fraction of the average density: $\frac{\delta \rho}{\rho}$), as (Ref. [23]):

$$\frac{\Delta T}{T} - \Psi \propto - \left(\frac{\delta \rho}{\rho} \right) \quad (1.7)$$

Equation 1.7 shows that a compressive mode ($\frac{\delta \rho}{\rho} > 0$) has a temperature which is lower than the background temperature, while the opposite is true for the rarefied mode ($\frac{\delta \rho}{\rho} < 0$). This is caused by the Sachs-Wolfe effect: although over-dense regions are hotter, the dominant effect results from the fact that photons must climb out of a larger potential during compression and hence are red-shifted, while photons in

the rarified state will be blue-shifted. These temperature fluctuations are imprinted on the CMB, creating cold regions where an oscillatory mode was at a maximum of its compression and hot regions at the rarified maximum. The resulting temperature anisotropies in the CMB encode these "acoustic spectra" formed from scalar perturbations. These acoustic spectrum can be seen in Figure 1-7 as the periodic peaks ($\Theta\Theta$ in the figure). The low- ℓ portion of the spectrum ($\ell < 100$) represent modes which were too large to have been in causal contact at decoupling. The first peak at $\ell \simeq 200$ represents the first mode, which had just compressed at decoupling, the second peak had just had time to compress and rarify, and so on.

1.3.2 Polarization

Polarization in the CMB is generated when radiation incident on a free electron has a quadrupole moment, as shown in Figure 1-2. This quadrupole pattern is produced primarily by acceleration of the photon-baryon fluid. This fluid flow can be sourced both by potential wells or by the gravity waves generated by tensor perturbations during inflation.

The oscillatory modes discussed in Section 1.3.1 accelerate the photon-baryon fluid. As shown in Figure 1-3, as the photon-baryon fluid falls into a potential well, the photons emitted from that region will appear blue-shifted in the rest-frame of a falling electron. This produces a quadrupole temperature anisotropy and results in polarization which is radial around the potential well. Polarization generated while the oscillatory mode is rarifying will have a tangential pattern (see Ref. [41] for a review, [51] for evidence of this from WMAP data).

Gravity waves generated during inflation will stretch and compress space as they propagate. As shown in Figure 1-4, this will create red-shifted photons where space is stretched in the rest-frame of a stationary electron in the middle of this distortion, and blue-shifted photons from areas where space is compressed. This generates a quadrupole temperature pattern and hence polarization via Thomson scattering

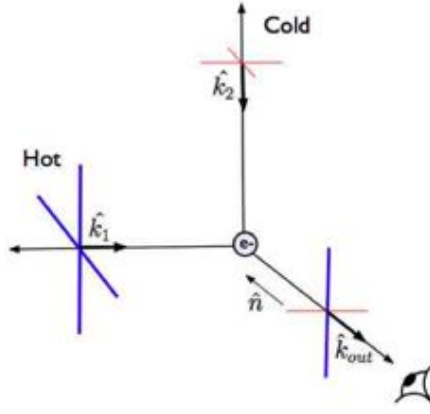


Figure 1-2: Figure adapted from Ref [41], courtesy Britt Reichborn-Kjennerud (Ref. [75]). Thomson scattering of CMB photons off of an electron located in a quadrupole radiation field. As discussed in the text, a quadrupole radiation field is sourced by cold spots from regions which are red-shifted, and hot spots from regions which are blue-shifted, due to bulk fluid flow. The scattered radiation from the blue-shifted region to the observer will be polarized vertically since the component along the line-of-sight will not be seen, while the scattered light from the red-shifted region will be polarized horizontally. The intensity of the scattered light from the blue-shifted region is greater than that of the red-shifted region, this produces overall linear polarization.

(Figure 1-2).

1.3.3 Angular Power Spectrum Decomposition

We can write polarization in the basis of the Stokes vectors I , Q , U , and V . The coordinate system is shown in Figure 1-5, and the vectors are defined as:

$$\mathcal{E} = \hat{\mathbf{x}}\mathcal{E}_x e^{i\mathbf{k}\cdot\mathbf{x}-\omega t} + \hat{\mathbf{y}}\mathcal{E}_y e^{i\mathbf{k}\cdot\mathbf{y}-\omega t} \quad (1.8)$$

$$I = \mathcal{E}_x^2 + \mathcal{E}_y^2 \quad (1.9)$$

$$Q = \mathcal{E}_x^2 - \mathcal{E}_y^2 \quad (1.10)$$

$$U = \mathcal{E}_x \mathcal{E}_y \cos \theta \quad (1.11)$$

$$V = \mathcal{E}_x \mathcal{E}_y \sin(\theta) \quad (1.12)$$

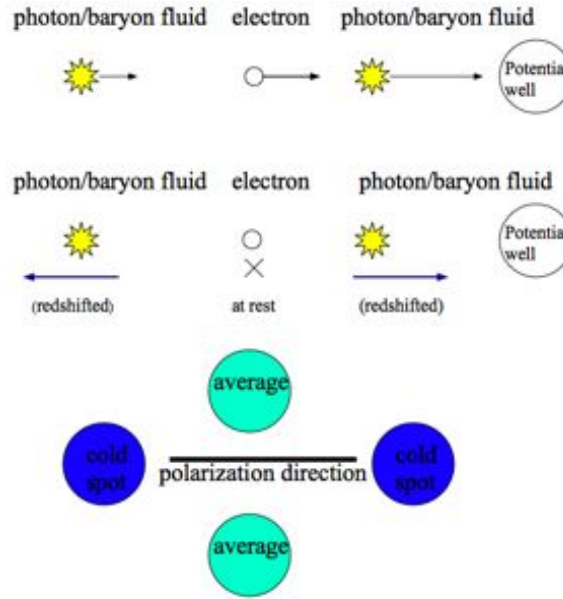


Figure 1-3: *Top:* An electron falling into a potential well (the length of the lines denote the magnitude of acceleration). *Middle:* In the rest frame of the electron, the plasma nearer to the potential well and also further away from the potential well is accelerating away, and so the light appears red-shifted. *Lower:* As a result, the electron will see a quadrupole temperature pattern, which generates polarization via Thomson scattering (Figure 1-2). In this case, the resulting polarization will be horizontal, and will form a radial polarization pattern around the potential well.

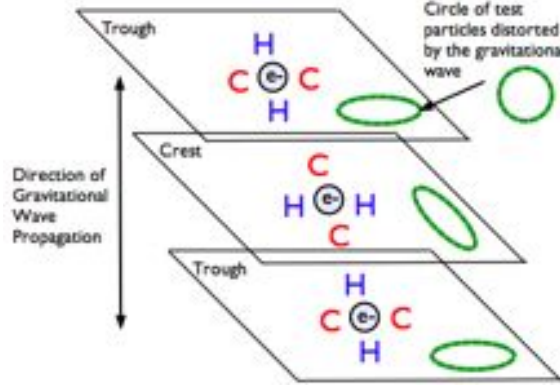


Figure 1-4: Figure adapted from Ref [41], courtesy Britt Reichborn-Kjennerud (Ref. [75]). The effect of a gravity wave on a set of test particles. As the gravity wave propagates, it will stretch and squeeze space. In the rest-frame of an electron at the center of the test particle ring, when the gravity wave squeezes space, the photons from the squeezed region will appear blue-shifted. Likewise, photons from a region of stretched space will appear red-shifted. The resulting intensity pattern is a quadrupole, which generates polarization in the CMB via Thomson scattering (Figure 1-2).

The parameter I gives a measurement of intensity of the radiation and for the black-body CMB, reflects the temperature of the plasma. The Q and U vectors parametrize linear polarization. The Stokes V parameter represents circular polarization, which is not generated from Thomson scattering and is therefore expected to be zero.

The temperature and polarization anisotropies in the CMB have a distribution across the sky which can be decomposed into spherical harmonics. This is a convenient basis to use to probe the underlying physics operating during decoupling. The Stokes Q and U vectors transform as a spin-2 field, as equation 1.14 (Ref. [47], [92]).

$$T(\hat{n}) = \sum_{\ell,m} a_{\ell m}^T Y_{\ell m}(\hat{n}) \quad (1.13)$$

$$(Q \pm iU)(\hat{n}) = \sum_{\ell,m} a_{\ell m}^{\pm 2} [\pm 2 Y_{\ell m}(\hat{n})] \quad (1.14)$$

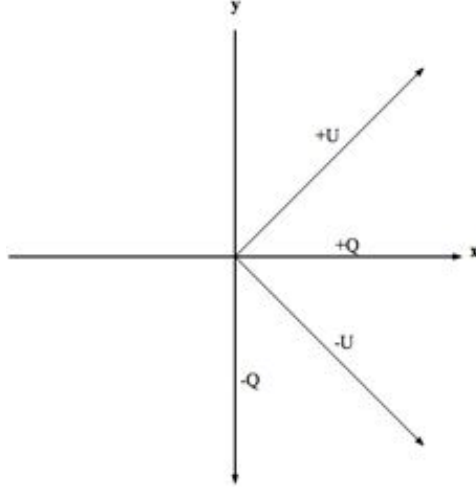


Figure 1-5: The Stokes parameters Q and U ; the sign convention is variable, but the angle between the Q and U vectors is defined to be 45° .

where \hat{n} is the line-of-sight vector. The multipole ℓ is related to angular distance on the sky¹. These are transformed into ‘E-modes’ and ‘B-modes’:

$$E(\hat{n}) = \sum_{\ell,m} a_{\ell m}^E Y_{\ell m}(\hat{n}) \equiv \sum_{\ell,m} \left(-\frac{1}{2} (a_{\ell m}^{(2)} + a_{\ell m}^{(-2)}) \right) Y_{\ell m}(\hat{n}) \quad (1.15)$$

$$B(\hat{n}) = \sum_{\ell,m} a_{\ell m}^B Y_{\ell m}(\hat{n}) \equiv \sum_{\ell,m} \left(-\frac{1}{2i} (a_{\ell m}^{(2)} - a_{\ell m}^{(-2)}) \right) Y_{\ell m}(\hat{n}) \quad (1.16)$$

E-modes ($E(\hat{n})$) are curl-free and B-modes ($B(\hat{n})$) are divergence-free, as illustrated by the sketches in Figures 1-6(a) and Figure 1-6(b), respectively. The E/B decomposition is convenient for describing the polarized CMB radiation field since scalar perturbations in the early Universe will produce only E-modes, while tensor perturbations, if they are present, will produce both E- and B-modes. Hence, gravity waves generated during inflation can in principle be uniquely detected in the CMB by a measurement of the B-mode amplitude. The B-mode amplitude is expected to be much smaller than the E-mode amplitude, so tensor E-modes are not separable

¹ $\ell \simeq \frac{180^\circ}{\theta}$ where θ is an angular distance on the sky in degrees.

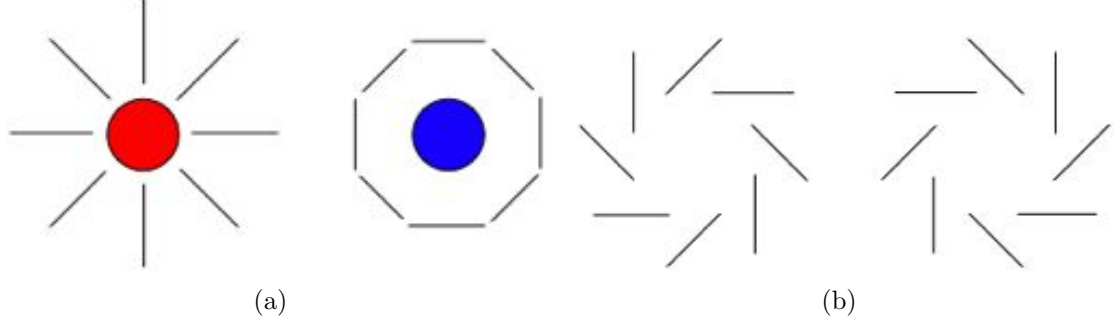


Figure 1-6: *a*: E-modes around a hot spot (left) and cold (right) spot. *b*: B-modes, left- and right- handed helicity states.

and the cleanest measurement of gravity waves from the CMB would come from a B-mode detection.

The two-point correlation functions of $T(\hat{n})$, $E(\hat{n})$ and $B(\hat{n})$ have the form:

$$C_\ell^{X,Y} = \frac{1}{2\ell + 1} \sum_m \langle a_{\ell m}^{*X} a_{\ell m}^Y \rangle ; X, Y \in T, E, B \quad (1.17)$$

This yields the auto- and cross-correlations between the temperature and polarization anisotropies expressed in spherical harmonics at a given multipole ℓ . The C_ℓ^{TT} angular power spectrum (hereafter: TT power spectrum) has been measured up to multipoles of $\ell > 8000$ (a large number of experiments have contributed to the TT spectrum measurement, the most recent measurements at high- ℓ are Refs. [27],[62]). The C_ℓ^{EE} angular power spectrum (hereafter: EE power spectrum) has been measured (Refs. [52], [78], [7], [74], [10], [16]), the C_ℓ^{BB} angular power spectrum (hereafter: BB power spectrum) has not been detected.

As discussed above, a measurement of the C_ℓ^{BB} power spectrum at angular scales $\ell \simeq 100$ would yield a measurement of the tensor-to-scalar ratio and hence a measurement of r and the energy scale of inflation. A lower bound on r will discriminate between inflationary models and rule out a large class of models. Although we do not know the energy scale of inflation (and hence how sensitive experiments must be to possibly measure it), we can predict constraints on the amplitude given a set of likely

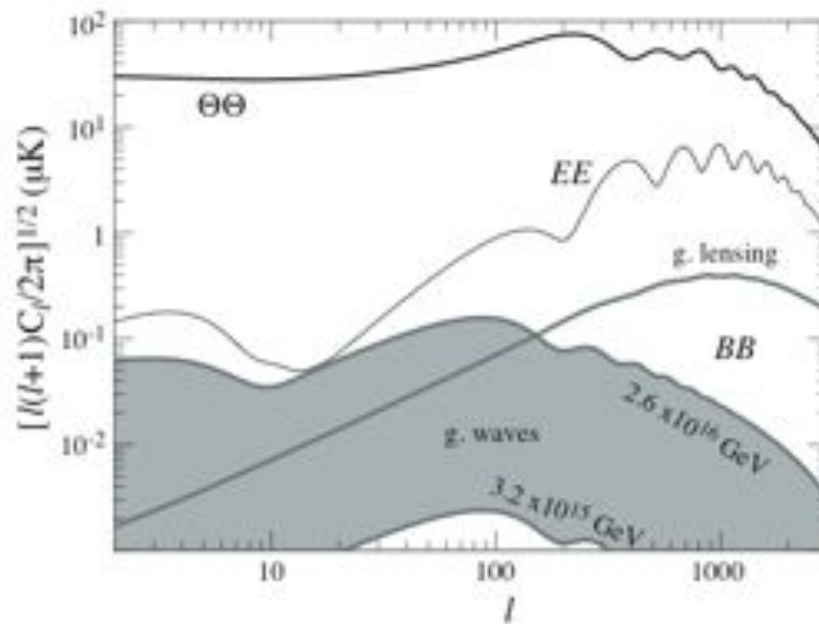


Figure 1-7: Figure from Ref. [40]. TT ($\Theta\Theta$) power spectrum, EE power spectrum, and region of possible BB power spectra shown in grey. Curves are theoretical for a standard Λ CDM cosmology. The BB spectrum is a combination of the primordial gravity wave signal, discussed in the text, and a spectrum generated by gravitational lensing of EE modes into BB modes.

inflationary models; these are shown in Figure 1-7. These models represent a particular case of compelling models, all of which would be ruled out by a non-detection of B-modes. This also shows the relative amplitudes of the TT ($\Theta\Theta$) and EE spectrum.

As the CMB photons traverse space, they can be scattered by local gravitational potentials (e.g. clusters, superclusters) which introduces leakage between the EE spectrum and BB spectrum on scales commensurate with large-scale structure angular sizes. The resulting BB spectrum is shown in Figure 1-7 peaking at small scales (labeled ‘g.lensing’). The BB spectrum from lensing is expected regardless of cosmological model given the measured EE spectrum and measurements of large-scale structure. Thus, the lensed spectrum can be used to probe the evolution of structure and possibly the expansion history of the Universe (Refs. [93], [37], for a review see [81]) and also represents a way to verify measurement and analysis techniques to demonstrate our ability to differentiate between the EE spectrum from the BB spectrum from a cosmological signal.

1.4 Foregrounds

The primary known sources of foreground contamination to the polarized CMB signal are synchrotron and dust emission. The spectral dependence of each foreground source is shown in Figure 1-8: synchrotron emission is the dominant foreground at lower frequencies, while dust dominates the foreground emission at higher frequencies. Many current CMB polarization experiments observe regions of the sky which have been measured to have low foreground emission in temperature (we do not yet have sensitive enough measurements of the polarized foregrounds so we need to extrapolate the expected signal from the temperature emission). As seen in Figure 1-9(b) the EE spectrum can be measured from clean patches of sky without careful attention to foreground subtraction, however measuring the B-mode signal (Figure 1-9(c) for $r \sim 0.01$) will possibly require measurement and cleaning of foreground emission. Most

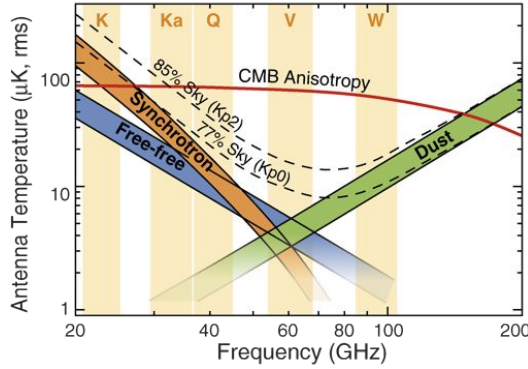


Figure 1-8: Figure from NASA/WMAP Science Team (Ref. [6]). Frequency dependence and amplitude of foreground emission. The CMB TT anisotropy power level is shown in comparison. The magnitude of the polarization anisotropy spectrum will be lower, and free-free emission is not strongly polarized.

current CMB polarization experiments have chosen to observe at multiple frequencies to measure the slope of the foreground emission dominant at their observing frequency to separate it from the signal.

1.5 CMB Science with QUIET

QUIET observes at 40 and 90 GHz (Q- and W-band). The QUIET Phase I Q-band array is the subject of this thesis. The Q- and W-band arrays comprise a pathfinder experiment for QUIET Phase II. The QUIET Phase I science goals include:

- Measure the first three peaks of the EE power spectrum σ .
- Place a competitive upper limit on the BB power spectrum, both the primordial and lensed signals.
- Measure or place upper limits on the amplitude of polarized synchrotron emission in the cleanest regions of the sky (we selected low-foreground-emission sky regions for observations).

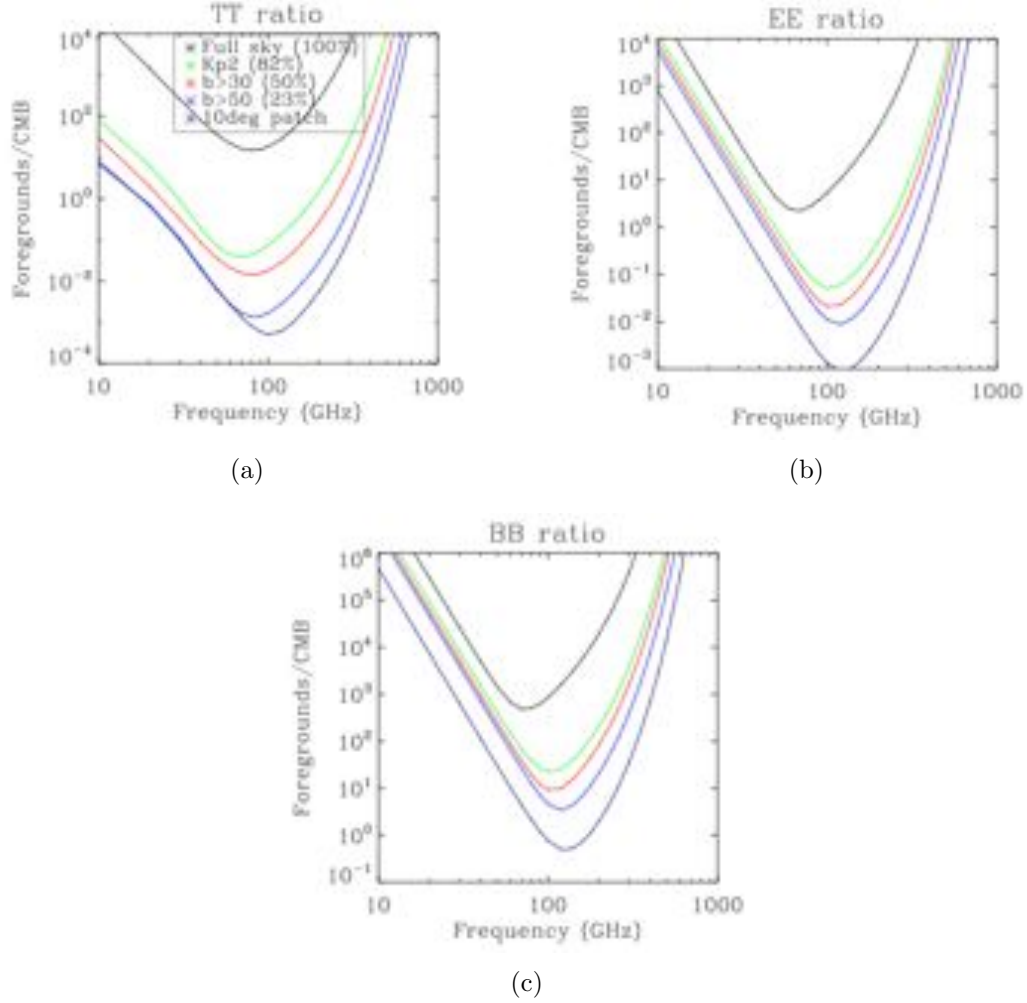
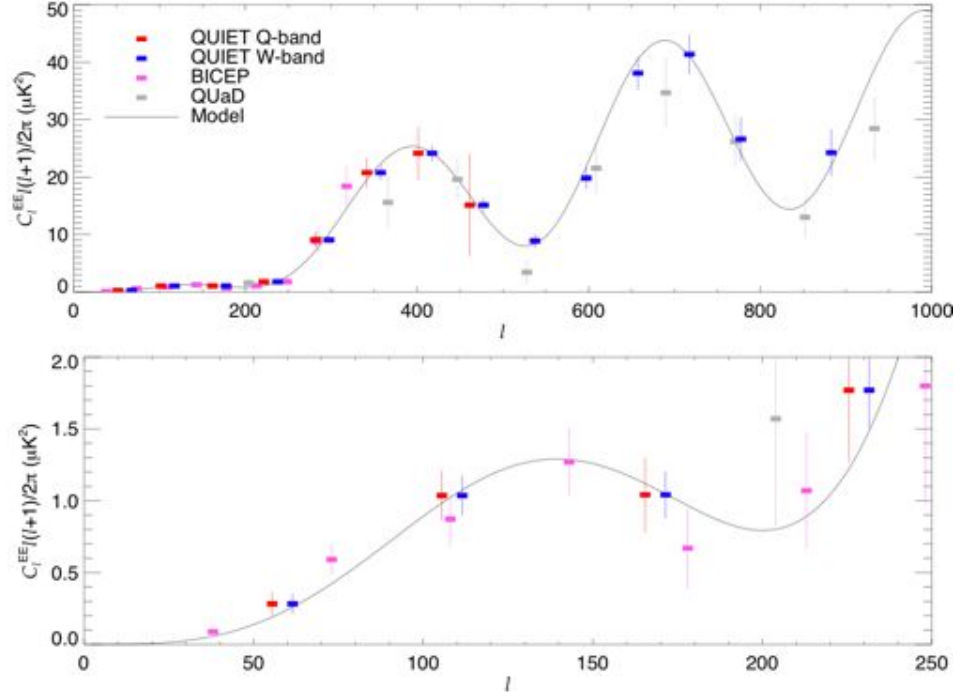


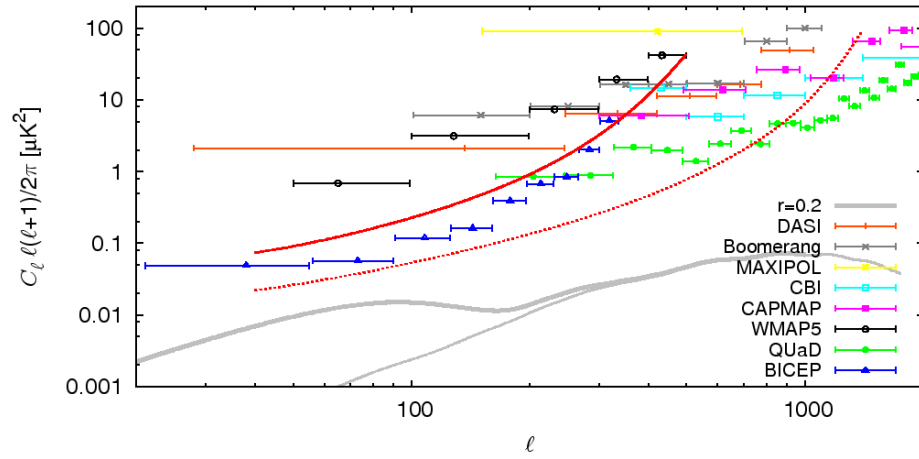
Figure 1-9: Figure from Ref. [25]. The ratio of foreground emission to CMB signal for: *a*: TT, *b*: EE, and *c*: BB power spectra at ℓ of 80-120 (where the primordial spectrum is predicted to peak) for various sky cuts. The lower frequency foreground contamination is dominated by synchrotron emission, while the higher frequency foregrounds are dominated by dust (as shown in Figure 1-8). The magnitude of the dust emission assumes a polarization fraction of 1-2%. The amplitude used for the BB spectra is computed assuming $r=0.01$. The black line shows the ratio for the full sky, in this case all CMB anisotropy power spectra are dominated by foregrounds. The green line shows the ratio for the WMAP sky-cut template known as KP2, for this case the emission is lower than the TT and EE anisotropy power, but dominates the BB spectrum. The same is true for sky regions including only galactic latitudes greater than $|30^\circ|$ (red line) and galactic latitudes greater than 50° (blue line). The most conservative sky cut, a 10° patch of sky centered around the ‘southern hole’ a region of minimal dust contamination, is the only region of sky in which the primordial BB power might dominate the foreground emission.

- Serve as a demonstration of technology and techniques for the larger QUIET Phase II experiment.

The Q-band data set is complete and the W-band measurements are underway, the expected bounds on the EE spectrum and BB spectrum are shown in Figures 1-10(a) and 1-10(b). The Q-band channel was designed as a foreground monitor, the BB spectrum from this receiver will not place a competitive bound on the amplitude of the BB power spectrum and resulting tensor-to-scalar ratio. The W-band channel with the data currently taken will place competitive bounds on the BB amplitude, and will measure the third peak of the EE spectrum with greater precision than current experimental results.



(a)



(b)

Figure 1-10: *a*: Expected EE measurement and error bars for Q-band and W-band arrays given the data already taken. The top panel shows angular scales from $0 < \ell < 1000$, the lower panel contains the region from $0 < \ell < 250$. The model assumes standard Λ CDM parameters (Ref. [51]). *b*: BB sensitivity curve for the Q-band receiver (solid red line) and W-band receiver (dashed red line) compared to recent experiments and to a BB spectrum with $r=0.2$. Both figures courtesy Akito Kusaka (Ref. [12]).

Chapter 2

The Q/U Imaging Experiment Instrument

This chapter addresses the QUIET Phase-I Q-band instrument and is organized as follows: section 2.2 contains a description of the telescope mirror design, the feed-horn array, the orthomode-transducers (OMTs), and hybrid-tee splitters; section 2.3 describes the QUIET Q-band polarimeters, signal processing, and polarimeter systematics. Section 2.5 details the electronics boards that power the module components and perform data acquisition functions, and section 2.6 contains a description of the cryostat, which maintains the polarimeters at constant cryogenic temperatures during observations.

2.1 QUIET Q-band Instrument Overview

The QUIET Q-band instrument consists of a receiver array including feedhorns, two focusing mirrors, and bias and data acquisition cards. The receiver comprises a hexagonal array of 19 High Electron Mobility Transistor (HEMT)-based polarimeters and orthomode transducers (OMTs) coupled to a feedhorn array.

Light from the sky first is focused by a set of dual-reflecting 1.4-m diameter mir-

Description	Q / W
Frequencies	40 / 90 GHz
# of Detectors	17 Pol. and 2 hybrid-Tee / 84 Pol. and 6 hybrid-Tee
Telescope	Cross-Dragone
Angular Resolution	27 arcmin / 12 arcmin
Field Centers	181°/-39°, 78°/-39°, 12°/-48°, 341°/-36° (J2000 RA/Dec)
Field Size	15° × 15°
Instrument Sensitivity	64 μ K \sqrt{s} / 57 μ K \sqrt{s}

Table 2.1: QUIET Phase I instrument and observations overview. The values for the W-band array, when different, are also included. Pol. indicates polarization-sensitive modules.

rors through the cryostat window. It impinges upon a set of corrugated feedhorns, and is directed into septum polarizer OMTs, which separate radiation into left- and right-circularly polarized components, and is then guided into the two input legs of a QUIET polarimeter. The signal is amplified, phase-modulated, and read out in each QUIET polarimeter. The Q-band receiver dedicates one pair of polarimeters (hereafter: hybrid-Tee channels) to the observation of the CMB temperature anisotropy spectrum. The signal is differenced at the phase switching rate, providing mitigation of systematics which arise from lower-frequency noise drifts. As will be shown in section 2.3, differencing also allows us to simultaneously measure both Q and U Stokes parameters while observing the sky, which has helped keep our optical chain simple.

Salient characteristics of the QUIET Phase I experiment are shown in Table 2.1, quantities in this table will be discussed further in this chapter, except for the locations of the sky regions, whose field centers and size are discussed in Chapter 4, and the instrument sensitivity, which is discussed in Chapter 5. A view of the receiver array and cryostat, two mirrors, and electronics enclosure is shown in Figure 2-1(a), and figure 2-1(b) shows the cryostat and two mirrors. The numbering scheme for the Q-band array, including its physical indexing during observations, is given in Figure 2-2.

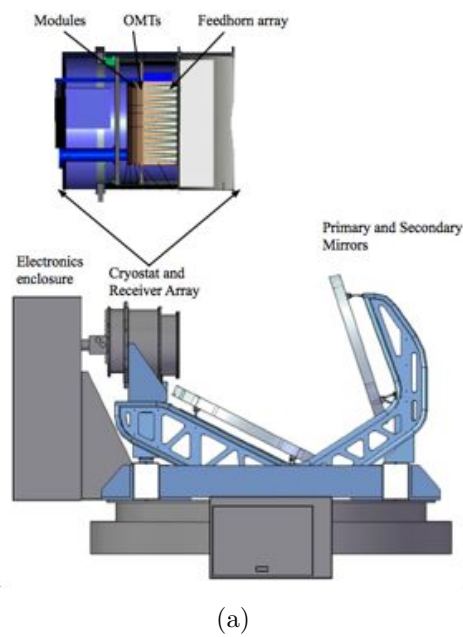


Figure 2-1: *a*: Schematic of the QUIET instrument, showing the electronics enclosure, cryostat, and mirrors. A view of the inside of the cryostat is shown as well, detailing the feedhorns, OMTs and polarimeter modules. *b*: Photograph of the cryostat (the top section had been removed for a measurement when the photograph was taken, allowing a view of the hexagonal array of feedhorns) and mirrors.

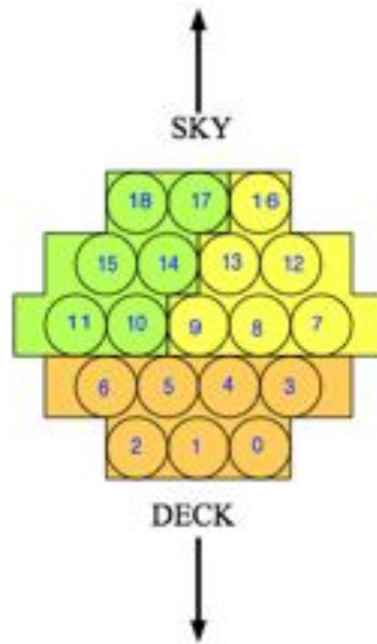


Figure 2-2: A schematic showing the physical location of the modules, the bottom and top rows are parallel to the ground. Modules RQ00-RQ02 are located at the bottom of the array (closer to the telescope deck); RQ16-RQ18 are located at the top of the array (further from the telescope deck). The color coding shows which sets of modules are biased by the same set of bias and data acquisition boards. Each feedhorn array is a hexagonal pattern, where the number of horns goes as $H_{\text{feeds with } N \text{ rings}} = 3*N^2 + 3N + 1$ (the indexing is such that 0 rings has 1 horn).

2.2 QUIET Optical Chain

2.2.1 Introduction

The QUIET optical chain consists of a Cross-Dragone side-fed dual-reflector system coupled to an array of diffusion-bonded corrugated feeds. The feedhorns attach either to a set of septum polarizer ortho-mode transducers (OMTs) or to hybrid-Tee assemblies. The output of those optical elements is directed into the QUIET polarimeters. The measured performance of the system is found to be consistent with simulations and all optical systematics are within the required specification to meet QUIET Phase I science goals.

This section will address each of the components in the QUIET optical chain, including design principles, expected performance, the design realization, and resulting sources of systematic error. Measurements presented in this section are based on laboratory measurements; confirmation with astronomical calibrators during the course of the observing season will be discussed in chapter 5.

2.2.2 Telescope Optics

Terminology

- Co-polarization: the fraction of linearly polarized light transmitted for a particular polarized state (E_x or E_y) given an input of the same state (E_x or E_y).
- Cross-polarization: the fraction of linearly polarized light transmitted for a particular polarized state (E_x or E_y) given an input of the orthogonal state (E_y or E_x). Typically this is used as a measurement of leakage from one polarization state to the other. Cross-polarization leakage in an optical system is typically quoted between linear polarization states E_x and E_y . For CMB polarization systematics studies, we will also use the linear polarization Stokes Q and U parameters to describe cross-polarization.

Parameter	Description	Value
D	projected aperture of primary mirror	1.47 m
e_s	eccentricity of the (hyperbolic) secondary	2.244
ℓ	distance between the two mirrors	1.27 m
θ_0	offset angle of the primary	-53°
θ_e	angle at which the feed sees the edges of the secondary	37°
θ_p	angle between boresight of the feed and the axis of the secondary	-90°

Table 2.2: Parameters for the QUIET mirror design, see Ref. [42]. Positive (negative) angles are counterclockwise (clockwise) directions. These parameters are defined in the Cross-Dragone design schematic in Figure 2-3(a).

- Spill-over: Any part of the beam which can ‘spill’ past an optical element, illuminating regions other than the pointing of the main beam.
- Differential Ellipticity: the ellipticity of the beam for one linear polarization state compared to the ellipticity of the beam for the orthogonal polarization state.

Telescope Design Overview

The QUIET telescope design is a dual reflector Cross-Dragone system. The Cross-Dragone design has numerous advantages for our polarization measurements (Ref. [14]):

- minimal spill-over past the mirrors
 - limits pathways into the receiver from emission from scan synchronous signals (e.g. the ground) and astronomical sources (e.g. the sun, moon).
- minimal cross-polarization characteristics
- uniform illumination across a large focal plane
 - Optical distortions (such as astigmatism) can cause various forms of systematic errors, including increased cross-polarization. A flat beam characterized by uniform mirror illumination will reduce these systematics.

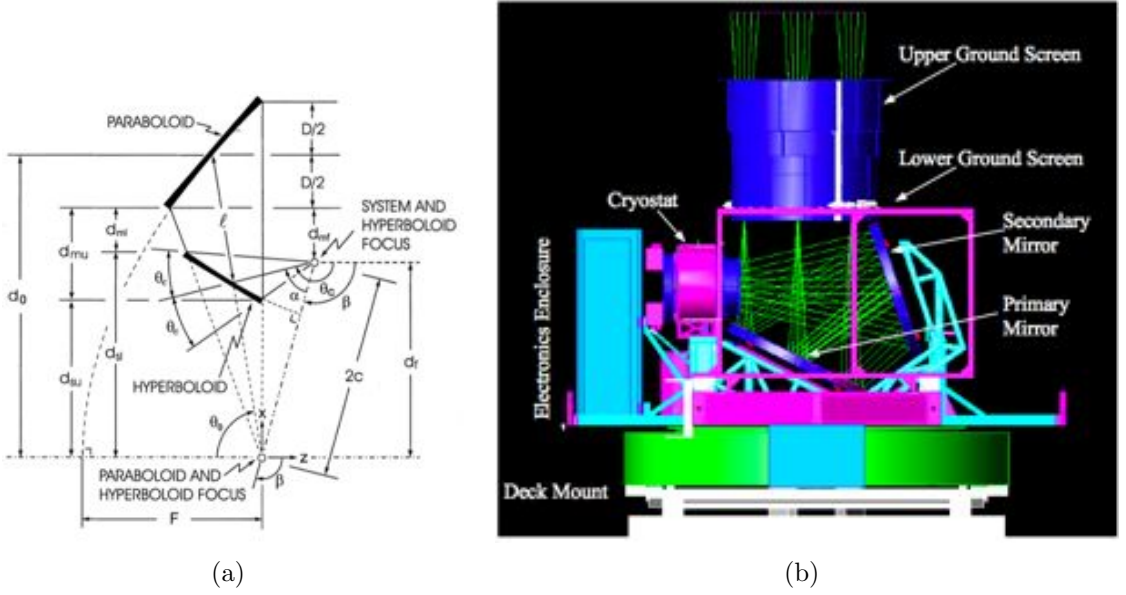


Figure 2-3: *a*: Cross-Dragone telescope design schematic. Shown are the parameters which define the design (Ref. [14]). Only five of the parameters are independent, typically the five parameters chosen to characterize a Cross-Dragone system are: D , ℓ , θ_0 , θ_p , and θ_c . QUIET has a side-fed version: $\theta_c \equiv -90^\circ$ (front-fed designs have $\theta_c \equiv 180^\circ$). *b*: QUIET telescope, utilizing the Cross-Dragone design. Shown are a model of the cryostat, the primary and secondary mirrors, the support structure, and the ground screens. Courtesy Keith Thompson.

The generalized Cross-Dragone mirror geometry is shown in Figure 2-3(a); it is characterized by a confocal concave hyperboloid subreflector with a parabolic main reflector (Ref. [14], [13]). The mirror design and support structure for QUIET are shown in Figure 2-3(b); each mirror is made from a single piece of aluminum 6061 and support structures are steel. A ray trace of the optical path through the telescope system is shown in Figure 2-3(b): the thin green lines show light originating from the sky (top of the figure) and incident on the primary mirror, reflecting into the secondary, and terminating in the cryostat. The image formed in the cryostat is inverted from the image on the sky. The design parameters for the QUIET telescope are given in Table 2.2.

Optical Design Goals and Systematics Limits

We determined a set of requirements for the optical design based on the science goals for QUIET. These include:

- Beam Size:** The diameter of each mirror was chosen such that QUIET would be able to measure the first three peaks of the E-mode polarization spectrum with the W-band receiver: with effective diameters of around 1.4m, the simulated beamsize for the central horn at 42 GHz is 27.9 arcmin and 12.6 arcmin at 90 GHz, corresponding to multipoles of up to $\ell \simeq 500$, $\ell \simeq 900$, respectively. The beamwidth of the system has been measured with astronomical calibrators during the observing season, those values will be discussed in chapter 5 and are consistent with these design specifications.
- Differential ellipticity:** Differential ellipticity will cause one polarization state to be transmitted preferentially relative to the perpendicular polarization state, systematically rotating the polarization direction of the incoming radiation. Contributions from this instrumental polarization can be minimized by choosing an observation strategy with multiple observing angles, as the polarization from differential ellipticity will rotate with the telescope and so, unlike the sky signal, will not remain constant in celestial coordinates. We require the differential ellipticity to be $< 10^{-3}$ (Ref. [22]).
- Cross-polarization leakage:** this can contribute in much the same way as differential ellipticity, the design requirement is that this systematic is < -40 dB (0.01%) (Ref. [22]).
- Mirror Surface Quality:** The surface of the mirrors was specified to have distortions less than ± 0.2 mm and an RMS surface finish of 0.02mm-per-cm, corresponding to $\frac{\lambda}{37.5}$ and $\frac{\lambda}{375}$ -per-cm (Q-band) and $\frac{\lambda}{17}$ and $\frac{\lambda}{167}$ -per-cm (W-band).

2.2.3 Feedhorns and Interface Plate

Feedhorn Array

Corrugated feedhorns impedance-match free-space radiation to waveguide. The Q-band feedhorn array is a set of 19 corrugated feeds in a hexagonal pattern. A cut-away view of the Q-band feedhorns is shown in Figure 2-4(a). Corrugated feeds generally exhibit:

- High gain (> 26 dB)
- Minimal cross-polarization (generally better than -35 dB)

Typically, machining corrugations into the feedhorns is difficult and expensive given their long, narrow profiles. Instead, they are generally formed via a process known as electroforming: a mandrel is made such that its outer profile is the cast of the desired inner dimensions of the feedhorn and metal (usually aluminum) is deposited onto the mandrel. The mandrel is then dissolved, leaving a metal shell with corrugations.

Electroforming is expensive, so we have taken a different approach: A set of plates is machined such that each plate will have 19 holes with a few easily machined corrugations. These plates are stacked and diffusion-bonded together such that they form a monolithic feedhorn array with a corrugated feed profile for each polarimeter. A picture of the Q-band feedhorn array after diffusion bonding is shown in Figure 2-4(b).

Laboratory measurements of the co- and cross-polarization characteristics for one horn are shown in Figure 2-5(a) where E-plane and H-plane refers to the linear polarization inputs. Detailed measurements of the return loss and beam characteristics of these horns show that they perform well in comparison to a electroformed horn of the same design (Figure 2-5(b)), while the combined cost of machining and diffusion bonding these arrays is at least an order of magnitude less than the cost of producing the same number of electroformed feedhorns.

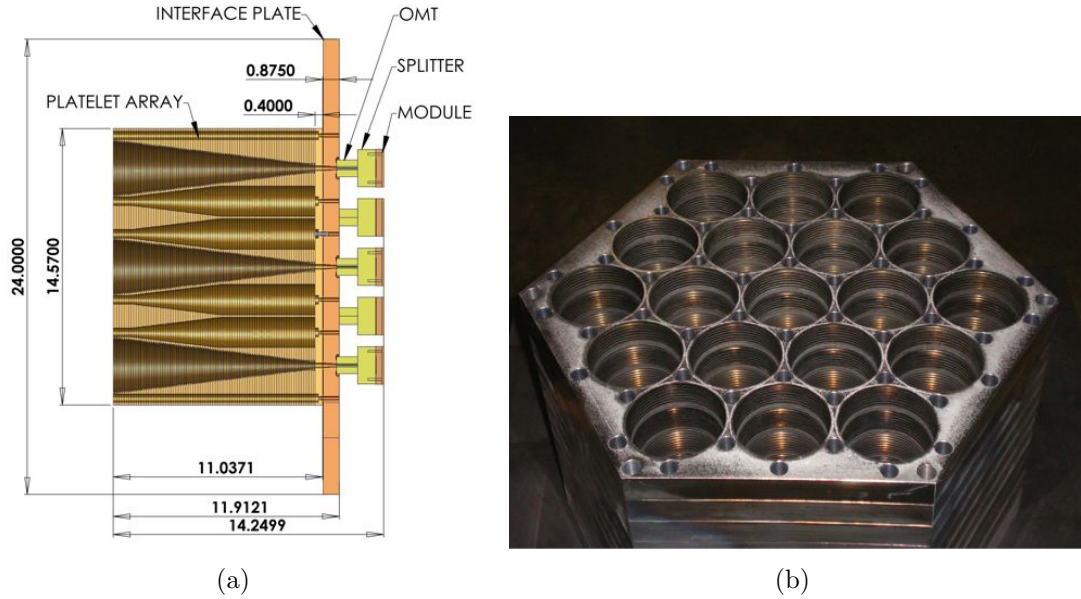


Figure 2-4: Q-band feedhorns *a*: Cut-away and *b*: Photograph after diffusion bonding. Note the corrugations inside of the large plates, each forming a layer of the corrugated feedhorn set (courtesy Josh Gundersen).

Interface Plate

The feedhorn array attaches to an interface plate that serves as a cryogenic attachment point for the polarimeters, and has 19 holes which form circular-to-circular transitions between the narrow diameter of the feedhorns and the (smaller) diameter of the waveguide aperture of the septum-polarizer OMTs (Section 2.2.4).

2.2.4 Ortho-mode Transducer Assemblies

Light from the interface plate is directed into either a septum-polarizer ortho-mode transducer (OMT) assembly or a hybrid-Tee assembly (Section 2.2.5). Each of the 17 Q-band septum polarizer OMT assemblies transform linearly-polarized into circularly-polarized light which is then directed to a QUIET module (Section 2.3). A septum-polarizer OMT assembly has two main components (Figure 2-6): a septum-polarizer OMT (1 inch×1 inch) and a waveguide splitter (1 inch×2 inches). A schematic of the septum polarizer OMT is shown in Figure 2-7(a), it consists of a square waveguide

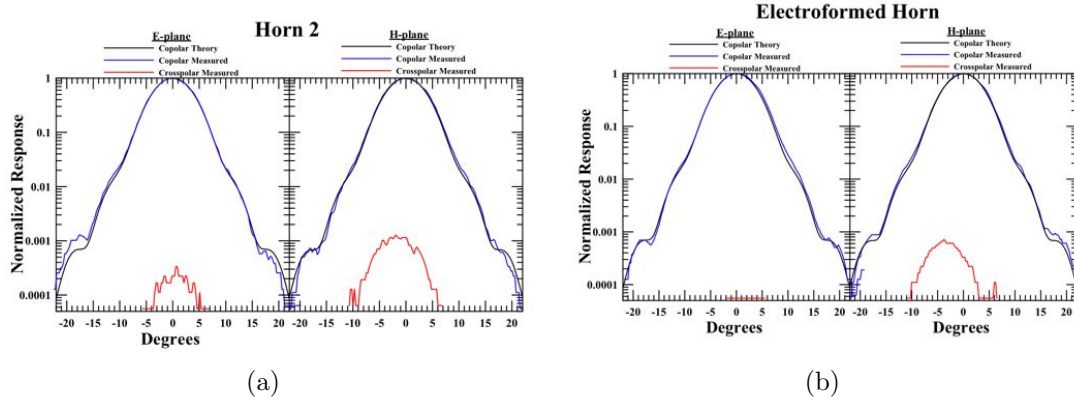


Figure 2-5: Measured Co- and Cross-polarization patterns for *a*: horn # 2 and *b*: an electroformed horn. Courtesy Josh Gundersen.

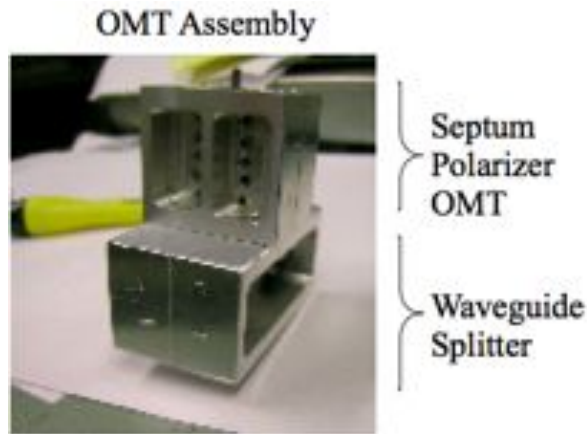


Figure 2-6: Photograph of the septum polarizer OMT assembly (courtesy Glen Nixon).

with a septum (a thin aluminum piece with a stair-shaped profile) in the center. The port definitions are also shown in Figure 2-7(a) and are labelled E_1 - E_4 :

- E_1 is the signal at the horn/OMT interface which is polarized parallel to the septum (TE_{01} mode, H-plane polarized)
- E_4 is also at the horn/OMT interface but is polarized perpendicularly to the septum (TE_{10} mode, E-plane polarized)
- E_2 and E_3 are at the OMT/splitter interface and are left- and right-circularly

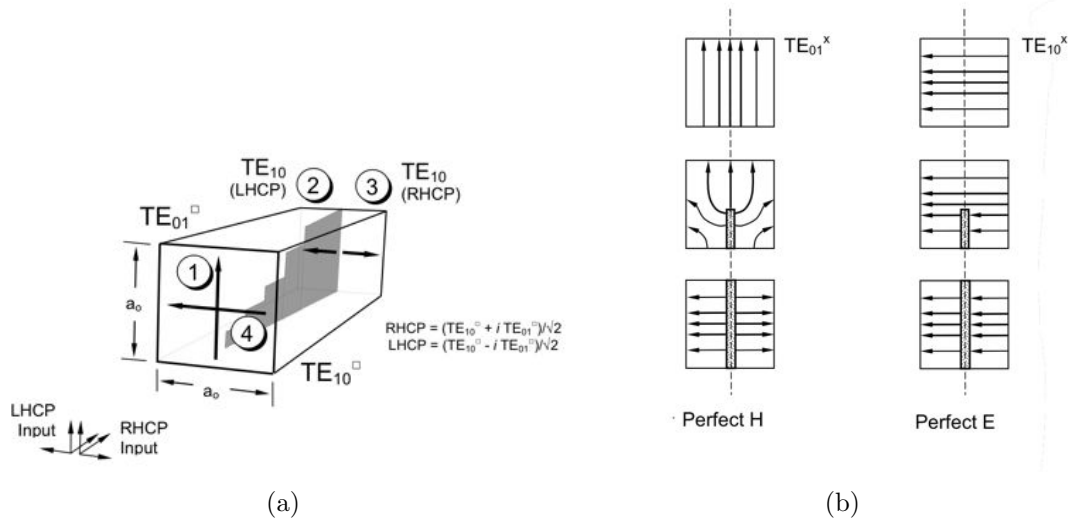


Figure 2-7: Septum Polarizer *a*: geometry and port definition (input ports 1, 4 and output ports 2, 3) and *b*: E- and H- plane septum polarizer excitation. The top panels show the input modes to the OMT, the middle and bottom panels show the action of the septum on the two modes. Courtesy Ed Wollack.

polarized, respectively.

The output ports 2 and 3 of the septum polarizer OMT are attached to a waveguide splitter. The splitter transitions from the narrow waveguide spacing of the septum-polarizer component to the wider waveguide separation of the module input feeds.

The function of the septum is shown in Figure 2-7(b): the TE_{10} waveguide mode is unchanged as it propagates through the OMT cavity and is simply split in two by the septum. The TE_{01} waveguide mode acquires a $\frac{\pi}{4}$ phase factor as it bends around the septum. The resulting rectangular waveguide outputs are a combination of the two states, and will be circularly polarized: $RHCP = \frac{TE_{10} + jTE_{01}}{\sqrt{2}}$ and $LHCP = \frac{TE_{10} - jTE_{01}}{\sqrt{2}}$.

A perfect OMT has scattering matrix, S^{ideal} (Ref. [49]):

$$S^{ideal} = \frac{1}{\sqrt{2}} \begin{pmatrix} 0 & 1 & 1 & 0 \\ 1 & 0 & 0 & i \\ 1 & 0 & 0 & -i \\ 0 & i & -i & 0 \end{pmatrix}$$

With basis vectors:

$$E^{OMT-basis} = \begin{pmatrix} E_1 \\ E_2 \\ E_3 \\ E_4 \end{pmatrix} = \begin{pmatrix} H-plane \\ LHCP \\ RHCP \\ E-plane \end{pmatrix}$$

In practice, the OMT will have reflections and losses at each port:

- r_1 : the reflection at port 1
- r : the reflection at either of the OMT output ports 2 and 3
- c : cross talk between the OMT output ports 2 and 3
- t_1 : the transmission at input port 1
- t_4 : the transmission at input port 4
- r_L : the reflection between the one leg of the module and OMT output port 2
- r_R : the reflection between the other leg of the module and OMT output port 3
- g : the combined transmission from both ports of the OMT

When taking these into account, the resulting scattering matrix, S (Ref. [1]) will be:

$$S = \begin{pmatrix} r_1 & t_1 & t_1 & 0 \\ t_1 & r & c & t_4 \\ t_1 & c & r & -t_4 \\ 0 & t_4 & -t_4 & r_4 \end{pmatrix}$$

The effect of the true scattering matrix can be parametrized by the following quantities:

$$\begin{aligned}
\theta &\equiv \arg(t_1^* t_4) \approx 90^\circ \\
g &\equiv |t_1|^2 + |t_4|^2 \approx |t_1||t_4| \\
C &\equiv r_L^* C^* + r_R C \\
D &\equiv |t_1|^2 - |t_4|^2
\end{aligned}$$

such that the Stokes vectors (Q, U, I) will be slightly transformed as a result of these non-idealities into Q' , U' as:

$$Q' = gQ + |Re(C) + D|I \quad (2.1)$$

$$U' = g \sin(\theta)U + Im(C)I \quad (2.2)$$

thus g is a measure of the total transmission such that its maximum value should be 1, therefore $1-g$ encodes the deviation from perfect transmission. θ gives the angle between the two output states, it should be 90° , therefore $1-\sin(\theta)$ encodes the phase introduced by the OMT. D is a measure of difference between the amplitudes of the transmitted states and C is a measure of the reflection at the output port of the OMT; both will lead to leakage from total power into polarization. Representative values for these quantities for the Q OMT are $1 - g = -10$ dB, $1 - \sin(\theta) = -19$ dB, $D = -20$ dB, $Re(C) = -35$ dB (Ref. [69], [20]). Thus we expect total power leakage on the order of 1% from D , which will contribute only to leakage into the Stokes Q parameter. The $1 - g$ value indicates we lose 10% of the signal through losses in the OMT.

The lower edge of the bandwidth of the OMT is limited by the lowest frequency the TE_{10} mode of the OMT can support. This is given by the dispersion relation

(Ref. [43]):

$$\omega_{10} = 2\pi\nu = \frac{c\pi}{a} \quad (2.3)$$

where a is the longest dimension of the waveguide. In the OMTs, $a=0.1636''$, which gives a cutoff frequency of 36 GHz. The upper edge of the bandwidth is limited by the excitation of the TE_{11} and TM_{11} modes. The TE_{11} and TM_{11} waveguide modes produce a resonance at 46 GHz, which was apparent as a spike at 46 GHz in all OMT systematics quantities (Ref. [69]).

2.2.5 Hybrid-Tee Assembly

The QUIET Q-band array contains one hybrid-Tee assembly which couples the output of two horns before sending the signal into two modules. The processing and resulting signal will be discussed further in section 2.3 where it will be shown that the hybrid-Tee assembly measures the difference in temperature between the two horns and maintains sensitivity to the Stokes Q parameter. Measuring the temperature difference between the horns gives a measurement of the CMB temperature anisotropy, and is useful for essential data quality checks such as weather and sidelobe emission.

A schematic of the waveguide signal coupling is given in Figure 2-8(a) and a photograph is shown in Figure 2-8(b). The full assembly has two X-Y Ortho-mode transducers (distinct from the left-right septum-polarizer OMTs discussed in Section 2.2.4) and two hybrid-Tees. An X-Y orthomode-transducer couples to the output of the feedhorn and splits the light into E_x and E_y linear polarization states. The E_y linear polarization state is transmitted to a Hybrid-Tee sitting below its X-Y OMT, and the E_x polarization state is transmitted to the neighbor Hybrid-Tee. The Hybrid-Tee will sum the two inputs and output that to one port, and difference the inputs and output that to a second port. The scattering matrices of these elements are:

$$S^{XY-OMT} = \begin{pmatrix} 1 & 0 \\ 0 & 1 \end{pmatrix}$$

$$S^{hybrid-Tee} = \frac{1}{\sqrt{2}} \begin{pmatrix} 1 & 1 \\ 1 & -1 \end{pmatrix}$$

With basis vectors:

$$E^{input} = \begin{pmatrix} E_{x,i} \\ E_{y,j} \end{pmatrix}$$

where x, y denotes polarization state and i, j denotes horn number. Thus the output of the hybrid Tee assembly is: $E_{y,1} - E_{x,2}$ and $E_{y,1} + E_{x,2}$ to one module, and $E_{y,2} - E_{x,1}$ and $E_{y,2} + E_{x,1}$.

Interfaces

Both cryostats are mounted on the telescope such that the phase center of the feedhorn array are located at the focal point of the mirrors. The phase center of the W-band feedhorn array is 5 cm below the top face of the horns, and 11 cm for the Q-band array. Because the Q-band cryostat is taller than the W-band cryostat, the Q-band cryostat projects over the primary mirror by 3 inches. It was determined from optical simulations that this would not impact instrument performance.

2.2.6 Optics Performance

Optics Simulations: Beams and Spillover

Beams

Physical Optics (PO) simulations were performed at 40 and 90 GHz to assess the performance of the QUIET optical design. The mirror design (section 2.2.2) and final parameters for the corrugated horns (section 2.2.3) were used for this simulation, none

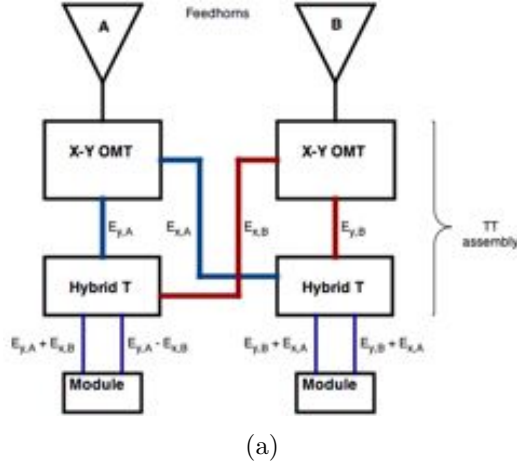


Figure 2-8: *a*: Schematic of the TT assembly. Horns A and B are adjacent horns in the array; the OMT assembly couples the E_x polarization from the horn above to the E_y polarization output of the neighboring horn. This gives the modules attached to the TT assembly sensitivity to the difference in temperature between the two horns, and also maintains sensitivity to the Stokes Q parameter, as will be discussed in Section 2.3. *b*: Photograph of an X-Y OMT and hybrid-T assembly: one half of the TT assembly.

of the other optical components (OMTs, TTs, or modules) were included. For the current Q-band array, simulations show the 3 dB half-power bandwidth (HPBW) is 28 arcmin and cross-polarization is -49 dB below the co-polar peak. The beam ellipticity, which characterizes the width of the beam in one spatial direction compared to the orthogonal direction, is <1% and the peak gain of the telescope, which describes its focusing power, is estimated to be $\simeq 52$ dB across the surface (Ref. [42]). Analysis of measurements during observations in Chile of calibration sources are consistent with these values, the beamwidth is slightly smaller and the ellipticity is slightly larger (section 5.9). The primary mirror has a -30 dB edge taper and the secondary a -40 dB edge taper for W-band, and would be similar but slightly larger for Q-band (the value for the Q-band array from the simulations was not given).

Beam performance will change with location in the focal plane. To evaluate the effects of cross-polarization leakage on the edge horns, two simulations with orthogonal polarization states were performed: they are denoted as ‘ E_x ’ and ‘ E_y ’ (as the horn looks at the secondary, ‘ E_x ’ is in the horizontal direction and ‘ E_y ’ is in the vertical direction). With an input state of ‘ E_x ’, the simulated response can be measured in the parallel polarization state, yielding a measurement of co-polar beam throughput and ellipticity for one polarization input state. A simulation with an input state of ‘ E_x ’ and a measured response in the orthogonal state yields a measurement of the cross-polarization characteristics of the system. This can be repeated with an input of ‘ E_y ’ and measurements in ‘ E_y ’ and ‘ E_x ’. The differences in beam ellipticities between the two co-polar measurements is the differential ellipticity. The results of the simulation are summarized in Table 2.3 and the beam shapes for the central horn and an edge horn can be seen in Figure 2-9.

Horn	Input polarization	HPBW arcmin	ellipticity	Peak cross-pol dB	Peak gain dB
center	E_x	27.9×27.8	0.004	-44.9	52.1
edge	E_x	28.1×27.9	0.010	-42	52.0
edge	E_y	28.1×27.9	0.006	-41.9	52.0

Table 2.3: Simulated beam characteristics for Q-band system at 42 GHz with 19 elements in 3 rings (Ref. [22]). The values for the ‘ E_y ’ input state for the central horn to appear in Ref. [20].

As noted in Section 2.1, the Q-band array is composed of a hexagonal pattern with three rings (here ring denotes a hexagonal annulus around the central horn). The beam ellipticity as a function of ring number is given in Figure 2-10(a). Similar plots for the variation of the cross-polarization leakage as a function of ring number are shown in Figure 2-10(b). Differential ellipticity and cross-polarization leakage are within specifications (0.1% and -40 dB, respectively, given in section 2.2.2) for all pixels in both the W-band and Q-band arrays for this design.

Spillover (Sidelobes)

The Cross-Dragone design minimizes sidelobe power, but does not eliminate it.

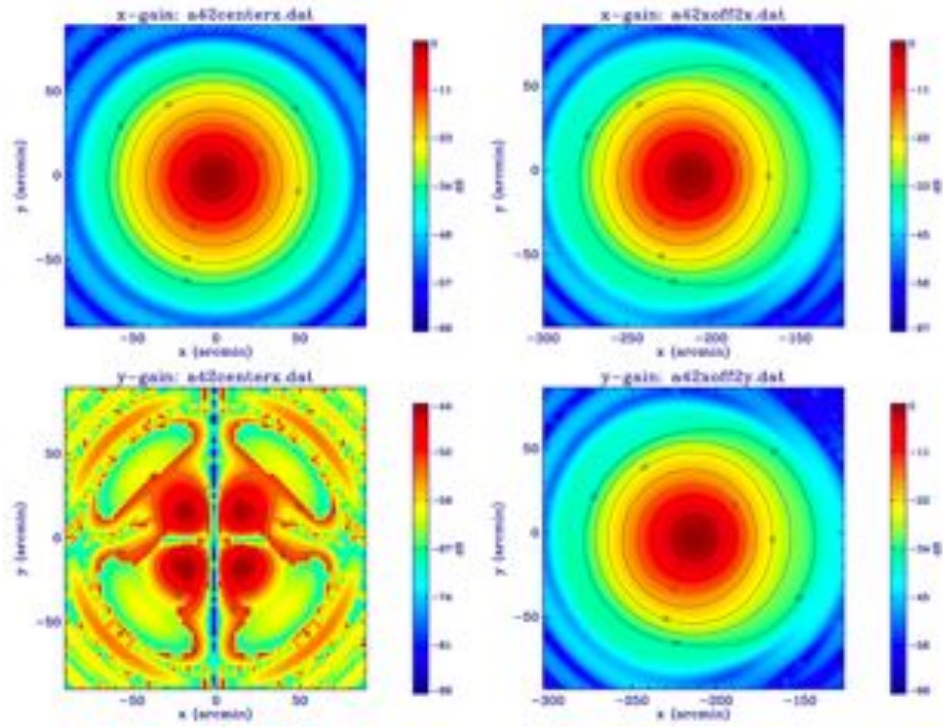


Figure 2-9: *Upper left* Central horn co-polar beam *Upper right* Edge horn co-polar beam, ‘ E_x ’ linear polarization input *Lower left* Central horn cross-polar beam *Lower right* Edge horn co-polar beam, ‘ E_y ’ linear polarization input at 42 GHz. The peak is normalized to 0 dB and last contour line drawn is -35 dB from the peak. The co-polar response from the edge horn is distorted near the beam edge compared to the central horn’s co-polar beam. The central-horn cross-polarization beam is -42 dB below the co-polar peak, and has a distinctive but expected quadrupolar pattern. This visualization of the cross-polarization beam was not available for the edge horn, but the beam performance is given in Table 2.3. Courtesy Clive Dickinson (Ref. [22]).

Simulations (Ref. [39]) show that we expect power from a number of sidelobe regions. The signal can be contaminated by sources coincident with the sidelobe structure, for example if a portion of the sidelobe structure is pointed at the ground or an astronomical source (such as the sun or moon). Mitigation of the effects of these sidelobes will be discussed in Section 2.2.6. The coordinate system we will use for most of our sidelobe definitions is shown in Figure 2-11(a) and 2-11(b). $\theta=0$ corresponds to the main beam (‘boresight’) of the telescope, with the telescope pointing directly at the source, and ϕ rotates around the boresight. Figure 2-12 shows the beam profile:

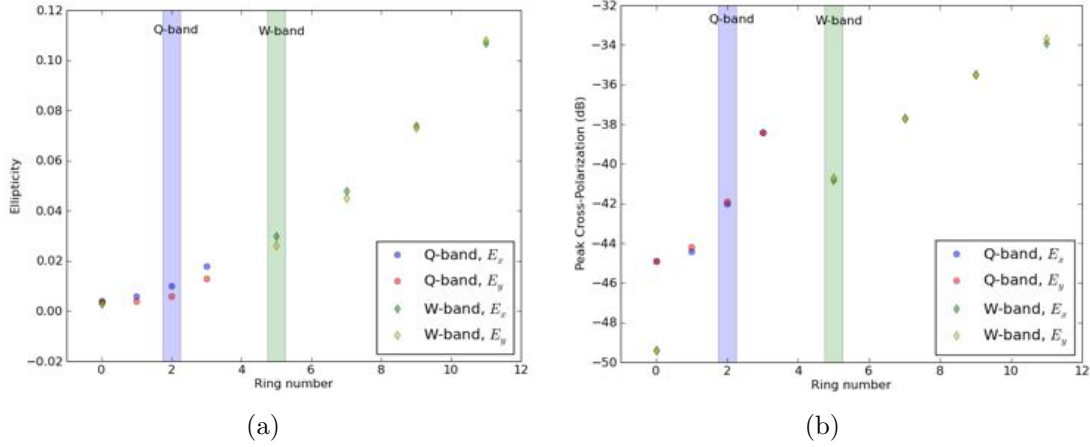


Figure 2-10: *a*: Ellipticity and *b*: Cross-polarization as a function of ring number for Q- and W- band arrays, ' E_x ' and ' E_y ' input polarization states. The vertical distance between the points gives a measure of differential ellipticity. The purpose of the simulations was to investigate the ellipticity and cross-polarization for larger arrays meant for QUIET Phase II, and assess the values for the current Q-band and W-band arrays. The ring number is indexed from zero, so the expected performance of the current Q-band system has ring index = 2 and is highlighted, the current and the 91 element W-band array has ring index=5 and is also highlighted. The first four rings of the W-band system were not simulated because 91 elements is the smallest number of radiometers we would consider to remain competitive with other experiments, and large ring numbers for the Q-band modules are not physically feasible.

the power a receiver would detect with a source located at an angle θ away from the optical axis of the system. For this plot, two directions were considered to chart the sidelobes: the E- and H-field directions as shown in Figure 2-11(c). The E-field simulation corresponds to scanning a source along the E-field axis of the telescope, and the H-field simulations corresponds to scanning a source along the H-field axis of the telescope, as you move the source from $\theta = -90$, to the on-axis position ($\theta = 0$), and to $\theta = 90$. With the telescope deck angle set such that the secondary mirror is parallel with the ground, the H-plane input state would correspond to scanning the telescope in azimuth across a source and the E-plane input state would correspond to scanning the telescope in elevation across a source. Simulations show that the sidelobes are aligned along the E-plane of our telescope (Figure 2-12). This is because

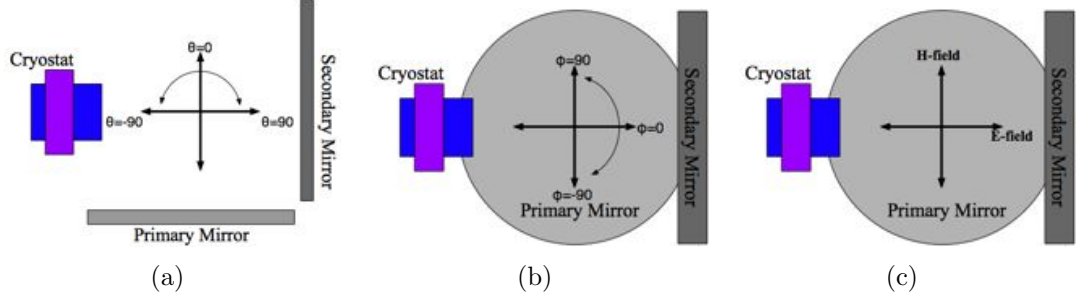


Figure 2-11: *a*: definition of θ coordinate *b*: definition of ϕ coordinate. *c*: E- and H-plane definitions for sidelobe simulations.

the symmetric axis of our telescope is aligned with the H-plane, while the E-plane axis contains effects from asymmetries in the design (e.g. the tilt of the mirrors). The corresponding positions of the expected sidelobe features are shown Figure 2-13:

1. $\theta=-50$ **'triple reflection' sidelobe** (-45 dB from peak) Corresponds to sidelobe #1 in Figure 2-13.
2. $\theta=65, 110$ **spillover past the secondary mirror** (-50 dB from peak). Corresponds to sidelobes # 2a, 2b respectively in Figure 2-13.
3. $\theta=-120,-135$ **spillover past the primary mirror** (-45 dB from peak). Corresponds to sidelobes # 3b, 3a respectively in Figure 2-13.

We can gain additional insight from a 2D plot of the sidelobe locations, including the shape of each of these lobes. The full two dimensional sidelobe structure can be seen in the combination of Figures 2-14(a) and 2-14(b). Each figure is half of the sphere, in our coordinate system one half-sphere is defined as $-90^\circ < \theta < 90^\circ$ and the other as $-90^\circ < \phi < 90^\circ$. The sidelobes above the platform are shown in Figure 2-14(a). The bottom half of the sphere, the sidelobes below the deck, are shown in Figure 2-14(b). The structures seen in the map can be related to the peaks seen in the beam profile (Figure 2-12):

1. The feature stretching across ϕ at a $\theta=0$ in Figure 2-14(a) is the main beam: a constant θ and the full span of ϕ from 0 to 2π

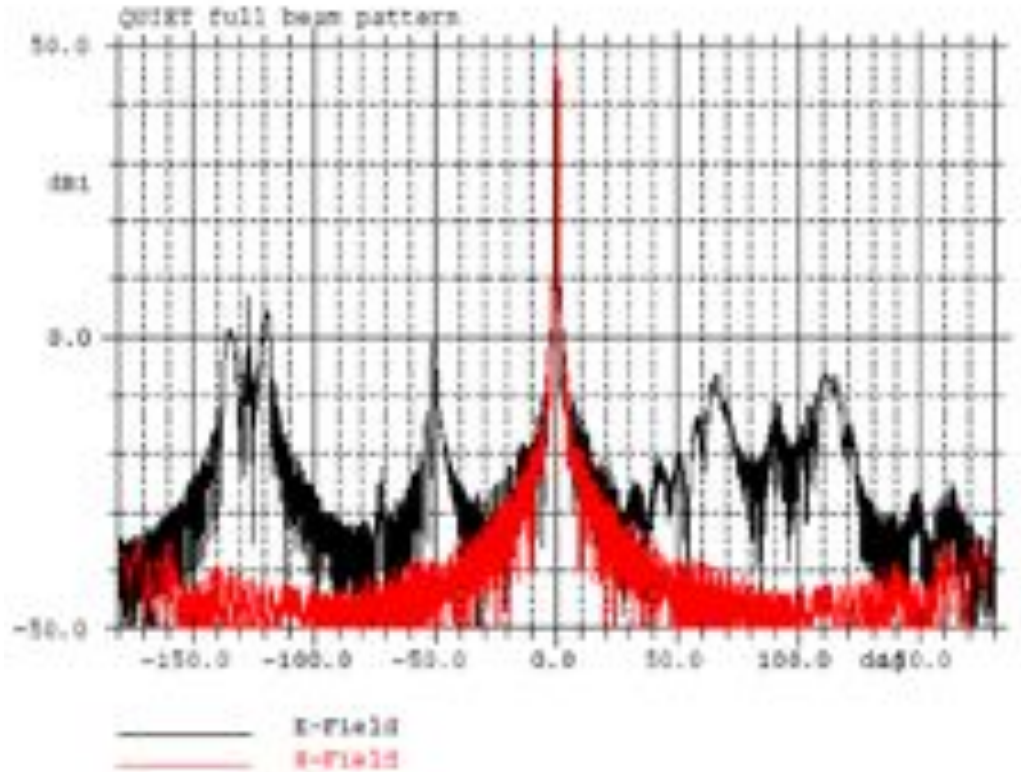


Figure 2-12: Beam profile as a function of angle θ away from boresight. Courtesy Christian Holler (Ref. [39]).

2. $\theta = -50$, $-5 < \phi < 5$ in Figure 2-14(a): triple reflection sidelobe. Corresponds to sidelobe #1 in Figure 2-13.
3. $\theta=75$, $-40 < \phi < 40$ in both Figures 2-14(a) and 2-14(b): spillover past the secondary mirror, a continuation of the same feature seen in Figure 2-14(a). Corresponds to sidelobe #2a and #2b in Figure 2-13
4. $\theta=-50$, $-20 < \phi < 20$ in Figure 2-14(b): spillover past the primary mirror. Corresponds to sidelobes #3a and #3b in Figure 2-13.

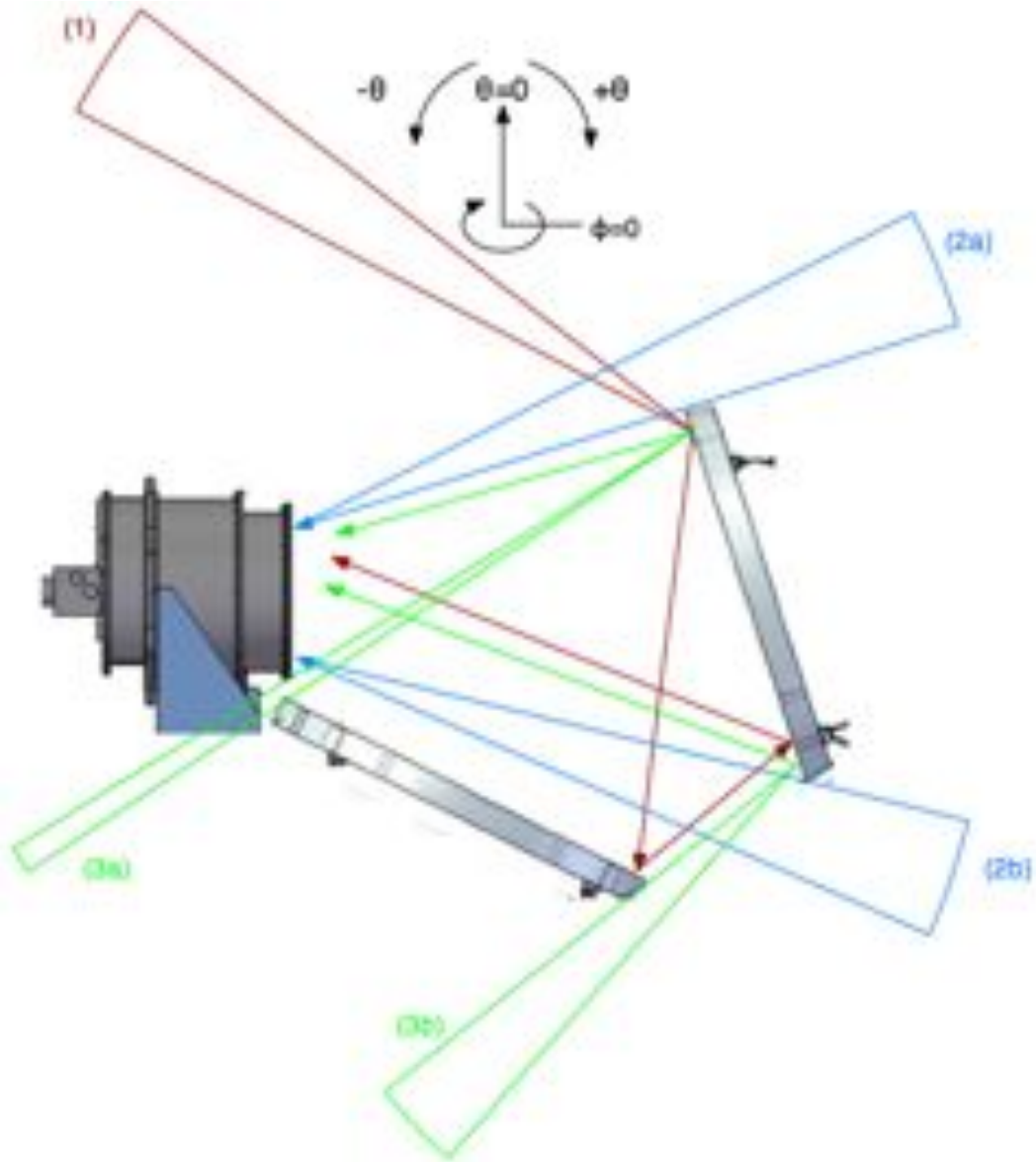


Figure 2-13: The definition of the E- and H-plane axes, as well as the θ and ϕ for the system. *c*: Location of the sidelobes around the telescope, in particular the 'triple reflection' sidelobe (#1), spillover past the secondary (#2a,b) and spillover past the primary (#3a,b).

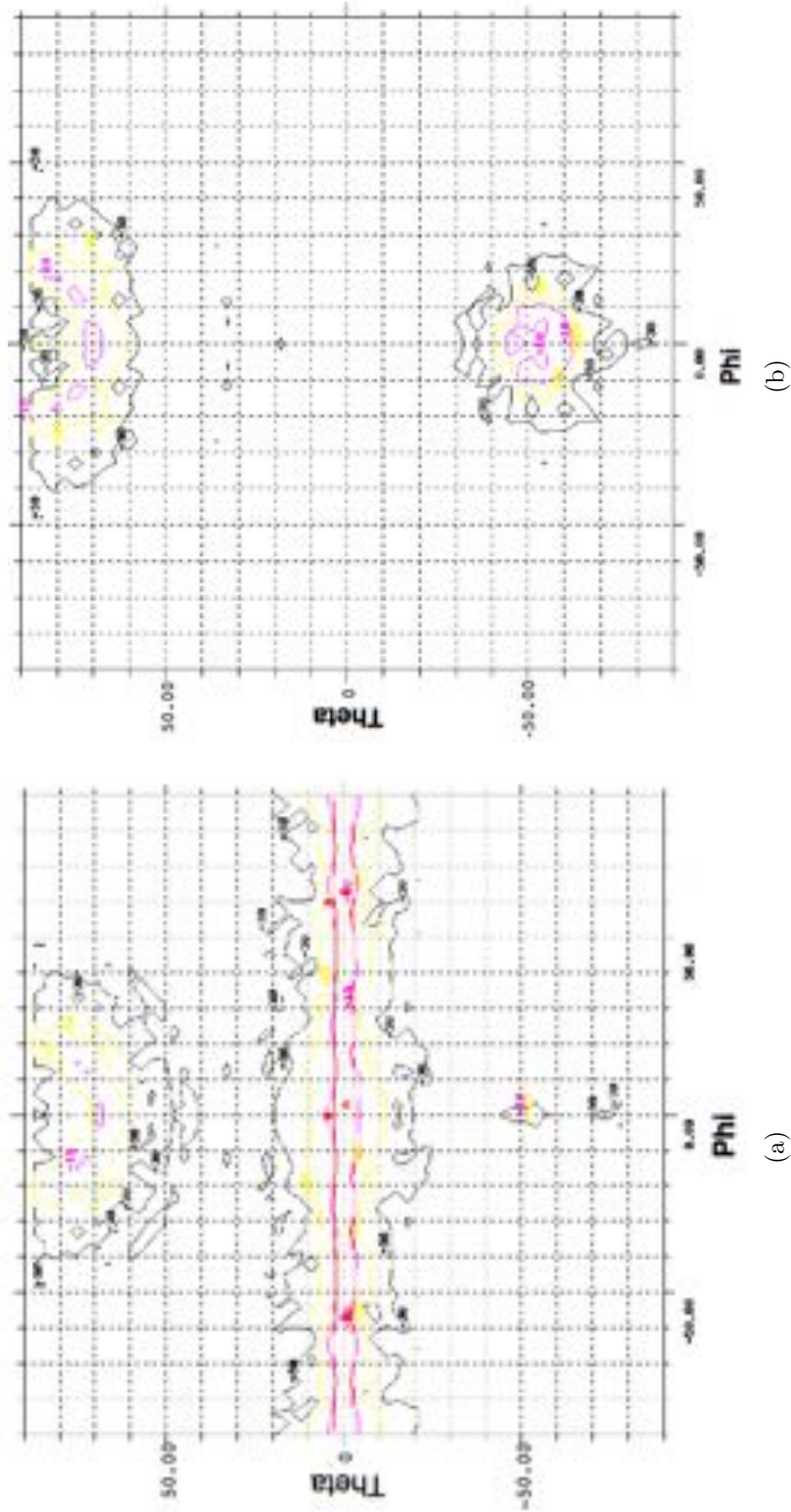


Figure 2-14: Beam profile in two dimensions. *a*: northern half of the beam (sidelobes in the hemisphere directly above the primary mirror). *b*: the southern half of the beam (sidelobes in the hemisphere below the primary mirror). The 0 dB, -10 dB, -20 dB, and -30 dB contours are marked; these show a variety of sidelobe features. It should be noted that the northern hemisphere sidelobes would correspond to features above the primary mirror, namely the 'triple reflection' sidelobe and spillover past the secondary. The southern hemisphere plots show sidelobes from spillover past the primary mirror. Courtesy Kieran Cleary.

The sidelobe structures in the two dimensional plot are symmetric around θ , in the sense that for a particular ϕ point, the structure at $+\theta$ is the mirror image of that at $-\theta$. This confirms that the symmetric axis of the telescope runs along the primary mirror (perpendicular to a vector drawn between the secondary mirror and the cryostat).

Design Tolerances

We considered a variety of effects to understand and characterize our optical design tolerances. These include the position of the feedhorns with respect to the focus of the mirrors, the effects of thermal contraction and expansion on the positions of the mirrors while observing in the field, and the surface finish of the mirrors.

The QUIET optical system is ‘slow’; the rays coming from the secondary mirror and converging into the cryostat do not converge at a particularly acute angle, and so the tolerance for the location of the feedhorns with respect to the focus of the telescope is generous. Shifts of the feedhorns within the mirror system of ± 1 cm will still yield beam cross-polarization and ellipticity values within specifications. This slow convergence minimizes the impact of thermal contraction and expansion on the system as well, which can cause shifts of up to $\simeq 4\text{mm}$ ¹.

Alignment was performed in Chile, the mirrors were aligned to within $400\mu\text{m}$ of the true 3D mirror model, this is within the specifications developed from optical simulations. In addition, the Q-band cryostat hangs over the primary mirror by 3 inches; it was determined that this did not compromise instrument performance because the telescope edge taper is -30 dB, enough that there is insignificant contribution to the beam from this region of the mirrors.

Light incident on the mirror will bounce off of any surface irregularities, decreasing instrument sensitivity and increasing power in the beam sidelobes. The scattering

¹The length of the support structure between the two mirrors is around 1.4 m, with typical temperature variation of 40°F and a coefficient of thermal expansion for steel of $\simeq 7 \times 10^{-6}$ inches/inch°F (<http://www.matweb.com>) gives an expansion value of 4mm.

amplitude and angular dependence is a function of the size of the irregularities relative to the observing wavelength. This effect was quantified by Ruze (Ref. [76]). After machining, both the primary and secondary mirror surfaces were measured. These measurements were used to simulate the main beam and sidelobe structure for the 90 GHz beam, shown in Figure 2-15. Generally surface irregularities will scatter power from the main beam into the sidelobes, this is not apparent from Figure 2-15 because the peak of both the measurements and simulations were normalized to one.

Scattering scales with frequency, such that the surface irregularities will impact the sidelobe structure of the Q-band array to a smaller degree; this is apparent in comparisons between beam gain from the simulations (52.1 dB gain, section 2.2.6 Table 2.3) and from measurements with calibration sources (52.4 dB gain, section 5.9).

Ground-Screen

To minimize contamination from the ground and astronomical sources entering the data stream via sidelobe spillover, we designed an absorbing ground-screen to shield the mirrors from the ground and so allow the sidelobes to terminate on a constant temperature source. The ground-screen structure, shown in Figure 2-3(b), consists of two parts: an aluminum box ('Ground Screen'), which encloses both mirrors and the front half of the cryostat, and a cylindrical tube that attaches to the ground screen directly above the primary mirror ('Upper Ground Screen'). The external surface of the ground-screen was coated in white paint to minimize radiative loading and reduce diurnal temperature variations. The interior of the ground-screen was coated with a broad-band absorber (Emerson Cumming HR-10) which absorbs radiation and re-emits it at a constant temperature, allowing the ground-screen to function as an approximately constant black-body source in both Q- and W- band frequencies. The absorptive ground-screen shields the instrument from ground pick-up and provide a stable, unpolarized emission source, which does not vary during a telescope scan (as the ground or an astronomical source would). The absorber was coated with sheets

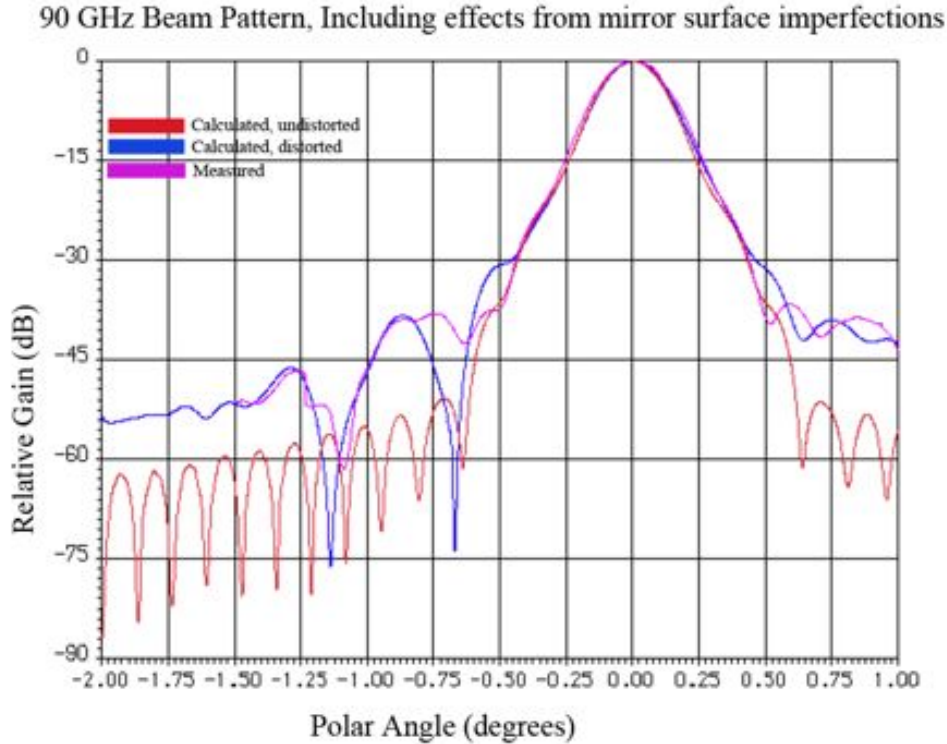


Figure 2-15: A comparison of the measured beams with two simulations: one assuming no surface irregularities, and the other including the full 3-D model of surface irregularities. The measurements match the simulation of the beams from the imperfect mirror ('distorted'), and both show that the surface irregularities cause an additional 15 dB of sidelobe power. Courtesy Josh Gundersen.

of expanded teflon, which are transparent at our observing frequencies, to function as weather-proofing.

The ground-screen box alone does not remove all sidelobes – in particular the triple-reflection sidelobe and some spillover past the secondary is not intercepted by the ground-screen. The upper ground screen is designed to remove this sidelobe, unfortunately it was not ready in time for Q-band observations, as a results we have had to excise data which is contaminated by sources in the sidelobe (see section 4.4.8).. The effectiveness of the upper ground screen was assessed by measurements performed with the W-band array in January 2010. For these measurements, a polarized source was placed on the top of a container at the observing site and the telescope was

scanned over its entire azimuth and elevation range (-180° to 200° azimuth, 43° to 75° elevation) at four different deck angles (0° , 90° , -90° , -180°). When the telescope scans a region where the source has a path into the receiver through a sidelobe, the radiometers detect a higher signal than background noise. We performed the measurements without the upper ground screen section and then repeated them with this upper section included. As seen in Figures 2-16(a), 2-16(b), the main sidelobe feature at the bottom of the map, which in this case corresponds to spillover past the secondary, was removed. Additional sidelobe flares were discovered which were caused by holes in the floor of the ground screen. A third measurement was taken after placing absorber over these holes (Figure 2-16(c)).

The ground screen is designed to shield the optics from ground emission. Because it is an absorbing groundscreen, changes in the ground screen temperatures will change the emission temperature and could potentially be detected by the polarimeters through sidelobe pickup. To monitor the temperature of the ground screen, we placed 26 temperature sensors on various external surfaces of the ground screen, mirrors, and cryostat (shown in Figures 2-17(a) and 2-17(b)).

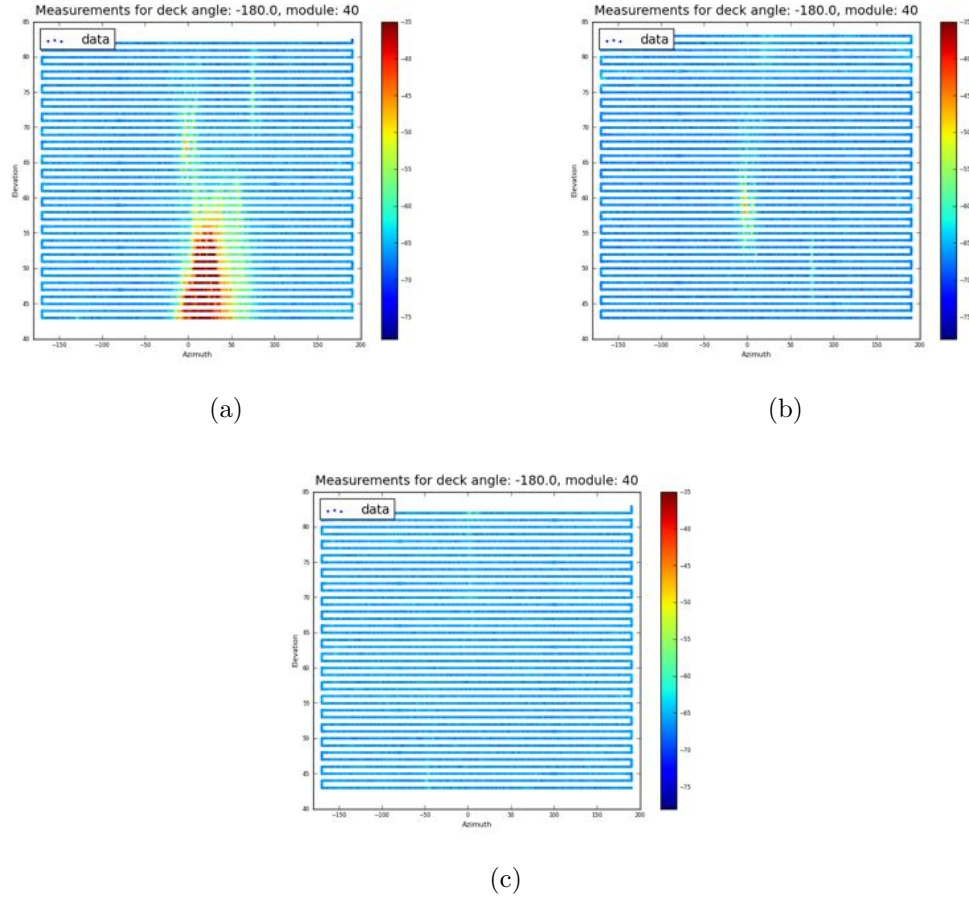


Figure 2-16: Sidelobe measurements for W-band Module 40 (located on the edge of the array), deck angle of -180. *a*: Ground screen only, *b*: ground screen and upper ground screen, *c*: ground screen, upper ground screen, and additional absorber placed over holes in the floor of the ground screen. The source is located at an azimuth of $\simeq 20^\circ$ and an elevation of $\simeq -5^\circ$. The color scale is the same between all three measurements. The flare seen at the bottom of the map is from spillover past the secondary, this was removed when the upper ground screen was added. The flare at the top of *b* is generated by spill-over due to holes in the absorber from the ground screen structure, and is present before the upper ground screen was added as well, but its position has shifted slightly because the source was moved between measurements. Measurements courtesy Jeff McMahon and Jaclyn Sanders.

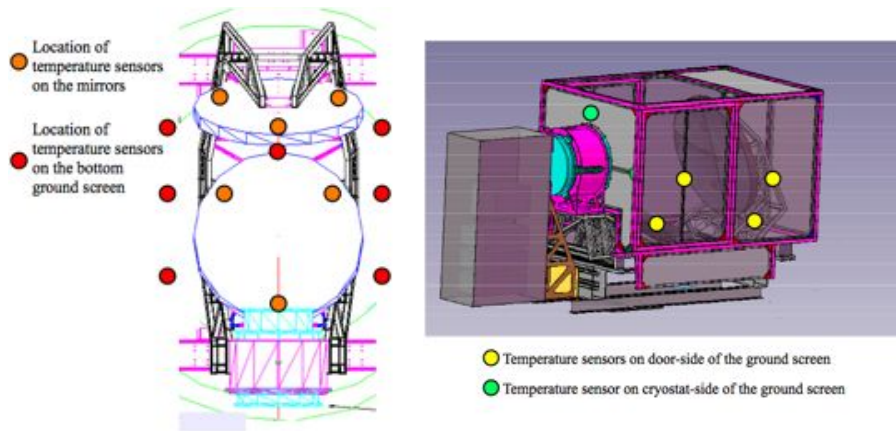


Figure 2-17: *a*: (Orange) Location of the temperature sensors on the primary and secondary mirrors. (Red) Location of temperature sensors on the surface of the bottom ground screen *b*: (Yellow and Green) Location of the temperature sensors on the ground screen box.

2.3 Polarimeter Modules

2.3.1 Introduction

Each QUIET module is a polarimeter employing High-electron-mobility transistor (HEMT) technology for amplification as part of a signal processing chain. Recent polarization experiments such as WMAP, DASI, CBI, and CAPMAP (Refs. [45], [58], [70], [2]) all used HEMT-based polarimeters, but QUIET uses a revolutionary compact-profile design (Ref. [56]) suitable for large arrays. The QUIET polarimeter design replaces waveguide-block components and connections with strip-line coupled devices, producing modules with a footprint of $2.5\text{cm} \times 2.5\text{cm}$ (W-band) and $5\text{cm} \times 5\text{cm}$ (Q-band). This chapter discusses the Q-band modules: their design, components, and signal processing.

Design Principles

The QUIET modules were developed according the following design principles:

- Scalability to multiple detectors: Instrument sensitivity scales as $N^{-1/2}$, where N is the number of detectors. To increase the sensitivity of the QUIET instrument, we employ an array of polarimeters for both frequency bands. Scalability is a motivation for limiting the size of the modules: more compact modules allow us to deploy more polarimeters in one cryostat (prior to the QUIET modules, each component was packaged individually, such that a single polarimeter was $\simeq 5\times$ larger than a QUIET polarimeter).
- Minimize instrument systematics:
 - The polarization signal in a QUIET module is the result of a differencing operation of two phase-switched states. As a result, non-polarized signals which are common-mode between phase-switch states are removed and do not contribute to our signal-to-noise ratio.

- We employ fast phase switching to difference faster than typical noise time scales (e.g. radio-frequency-interference) and decrease the range over which the low-frequency high-noise portion of the $1/f$ noise spectrum effects the data.
- We designed a low noise system: Noise is the most important parameter to be considered when building radio-frequency (RF) circuits for the detection of extremely small signals. The total noise temperature of a multi-component system can be expressed as (Ref [73]):

$$T_{sys} = T_1 + \frac{T_2}{G_1} + \frac{T_3}{G_2 G_3} + \dots \quad (2.4)$$

where for a QUIET module:

- T_{sys} is the total noise temperature of the module.
- T_1 is the noise temperature from the first element (for the module this is the first amplifier), which has gain G_1 .
- T_2 is the noise temperature from the second element (for the module this is the second amplifier) with gain G_2 .
- Followed by the phase switch, a third amplifier, etc. The noise is dominated by the first few terms in a well-designed system.

To optimize the module for the lowest noise, the first element in the chain should have low noise and high gain such that the first term dominates the system noise and is as small as possible. The QUIET amplifier chain has the lowest noise amplifier as its first stage, typical noise temperatures of this amplifier are 18K with gain of 24 dB (Ref. [48]).

The response of the amplifiers across the QUIET bandpass is not flat, and the second stage amplifier has a different slope than the first and third stage amplifiers. When the amplifiers are combined together, the resulting bandpass is designed to be flatter than either of the amplifier bandpasses individually, as shown schematically in Figure 2-18.

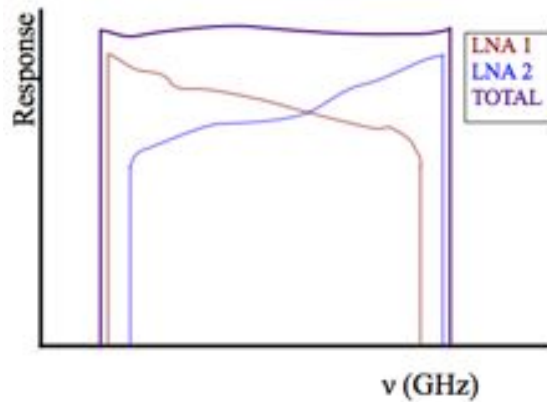


Figure 2-18: A schematic of the bandpasses of the amplifiers.

2.3.2 Polarimeter Module Components

Overview

A single module is comprised of a collection of microwave circuits, creating an integrated circuit which functions as a polarimeter. A schematic of the signal processing components in a single QUIET polarimeter is shown in Figure 2-19(a) and a photograph of the interior of a Q-band polarimeter is shown in Figure 2-19(b). Each module has two input ports which connect to two ‘legs’ in the module and contains:

- Three low-noise High-electron mobility transistor (HEMT)-based amplifiers on each input leg.
- Phase switches on each leg.
- A phase discriminator: one passive chip with two hybrid couplers.

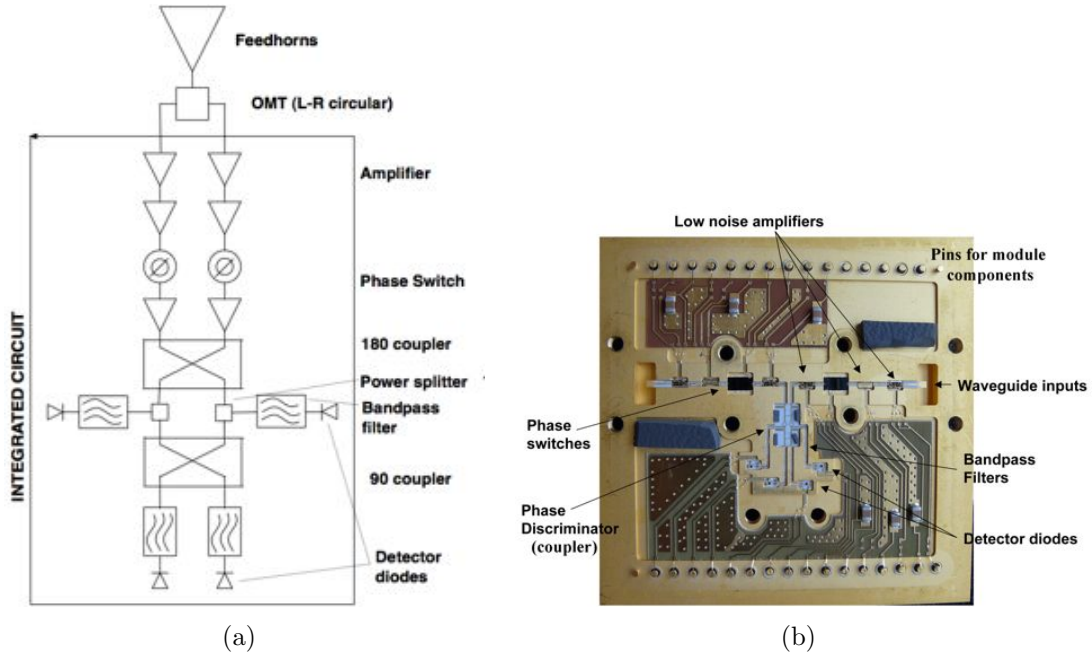


Figure 2-19: *a*: Schematic of signal processing components in a QUIET polarimeter. *b*: Internal components of a Q-band polarimeter.

- Four diodes: zero-bias Schottky diodes.

Both the amplifiers and phase switches are circuits built from a single piece of semiconductor substrate to form microwave monolithic integrated circuits (MMICs).

The modules are packaged into brass housings which have been precision-machined for component placement and signal routing. Each housing has 34 pins which connect to the module components via strip-line. We bias the active components through connections to these pins and measure the signal across pins connected to detector diodes. The pins form the two parallel rows of connections along the upper and lower edge of the casing in Figure 2-19(b). The physical layout of the components in a Q-band module was designed such that the two input legs are physically far (multiple wavelengths at 40 GHz) from each other to reduce interactions and coupling between the signal legs.

We will describe each component and give its scattering (Jones) matrix. This will allow us to compute the signal processing of the module.

Waveguide Probe

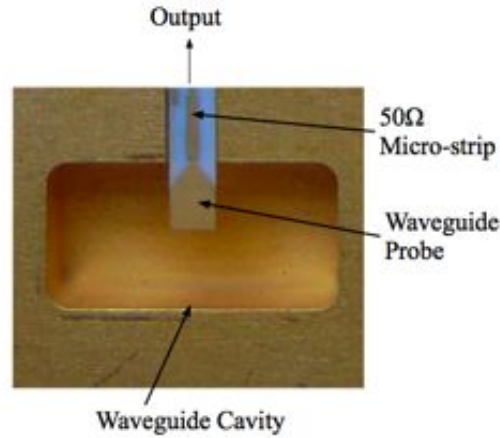


Figure 2-20: One Q-band waveguide probe.

The signal from the OMTs or hybrid-Tees is incident on two waveguide probes (Figure 2-20), situated in a waveguide cavity in the module casing. The probes couple to 50 Ω microstrips that propagate the signal to the processing components in the module.

Low Noise Amplifiers

LNA Composition

Each Q-band QUIET Low-Noise Amplifier (LNA) has three HEMT transistors in series (the W-band LNAs have four HEMTS each). A photograph of a QUIET amplifier is shown in Figure 2-21(a), and the three-stage cascade of transistors is shown schematically in Figure 2-21(b). All three HEMTs in the LNA have a common drain and gate voltage.

The signal is input to the source terminal of the first transistor, amplified, and output to the transistor drain. The output is composed of the amplified radio frequency (RF) alternating-current signal and the direct-current bias voltage. It travels through a capacitor, where the direct current component is removed and the amplified

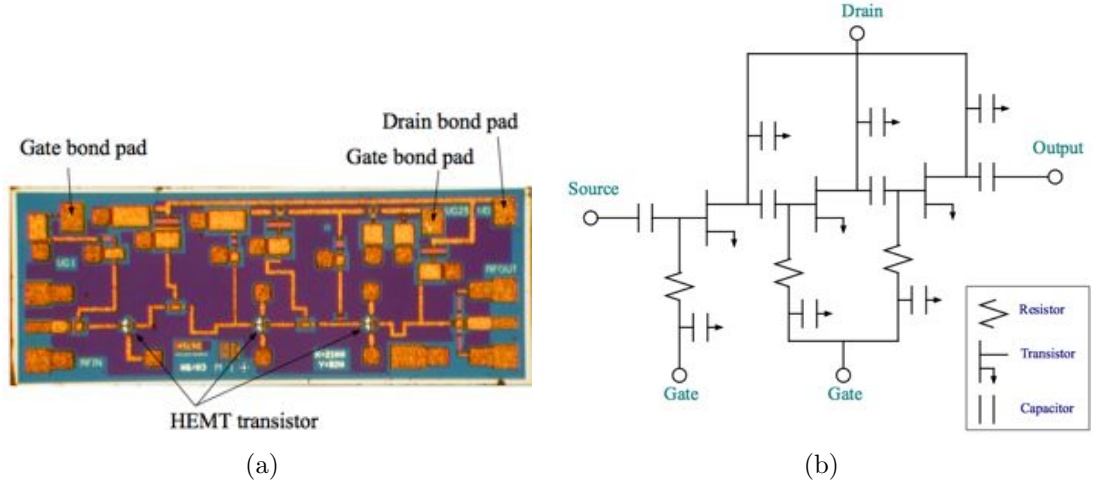


Figure 2-21: QUIET Low Noise Amplifier *a*: photograph (Q-band) *b*: schematic, showing the three-stage cascaded design of HEMT transistors.

signal is transmitted to a second transistor. The second transistor will amplify the signal, output to the drain, and the direct current bias component is again removed by a capacitor. The third transistor operates similarly, and the output of the entire LNA is amplified signal.

Each module leg has three LNAs, together they combine to give gain g_A on leg A and g_B on leg B. The Jones Matrix for the amplifiers is given by:

$$S^{amplifier} = \begin{pmatrix} g_A & 0 \\ 0 & g_B \end{pmatrix}$$

Where the input and output states have basis vectors (E_A, E_B) , where A and B refer to the module legs.

LNA noise

The noise in the module is dominated by the noise from the LNAs. The noise in an LNA comes primarily from thermal noise ('Johnson' noise), which causes an additional current between the gate and drain terminals of the transistors. The noise power is described by equation 2.5.

$$P \propto kT\Delta\nu \quad (2.5)$$

where k is Boltzmann's constant, T is the temperature of the LNA, and $\Delta\nu$ is the bandwidth. The thermal noise can vary with:

- LNA temperature: To reduce thermal noise, we cryogenically cool the modules to $\simeq 20\text{K}$.
- Bandwidth: LNA noise scales with $\Delta\nu$, which in practice scales with the frequency of interest. As a result, LNAs operating at higher frequencies will have higher noise.

The lower limit for noise in an LNA is fundamentally set by quantum mechanics: the noise cannot be lower than the quantized energy of a photon at the detector frequency, which will have an associated temperature given by:

$$kT_q = h\nu \rightarrow T_q = \frac{h\nu}{k} \quad (2.6)$$

where h is Planck's constant, ν is frequency, and k is Boltzmann's constant. At 40 GHz, this is 1.9K, and at 90 GHz this is 4.3K. The best performing Q-band module operates at $\simeq 11.5\times$ the quantum limit, and the best performing W-band module is operating at $\simeq 14\times$ the quantum limit.

Phase Switch

The QUIET module has two phase switch circuits, one on each leg of the module. A single phase switch operates by sending the signal down one of two paths within the phase switch circuit. One path has an added length of $\frac{\lambda}{2}$ to give the signal a phase

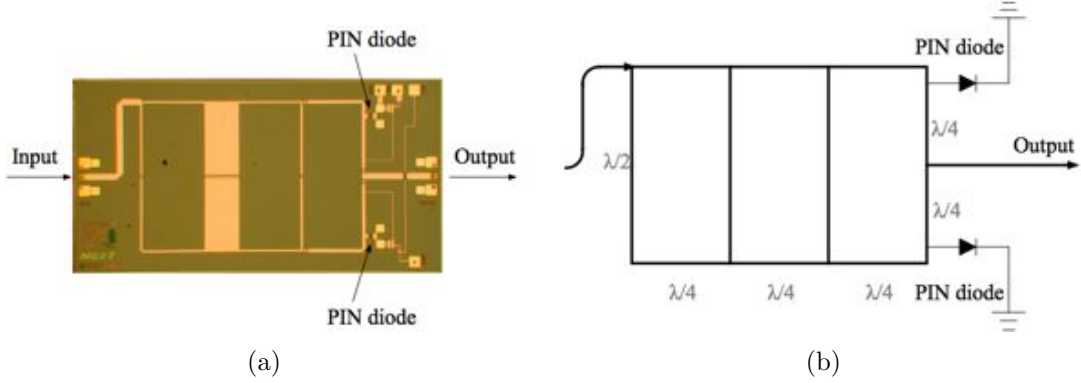


Figure 2-22: *a*: Photograph of a phase switch. *b*: Schematic of the phase switch. There are two paths through the phase switch; in the schematic and the photograph, the two paths travel around the perimeter of the phase switch circuit, the longer path has an additional $\lambda/2$ segment directly after the input. As a result, the two paths have a 180° phase difference. The biasing of each PIN diode will determine which path the signal will take.

shift of 180° degrees compared to the other (straight) path segment. A photograph of a phase switch circuit is shown in figure 2-22(a), and a schematic of the phase switch paths is shown in Figure 2-22(b).

Two Indium-Phosphide MMIC PIN (p-doped, intrinsic-semiconductor, n-doped) diodes control which path the signal will take. When forward biased, the diode allows current to flow; when reverse biased, it stops current flow. With only one of the two diodes biased, the signal will be sent down whichever path has the forward biased diode. When neither or both PIN diodes are biased, the signal cancels. PIN diodes are capable of fast switching, allowing QUIET to switch between the two phase states at a rate of 4kHz. The Jones matrix for the phase switch is given by:

$$S^{PhaseSwitch} = \begin{pmatrix} e^{i\phi_A} & 0 \\ 0 & e^{i\phi_B} \end{pmatrix} \quad (\phi_A, \phi_B) \in \{0, 180^\circ\} \quad (2.7)$$

Phase Discriminator

The phase discriminator consists of two hybrid couplers, each of which is composed of Schiffman phase delay lines (Ref. [73]) and broadband branchline stripline couplers. A photograph of a Q-band phase discriminator is shown in Figure 2-23(a), and accompanying schematic in Figure 2-23(b). The signal processing of these components is given in the caption to Figure 2-23(b).

180° coupler

The 180° coupler consists of the Schiffman delay line and coupler shown in the upper half of Figure 2-23(b). This coupler has a Jones matrix of:

$$S^{180^\circ \text{ coupler}} = \frac{1}{\sqrt{2}} \begin{pmatrix} 1 & 1 \\ 1 & -1 \end{pmatrix} \quad (2.8)$$

Power Splitter

The output of the 180° coupler is split, and half is sent to a set of detector diodes. The power splitter has a Jones matrix of:

$$S^{\text{powersplitter}} = \frac{1}{\sqrt{2}} \begin{pmatrix} 1 & 0 \\ 0 & 1 \end{pmatrix} \quad (2.9)$$

90° coupler

The other half of the signal is sent through a phase-delay and coupler structure identical to the first coupler, shown as the lower half of Figure 2-23(b). The resulting output is a 90° coupler, with Jones matrix of:

$$S^{90^\circ \text{ coupler}} = \frac{1}{\sqrt{2}} \begin{pmatrix} 1 & i \\ i & 1 \end{pmatrix} \quad (2.10)$$

This signal is read out by a second set of detector diodes.

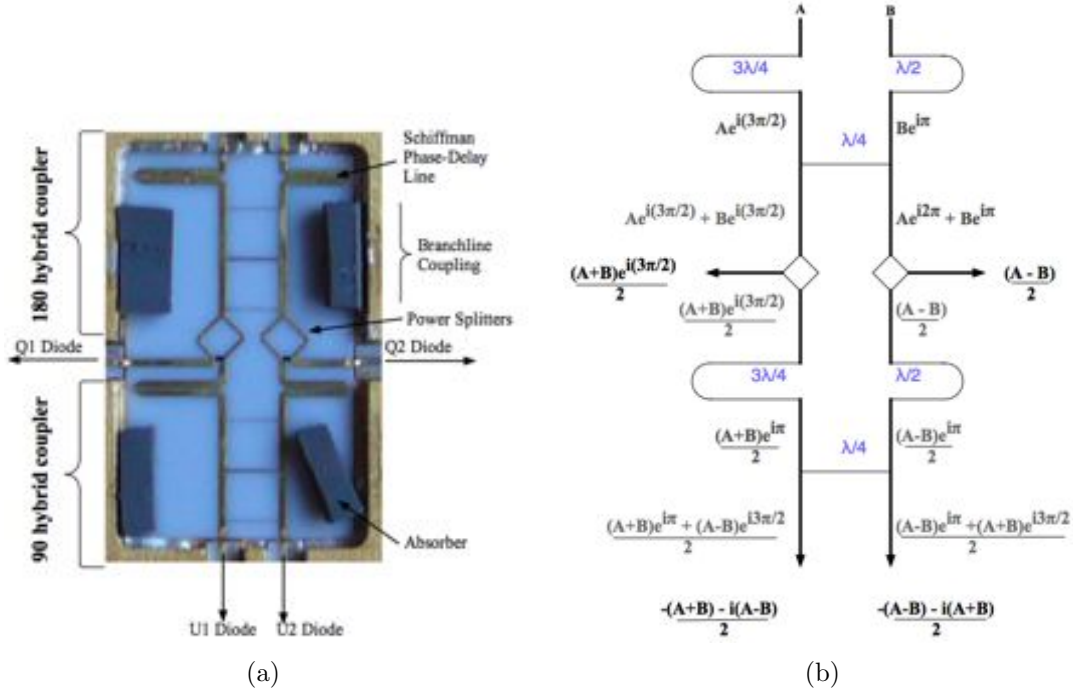


Figure 2-23: *a*: Photograph of a Q-band hybrid coupler or phase discriminator. The upper half of the photograph shows the 180° coupler composed of Schiffman phase delay lines and a branchline coupler. The signal is split by a power splitter, and half of it is read out by a set of detector diodes. The other half of the signal is processed by an identical set of Schiffman phase delay lines and branchline coupler and read out by a second set of detector diodes. Because the input states to this second coupler are the output of a 180° coupler, it will function as a 90° coupler. The faint horizontal traces seen in the branchline couplers increase the bandwidth of the coupler. One piece of absorber was shifted slightly when the lid of the module was opened. *b*: Processing in the hybrid couplers. The first Schiffman phase delay line within the discriminator will introduce a $\frac{3\lambda}{4}$ shift on one module leg, and a $\frac{\lambda}{2}$ on the other leg, producing a $\frac{\lambda}{4}$ phase shift between the legs. Half of the signal on the A leg after the shifter will proceed down the leg, the other half will propagate through the coupling line and will be shifted by $\lambda/4$. An identical process will occur for the second leg. Half of the signal on each leg is then split (the square structures in the center of the diagram) and be read by the detector diodes. The signal measured on leg A will be $\propto A+B$ while the signal measured on leg B will be $\propto A-B$. The rest of the signal will propagate through an identical structure (lower half of the figure), with the resulting signal described by the output of a 90° coupler.

Bandpass Filters

We employ a set of bandpass filters which help match the bandpass of the module to the optical components (OMTs, primarily) and regularize the bandpasses between the diodes. This optimizes our signal-to-noise by reducing noise measured on detector diodes that was generated outside of the OMT bandpass (and hence contains no signal).

Detector Diodes

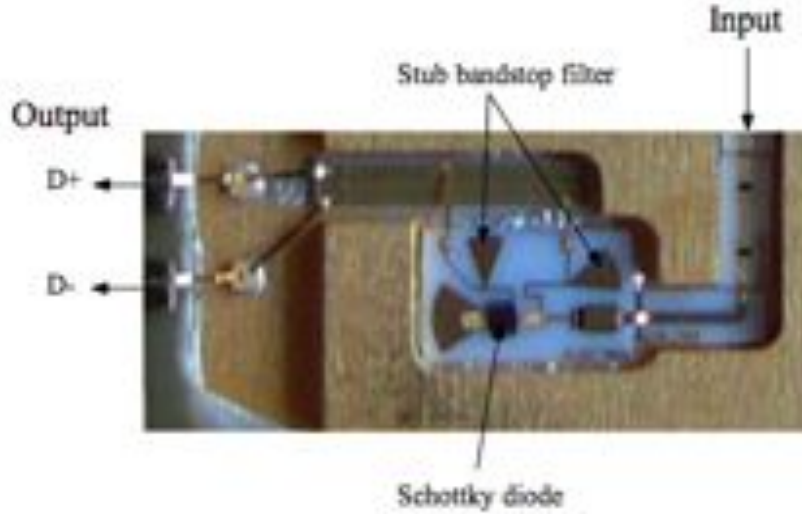


Figure 2-24: Photograph of a Q-band detector diode.

After filtering, the signal passes through a detector diode. A photograph of a Q-band detector diode is shown in Figure 2-24, along with our bandstop filters, which function as low-pass filters. The detector diodes are beam-lead zero-bias Schottky diodes. Following the prescription in Ref [73], diode response can be modeled by:

$$I(V) = I_s(e^{\alpha V} - 1) \quad (2.11)$$

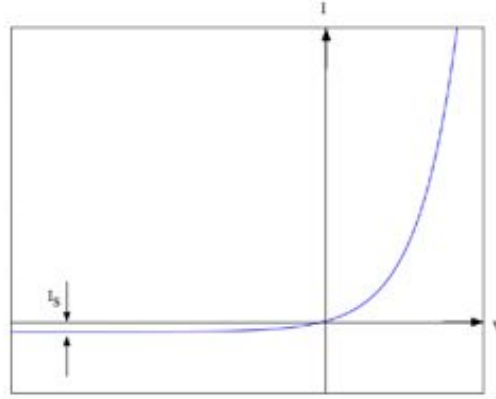


Figure 2-25: Typical diode response; the output current of the diode has an exponential dependence on voltage. I_S is the saturation current for the diode, where the diode will act as a resistor.

The result for an alternating-current input signal with a modulation frequency (our input signal is 40 GHz with a 4kHz modulation frequency) can be Taylor-expanded, and after low-pass filtering we obtain a signal proportional to V_{AC}^2 .

2.3.3 Module Bias Optimization

We bias each leg of the module independently, turning off the phase switch on one leg such that the signal is propagated through only the second leg. We then bias the amplifiers on the second leg such that the first stage amplifier drain current is in the range 0-5mA, the second stage drain current is in the range 5-15mA, and the third stage amplifiers is in the range 15-30mA, and in particular, that the signal measured by the detector diodes while looking at a 300K load is 5mV. We then repeat for the first leg, and adjust again to obtain a signal difference between the two legs of 0.6mV.

This biasing scheme is optimized for reducing system noise, as a low current on the first stage will generally keep the noise on the first stage low but still dominant in equation 2.4. In addition, we measure two separate data streams from the module (described in section 2.3.5), and balancing the module legs such that the signal is

roughly equal will keep the gain between these two data streams similar.

2.3.4 Compression

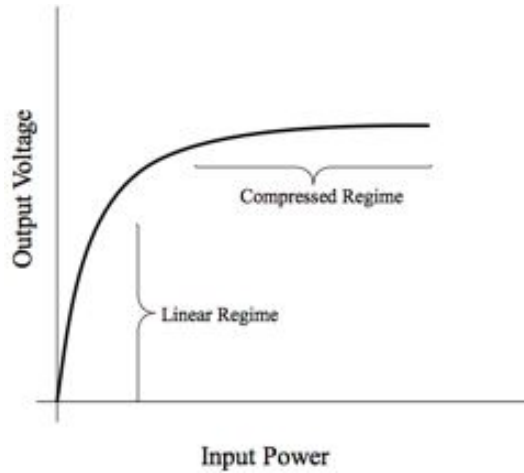


Figure 2-26: Illustration of amplifier compression: the response of the amplifiers to changes in input power is a function of the input power. Generally the response of the amplifiers tapers off at higher input powers.

The amplifiers can exhibit compression, illustrated in Figure 2-26; the response of the amplifier to *changes* in input power depends on the input power such that slope of the response curve is shallower at higher input powers. As a result, response measured at high input power can underestimate the responsivity when interpolated to lower input power. This is a concern for laboratory testing of the QUIET modules because the modules are designed to operate with input loading from the Chilean sky ($\simeq 10\text{K}$) while laboratory measurements use cryogenic loads (77K, 90K) to characterize performance. To know whether responsivity measurements performed in the laboratory with 300K and cryogenic thermal loads can be used to estimate the responsivity in Chile, we need to determine whether amplifiers are likely to be compressed for various input powers given the biasing scheme outlined above in section 2.3.3.

For the transistors in each amplifier, 1% deviation from linear operation occurs -20dB below the 1dB compression point, where the 1dB compression is usually -10

dB below the bias power; thus compression occurs at -30dB below the bias power (Ref. [73]). The biasing current is split among the three transistors which compose an LNA. Typical bias voltages for each amplification stage is given in Table 2.4, along with the compression point at -30dB from the bias power. With 7dB of loss between the last amplifier and the diode stage, the condition that the last transistor in the third amplifier stage is not compressed¹ is equivalent to the condition that the detector diode should measure a signal of -30.5 dB or less. Given the definition:

$$P_{\text{dBm}} = 10 \times \log\left(\frac{P_{\text{in}}}{P_{1\text{mW}}}\right) \quad (2.12)$$

-30.5dB is equivalent to $0.9\mu\text{W}$. The detector diodes will output $\simeq 1\text{mV}$ per $1\mu\text{W}$ (Ref. [28]), so the maximum uncompressed signal corresponds to 0.9mV . Thus measured signals less than 0.9mV are not expected to compress the last transistor in the third stage amplifier. Biasing the modules such that the detector diode output is $5\text{--}6\text{mV}$ while a module observes the 300K load indicates that we are operating with the third stage amplifier compressed. Detector diode values while a module observes the cryogenic loads were $\simeq 1.3\text{mV}$, so these may exhibit some compression from the third stage amplifier. Detector diode values while looking at the Chilean sky ($\simeq 0.3\text{--}0.5\text{mV}$) indicate the third stage amplifier is uncompressed during observations.

2.3.5 Signal Processing by the QUIET Module

We can combine the Jones matrices of the individual module components to write an expression for the processing action of the module, independent of the input, for each of the diodes. We will neglect the filter term as it will simply function as a constant for each diode. Because we do not combine any of the diodes in the following analysis, including this factor is unnecessary.

¹The other transistors amplify lower input powers, such that this final stage transistor is the only transistor near a compression point.

Component	Bias (V, mA)	Transistor Bias (V, mA)	DC bias power (dBm)	Compression (dBm)
LNA ₁	0.9, 5	0.9, 1.7	1.76	-28
LNA ₂	1.2, 20	1.2, 6.7	9	-21
LNA ₃	0.9, 15	0.9, 5	6.5	-23.5

Table 2.4: Table showing compression points of each of the amplifiers. Typical bias points are shown, because each amplifier has three transistors (effectively in parallel), the bias current is split among them. The resulting bias power in dB is shown, and also the compression point, which is -30dB below the bias power.

The signal for both the Q diodes and U diodes are processed first by the amplifiers, followed by the phase switch the 180° coupler, and then the power splitter. The U diode signal is additionally processed by a 90° coupler, so we will consider each diode separately.

$$\begin{pmatrix} E_{Q1} \\ E_{Q2} \end{pmatrix} = S^{powersplitter} S^{180^\circ coupler} S^{amplifier} S^{phaseswitch} \begin{pmatrix} E_A \\ E_B \end{pmatrix}^{in} \quad (2.13)$$

The Jones matrices for all components were given in proceeding sections, and substituting them into the expression above gives:

$$\begin{pmatrix} E_{Q1} \\ E_{Q2} \end{pmatrix} = \frac{1}{\sqrt{2}} \begin{pmatrix} 1 & 0 \\ 0 & 1 \end{pmatrix} \frac{1}{\sqrt{2}} \begin{pmatrix} 1 & 1 \\ 1 & -1 \end{pmatrix} \begin{pmatrix} g_A & 0 \\ 0 & g_B \end{pmatrix} \begin{pmatrix} e^{i\phi_A} & 0 \\ 0 & e^{i\phi_B} \end{pmatrix} \begin{pmatrix} E_A \\ E_B \end{pmatrix}^{in} \quad (2.14)$$

And similarly for the U diodes:

$$\begin{pmatrix} E_{U1} \\ E_{U2} \end{pmatrix} = S^{90^\circ coupler} S^{powersplitter} S^{180^\circ coupler} S^{amplifier} S^{phaseswitch} \begin{pmatrix} E_A \\ E_B \end{pmatrix}^{in} \quad (2.15)$$

$$\begin{aligned}
\begin{pmatrix} E_{U1} \\ E_{U2} \end{pmatrix} &= \frac{1}{\sqrt{2}} \begin{pmatrix} 1 & i \\ i & 1 \end{pmatrix} \frac{1}{\sqrt{2}} \begin{pmatrix} 1 & 0 \\ 0 & 1 \end{pmatrix} \frac{1}{\sqrt{2}} \begin{pmatrix} 1 & 1 \\ 1 & -1 \end{pmatrix} \\
&\times \begin{pmatrix} g_A & 0 \\ 0 & g_B \end{pmatrix} \begin{pmatrix} e^{i\phi_A} & 0 \\ 0 & e^{i\phi_B} \end{pmatrix} \begin{pmatrix} E_A \\ E_B \end{pmatrix}^{in}
\end{aligned} \tag{2.16}$$

We will use these matrices to understand the signal output from modules attached to the OMTs (17 modules) and the hybrid-Tees (2 modules), examine the effects on the output signal from a variety of possible imperfections in the module components, and make predictions of correlated noise between diodes in a module.

Processing with Septum Polarizer OMT Assembly Input

An expression for the module signal output with an input from an OMT is presented, first considering the simplest case: the phase switch on the A leg of a module has transmission = 1, and leg B is switched, so $(e^{i\phi_A}, e^{i\phi_B}) = (1, \pm 1)$. The output of an OMT is left- and right- circularly polarized light (section 2.2.4):

$$\begin{pmatrix} E_A \\ E_B \end{pmatrix}^{in} = \frac{1}{\sqrt{2}} \begin{pmatrix} E_{LHCP} \\ E_{RHCP} \end{pmatrix} = \frac{1}{\sqrt{2}} \begin{pmatrix} E_L \\ E_R \end{pmatrix} = \frac{1}{\sqrt{2}} \begin{pmatrix} E_x + iE_y \\ E_x - iE_y \end{pmatrix} \tag{2.17}$$

Substituting this into equations 2.14 and 2.17 gives

$$\begin{pmatrix} E_{Q1} \\ E_{Q2} \end{pmatrix} = \frac{1}{2\sqrt{2}} \begin{pmatrix} g_A E_L \pm g_B E_R \\ g_A E_L \mp g_B E_R \end{pmatrix} \tag{2.18}$$

$$\begin{pmatrix} E_{U1} \\ E_{U2} \end{pmatrix} = \frac{1}{4} \begin{pmatrix} (1+i)g_A E_L \pm (1-i)g_B E_R \\ (1+i)g_A E_L \mp (1-i)g_B E_R \end{pmatrix} \quad (2.19)$$

The diodes square the signal, this yields:

$$\begin{pmatrix} |E_{Q1}|^2 \\ |E_{Q2}|^2 \end{pmatrix} = \begin{pmatrix} Q1 \\ Q2 \end{pmatrix} = \frac{1}{8} \begin{pmatrix} g_A^2 E_L E_L^* + g_B^2 E_R E_R^* \pm g_A g_B (E_L E_R^* + E_R E_L^*) \\ g_A^2 E_L E_L^* + g_B^2 E_R E_R^* \mp g_A g_B (E_L E_R^* + E_R E_L^*) \end{pmatrix} \quad (2.20)$$

$$\begin{pmatrix} |E_{U1}|^2 \\ |E_{U2}|^2 \end{pmatrix} = \begin{pmatrix} U1 \\ U2 \end{pmatrix} = \frac{1}{8} \begin{pmatrix} (g_A^2 E_L E_L^* + g_B^2 E_R E_R^*) \pm i g_A g_B (E_L E_R^* - E_R E_L^*) \\ (g_A^2 E_L E_L^* + g_B^2 E_R E_R^*) \mp i g_A g_B (E_L E_R^* - E_R E_L^*) \end{pmatrix} \quad (2.21)$$

To write the detector diode signal in terms of the Stokes parameters Q , U , I , and V , we note the Stokes parameters are defined as (first presented in chapter 1):

$$\begin{aligned} I &= E_L E_L^* + E_R E_R^* = |E_L|^2 + |E_R|^2 = |E_x|^2 + |E_y|^2 \\ Q &= E_x E_x^* - E_y E_y^* = |E_x|^2 - |E_y|^2 = 2\Re(E_L^* E_R) \\ U &= -2\Im(E_L^* E_R) \\ V &= |E_L|^2 - |E_R|^2 \end{aligned} \quad (2.22)$$

Where I is a measure of intensity, V is a measure of circular polarization, and Q and U are measurements of linear polarization. We will use the following identities

to evaluate the signal processing results:

$$\begin{aligned}
E_L E_L^* &= |L|^2 = \frac{I+V}{2} \\
E_R E_R^* &= |R|^2 = \frac{I-V}{2} \\
\Re(E_R E_L^*) &= \Re(E_R^* E_L) \\
\Im(E_R E_L^*) &= -\Im(E_R^* E_L) \\
E_R E_L^* &= \Re(E_R E_L^*) + i\Im(E_R E_L^*) = \frac{Q}{2} - i\frac{U}{2} \\
E_L E_R^* &= \Re(E_R E_L^*) - i\Im(E_R E_L^*) = \frac{Q}{2} + i\frac{U}{2} \\
E_L E_R^* + E_R E_L^* &= Q \\
E_L E_R^* - E_R E_L^* &= iU
\end{aligned} \tag{2.23}$$

With these identities, the Q and U diodes will have signals:

$$\begin{pmatrix} Q1 \\ Q2 \end{pmatrix} = \frac{1}{8} \begin{pmatrix} g_A^2 \frac{I+V}{2} + g_B^2 \frac{I-V}{2} \pm g_A g_B Q \\ g_A^2 \frac{I+V}{2} + g_B^2 \frac{I-V}{2} \mp g_A g_B Q \end{pmatrix} \tag{2.24}$$

$$\begin{pmatrix} U1 \\ U2 \end{pmatrix} = \frac{1}{8} \begin{pmatrix} g_A^2 \frac{I+V}{2} + g_B^2 \frac{I-V}{2} \pm i g_A g_B (iU) \\ g_A^2 \frac{I+V}{2} + g_B^2 \frac{I-V}{2} \mp i g_A g_B (iU) \end{pmatrix} \tag{2.25}$$

The \pm which appears in front of terms $\propto g_A g_B$ originated from the phase switching action, where we had set $\phi = 0, 180$. When the phase switch is flipped, the signal on a given diode will change from $+$ to $-$ and back again. During signal processing after detection by the module detector diodes, we can either add the phase switched stages together ('total power' stream), or difference them ('demodulated' stream). Averaging the two phase switch states will remove components which change sign with the phase switch state, yielding:

$$\begin{pmatrix} Q1 \\ Q2 \end{pmatrix}^{total-power} = \begin{pmatrix} U1 \\ U2 \end{pmatrix}^{total-power} = \frac{1}{4} \begin{pmatrix} (g_A^2 + g_B^2)\frac{I}{2} + (g_A^2 - g_B^2)\frac{V}{2} \\ (g_A^2 + g_B^2)\frac{I}{2} + (g_A^2 - g_B^2)\frac{V}{2} \end{pmatrix} \quad (2.26)$$

Differencing (‘demodulating’) instead removes terms which are constant between the two phase switch states, yielding:

$$\begin{pmatrix} Q1 \\ Q2 \\ U1 \\ U2 \end{pmatrix}^{demodulated} = \frac{1}{4} \begin{pmatrix} g_A g_B Q \\ -g_A g_B Q \\ -g_A g_B U \\ g_A g_B U \end{pmatrix} \quad (2.27)$$

The signal on the diodes from modules which are connected to OMTs can be summarized by:

- The averaged voltage on both the Q and U diodes is a measure of the intensity, or total power, of the incoming signal. For a black-body emitter such as the CMB, this is proportional to the temperature.
- The differenced voltage on the Q diodes is a measure of the Q Stokes parameter.
- The differenced voltage on the U diodes is a measure of the U Stokes parameter.

Processing with Hybrid-Tee Assembly Input

As discussed in section 2.2.5, the hybrid-Tee assembly combines the linear polarization signals from two adjacent horns. Half of the hybrid-Tee assembly outputs the signals $(E_{y,1} + E_{x,2}, E_{y,1} - E_{x,2})$ to the input ports of a module, where 1 and 2 refer to the horn, and x and y are the two linear polarization states. The second half of the hybrid-Tee assembly outputs $(E_{y,2} + E_{x,1}, E_{y,2} - E_{x,1})$ to a second module. The signal output from one half of the hybrid-Tee assembly can be expressed as follows:

$$\begin{pmatrix} E_A \\ E_B \end{pmatrix}^{in} = \frac{1}{\sqrt{2}} \begin{pmatrix} E_{y,1} + E_{x,2} \\ E_{y,1} - E_{x,2} \end{pmatrix} \quad (2.28)$$

The signal output from the diodes is:

$$\begin{pmatrix} Q1 \\ Q2 \end{pmatrix} = \frac{1}{8} \begin{pmatrix} (g_A^2 + g_B^2)(|E_{y,1}|^2 + |E_{x,2}|^2) + (g_A^2 - g_B^2)(E_{y,1}^* E_{x,2} + E_{y,1} E_{x,2}^*) \\ \pm 2g_A g_B (|E_{y,1}|^2 - |E_{x,2}|^2) \\ (g_A^2 + g_B^2)(|E_{y,1}|^2 + |E_{x,2}|^2) + (g_A^2 - g_B^2)(E_{y,1}^* E_{x,2} + E_{y,1} E_{x,2}^*) \\ \mp 2g_A g_B (|E_{y,1}|^2 - |E_{x,2}|^2) \end{pmatrix} \quad (2.29)$$

$$\begin{pmatrix} U1 \\ U2 \end{pmatrix} = \frac{1}{8} \begin{pmatrix} (g_A^2 + g_B^2)(|E_{y,1}|^2 + |E_{x,2}|^2) + (g_A^2 - g_B^2)(E_{y,1}^* E_{x,2} + E_{y,1} E_{x,2}^*) \pm 0 \\ (g_A^2 + g_B^2)(|E_{y,1}|^2 + |E_{x,2}|^2) + (g_A^2 - g_B^2)(E_{y,1}^* E_{x,2} + E_{y,1} E_{x,2}^*) \mp 0 \end{pmatrix} \quad (2.30)$$

As before, the \pm which appears in front of terms $\propto g_A g_B$ originated from the phase switching action. Adding the phase switched stages together will yield ‘total power’ stream and will remove components which change sign with the phase switch state::

$$\begin{pmatrix} Q1 \\ Q2 \\ U1 \\ U2 \end{pmatrix}^{tp,hyb-T} = \frac{1}{4} \begin{pmatrix} (g_A^2 + g_B^2)(|E_{y,1}|^2 + |E_{x,2}|^2) + (g_A^2 - g_B^2)(E_{y,1}^* E_{x,2} + E_{y,1} E_{x,2}^*) \\ (g_A^2 + g_B^2)(|E_{y,1}|^2 + |E_{x,2}|^2) + (g_A^2 - g_B^2)(E_{y,1}^* E_{x,2} + E_{y,1} E_{x,2}^*) \\ (g_A^2 + g_B^2)(|E_{y,1}|^2 + |E_{x,2}|^2) + (g_B^2 - g_A^2)(E_{y,1}^* E_{x,2} + E_{y,1} E_{x,2}^*) \\ (g_A^2 + g_B^2)(|E_{y,1}|^2 + |E_{x,2}|^2) + (g_B^2 - g_A^2)(E_{y,1}^* E_{x,2} + E_{y,1} E_{x,2}^*) \end{pmatrix} \quad (2.31)$$

Differencing the two phase switch states will yield a ‘demodulated’ stream, con-

taining only components which change with the phase switch state:

$$\begin{pmatrix} Q1 \\ Q2 \\ U1 \\ U2 \end{pmatrix}^{demodulated, hybrid-Tee} = \frac{1}{4} \begin{pmatrix} g_A g_B (|E_{y,1}|^2 - |E_{x,2}|^2) \\ -g_A g_B (|E_{y,1}|^2 - |E_{x,2}|^2) \\ 0 \\ 0 \end{pmatrix} \quad (2.32)$$

We will consider the case with $g_A = g_B = 1$, which yields a simplified expression for the expected signals for both of the modules attached to the hybrid-Tee assembly (denoted as modules 1, 2):

$$\begin{pmatrix} Q1 \\ Q2 \end{pmatrix}^{total-power, module1} = \begin{pmatrix} U1 \\ U2 \end{pmatrix}^{total-power, module1} = \frac{1}{4} \begin{pmatrix} (|E_{y,1}|^2 + |E_{x,2}|^2) \\ (|E_{y,1}|^2 + |E_{x,2}|^2) \end{pmatrix} \quad (2.33)$$

$$\begin{pmatrix} Q1 \\ Q2 \end{pmatrix}^{total-power, module2} = \begin{pmatrix} U1 \\ U2 \end{pmatrix}^{total-power, module2} = \frac{1}{4} \begin{pmatrix} (|E_{y,2}|^2 + |E_{x,1}|^2) \\ (|E_{y,2}|^2 + |E_{x,1}|^2) \end{pmatrix} \quad (2.34)$$

$$\begin{pmatrix} Q1 \\ Q2 \\ U1 \\ U2 \end{pmatrix}^{demodulated, module1} = \frac{1}{4} \begin{pmatrix} (|E_{y,1}|^2 - |E_{x,2}|^2) \\ -(|E_{y,1}|^2 - |E_{x,2}|^2) \\ 0 \\ 0 \end{pmatrix} \quad (2.35)$$

$$\begin{pmatrix} Q1 \\ Q2 \\ U1 \\ U2 \end{pmatrix} \xrightarrow{\text{demodulated,module2}} \begin{pmatrix} (|E_{y,2}|^2 - |E_{x,1}|^2) \\ -(|E_{y,2}|^2 - |E_{x,1}|^2) \\ 0 \\ 0 \end{pmatrix} = \frac{1}{4} \begin{pmatrix} (|E_{y,2}|^2 - |E_{x,1}|^2) \\ -(|E_{y,2}|^2 - |E_{x,1}|^2) \\ 0 \\ 0 \end{pmatrix} \quad (2.36)$$

The signals measured by modules attached to the hybrid-Tee assembly have the following characteristics:

- The demodulated stream has no sensitivity to the Stokes U parameter
- When looking at a purely unpolarized source, such that $E_{x,1}^2 = E_{y,1}^2 = T_1$ and $E_{x,2}^2 = E_{y,2}^2 = T_2$, the demodulated signal (difference) of any of the Q diodes will measure the difference in temperature seen by the two horns: $\frac{T_1 - T_2}{2}$.
- When looking at a purely unpolarized source, the summed signal of any of the diodes will measure the average temperature seen by the two horns: $\frac{T_1 + T_2}{2}$.
- For a polarized source, the demodulated signal of the Q diodes is the difference between the E_x state of one horn, and the E_y state of the neighboring horn.

Phase Switch Imbalance and Double Demodulation

A phase switch circuit has different transmission coefficients between the two phase switch states. To understand the effect of this phase switch imbalance, and investigate a possible mitigation strategy, we will consider the Jones matrix for an imbalanced phase switch circuit and discuss the impact of switching both legs in the following analysis. The results are presented here and the detailed computation is given in Section A.1.

$$\begin{pmatrix} e^{i\phi_A} & 0 \\ 0 & e^{i\phi_B} \end{pmatrix} \rightarrow \begin{pmatrix} +1 & 0 \\ -\beta_A & +1 \\ 0 & -\beta_B \end{pmatrix} \quad (2.37)$$

Before, we considered $e^{i\phi_A} = 1$ and $e^{i\phi_B} = \pm 1$. With this new expression for the phase switching matrix, we have added the following elements:

- We can phase-switch both phase switches, such that $e^{i\phi_A}$ has two possible states $(1, -\beta_A)$, and similarly for $e^{i\phi_B}$: $(1, -\beta_B)$.
- The two phase-switch states for each phase switch can have unequal transmission coefficients. Here we assume the transmission is normalized such that in one state, a phase-switch will transmit with a coefficient of 1, while in the other state it transmits with a reduced coefficient of $\beta_{A,B}$.

Thus, we have four possible phase-switch states corresponding to: $((1,1),(1,-\beta_B),(-\beta_A,1),(-\beta_A,-\beta_B))$. In section 2.3.5 we held the A leg fixed and switched the B leg; in this new case the output depends on which phase state of leg A we chose. Thus phase switching the B leg between 1 and $-\beta_B$ will yield two possible output values, depending on the phase-switch state of leg A (one for $e^{i\phi_A}=1$, one for $e^{i\phi_A} = -\beta_A$). Differencing the signal between the two phase switch states on the B leg will yield a demodulated stream, for two example diodes, of:

$$\begin{pmatrix} (1, 1) - (1, -\beta_B) \\ (-\beta_A, 1) - (-\beta_A, -\beta_B) \end{pmatrix}^{Q1} = \frac{1}{4} \begin{pmatrix} g_B^2(1 - \beta_B^2)E_R E_R^* + g_A g_B(E_L E_R^* + E_R E_L^*) \\ g_B^2(1 - \beta_B^2)E_R E_R^* + \beta_A g_A g_B(E_L E_R^* + E_R E_L^*) \end{pmatrix} \quad (2.38)$$

$$\begin{pmatrix} (1, 1) - (1, -\beta_B) \\ (-\beta_A, 1) - (-\beta_A, -\beta_B) \end{pmatrix}^{U1} = \frac{1}{4} \begin{pmatrix} g_B^2(1 - \beta_B^2)E_R E_R^* + i g_A g_B(E_L E_R^* - E_R E_L^*) \\ g_B^2(1 - \beta_B^2)E_R E_R^* - i \beta_A g_A g_B(E_L E_R^* - E_R E_L^*) \end{pmatrix} \quad (2.39)$$

Without phase switch transmission imbalance, the demodulated stream was proportional to only Stokes Q or U. With phase switch imbalances, the demodulation

stream includes the term $g_B^2(1 - \beta_B^2)E_R E_R^* = g_B^2(1 - \beta_B^2)(\frac{I-V}{2})$. This represents leakage from total power into polarization, and is dependent on the gain in only one leg (in this case, g_B). This is not ideal, we would like the demodulated signal to have no contributions from total power and depend on the gain from both legs equally. Phase switching a second time (switching between the two states on leg A: 1 and $-\beta_A$) and differencing again (‘double demodulation’) gives:

$$\begin{pmatrix} Q1 \\ Q2 \\ U1 \\ U2 \end{pmatrix} = \frac{1}{4} \begin{pmatrix} g_A g_B (1 + \beta_A)(1 + \beta_B) Q \\ -g_A g_B (1 + \beta_A)(1 + \beta_B) Q \\ -g_A g_B (1 + \beta_A)(1 + \beta_B) U \\ g_A g_B (1 + \beta_A)(1 + \beta_B) U \end{pmatrix} \quad (2.40)$$

Thus, double demodulation removes the effects of total power leakage, generated by transmission imbalances in the phase switches.

Module Systematics

We considered a variety of possible systematics which could effect the signal output of the module. We will use the Jones matrices obtained in previous sections for the action of each module component, and add a few possible systematics:

- Complex gain in the amplifiers. It is common for the amplifiers to add a phase contribution to the signal, so we will investigate its effect on the data stream.
- Imperfect *input* into the 180° coupler. This sort of imperfection could occur if the coupling leg in the branchline coupler had a slight phase delay. This would effect the signal processing of both legs.
- Imperfect *output* from the 180° coupler. This would appear as a phase lag after the coupler on only one leg.

We will investigate these effects with the single-demodulated stream to reduce algebraic complication, and because double demodulation was meant to remove a very specific systematic which will not effect the systematics we investigate here. The full analysis is presented in section A.2, a summary table of the effects of these imperfections is given in Table 2.5. All of these imperfections will generally cause a rotation of the Q and U axes, such that the Q and U diodes are not exactly 45° degrees apart from each other. This is consistent with analysis performed on measurements from calibration observations performed during the observing season in Chile (section 5.7) which show that the measured detector angles for diodes within a given module are generally not 45° and 90° apart.

Systematic	(Q1,Q2) Demodulated Stream
None	$\pm \frac{1}{4}g_A g_B Q$
Complex gain	$\pm \frac{1}{4}g_A g_B (Q \cos(\theta) + U \sin(\theta))$
Phase lag on coupled leg	$\pm \frac{1}{4}g_A g_B (Q \cos(\theta) - U \sin(\theta))$
Phase lag on output leg	$\pm \frac{1}{4}g_A g_B Q, -g_A g_B (Q \cos(\theta) - U \sin(\theta))$
(U1, U2) Demodulated Stream	
None	$\pm \frac{1}{4}g_A g_B U$
Complex gain	$\pm \frac{1}{4}g_A g_B (U \cos(\theta) - Q \sin(\theta))$
Phase lag on coupled leg	$\pm \frac{1}{4}g_A g_B (U \cos(\theta) + Q \sin(\theta))$
Phase lag on output leg	$\mp \frac{1}{4}U(1 + \cos(\theta) + \sin(\theta)) + Q(1 - \cos(\theta) + \sin(\theta))$
Averaged Stream	
None	$\frac{1}{4}((g_A^2 + g_B^2)\frac{I}{2} + (g_A^2 - g_B^2)\frac{V}{2})$
Complex gain	$\frac{1}{4}((g_A^2 + g_B^2)\frac{I}{2} + (g_A^2 - g_B^2)\frac{V}{2})$
Phase lag on coupled leg	$\frac{1}{4}((g_A^2 + g_B^2)\frac{I}{2} + (g_A^2 - g_B^2)\frac{V}{2})$
Phase lag on output leg	$\frac{1}{4}((g_A^2 + g_B^2[1 + \sin(\theta)])\frac{I}{2} + (g_A^2 - g_B^2[1 + \sin(\theta)])\frac{V}{2})$
(Q1,Q2) hybrid-Tee Demodulated Stream	
None	$\pm \frac{1}{4}g_A g_B (E_{y,1} ^2 - E_{x,2} ^2)$
Phase lag on input leg	$\pm \frac{1}{4}g_A g_B (E_{y,1} ^2 - E_{x,2} ^2) \cos(\theta) + [E_{y,1}^* E_{x,2} - E_{y,1} E_{x,2}^*] \sin(\theta)$
(U1,U2) hybrid-Tee Demodulated Stream	
None	0
Phase lag on input leg	$\pm \frac{1}{4}g_A g_B (E_{y,1} ^2 - E_{x,2} ^2) \sin(\theta) + [E_{y,1}^* E_{x,2} - E_{y,1} E_{x,2}^*] \cos(\theta)$
(all diodes) Hybrid-Tee Average Stream	
None	$\frac{1}{4}(g_A^2 + g_B^2)(E_{y,1} ^2 + E_{x,2} ^2) + (g_A^2 - g_B^2)(E_{y,1}^* E_{x,2} + E_{y,1} E_{x,2}^*)$
Phase lag on input leg	$\frac{1}{4}(g_A^2 + g_B^2)(E_{y,1} ^2 + E_{x,2} ^2) + (g_A^2 - g_B^2)(E_{y,1}^* E_{x,2} + E_{y,1} E_{x,2}^*)$

Table 2.5: Summary of possible systematics with their effects on the demodulated and averaged streams, as well as the hybrid-Tee modules.

Correlated Noise

We investigate the effects of correlated noise in a module. This analysis was presented in Ref. [8].

We express $E_L = a_0 + ia_1$ and $E_R = b_0 + ib_1$, and assume the variables a_0, a_1, b_0, b_1 are Gaussian random, and that a_0 and a_1 are drawn from the same distribution, but a different distribution from b_0 and b_1 . As Gaussian variables, they have the following properties:

$$\begin{aligned} \langle a_0^2 \rangle &= \langle a_1^2 \rangle = \sigma_a^2 \\ \langle b_0^2 \rangle &= \langle b_1^2 \rangle = \sigma_b^2 \end{aligned} \tag{2.41}$$

Basic Correlation

The correlation expression we use is a standard correlation coefficient (Ref. [63]), given by:

$$C_{XY} = \frac{\langle XY \rangle - \langle X \rangle \langle Y \rangle}{\sqrt{(\langle X^2 \rangle - \langle X \rangle^2)(\langle Y^2 \rangle - \langle Y \rangle^2)}} \tag{2.42}$$

In this case, X is the TOD for one diode (Q1, Q2, U1 or U2), and Y is the TOD for the second diode under consideration (also one of Q1, Q2, U1, or U2). The correlations for the various systematics considered above are given in Table 2.6 and the computation is presented in Section A.4.

We found that:

- For a case with no systematics where the gain and noise are equal in the two legs, the Q diodes should be uncorrelated with each other, the U diodes should be uncorrelated with each other, and all pairs of Q and U diodes (Q1U1, Q1U2, Q2U1, Q2U2) should be correlated with a coefficient of 0.5.

- Introducing complex gain or a phase lag in the input to the coupler does not result in additional correlated noise.
- In the case where there is a lag at the output of the 180° hybrid, there is increased correlation between the diode pairs.

We compute this correlation coefficient for each scan in the observing season (this processing will be discussed in chapter 6). We find each module has some additional correlated noise, a few modules have correlation coefficients in excess by as much as 0.3, which may be pointing to a non-ideality in the output of the coupler. We include noise correlation coefficients in the analysis pipelines, this will be discussed in chapter 6.

Systematic	(Q1-Q2)	(U1-U2)	Q-U
None	$\frac{(g_A^2\sigma_a^2 - g_B^2\sigma_b^2)^2}{(g_A^2\sigma_a^2 + g_B^2\sigma_b^2)^2} g_A = g_B, \sigma_a = \sigma_b \rightarrow 0$	$\frac{(g_A^2\sigma_a^2 - g_B^2\sigma_b^2)^2}{(g_A^2\sigma_a^2 + g_B^2\sigma_b^2)^2} g_A = g_B, \sigma_a = \sigma_b \rightarrow 0$	$\frac{(g_A^4\sigma_a^4 + g_B^4\sigma_b^4)}{(g_A^2\sigma_a^2 + g_B^2\sigma_b^2)^2} g_A = g_B, \sigma_a = \sigma_b \rightarrow 0.5$
Complex gain	$\frac{(g_A^2\sigma_a^2 - g_B^2\sigma_b^2)^2}{(g_A^2\sigma_a^2 + g_B^2\sigma_b^2)^2} g_A = g_B, \sigma_a = \sigma_b \rightarrow 0$	$\frac{(g_A^2\sigma_a^2 - g_B^2\sigma_b^2)^2}{(g_A^2\sigma_a^2 + g_B^2\sigma_b^2)^2} g_A = g_B, \sigma_a = \sigma_b \rightarrow 0$	$\frac{(g_A^4\sigma_a^4 + g_B^4\sigma_b^4)}{(g_A^2\sigma_a^2 + g_B^2\sigma_b^2)^2} g_A = g_B, \sigma_a = \sigma_b \rightarrow 0.5$
Phase lag on coupled leg	$\frac{(g_A^2\sigma_a^2 - g_B^2\sigma_b^2)^2}{(g_A^2\sigma_a^2 + g_B^2\sigma_b^2)^2} g_A = g_B, \sigma_a = \sigma_b \rightarrow 0$	$\frac{(g_A^2\sigma_a^2 - g_B^2\sigma_b^2)^2}{(g_A^2\sigma_a^2 + g_B^2\sigma_b^2)^2} g_A = g_B, \sigma_a = \sigma_b \rightarrow 0$	$\frac{(g_A^4\sigma_a^4 + g_B^4\sigma_b^4)}{(g_A^2\sigma_a^2 + g_B^2\sigma_b^2)^2} g_A = g_B, \sigma_a = \sigma_b \rightarrow 0.5$
Phase lag on output leg	$\frac{\sigma_a^4 - 2\sigma_a^2\sigma_b^2 \cos(\theta) + \sigma_b^4}{(\sigma_a^2 + \sigma_b^2)^2} \rightarrow 0$	$\frac{(g_A^2\sigma_a^2 - g_B^2\sigma_b^2)^2 \cos^2 \theta}{(g_A^2\sigma_a^4 + 2g_A g_B \sigma_a^2 \sigma_b^2 + \sigma_b^4 \cos^2 \theta)} \rightarrow 0$	$\frac{\sigma_a^4 + \sigma_a^2\sigma_b^2[1 - \cos(\theta) + \sin(\theta)] + \sigma_b^4[1 + \sin(\theta)]}{(\sigma_a^4 + \sigma_a^2\sigma_b^2(2 + \sin(\theta)) + \sigma_b^4[1 + \sin(\theta)])^2} \rightarrow 0.5$

Table 2.6: Summary of correlation coefficients, including the systematics studies. Because Q1 and Q2 differ by only a sign, and U1 and U2 differ by only a sign, the correlation expression is identical between all Q-U pairs, such that in this table Q-U denotes Q1U1, Q1U2, Q2U1, and Q2U2. The only case which introduced additional correlation was the case with a phase lag on the output leg.

2.4 Single Module Testing at the Jet Propulsion Laboratory and Columbia University

We measured bandpasses and intrinsic module noise for each module individually in test cryostats both at the Jet Propulsion laboratory and at Columbia University. The cryostat used for testing at Columbia was designed to closely mimic the Q-band receiver; it contains a single feedhorn similar to the Q-band feedhorns, an OMT of nearly the same design we use in the receiver, and a small window prepared identically to the Q-band receiver window (see section 2.6.5). This allowed us to perform tests which were also similar to tests performed with the receiver array, the results of which we could use to predict the end-to-end performance of the receiver.

Bandpasses are measured by injecting a frequency-swept input signal into the module through the window of the test cryostat. The polarized frequency-swept input signal allows us to measure the module response as a function of frequency, and compute module bandwidth and central frequency (these equations, and the measurements with the array, are described in section 3.2). Two small cryogenic thermal loads were used to assess the module noise with this setup, they were built identically to the large thermal loads used for noise tests with the receiver. Measuring the module response for each of two thermal loads at a known temperature allows us to extract module noise temperature (this is outlined in detail in section 3.3).

To achieve QUIET science goals, we required that each module have a noise temperature less than 35K and a bandwidth greater than 7.5GHz (these criteria are described in section 3.3). The single-module tests were used to evaluate whether or not a module should be included: if each diode in the module met these criteria in the test setup, then the module was included in the array. Ultimately we did not compare values for these quantities obtained in the testing setup and the receiver as differences are more likely attributable to the differences two setups than changes in module performance: the OMT in the single-module test cryostat has a slightly dif-

ferent central frequency and the amplifier biasing is very different from the electronics boards used for the receiver.

2.5 QUIET Electronics

2.5.1 Introduction

This section will discuss the electronics boards, weather-proofing, enclosure system, and the cabling scheme in the QUIET experiment. The electronics boards are comprised of:

- Protection circuitry: protect the QUIET modules from voltage spiking.
 - Module Attachment Board
 - Array Interface Board
- Bias Circuitry: provide bias voltage to QUIET module components (section 2.3.2).
 - Amplifier Bias Boards
 - Phase-Switch Bias Boards
 - Pre-amplifier Boards (detector diode bias)
- Analog-to-digital conversion: The Analog-digital conversion (ADC) boards contain ADC chips (AD7674) which convert analog signals from the module detector diodes to a digital signal readable by a control computer. The master ADC has the additional task of relaying biasing commands and timing signals to the other boards.
- Housekeeping Board: monitor amplifier and phase switch bias voltages and currents as well as cryostat temperatures.
- Timing Card and Auxiliary Timing Card: provide a timing signal to the master ADC that is synchronized to the telescope timing.
- External-temperature Monitor Boards: monitor the temperature of the mirrors and ground screen.

The quantity of each type of board for the Q- and W-band instruments, and the number of modules each board-type can support, is given in Table 2.7.

2.5.2 Electronics Overview

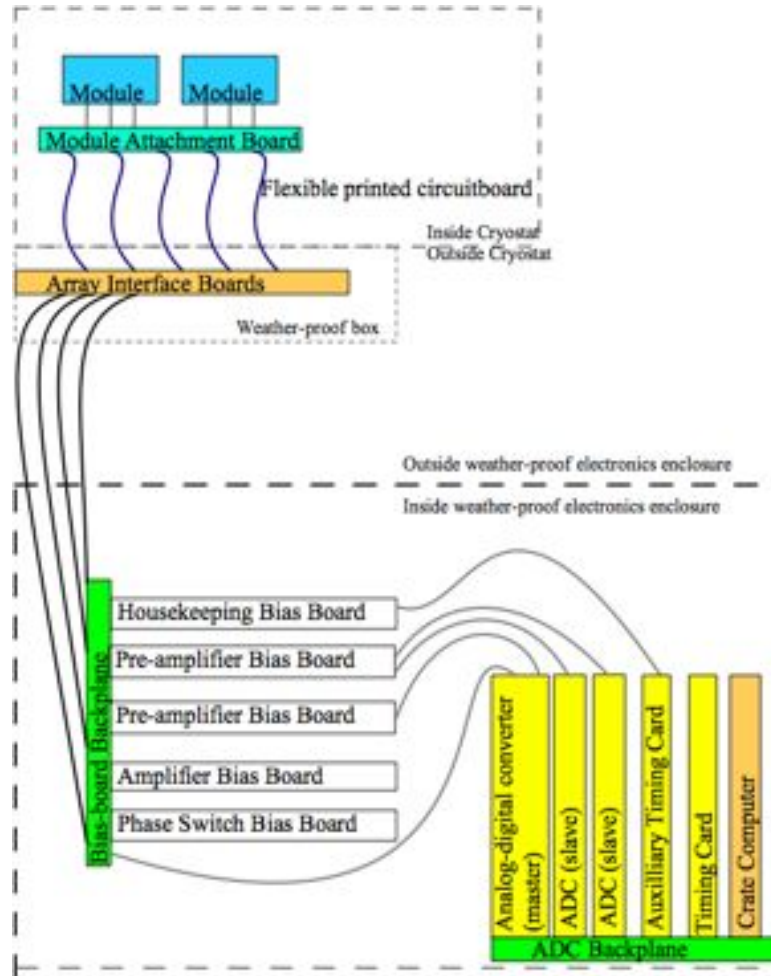


Figure 2-27: A simplified schematic of the QUIET Q-band electronics. Shown are the boards described in the text: the ADC boards (master and two slaves), two timing cards, crate computer, and ADC backplane. Also shown are the bias boards, housekeeping board, and bias-board backplane. These boards are all located within an electronics enclosure. The Array Interface Boards are housed separately, and the Module Attachment Boards are located within the cryostat.

Figure 2-27 shows a simplified diagram and connection scheme for the electronics

Board Label	# of modules supported	# of Boards	
		Q-band	W-band
Phase Switch	23	1	4
Amplifier Bias	7	3	13
Preamp Bias	7	3	13
Analog-digital converter	8	3	13
Housekeeping	NA	1	1
Timing+Auxiliary Timing	NA	1	1

Table 2.7: Summary of electronics boards for the Q- and W-band polarimeter arrays.

boards in the QUIET experiment. The connection between the modules to the control computer is as follows:

1. The modules attach to the Module Attachment Boards (MABs) inside of the cryostat.
2. The MABs are connected to the Array Interface Boards (AIBs) with flexible printed circuitboards (FPCs).
3. The AIBs connect to the amplifier bias boards, phase switch bias boards, and pre-amplifier boards via custom cables.
4. The bias boards and housekeeping board communicate along a common backplane ('bias-board' backplane). Custom cables form the connection from the preamplifier boards and housekeeping board to the analog-digital converter (ADC) boards.
5. The ADC boards, timing card, an auxiliary timing board, and a crate computer are connected through a second backplane ('ADC backplane').

All electronics boards are controlled by software loaded onto a Versamodule Eurocard bus (VME) crate-computer; commands are sent to this computer from the control room.

Electronics Enclosures

The backplanes, bias boards, ADC boards, timing cards, external temperature monitor boards, and crate computer are all housed in a thermally-regulated electronics enclosure. The enclosure is water- and weather-proof, protecting the electronics from the harsh conditions of the Chilean desert and serving as a Faraday cage to minimize radio-frequency interference, which can introduce unwanted spikes in the science data signal. The enclosure also supports a set of linear power supplies – which power the bias boards – and regulation circuits for controlling the cryostat temperatures and the enclosure temperatures.

The temperature of the electronics enclosure is regulated at 25°C and is set to control the temperature to $\pm 1^\circ\text{C}$. The enclosure temperature during the Q-band observing season is shown in Figure 2-28 for one of the enclosure temperature sensors. This sensor has an average value of 25.4°C with root-mean-square (RMS) of $\pm 1.1^\circ\text{C}$ (these sensors are not absolutely calibrated, so while we regulate to 25°C, the sensor will have offset – in this case 0.5°C). There was a downward linear trend in enclosure temperature over the course of the season, dropping by $\simeq 1^\circ$ over the entire season. This is not correlated with ambient temperature and the cause is unknown. The large deviations in temperature occurred when regulation failed, this represents $\simeq 10\%$ of the full data set.

Cabling and Backplanes

Each module requires $\simeq 25$ independent wires to bias the active components and read the signals from the detector diodes. The 19 modules in the Q-band array require a total of $\simeq 500$ bias and signal connections (the W-band array will require $\simeq 5\times$ more connections), which must be made through a hermetic seal. To keep the cabling manageable within the cryostat, QUIET opted to use flexible printed circuit boards (FPCs), depicted in Figure 2-29, to make the connection between the MABs and the AIBs. FPCs have extremely high-density traces, necessary for the number of bias

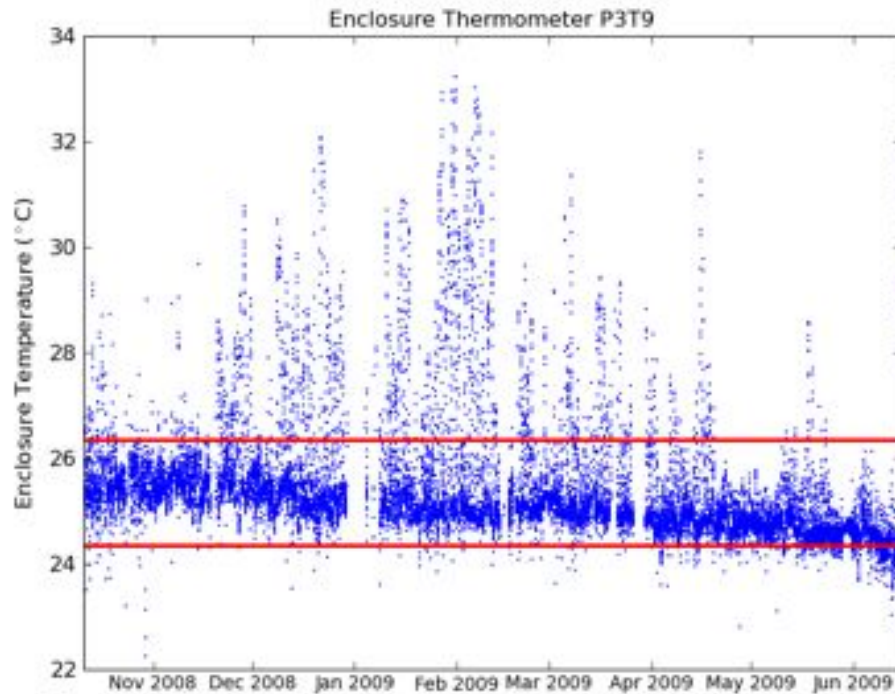


Figure 2-28: Enclosure temperature during the Q-band observing season for one of the temperature sensors in the enclosure. The red lines shown are $25.4 \pm 1.0^\circ\text{C}$, showing regulating temperatures. 11.5% of the data lies outside of the regulating temperatures, regulation generally failed during the hottest periods of the day. We chose the setpoint of 25°C because the output of the amplifier bias boards are less dependent on enclosure temperature around 25°C . We still included data from times when the enclosure was not regulating, the correction for enclosure temperature is detailed in section 5.3. Data courtesy Robert Dumoulin.

lines we require, and can be easily potted into connectors to form a vacuum-tight feed-through system.

QUIET has two backplanes, both conform to a VME-6U standard size. I will refer to them as the ‘ADC backplane’ and the ‘bias-board backplane’.

The ADC cards, timing cards, and crate computer all connect to the ADC backplane (Figure 2-30(a)); this transfers commands between the crate computer and ADCs as well as timing signals between all of the boards. The custom-built bias-board backplane (Figure 2-30(b)) supports the bias boards and housekeeping board

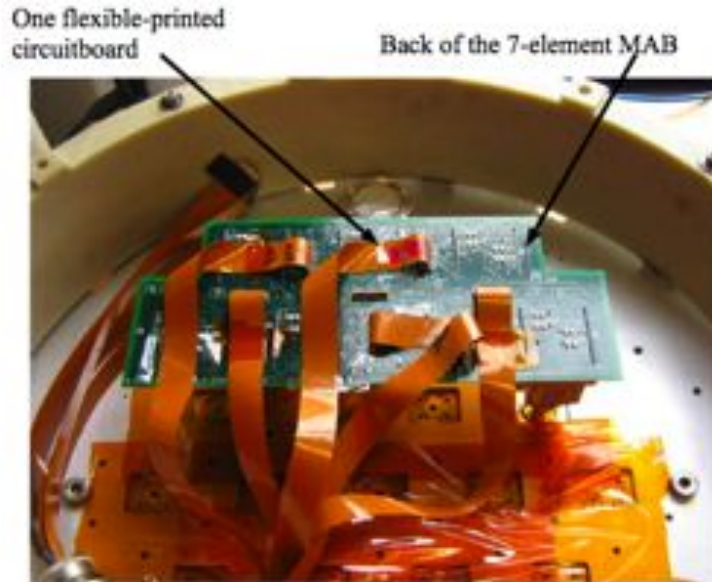


Figure 2-29: A photograph of the flexible printed circuitboards (FPCs) connected to the Q-band 7-element MAB. Courtesy Ross Williamson.

and transmits timing and command signals from the master ADC. The connection between the master ADC and the bias-board backplane is formed with a low-voltage differential-signaling (LVDS) cable. The LVDS protocol allows us to transmit fast timing signals with minimal loss and interference between the signal lines.

The remaining cables in the QUIET connection scheme are custom cables with standard connectors.

2.5.3 Protection Circuitry

The QUIET electronics scheme contains two layers of protection circuitry for the modules: the first layer is located inside of the cryostat on the Module Attachment Boards (MABs), the second layer sits just outside of the cryostat, on the Array Interface Boards (AIBs).



Figure 2-30: *a*: Manufacturer's picture of the Weiner crate and backplane (<http://www.wiener-d.com/index2.php>). This houses the ADC cards, crate computer, and timing cards for QUIET. *b*: A photograph of the backplane, populated with two amplifier bias cards, a phase switch bias card, and a preamplifier bias board.

Module Attachment Boards - MABS

The MABs serve two functions: the pins on each module attach to spring-loaded pin sockets on the MAB, thus the MABs are the point of contact between modules and the other electronics boards for biasing and signal retrieval. The MABs also contain protection circuitry to guard the module components from potentially damaging voltage spikes. The Q-band array has three MABs (two of which support six modules each, the third supports seven modules), the W-band array has 13 MABS (all W-band MABs support seven modules). A photograph of all Q-band MABs is shown in Figure 2-31(a), and the populated Q-band seven-element MAB is shown in Figure 2-31(b). Each MAB has a set of protection circuitry for each of the active components in the module (Ref. [24]):

- Amplifier Gate protection: this consists of a voltage clamp, limiting the allowed voltage to the gate circuit to within $\pm 0.38\text{V}$.
- Amplifier Drain protection: this consists of a voltage clamp, limiting the allowed voltage to the drain circuit to within -0.75 to 1.5 V .

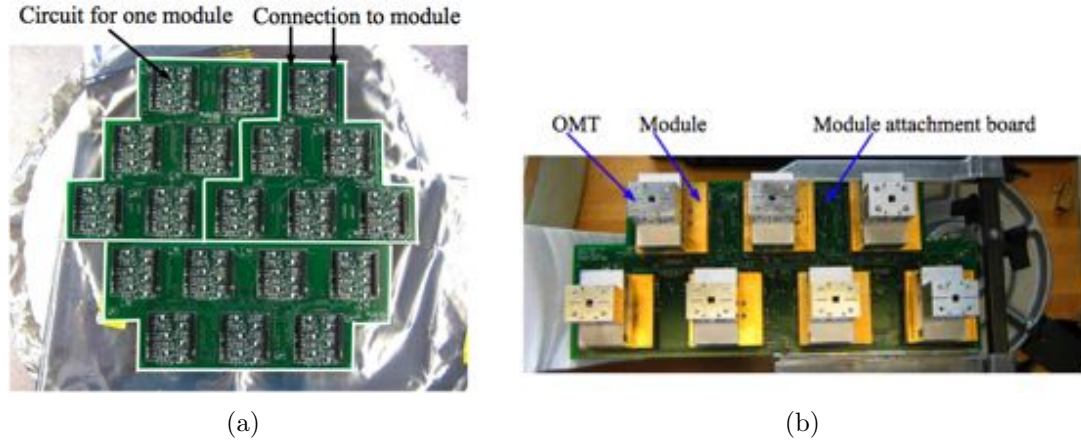


Figure 2-31: *a*: A photograph of all three Q-band MABs. Each MAB contains either six or seven independent circuits, for a total of nineteen attachment points, one per module. *b*: A photograph of the Q-band seven-element MAB, populated with modules and OMTs.

- Phase switch protection: this consists of a voltage clamp, which limits the allowed voltage to within -3 to 1.43 V. It also has a capacitor to ground, which will isolate the phase switch bias from fast transients.

The protection circuitry on the MABs is only rated to work above $\simeq 200\text{K}$. We cool the modules and MABs to $\simeq 20\text{K}$ in the cryostat, so the protection circuitry designed to protect against transients present during assembly and testing will cease to fully function while we are taking science data.

Array Interface Boards - AIBs

The AIBs serve as the cabling interface between the FPCs from the receiver and the board connectors on the bias boards. They are located on a flange on the outside of the cryostat and contain identical protection circuitry to the MABs such that they serve as the protection circuitry when the cryostat (and hence the MABs) are cryogenically cooled. They are protected from ambient weather conditions by a water-proof sealable box placed over the boards. There are six AIBs for the Q-band array: one AIB for the phase switch board, three AIBs for the three amplifier bias boards,

and two AIBs for the three preamp boards.

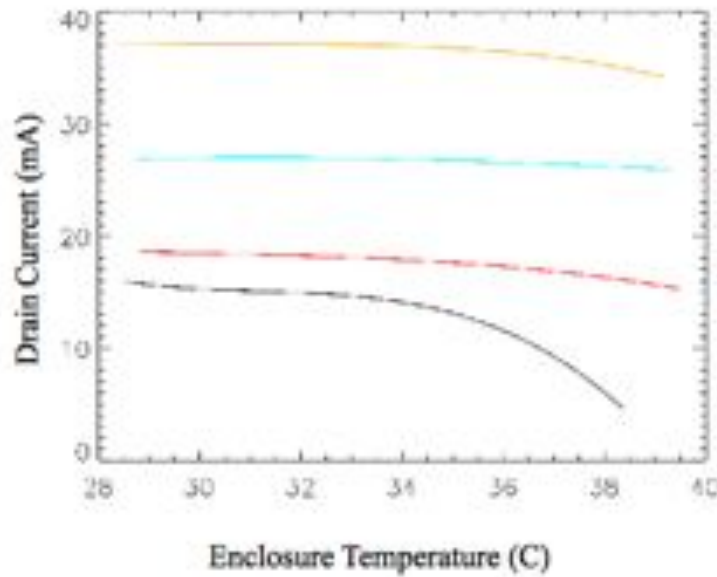


Figure 2-32: Output bias current for one channel of the amplifier bias board as a function of board temperature. Ideally this would be a flat line, indicating that the bias is constant as a function of enclosure temperature. Instead, the bias values change as temperature increases. The four different curves are different bias set-points, typical bias currents for the three stages of amplification in the module are 5mA, 10mA, and 15mA (this data was taken with the W-band modules, which have different biasing procedures). Lower bias values have a steeper dependence on the board temperature. During observations in Chile the enclosure temperature is regulated to 25°C, so the temperature range explored in this plot is far higher than we will typically see while observing. Courtesy Dan Kapner.

2.5.4 Bias Boards

The active components in each module require biasing. This section discusses the function and performance of the electronics boards used to bias these components: the amplifier, phase switch, and pre-amplifier bias boards.

Amplifier Bias Boards

The Q-band array has three amplifier bias boards. Each amplifier board provides a constant current source for the LNAs in up to seven modules. Typical bias values are tuned to independently optimize performance of each module, and range between

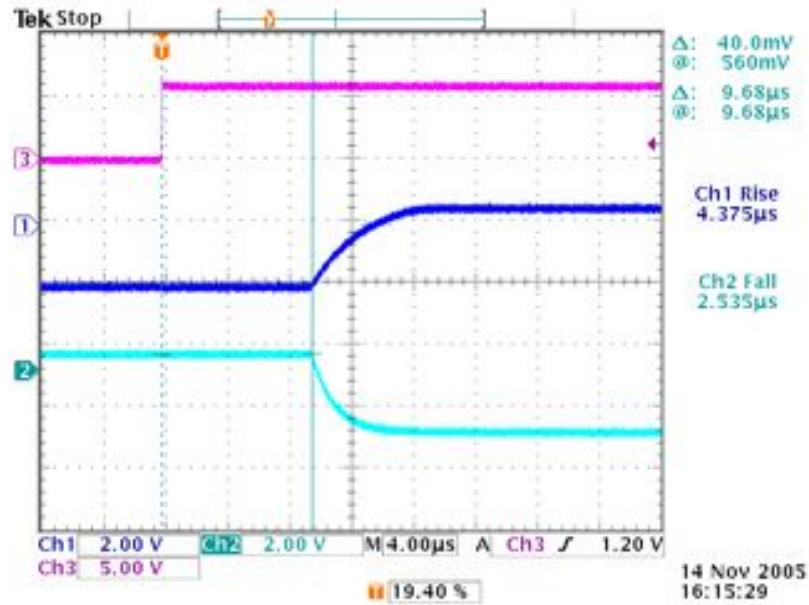


Figure 2-33: Voltage measured from the output of the phase switch board (blue and green), compared to the input command (pink). The time lag between the command to turn on (the sharp shift in the pink trace) and the turn-on of the phase switches is $\simeq 9.7 \mu$ s. The rise time of the phase switches (from off to fully on) is $\simeq 4.4 \mu$ s. Courtesy Joey Richards and Mike Seiffert.

5-30 mA for the drain current.

Laboratory testing showed that the current provided by the amplifier bias boards is dependent on the enclosure temperature. Laboratory data of this trend is shown in Figure 2-32 and indicates changes in drain current $\simeq 1$ -2%/°C (it should be noted that the temperature range of the lab data is higher than the design temperature for the boards of 25°C). Changes in signal level with enclosure temperature, regardless of source, will be mitigated by an enclosure temperature-dependent responsivity model, discussed in Chapter 5.

Phase Switch Boards

The Q-band array has one phase switch board. One phase switch board is capable of providing bias for 23 modules. Typical bias values are 0.0-1.2 mA, with a reverse

bias condition of -2V. We bias the phase switches at $\simeq 400 \mu\text{A}$.

The phase switch turn-on delay and rise-time are plotted in Figure 2-33. The phase switch delay (the time between when the board receives the commanded to turn on, and when the current begins to change) was measured to be $9.7\mu\text{s}$ and the rise-time of the phase switch current (from off to fully on) was measured to be $4.4\mu\text{s}$. The turn-off delay time is longer than the turn-on time, at $15.7 \mu\text{s}$, and the fall-time is shorter, at $2.6\mu\text{s}$. All values are acceptable given our switching rate of 4kHz (once per $250\mu\text{s}$). Masking of this transition will be discussed in Section 2.5.5

Pre-amplifier Boards

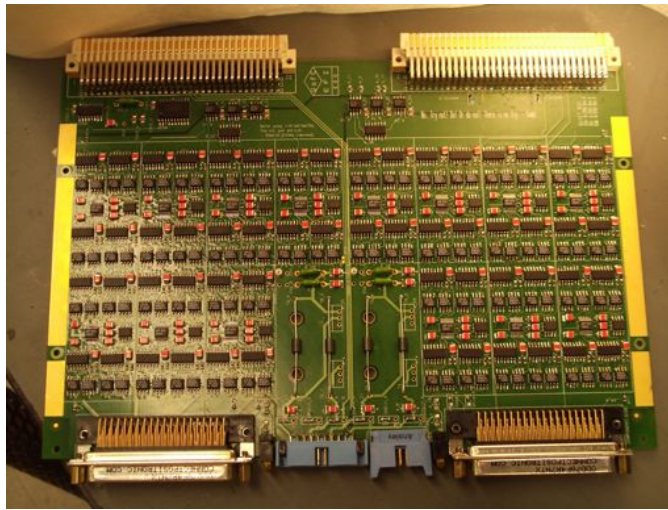
The Q-band array has two pre-amplifier boards, a photograph of one is shown in Figure 2-34(a); each board can support up to 14 modules. The pre-amplifier boards serve two functions: they bias the detector diodes in the modules and amplify the signal from the diodes prior to routing it to the ADC boards.

When cryogenically cooled, the zero-bias Schottky diodes in the Q-band modules require biasing to 0.25V, this is provided by the pre-amplifier biasing circuit (shown in Figure 2-34(b)). Amplification by a factor of 64 occurs after the biasing circuit (Ref. [8]), this allows us to utilize the full dynamic range of the ADC chips.

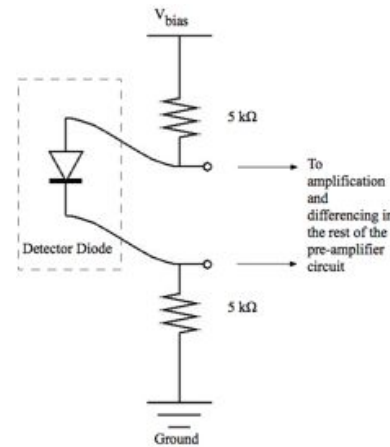
The noise of the preamplifier circuit was measured to be $8\text{nV}/\sqrt{Hz}$ (Ref. [8]), we are currently investigating whether this indicates the noise is dominated by preamplifier noise (which would not be a problem, it averages down as white noise).

2.5.5 Monitor and Data Acquisition Boards

Each receiver array has a set of analog-to-digital conversion boards and one house-keeping board.



(a)



(b)

Figure 2-34: *a*: A photograph of a preamplifier board. Each board contains enough circuitry to bias and amplify two MABs, so the two connectors on one edge are the inputs from two MABs, and the connectors on the opposite side are the outputs to the ADC via the backplane. *b*: A schematic of the preamp biasing circuit. Courtesy Colin Bischoff.

Analog-Digital Conversion Boards

The Q-band array has three analog-to-digital converter boards (ADCs): one master and two slaves. The ADC chips on each ADC board receive a voltage signal from the pre-amplifier boards, convert it to a digital signal, and send the digitized signal down the ADC backplane to the computer (where it can be stored). Each ADC board has 32 18-bit ADC chips, such that each ADC board can support digitization for 8 modules. The master ADC board has an additional set of tasks: it receives commands and bias information from the crate computer, and timing signals from the timing board, and distributes this to the bias-board backplane via a low-voltage differential-signal (LVDS) cable.

Each ADC chip collects data at a rate of 800 kHz. Because we phase switch at 4 kHz, each ADC chip collects 200 samples in one phase switch state, and another 200 samples in the second phase switch state. Each ADC board has a field-programmable gate-array (FPGA) chip: the FPGA firmware loaded on the chips commands the

ADCs to sum or difference the module data stream at the phase switch frequency. For each channel, an ADC will sum the 200 samples together, accumulate the result, and output the average of the summed stream as a 100 Hz ‘total power’ stream. It will also difference the first 200 samples from the second 200 samples, and accumulate the output as an averaged of the differenced stream as a 100 Hz ‘demodulated’ stream. There is an additional high-speed data-taking mode, in which 32 samples of the 800 kHz stream are written to a file; this is useful for debugging and timing monitoring purposes. During observations in Chile we take one snapshot of high-speed data once every minute, and save only one in ten snapshot data sets.

In practice, instead of counting by sample, an ADC will use the 4 kHz clock as a timing signal to difference and sum, and employ a mask to remove the spikes in the data which occur during a phase switch transition. The mask is configurable and selecting a mask can be delicate: if you mask too much you will unnecessarily reduce instrument sensitivity (instrument sensitivity scales as $\frac{1}{\sqrt{t}}$, and the masking factor will reduce the time, t), but the spiking from the transition region will negatively impact science data. For science observations, we have set it to mask 13% of the data after a series of tests, reducing the masking percentage until transients appeared in the data stream.

During observations at the site, it was discovered that the ADC chips have a discontinuity in their output voltage. The discontinuity is present at a particular bit value and also at integer values of that bit number (depicted in Figure 2.5.5). Because the voltage on the ‘total power’ channel is the average of the input voltage to the chip, the bit value at which the ADC glitches will correspond to a particular total power value; because ADC outputs the average of $\simeq 85$ samples, the effect of this glitch is spread over a range of measured total power values around the true glitching value. We correct for this glitch in the analysis pipelines, discussed in more detail in section 4.4.4.

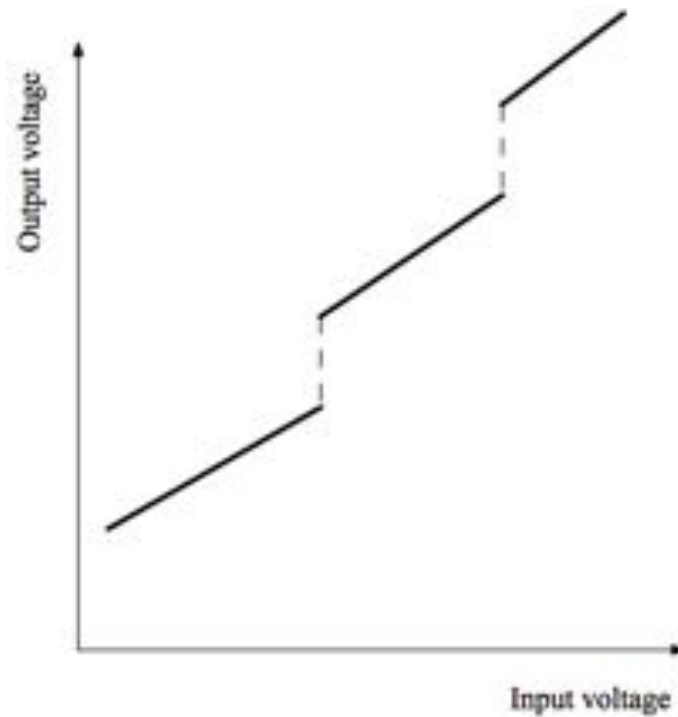


Figure 2-35: A diagram of the ADC glitch, which causes a discontinuity in the output voltage at integer values of a (channel-dependent) bit value.

Housekeeping Board

The housekeeping board monitors the following quantities:

- Amplifier bias currents
- Phase switch bias currents
- Cryogenic temperature sensors
- Electronics enclosure temperature sensors
- Pressure sensor

The output of the housekeeping board is multiplexed such that the master ADC selects which channel is read out, one housekeeping quantity at a time in series, via changing address lines in commands to the housekeeping board. It is desirable that

the ADCs do not send commands to the housekeeping board while science data is being taken, so the address lines are changed only during the delay time in the phase switch ($\simeq 10\mu s$) when we are masking the data. Given the number of channels read out (515) and the time it takes to read a single channel, this gives a sample rate for any of the housekeeping channels of almost exactly 1 Hz. The housekeeping board monitoring is sent across the backplane and down the LVDS cables to the ADC.

2.5.6 Timing cards

The Q-band array has one timing card and one auxiliary timing card. Together, they are responsible for synchronizing the timing of the receiver to the timing of the telescope such that we can match the receiver data stream with the telescope pointing. The timing card receives an absolute time signal from the telescope control electronics and sends a clocking signal to the auxiliary timing board, which distributes the clocking signal to the master ADC board.

2.5.7 External-Temperature Monitor Boards

The ground screen was discussed in section 2.2.6 where it was noted that we placed temperature sensors around the ground screen structure to monitor its temperature. These sensors are read by analog sensor cards (Sensorray cards) located in the electronics enclosure.

2.5.8 Software

We used pre-existing software to control the telescope that was developed for a previous experiment (Ref. [70]). The receiver control software (RCS) was developed for QUIET. The primary task of the RCS is to interface with the crate computer to send bias, phase switching, and data-taking commands. The data is stored in 28-minute files, which are retrieved by other computers located at the observing site.

The RCS also contains data flagging to identify periods when the software or receiver is not working properly. There are $\simeq 30$ flags, they generally look for timing problems (time-frames dropped, abnormal time separation between stamps, offsets between the timing between various boards, etc), uneven numbers of data samples for the various data streams, and phase-switch transition masking problems. A few of the flags are status flags instead of warning flags, they indicate the phase switch state and the data-taking rate (we take down-sampled when the telescope is stowed, for example).

2.6 Cryostat

2.6.1 Introduction

This section describes the design and performance of the cryostats for the W-band and Q-band receivers. The primary purpose of each cryostat is to maintain the modules, feedhorns, and OMTs at a constant cryogenic temperature of $\simeq 20\text{K}$ over the observing season.

Both cryostats were designed and tested at Columbia. The design phase included simulating the mechanical stresses on the system to ensure adequate vacuum and support for the optics under observing conditions, and computing the expected temperatures for relevant components given anticipated radiative and electrical heating loads. We validated the cryostats for use by cooling them with heat loading configurations meant to mimic the conditions with the receiver array installed. We also designed and built the cryostat vacuum windows for each of the two receiver arrays. This process included selecting viable materials for both the window and the anti-reflection (AR) coating, and developing a process for applying the AR coating.

2.6.2 Description of W- and Q- band Cryostats

The cryostat design, including cooling, external components, and internal components is described in this section.

Cryogenic Cooling

Cryogenic temperatures in each cryostat are achieved with two Gifford-McMahon dual-stage refrigerators. Each refrigerator is a CTI 1020 with its own 8600 water-cooled compressor. The first stage of the refrigerator has a minimum temperature of $\simeq 35\text{K}$ and the second stage of the refrigerator has a minimum temperature of $\simeq 8\text{K}$ under zero-load conditions (Ref. [21]).

External Cryostat Components

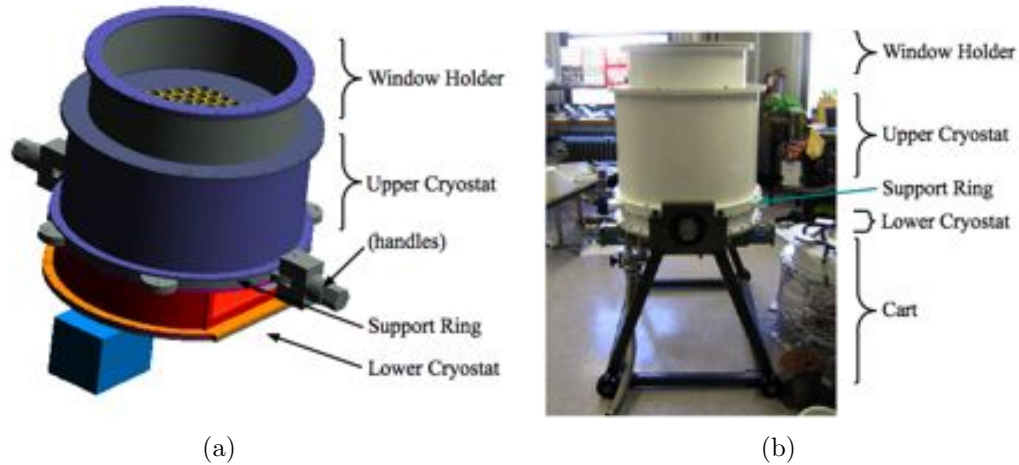


Figure 2-36: The outer cryostat consists of the Window Holder section, the Upper Cryostat section, the Support Ring, and the Lower Cryostat section. These are shown in *a*: CAD model of the outer shell of the W-band cryostat. *b*: A photograph of the outer shell of the Q-band cryostat. The W- and Q-band cryostat designs are similar.

Each cryostat is composed of four external stainless steel sections; a lower section, a support section, an upper cryostat section, and the window holder, as shown in Figure 2-36(a) and 2-36(b). The shell of the cryostat was designed as a vacuum vessel with simple disassembly procedure designed to provide access to the array engine during assembly and servicing. The base contains attachment points for connectors, refrigerators, vacuum gauge, vacuum pump, and access panels. The stainless steel support ring is supported by the cart for work in the laboratory and serves as the interface to the telescope mount. The window holder section houses the 4-inch thick infrared-blocking filter, with enough additional height to account for the bowing of the window under vacuum pressure. The diameter of the window holder section is designed to give an optical half angle of 22° from the outer edge of the outer horn, such that the top rim will not interfere with the feedhorn beam.

Internal Components

The internal components (Figure 2-37(a) and 2-37(b)) of each cryostat consist

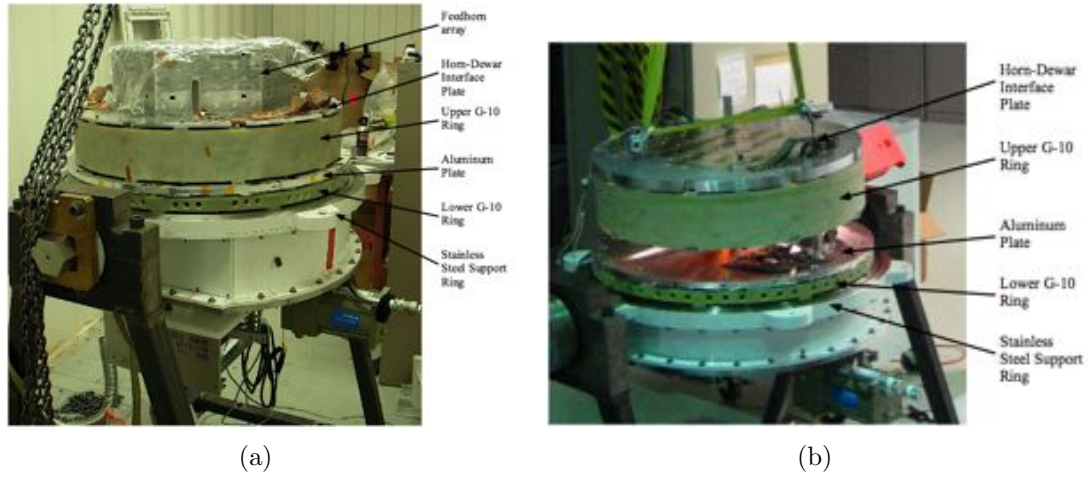


Figure 2-37: Internal components of each cryostat; shown are the horn-dewar interface plate, upper G-10 ring, aluminum plate, lower G-10 ring, and stainless steel support ring for the *a*: W-band cryostat (including feedhorns) and *b*: the Q-band cryostat. The horn-dewar interface plate and upper G-10 ring are being lifted by a crane in this photograph, such that you can see the plane of the aluminum plate.

of a lower G-10 ring (G-10 is a composite material with low thermal conductivity and high tensile strength), an aluminum plate, an upper G-10 ring, and the horn-dewar interface plate. The aluminum plate is thermally strapped to the first stages of the refrigerators, and is thermally isolated from the support ring by the lower G-10 ring. The aluminum plate and the aluminum walls which attach to it function as a radiation shield by absorbing radiation at 300K and re-emitting $\simeq 60\text{K}$ radiation, reducing the thermal loading on the second stages of the refrigerators. We wrap the radiation shield walls with Multi-layer insulation (MLI) to help reduce the load on the shield walls. The horn-dewar interface plate is thermally strapped to the second stages of the refrigerators, and is thermally isolated from the aluminum plate by the upper G-10 ring. It has waveguide holes for each horn that propagate the signal from the feedhorn array to the OMTs or TTs.

Both cryostats contain a 4" thick piece of polystyrene (styrofoam) of 3 lb/ft^3 density attached to the top of the radiation shield lid. The thermal insulation properties of the styrofoam allow us to keep the bottom surface at nearly the temperature of

the radiation shield, reducing the thermal loading on the cold stage of the refrigerators. Our minimum requirement is to hold the bottom surface at 140K, which was demonstrated in the laboratory.

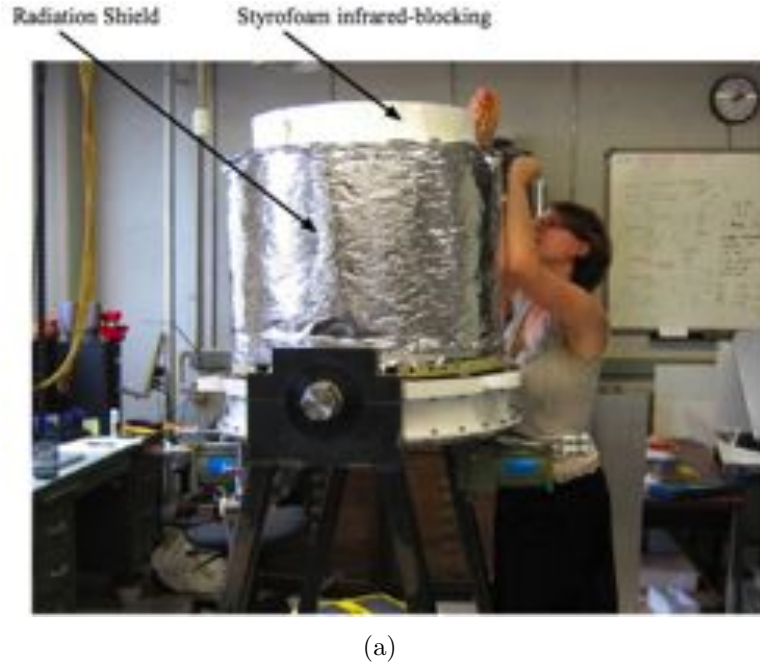


Figure 2-38: *a*: A photograph of the Q-band radiation shield, covered in multi-layer insulation (MLI), and the styrofoam used as an infrared radiation blocker.

Differences Between the W-band and Q-band Cryostat Designs

The diameters of the W-band and Q-band cryostats are identical to simplify the process of interchanging the receivers on the telescope. The Q-band feedhorn array is twice as tall, such that the Q-band cryostat is 7.25 inches taller above the support ring than the W-band cryostat.

Cryostat Dimensions and Design Details

2.6.3 Mechanical Simulations

We performed finite-element analysis (FEA) simulations with the 3-D CAD program IDEAS of critical pieces for the 91 element W-band and 19 element Q-band cryostats.

Part -	W-band		Q-band	
	Height (in)	Weight (lbs)	Height (in)	Weight (lbs)
Lower Cryostat	6.25	127.4	4.25	92.03
Stainless Steel Support Ring	1	67	1	67
Upper cryostat	12.125	55.9	19.375	72.8
Window Holder	7.25	61	7.25	64.5
Window	0.25"	—	0.375	—
Totals	26.875	311	31.875	296

Table 2.8: Dimensions of the external elements of each cryostat. Note that the these weights (both total and separate) do not include masses of the components inside the cryostat, e.g. horns, fridges, OMTs, etc.

The cryostat is mounted on the telescope such that it is oriented sideways with the length of the cryostat horizontal to the ground. During science observations, the telescope platform is tilted as much as 70° , so it is critically important that we understand how the design will behave at variety of angles. We focused our studies on the G-10 rings as they will have the highest stress due to their shape and the observing orientation. We simulated the effect of rotating the cryostat at a variety of different orientations, which is accomplished in practice by defining acceleration vector directions. The definition of the acceleration vectors is shown in Figure 2-39(a).

- X angle refers to a rotation around the axis of the cryostat
- Z angle of zero sets the axis of the cryostat to be horizontal.

Figure 2-39(b) shows the initial orientation from above. Our simulations show that we are always under ten percent of the maximum stress of G-10 (40,000 psi lower bound).

2.6.4 Expected and Measured Cryostat Temperatures

Loading on each of the two stages of the refrigerators is presented in this section, with an estimate of the final temperatures we expected to achieve with each cryostat.

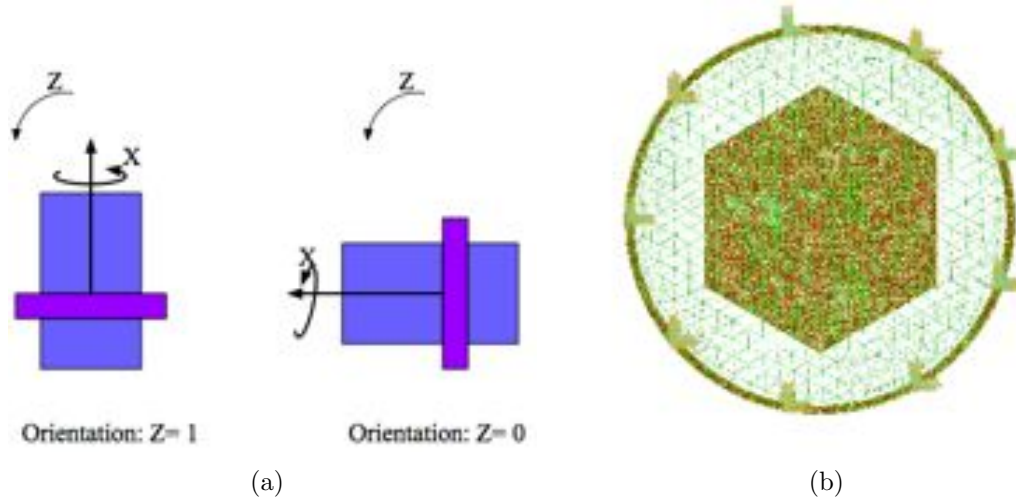


Figure 2-39: *a*: Definition of acceleration vector used for simulations, $Z=0$ implies the gravitational vector is applied sideways relative to the cryostat, or alternately, that the cryostat is on its side. *b*: A screen grab of the I-DEAS simulation to determine the maximum stress on the upper G-10 ring. The orientation of the hexagon is clear. The right angle shapes are the constraints placed on the G-10 feet.

Total Power-Loading and Expected Temperatures

We estimate the expected refrigerator temperatures given the thermal loading computed. We performed this computation this twice: once for an assumed ambient temperature of 300K, and again for an ambient temperature of 270K, to understand the effects of the diurnal temperature variation during observations in Chile will have on the cryostat temperatures. The loading is given in Table 2.9 and the expected temperatures are given in Table 2.10. The difference in refrigerator temperatures between the two ambient temperatures is $\simeq 1$ -2K. We compensate for this variation with power resistors attached to each refrigerator that are connected to a commercial temperature cryogenic regulator (Section 2.5).

We assumed temperatures of 80K and 20K for the two cold plates, however the calculations showed these temperatures are actually 50K and 20K. To see if we have reached a stable solution, we recomputed the plate temperatures with an assumed 50K and 20K plate temperatures, and the results differed by 1K, indicating we found

Heat Source	300K Load (W)		270K Load (W)	
	W-band	Q-band	W-band	Q-band
Conduction through lower G-10	5.7	5.7	5	5
ambient on radiation shield	12	21	8	13
ambient on Aluminum Plate	8	8	5.2	5.2
Conduction through FPCs	1.54	0.66	1.33	0.57
First stage TOTAL:	27	35	20	21
Conduction through upper G-10	2	2	2	2
80K from radiation shield	0.12	0.27	0.12	0.27
80K from aluminum plate	0.19	0.18	0.19	0.18
Heating from module components	4.6	0.95	4.6	0.95
Heating from module boards	1.1	0.47	1.1	0.47
Conduction through FPCs	1.26	0.54	1.26	0.54
Radiation from window	5	5	5	5
Second Stage TOTAL:	13	10	13	10

Table 2.9: Calculated thermal loading from various sources with 300K and 270K environment temperature, assuming 80K warm plate and 20K cold plate, for each cryostat.

a stable solution. This also implies that the loading on the warmer refrigerator stage is not the dominant factor contributing to the temperature of the coldest stage.

Table 2.10 includes the temperatures achieved in the cryostat in Chile. The temperature of the cold stages are within a few Kelvin of the predicted values. The final warm plate temperature for the Q-band array is 10K lower than expected, while it is 15K higher than expected for the W-band. Both achieved adequate cold plate temperatures for science observations. The fact that the W-band cryostat had adequate cold plate temperatures but higher than expected warm plate temperatures supports the assertion that the warm plate temperature is not the determining factor in the cold plate temperature. Possible discrepancies between the predicted and final temperatures for the warm plate include: non-ideal thermal strapping, non-ideal interfaces between thermal strapping and plates, and loading in excess of predictions from IR sources or from expectations of MLI performance for the W-band cryostat.

	300K Ambient		270K Ambient		Achieved: in Chile	
	W-band	Q-band	W-band	Q-band	W-band	Q-band
First stage total loading (W):	27	35	20	21		
Second Stage total loading (W):	13	10	15	7		
First stage temperature (K)	50	52	45	45	65	39
Second stage temperature (K)	16	12	15	11	18	16

Table 2.10: Refrigerator temperatures given loading for the W- and Q-band receivers. The 300K and 270K ambient temperatures are calculated from expected loading, the last column shows the temperatures in Chile (ambient temperature $\simeq 270\text{K}$). The Q-band values are an average over the season for the two plate temperatures, it should be noted that we regulate the plate temperature. The W-band values are given before regulation was implemented (the W-band cryostat is regulated around 25K).

Measured Performance

The temperatures of the cold plate and polarimeters in the Q-band cryostat during the observing season are shown in Figure 2-40. Two sensors (T0 and T2) are attached to the interface plate. Three sensors (T5, T6, and T7) are clamped to three modules in the array (RQ17, RQ02, and RQ07 respectively). RQ17 and RQ02 are both near refrigerators, RQ07 is furthest from a refrigerator. The connection to T2 was lost for a large part of the season. The average temperatures through the season for each cold-plate thermometer is given in Table 2.11, T0 (the most reliable temperature sensor) was regulating within $\pm 0.3\text{K}$ for 96.8% of the season.

Sensor	Description	Temperature
(P2)T0	Cold plate	14.5 ± 0.1
(P2)T2	Cold plate	14.6 ± 0.4
(P2)T5	on RQ17	20.0 ± 0.3
(P2)T7	on RQ07	25.8 ± 4.9

Table 2.11: Average temperatures for the cold plate and radiation shield components in the cryostat during the Q-band observing season. The errors given are one standard deviation. P2T5 and P2T7 are clamped to two modules and have a (likely) poor thermal contact.

Figure 2-41(a) shows a cool-down with the W-band cryostat during laboratory tests. At the site we regulate the temperature of the interface plate and modules to $\simeq 26\text{K}$.

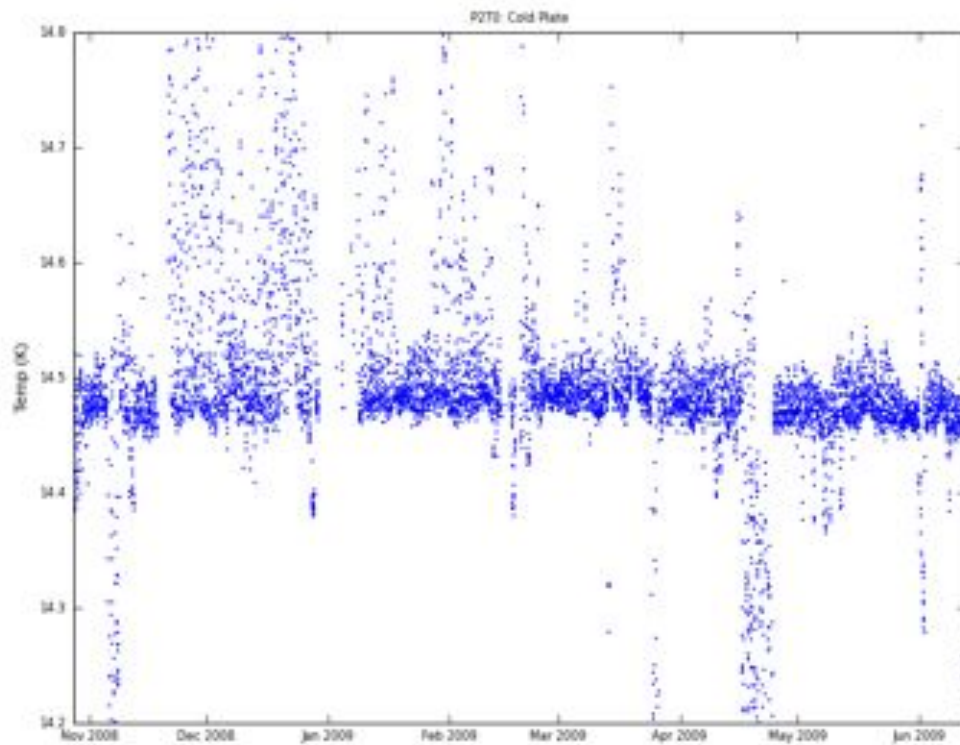
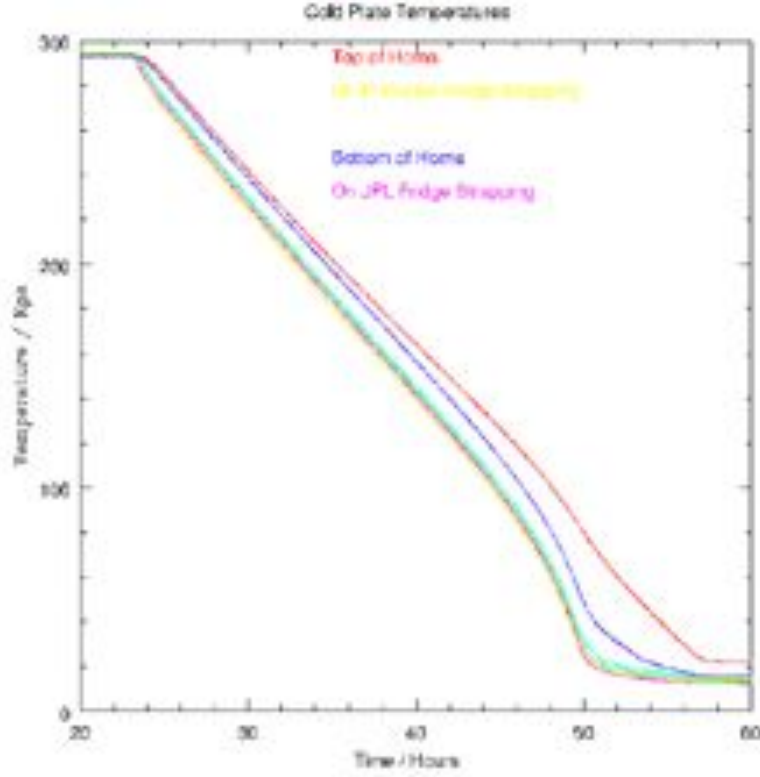


Figure 2-40: Receiver temperatures through the Q-band season for sensor P2T0. The deviations from the average trend are generally from periods of generator maintenance, when the compressors are turned off for a short period of time (and the cryostat warms up slightly).

Expected Thermal Gradient Across the Modules

The upper limit for the thermal gradient between the modules is computed and presented in Table 2.12 for both Q- and W-band arrays. We assume a loading of 5 W and thermal conductivity of k_{Al} ($8 \text{ W m}^{-1} \text{ K}^{-1}$), and compute the gradient between a module located nearest and furthest from a refrigerator.

The W-band thermal gradient is measured from the largest difference in temperature for the W-band modules. The Q-band thermal gradient are measured from the two temperature sensors on opposite sides of the interface plate (the thermal contact between the temperature sensors and the modules is poor). The values were within



(a)

Figure 2-41: Measurements during cooldown of the horn-dewar interface plate temperatures for the W-band cryostat. Temperature sensors were located on the second refrigerator stage, near a thermal mass (‘horns’), cold plate, and one sensor on the thermal strapping of each refrigerator.

0.1K of expectation for the Q-band array, but we overestimated the thermal gradient for the W-band array. This is likely a reflection that our approximation for the area available to conduct heat was a poor approximation for the W-band array, an effect which was magnified by the larger loading expected for the W-band array. This thermal gradient will not impact science observations.

$$\Delta T = \frac{Pl}{Ak}$$

$$\Delta T_{far} - \Delta T_{near} = \frac{P}{Ak}(l_{near} - l_{far})$$

	W-band	Q-band
Plate thickness (inches)	0.25	0.768
Expected Gradient (K)	4	1.5
Measured gradient (K)	2.7	1.4

Table 2.12: Calculated thermal gradient from a module closest to the refrigerator to the module furthest from the refrigerator attachment. The measured values for modules at the site is presented in the last row.

2.6.5 The Cryostat Window

The vacuum window of the cryostat must be strong enough to withstand vacuum pressure, and also should maximize transmission of the signal to have the smallest possible degradation of instrument signal-to-noise. This section describes the methods we used to select the window materials, and our estimate of the contribution to the system noise from the window.

Window Material

The cryostat windows are $\simeq 22$ inches in diameter, the largest vacuum window of its kind to date. The material used for the window must be strong enough to withstand the $\simeq 5500$ lbs of force exerted on the window when the cryostat is at vacuum. We used a small vacuum chamber to test a variety of materials, Table 2.13 lists the first materials we tried, their thicknesses, and the results of each test.

Vacuum Window

The loss tangent ($\tan(\delta)$) is a measurement of absorption in the material; smaller values are preferable because the relationship between absorption and the loss tangent is exponential. Polyethylene-based windows had the best transmission properties, but the high-density polyethylene (HDPE) windows broke along the edges of the window after 1-2 vacuum pump-downs in the QUIET cryostats, so we chose to use ultra-high molecular-weight polyethylene (UHMW-PE) instead. We vacuum pumped the windows multiple times, measuring the bowing each time. After 20 repetitions it was

Material	Thickness, mil (mm)	Test Results	$\tan \delta$	n
Mylar (PETP)	2 (0.0508)	failed	44×10^{-4}	1.73
Polypropylene	54 (1.37)	failed	7.3×10^{-4}	1.5
	158 (4)	bowed in 3"		
	256 (6.5)	bowed in 2"		
HDPE	35 (0.9)	failed	2.5×10^{-4}	1.52
	80 (2)	bowed in 3"		
	250 (6.4)	bowed in 1.14"		
UHMW-PE	78.74 (2)	bowed in 3"	$2.5 \times 10^{-4*}$	1.52 *

Table 2.13: Window Testing Results. HDPE = high-density polyethylene, UHMW-PE=ultra-high molecular-weight polyethylene.

* Assumed, no literature on microwave properties of UHMW-PE

determined the window was sufficiently strong.

We could not find an index of refraction and loss tangent for UHMW in the literature. However, the variation of the index of refraction for the polythylenes is small ($\simeq 2\%$), and it was decided we could approximate the microwave properties of UHMW-PE from the other polyethylenes. The transmission properties of UHMW-PE were confirmed in subsequent measurements of the windows (Section 2.6.5).

The index of refraction and loss tangent of HDPE over a range of frequencies is shown in Figure 2-42. The index of refraction varies only slightly over the measured frequency range, so for the purposes of studying window transmission and its impact on system noise we chose to approximate the index of refraction as a constant over the QUIET frequency bands. We use a value for the index of refraction of HDPE to be $n_{HDPE}=1.525$ and the loss tangent for HDPE of $\tan(\delta)=2.5 \times 10^{-4}$ (the value of the fit line at 90 GHz) to estimate the loss in the QUIET bands. Overestimating the loss tangent will yield an overestimate of the noise contribution from the window, and so the values derived will be conservative estimates of the noise contribution to the system.

Anti-reflection Coating Material

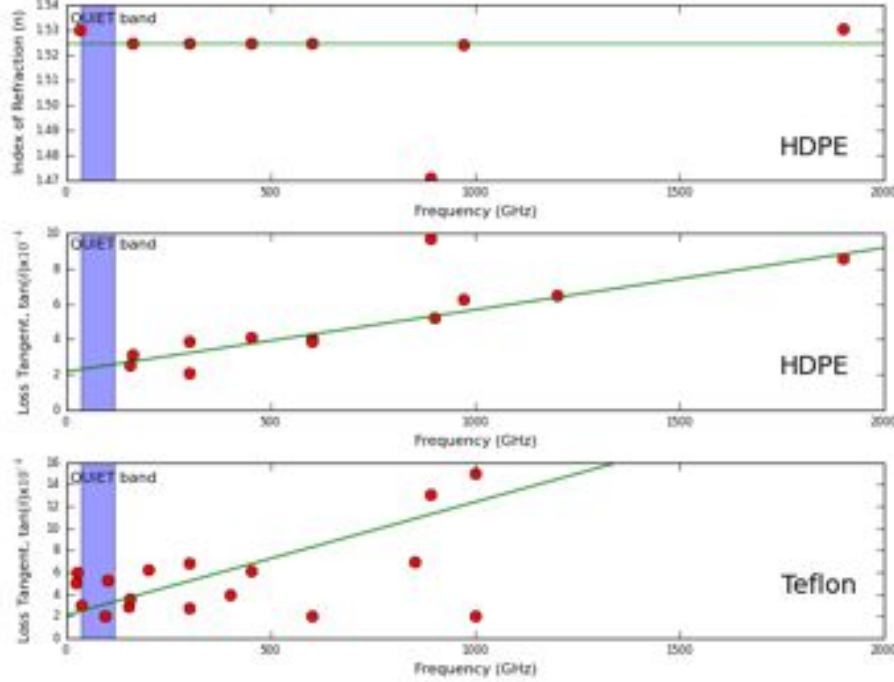


Figure 2-42: Index of refraction and loss tangent over a range of frequencies (values from Ref. [54]). The QUIET frequency band is shown as 35-115 GHz. A horizontal line is drawn at the index of refraction we chose for HDPE, and the two fit lines for the loss tangent of HDPE and teflon are shown. We used values at 90 GHz for the loss tangent: 3×10^{-4} for HDPE and 2.5×10^{-4} for teflon.

The condition for zero reflection in a single-layer film (Ref. [35]) is:

$$n_{ARcoating}^2 = n_{air} n_{UHMWPE} \quad (2.43)$$

With $n_{air} = 1$ and $n_{UHMWPE} = 1.525$, our AR coating material should have $n = 1.2$. The index of refraction of Zitex or Mupor expanded teflon was measured to be $n = 1.2 \pm 0.07$ (Ref. [5]) in the frequency range 400-1350 GHz, a well-matched anti-reflection material for the UHMW-PE vacuum window.

Ref. [5] included a comparison with non-expanded teflon, with index of refraction $n = 1.44$, and noted that the expected index of refraction of teflon with a 50% filling

factor (the decrease in density between teflon and expanded teflon) is predicted to yield an index of refraction of 1.22, confirming their measurement within error. We will approximate the index of refraction of expanded as constant, using the trend for non-expanded teflon as a guide, and use the loss tangent of non-expanded teflon at 90 GHz as the loss tangent of expanded teflon (which will overestimate the absorption and hence the noise temperature contribution). For the following analysis, we will estimate the loss tangent of the teflon layers as $\tan(\delta) = 3 \times 10^{-4}$.

AR Coating Adhesion

We adhere the teflon to the UHMW-PE window by placing an intermediate layer of LDPE between the teflon and the UHMW-PE. We then heat the materials above the melting point of LDPE while applying clamping pressure. This method was developed at Columbia as part of a technology development effort for multi-layer metal-mesh filters. LDPE is ideal for this purpose because its melting point is lower than either teflon or UHMW-PE, and should have similar optical properties as the latter. We demonstrated our ability to fuse teflon to UHMW-PE with a small test piece, and then scaled the press to the larger size required for the W- and Q-band windows. We avoid trapping air bubbles between the material layers by performing this hot-pressing in a vacuum chamber.

Window Transmission

We present the transmission formalism that will be used to calculate the transmission curves for our windows. The formulas are valid only for normal incidence, the effects from the curvature of the window are discussed in Section 2.6.5..

General Transmission and Absorption Matrix Formalism

Transmission through a material and through an interface is given by (Ref. [43]):

$$\begin{pmatrix} T_{layer} \end{pmatrix} = \begin{pmatrix} e^{ik_i t_i} & 0 \\ 0 & e^{-ik_i t_i} \end{pmatrix}$$

$$\left(T_{interface1 \rightarrow 2} \right) = \begin{pmatrix} \frac{1+n}{2} & \frac{1-n}{2} \\ \frac{1-n}{2} & \frac{1+n}{2} \end{pmatrix}$$

Where $k = \frac{2n\pi\nu}{c}$, t is the thickness of the material, and $n = \frac{n_1}{n_2}$ (the ratio of the indices of refraction of the two materials that form the interface). The absorption coefficient is given by:

$$A = e^{-t\alpha} \quad (2.44)$$

where

$$\alpha = \frac{2\pi\nu n}{c} \tan(\delta) \quad (2.45)$$

$$(2.46)$$

where $\tan(\delta)$ is the loss tangent, ν is frequency, n is the index of refraction of the material, and c is the speed of light in vacuum.

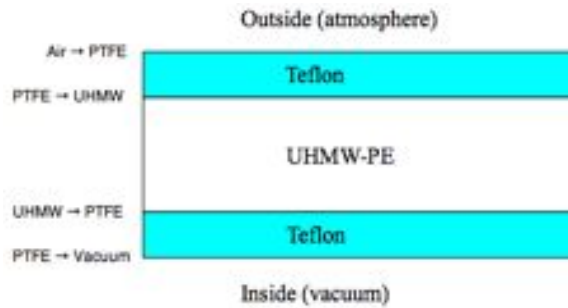


Figure 2-43: Schematic of the three layers in the window: ultra-high molecular weight polyethylene with two teflon anti-reflection coating layers.

A schematic of the layers in the window is shown in Figure 2-43 and consists of UHMW-PE bounded by two layers of teflon (PTFE).

$$\begin{aligned}
E_{out} &= T_{transfer} E_{incident} \\
T_{transfer} &= T_{PTFE \rightarrow air} [T_{PTFE} A_{PTFE}] \\
&\quad \times T_{UHMW \rightarrow PTFE} [T_{UHMW} A_{UHMW}] T_{PTFE \rightarrow UHMW} \\
&\quad \times [T_{PTFE} A_{PTFE}] T_{air \rightarrow PTFE}
\end{aligned} \tag{2.47}$$

The exponential in the propagation term changes sign in the transmission matrix depending on the direction of wave travel. The absorption does not have this directional dependence and is proportional to the identity matrix, so the sign is always the same and can be re-arranged in the transfer matrix as a constant factor. The transmitted and reflected components of the transmission matrix are expressed as (Ref. [43]):

$$\begin{aligned}
E_{trans} &= \frac{Det[T_{transfer}]}{T_{22}} E_{incident} \\
E_{refl} &= \frac{-T_{21}}{T_{22}} E_{incident}
\end{aligned}$$

Where E_{inc} is the incident signal and T_{22} is the (2,2) element of the 2×2 $T_{transfer}$ matrix. This yields the transmission coefficient ($T = |E_{trans}|^2$) and reflection coefficient ($R = |E_{refl}|^2$).

Measured and Expected Window Transmission Properties

After stress-testing a variety of UHMW-PE samples, we computed the expected transmission and reflection properties of the W- and Q-band windows for the “off-the-shelf” plastics which had material thicknesses nearest to integer wavelengths of the material. We produced samples of anti-reflection coated W-band window and measured its transmission properties in a vector-network-analyzer (VNA). A schematic of the VNA testing apparatus is depicted in Figure 2-44: it consists of two standard

gain horns with the sample window piece between them. Signal is transmitted from one horn, and measured at both horns, giving a measurement of the reflection from the window and transmission through the window. This setup can produce standing waves between the horn and the window, and also between the two horns, at frequencies where the distance between the two objects is $\frac{\lambda}{2}$. The VNA data and theoretical prediction for the reflection is given in Figure 2-45. The structure in the measured data set is likely produced by standing waves between the horn and the window sample, and possibly between the two horns as well, such that a fit to the envelope of the reflection curves is appropriate.

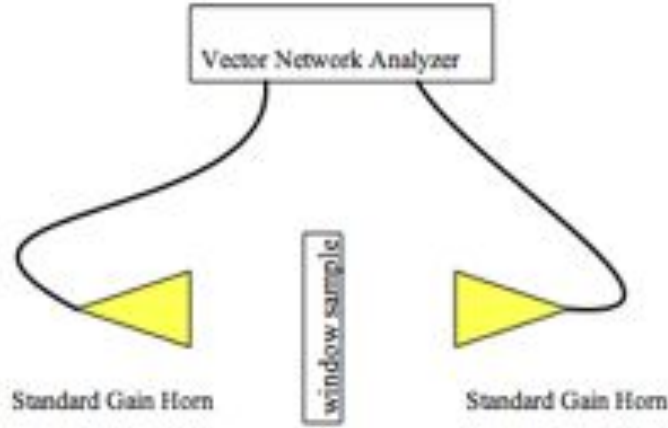


Figure 2-44: Schematic of the VNA testing setup to measure the transmission and reflection properties of sample windows.

The values for the optical properties and material thicknesses which fit this transmission data best for the W-band array are given in Table 2.14. We re-evaluated the transmission and reflection parameters across our bandpasses for the W- and Q-band windows with the optical parameters from the measured data and the thicknesses from the VNA measurements (W-band) and a caliper (Q-band). The predicted transmission without the AR coating, and with the AR coating are shown in Figures 2-46(a) and 2-46(b) for the W-band window, and in Figures 2-47(a) and 2-47(b) for the Q-band windows. A summary of the transmission properties for the uncoated and coated windows is given in Table 2.15. Both uncoated windows have transmission

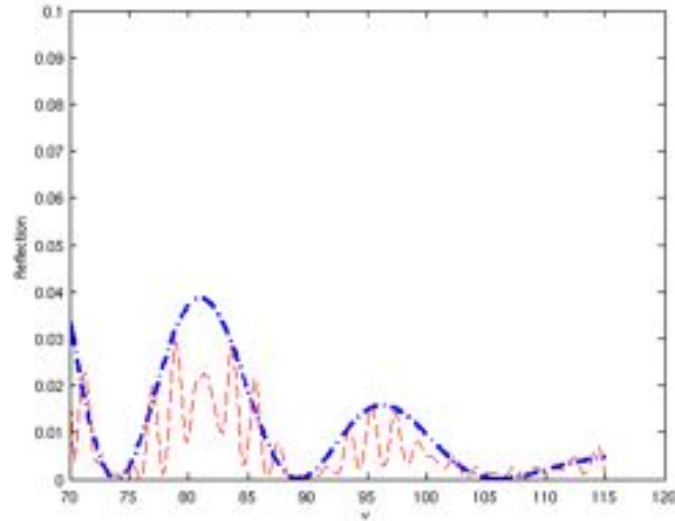


Figure 2-45: Reflection data from VNA measurements of the W-band window (red), with a theoretical prediction given the values in Table 2.14 (blue). We used parameters which fit the envelope of the measurements.

minima of 84%, while the teflon-coated window has minimum transmission of 95% for the W-band window and 98% for the Q-band window.

	UHMW-PE			LD-PE			teflon		
	inches	n	$m\lambda$	inches	n	$m\lambda$	inches	n	$m\lambda$
W-band	0.25	1.525	2.9	0.005	1.525	0.057	0.0213	1.19	0.195
Q-band	0.375	1.525	1.93	0.005	1.525	0.026	0.0625	1.19	0.23

Table 2.14: Thicknesses of the window and AR coating material for the W- and Q-band cryostat windows. m is the thickness of the material, in wavelengths, as seen by the photon at a frequency of either 40 GHz or 90 GHz: $t = m \frac{\lambda_0}{n}$. Thicknesses and index of refraction for teflon and UHMW-PE comes from the best-fit values to the VNA measurements at 90 GHz. We used ‘off-the-shelf’ plastics for both W-band and Q-band windows, and so we were not able to choose material thicknesses exactly integer and half-integer wavelengths. The best-fitting value for the thickness of the UHMW-PE was 0.25”, which most likely means much of the LDPE used as the adhesive thinned out considerably in the heat press.

	Uncoated			Coated		
	Min	Max	Average	Min	Max	Average
W-band	83.2%	99.1%	91.1%	97.4%	99.0%	98.3%
Q-band	83.5%	99.4%	89.8%	97.8%	99.2%	98.8%

Table 2.15: Transmission properties of each window, from theoretical predictions.

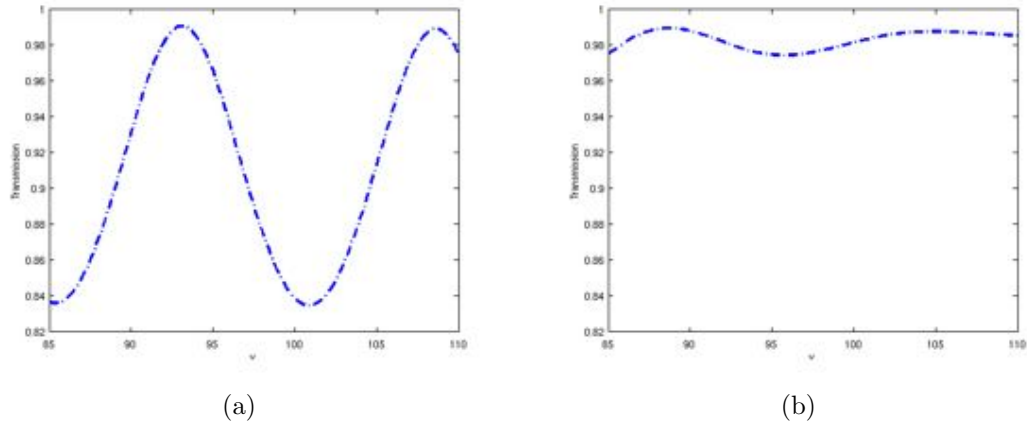


Figure 2-46: Transmission curves for *a*: 90 GHz for 1/4" of UHMW PE and two layers LDPE, no AR coating *b*: and with the teflon anti-reflection coating. Material thicknesses given in Table 2.14. The additional dip in the W-band window compared to the Q-band window (Figure 2-47(b)) is the result of the teflon coating thickness deviating more from the ideal $\frac{\lambda}{4}$ by 25%.

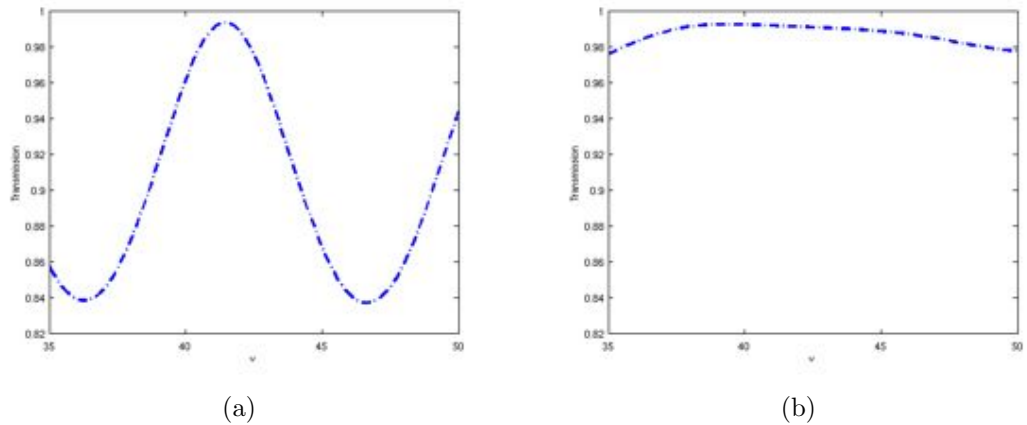


Figure 2-47: Transmission curves for *a*: 40 GHz for 3/8" of UHMW PE and two layers LDPE, no AR coating *b*: and with the teflon anti-reflection coating. Material thicknesses given in Table 2.14.

Noise Temperature Analysis

In this section, we consider the contribution of the window to the noise of the entire instrument. For an a system of components, the expression for the noise contribution is (Ref. [73], also discussed in section 2.3.1):

$$T_{sys} = T_{noise:1} + \frac{T_{noise:2}}{G_1} + \frac{T_{noise:3}}{G_1 G_2} + \frac{T_{noise:4}}{G_1 G_2 G_3} + \dots + \frac{T_{noise:N}}{G_1 \dots G_{N-1}} \quad (2.48)$$

Here $T_{noise:n}$ represents the noise temperature of a component with gain G_n . We can consider our window to be a three component system composed of the three material layers. We note that the noise of a lossy component, such as a window layer, is given by $T_{noise} = T_{physical}(Loss - 1)$ (Ref [73]). Then the noise from each layer is:

$$T_{noise:teflon} = T_{phys}(L_{teflon} - 1) \quad (2.49)$$

$$T_{noise:UHMW-PE} = T_{phys}(L_{UHMW-PE} - 1) \quad (2.50)$$

Noting that $G_{window} = \frac{1}{Loss}$, the total noise temperature contribution from the window can be expressed as:

$$T_{window} = T_{phys}(L_{teflon} - 1) + \frac{T_{phys}(L_{UHMW-PE} - 1)}{G_{teflon}} + \frac{T_{phys}(L_{teflon} - 1)}{G_{teflon} G_{UHMW-PE}} \quad (2.51)$$

$$T_{window} = T_{phys}(L_{teflon} - 1) + T_{phys}(L_{UHMW-PE} - 1)L_{teflon} + \quad (2.52)$$

$$T_{phys}(L_{teflon} - 1)L_{teflon}L_{UHMW-PE}$$

$$T_{window} = T_{phys}(L_{teflon}L_{UHMW-PE}L_{teflon} - 1) \quad (2.53)$$

$$L_{window} = L_{teflon}L_{UHMW-PE}L_{teflon} \quad (2.54)$$

For a material of thickness t , the loss is the reciprocal of the absorption:

$$Loss = A^{-1} = \exp[\alpha t] \quad (2.55)$$

To derive the total noise of the window and module system together, we will use equation 2.48 with $T_{noise:1}$ as the noise from the window, $T_{noise:2}$ as the noise from the module, and G_1 will be the loss from the window. We will use $T_{phys} = 300\text{K}$ and $T_{Rx} = 60\text{K}$ (W-band) and $T_{Rx}=35\text{K}$ (Q-band). The expression for the system noise temperature is given by:

$$T_{sys} = T_{window} + \frac{T_{detector}}{G_{window}} = T_{phys}(L_{window} - 1) + L_{window}T_{detector} \quad (2.56)$$

The first term is the result of unpolarized emission at the temperature T_{phys} , this will effect the noise of the total power stream but will not effect the polarized stream. The second term is the result of signal absorption, this will affect both streams. The contribution from only the window is the difference between T_{sys} and $T_{detector}$, and is given by:

$$\Delta T = T_{sys} - T_{detector} = (L_{window} - 1)(T_{phys} + T_{detector}) \quad (2.57)$$

Again, the T_{phys} term would not impact the polarization data stream. We calculated the noise temperatures for a range of thicknesses of HDPE (assuming each PTFE layer was $\frac{\lambda}{4}$). Figure 2-48 shows the noise temperature as a function of HDPE thickness for the W band, where $\nu_0 = \nu$ for thicknesses between $1-6\lambda$ (in this range, the noise contribution from the window is clearly linear to a good approximation). The estimated noise temperature for coated and uncoated windows are presented in Table 2.16. We expect 4K of noise temperature from the W-band window and 3K of noise temperature from the Q-band window from absorptive losses.

Noise Temperature Measurement of the Q-band window

We tested the contribution to system noise from a sample Q-band window in the laboratory. We have a small cryostat with a port for a window which we used to

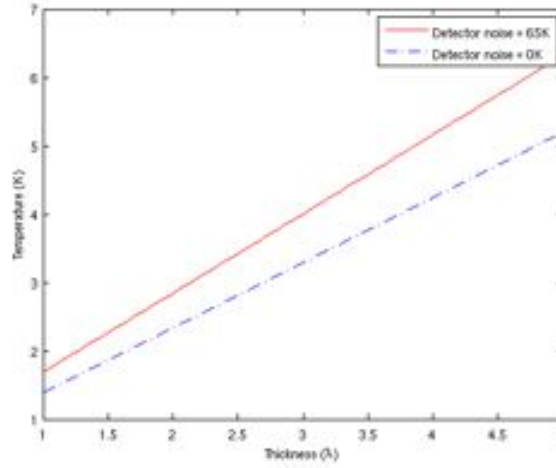


Figure 2-48: Noise temperature contribution from the window as a function of HDPE thickness, at W-band for a $1-5\lambda$ material thickness. The W-band window thickness has thickness $\simeq 3\lambda$, the Q-band window has thickness $\simeq 2\lambda$. The solid line assumes a detector noise temperature of 65K, the dashed line is the contribution from the window even with no detector noise.

test the noise and bandpass properties of the Q-band modules. These tests will be discussed further in Chapter 3, here I will just note that we are able to compute the noise of the module and the window together through the use of two blackbody loads at cryogenic temperatures. We use the total power data stream for these measurements, so the contribution from emission from the window should be considered when comparing the theoretical prediction to these measurements. We measured the system noise with one window, which sets a baseline for the contribution of a single window, all optical components (feedhorn, OMT), and the module itself. We then placed a second window in front of the first window, and re-measured the system noise. The difference between the first and second measurements is the contribution from a single window. The noise from the window for the Q-band window was measured to be 3K.

The predicted band-averaged noise temperatures from loss in the window for the Q- and W- band arrays are given in Table 2.16, assuming $T_{phys} = 300\text{K}$, and $T_{detector} = 60\text{K}$ (W-band) and 35K (Q-band). The expected values are 5K for the W-band

window and 3K for the Q-band window, $\simeq 8\%$ of the detector noise in each case.

ν_0 (GHz)	$L_1 L_2 L_3$ %	$\Delta T_{\text{absorption}}$ K	Δ : Measured K
90, no AR	1.099	35.6	-
90, with AR	1.0115	4.1	-
40, no AR	1.0065	2.2	-
40, with AR	1.0083	2.8	$\simeq 3$

Table 2.16: Noise temperature contribution for the W-band and Q-band windows, with and without AR coating. $L_1 L_2 L_3$ gives the loss in the window and $\Delta T_{\text{absorption}}$ is the contribution to the system noise from signal absorption in the window. We measured the contribution from the Q-band window in a testing setup.

Physical Optics Analysis

A physical optics analysis in GRASP was performed to investigate the effect of the curved surface of the window on the polarization properties of the transmission and reflection. The curvature of the window under vacuum pressure could introduce cross-polarization, and also increase absorption by presenting a variable material thickness to the incoming radiation. For these simulations, use those material properties with an assumed HDPE thickness of 0.25", a teflon thickness of $\frac{\lambda}{4}$, and a window curvature determined from measurements of the deflection of the window under vacuum, $\simeq 3$ inches. We considered two input states: E_x polarization and E_y polarization and investigated the transmission of the two different states, giving a predicted quantity for the instrumental polarization (the difference in transmission between the two polarization states) and peak transmission.

The simulations confirmed the flat-window values found in previous sections. With a curved window, the central feedhorn has negligible instrumental polarization. The off-center pixel has instrumental-polarization induced by the window curvature of 0.01%, occurring only at the edge of the bandpass. We are currently investigating the impact of this instrumental polarization more thoroughly, the results to appear in Ref. [20].

Chapter 3

Q-band Array Integration, Characterization, and Testing

3.1 Introduction

We integrated the feedhorns, OMTs, modules, and electronics boards together to form the Q-band QUIET receiver. We measured the bandpasses, noise, and responsivity of the receiver in the laboratory to verify that everything was properly characterized before beginning science observations. This chapter addresses Q-band instrument characterization and testing prior to observations in Chile.

3.2 Bandpasses

Bandpasses were measured for each diode of each module both in the laboratory during the course of array testing, and also during final calibration at the site in June 2009. We used a signal generator with standard gain horn to inject a polarized signal at frequencies in the range 35-50GHz into the receiver and measure response as a function of frequency (each sweep through the passband frequency range is termed a ‘bandsweep’). These measurements can be used to calculate bandwidths and central

frequencies.

The equation for the effective central frequency (Ref. [71]) is:

$$\text{Central Frequency: } \nu_e = \frac{\int \nu I(\nu) A_e(\nu) \sigma(\nu) d\nu}{\int f(\nu) A_e(\nu) \sigma(\nu) d\nu} \quad (3.1)$$

(no equivalent was given in the Reference for the bandwidth, however the extension to bandwidth is straightforward) where $I(\nu)$ is the response of the receiver and the optics, $A_e(\nu)$ is the effective area of the source in the beam at each frequency (it is not immediately obvious that this should be true, it was however found to be true in calibration measurements, described in Section 5.9), and $\sigma(\nu)$ is the spectrum of the source in thermodynamic temperature units. With these approximations, and noting that the source spectrum $\sigma(\nu)$ is convolved with the module bandpass $I(\nu)$ to obtain the bandpass we measure, yields:

$$\text{Central Frequency: } \frac{\int I \sigma \nu d\nu}{\int I \sigma d\nu} \xrightarrow{\text{const. } \Delta\nu} \frac{\sum I \sigma \nu}{\sum I \sigma} \quad (3.2)$$

$$\text{Bandwidth: } \frac{(\int I \sigma d\nu)^2}{\int (I \sigma)^2 d\nu} \xrightarrow{\text{const. } \Delta\nu} \frac{[\sum I \sigma]^2 \Delta\nu}{\sum (I \sigma)^2} \quad (3.3)$$

We flatten the output of the signal generator so that the measured bandpass has no contribution from the signal generator bandpass. Thus we can set $\sigma = 1$ to compute the central frequency and bandwidth:

$$\text{Central Frequency: } \frac{\sum I \nu}{\sum I} \quad (3.4)$$

$$\text{Bandwidth: } \frac{[\sum I]^2 \Delta\nu}{\sum I^2} \quad (3.5)$$

3.2.1 Columbia Laboratory Data

Eight cryogenic bandpass measurements were performed in the laboratory for 15 modules in the final configuration of the receiver array¹. Bandsweep data is taken by injecting a polarized signal from a signal generator and standard gain horn into the front window of the cryostat, as shown in Figure 3-1.

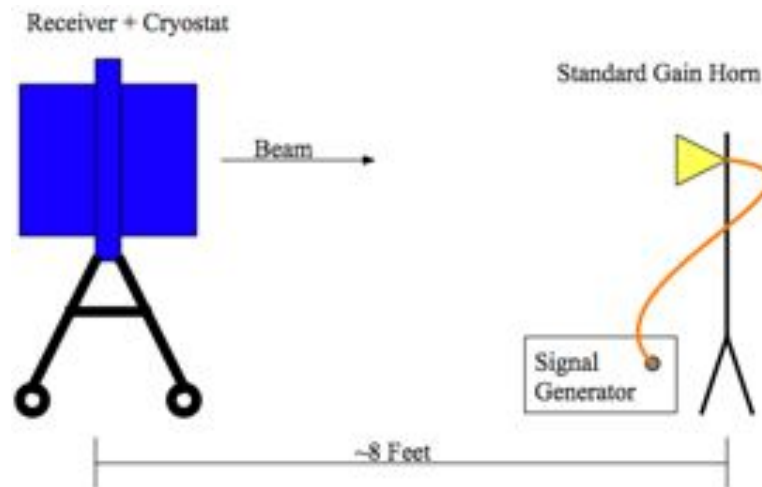


Figure 3-1: Schematic of the setup for bandpass measurements in the laboratory. We inject signal from a signal generator and standard gain horn into the receiver window. Maximizing the distance between the receiver and horn maintains a flat input beam. The receiver beam is large ($\simeq 20^\circ$) in the absence of the focusing mirrors, so the beam from each horn will generally detect the ground and walls as well, however the injected signal is at an effective temperature of a few thousand Kelvin, so the additional noise from the laboratory is negligible.

For these laboratory measurements the bandpass profiles were not stored, so we cannot reconstruct the bandpasses for error analysis, however the computed bandwidth and central frequency values for each sweep for each diode in the array were stored. As a result, we can find a statistical average bandwidth and central frequency for each diode. For a few bandpasses, the polarization angle of a diode was orthogonal to the standard gain horn input orientation, such that it was not sensitive to

¹four were swapped at the site later because they required a different biasing technique that complicated receiver turn-on. These four modules do not have recorded bandpasses for this analysis.

the signal¹. These bandpass measurements have unrealistically low or high computed bandwidths, so any scan with a bandwidth less than 6 GHz or greater than 9 GHz was removed from the data set. For a given diode, the remaining bandwidths and central frequencies were averaged and the standard deviation was computed. The central frequencies and bandwidths for the polarization modules are given in Tables 3.1 and 3.2.

3.2.2 Site Data

Bandpasses were measured with the Q-band receiver at the site in Chile over the course of two days (June 13 and 14, 2009) in four different data sets, yielding a total of 35 bandsweeps. A schematic of the experimental setup is shown in Figure 3-2. The carrier wave signal is produced by the signal generator, transmitted by radio-frequency cabling to a standard gain horn, where it is broadcast to a $6'' \times 6''$ square reflector plate, and reflected into the primary mirror. We positioned the reflector plate over the center of the primary, with the horn roughly 4 feet away. Alignment was performed by tuning the signal generator to output a carrier wave at 42.5 GHz and rotating the horn until it maximized the signal on the Q diodes for the largest number of modules possible. This would allow us to perform a second set of measurements for the U diodes, and ensure we had high quality bandpasses for most diodes. A spike was inserted at 37 GHz to reference the detector measurements in frequency. The data were taken in ‘double demodulation’ mode (see section 2.3). The measured signal is a combination of the signal generator carrier wave signal and any additional reflections in the system (e.g. off of any exposed metal in the ground shield, between the mirrors and the reflector plate, and between the horn and the reflector plate).

Unfortunately the signal generator stopped sweeping after the first three sweeps on the second day of data-taking, so measurements we performed to maximize the

¹We did not phase-switch the phase switches for these measurements and without phase switching there could be a horn orientation that happens to be orthogonal to (for example) the +Q axis of the module, resulting in a bandpass which is only noise.

signal for the U diodes (with the horn oriented 45° from the original orientation) were lost, along with additional measurements meant to average out reflections in the system. As a result, with a few exceptions, bandpasses for the U diodes are not measured well by the site data.

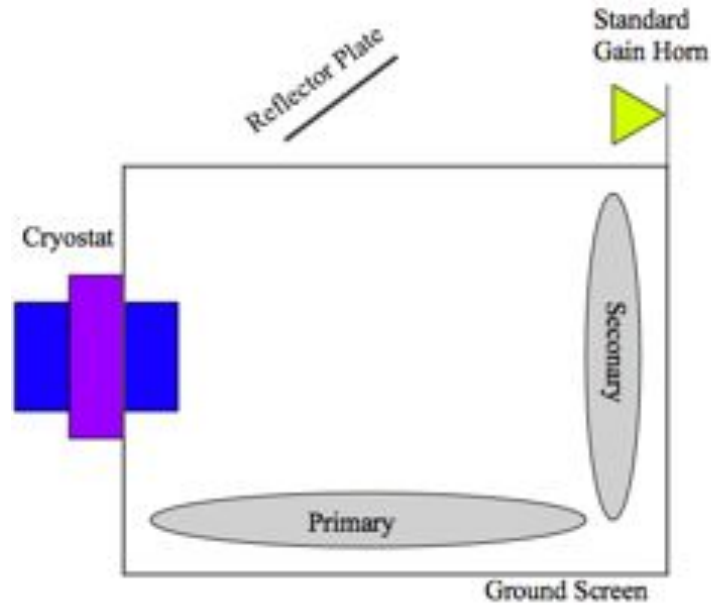


Figure 3-2: Schematic of the setup for bandpass measurements on the telescope at the site.

Plots of the bandsweeps are given in Appendix B.1 in Figures B-1 and B-2. We analyzed the data with two different methods, for two different data products. The first method computed the bandwidth and central frequency for each separate bandpass, and averaged the central frequencies and bandwidths; this is similar to the analysis of the laboratory measurements. Again, poor quality bandpasses have unrealistically low bandwidths (this was generally due to low signal-to-noise from the setup), so if a diode sweep had an unrealistic bandwidth (less than 6 GHz or greater than 9 GHz) the scan was not included. Some diode measurements have reflections in the center of their bandpasses, these take the form of 'drop-outs', where the signal drops to the detector noise level (these artifacts were not present in laboratory data); scans with

this property were also removed. We found that bandpasses taken on a given day were consistent, but that bandpasses measured on different days exhibited systematic shifts relative to each other. This inconsistency is likely the result of changing the position of the standard gain horn between the two days, which could change the nature of the reflections in the system. We assessed statistical and systematic errors for these measurements, based on the differences between the bandwidths and central frequencies between the two days (systematic), and the errors between bandpasses on one day (statistical).

The second method averaged the sweeps together, frequency point by frequency point, yielding an average bandpass for each frequency point. Before averaging, each sweep was normalized by the area under its curve. The sweeps which were included in this point-by-point average are the same as used in the first analysis method. In this case, because the bandsweeps were normalized and combined, it is difficult to disentangle the statistical from systematic errors and it is unclear what the best treatment is, so we settled on a quoting the standard deviation for the error on each point with the understanding that the error is not simply statistical, but also encodes a systematic error as well. The resulting averaged bandsweeps are given in Appendix B.1 in Figures B-3- B-4. The full bandpass shape as a function of frequency is useful for a number of systematics studies and calibration measurements.

3.2.3 Receiver Bandwidths and Central Frequencies

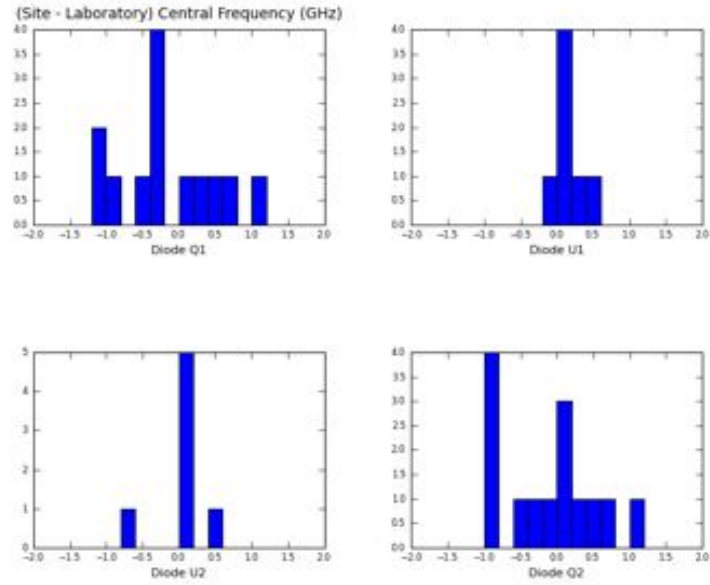
To assess the consistency between the measurements taken in the laboratory and at the site, we computed the differences between the central frequencies and bandwidths for laboratory data and site data. As shown in the distributions in Figures 3-3(a) and 3-3(b), the bandwidths for all diodes are generally consistent between the two measurements, although the distribution width is 0.5-1GHz. The two Q diodes have a systematic shift in the central frequency such that the measurements performed at the site are lower by up to 1.5 GHz. To obtain a single, final central frequency and

bandwidth for each diode, we chose to use laboratory values when possible because there was evidence of systematic variation between bandpasses in the site measurements, and because the site measurements did not measure the U diodes well. In addition, the lab measurements generally did not exhibit the drop-outs from reflections which were evident in the site measurements, which is likely attribute-able to the awkward site setup which requires a reflective plate with possible contamination from metal surfaces near the plate (e.g. the ground screen edges).

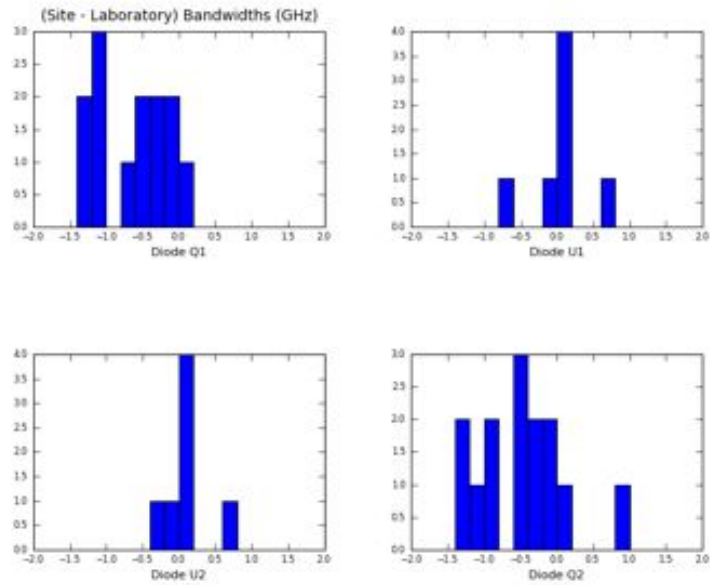
Four modules were swapped into the array in Chile and were not measured in the laboratory and one diode had a broken connection until we obtained new cables in Chile. For these cases, we use bandwidth and central frequencies from site measurements and the error is quoted as either the systematic error value, or if the diode had a good measurement on only one day such that we could not assign a systematic error to the diode, we assigned it the range of systematic error typical of site measurements (0.25-1 GHz) for both the bandwidth and central frequency values¹, which was obtained by investigating the systematic shifts and determining a range which best represented the systematic shifts present in data taken on both days. Because U diodes were not well measured by site data, we recommend using the average of the Q bandwidths and central frequencies. The average differences between the Q and U diodes for a given module are 0.15 GHz for bandwidth and 0.22 GHz for central frequency. The width of the distribution indicates an additional error of 0.25 and 0.12 GHz is incurred in bandwidth and central frequency, respectively, from using these values for the U diodes from site measurements. Because these are smaller than the systematic errors of 0.25-1GHz, I retained the systematic error values.

The bandwidth and central frequencies for each diode are given in Tables 3.1 and 3.2, respectively. The average bandwidth for the array is 7.6 ± 0.5 GHz, and the average central frequency is 43.1 ± 0.4 GHz.

¹The central frequencies are generally more consistent than the bandwidths, however because the absolute value of the central frequency is larger, coincidentally the quoted systematic error is the same value as for the bandwidth.



(a)



(b)

Figure 3-3: Difference between the *a*: Central Frequency and *b*: Bandwidths as measured in the laboratory (section 3.2.1) and the site (section 3.2.2). The distribution of U diodes is sparse because the U diodes were not measured well at the site.

Site	Module	Q1		U1		U2		Q2	
-	-	Mean	σ	Mean	σ	Mean	σ	Mean	σ
-	-	(GHz)	(GHz)	(GHz)	(GHz)	(GHz)	(GHz)	(GHz)	(GHz)
RQ00	27	43.21	0.41	43.41	0.22	43.27	0.22	43.27	0.23
RQ01	28	43.07	0.60	43.08	0.22	43.32	0.27	43.36	0.64
RQ02	29	43.09	0.55	42.71	0.17	42.70	0.12	42.80	0.20
RQ03	10	42.56*	0.19*	43.22	0.08	43.39	0.10	43.47	0.27
RQ04	36	43.00*	0.66*	42.95**	0.25-1**	42.95**	0.25-1**	42.90*	0.71*
RQ05	25	43.38	0.52	43.45	0.29	43.19	0.20	42.89	0.29
RQ06	26	43.43	0.91	42.86	0.16	43.07	0.19	42.85	0.25
RQ07	34	43.35	0.67	43.12	0.17	43.29	0.18	43.12	0.32
RQ08	33	43.37	0.90	43.17	0.14	43.10	0.14	43.30	0.32
RQ09	21	43.76	1.01	42.74	0.15	42.78	0.15	43.11	0.76
RQ10	24	43.02	0.24	43.20	0.24	43.11	0.23	43.13	0.23
RQ11	22	43.34*	0.25-1*	43.36**	0.25-1**	43.55*	0.25-1*	43.28*	0.25-1*
RQ12	30	43.45	1.35	42.82	0.16	42.77	0.11	43.26	1.04
RQ13	35	43.20	0.42	42.88	0.35	43.05	0.32	42.86	0.30
RQ14	37	43.85*	1.06*	43.37**	0.25-1**	43.37**	0.25-1**	43.09*	0.25-1*
RQ15	39	41.52*	0.25-1*	41.54**	0.25-1**	41.54**	0.25-1**	41.55*	0.25-1*
RQ16	17	43.19	1.02	42.46	0.21	42.33	0.21	43.12	1.08

Table 3.1: Central Frequencies: Values are taken from lab data unless noted with a ‘*’.

* Indicates the values came from site data for the modules which were not in the array during laboratory testing: RQ04, RQ11, RQ14, and RQ15 and one diode which was a loose cable connection and was fixed with new cables used on the telescope. Errors assigned for these diodes are either the systematic errors for the site measurement, or is set to 0.25-1GHz (this is assigned if there was a decent measurement for the diode on only one day, such that we could not compute a systematic error).

** Indicates the values are taken from the Q diode measurements, errors are discussed in the text.

TT Bandpasses

The bandpass structure is a combination of the bandpass of the optics and the module. The bandpass of the hybrid-Tee assembly is not necessarily the same as the bandpass of the OMTs, so we give these values separately. The central frequencies and bandwidths as measured in the laboratory for modules 9 and 23, which populate the hybrid-Tee assembly, are given in Tables 3.3 and 3.4. The central frequencies were consistent between the site and laboratory data. Similarly to the OMT measurements, the bandwidths measured at the site were systematically lower.

Site	Module	Q1		U1		U2		Q2	
-	-	Mean	σ	Mean	σ	Mean	σ	Mean	σ
-	-	(GHz)	(GHz)	(GHz)	(GHz)	(GHz)	(GHz)	(GHz)	(GHz)
RQ00	27	7.89	0.58	7.96	0.61	7.29	0.65	8.23	0.74
RQ01	28	8.15	0.60	7.63	0.87	8.04	0.68	8.22	0.71
RQ02	29	7.95	0.44	7.03	0.57	6.97	0.58	7.45	0.31
RQ03	10	6.28*	0.17*	7.67	0.60	7.28	0.33	7.75	0.81
RQ04	36	7.16*	0.39*	7.21**	0.25-1**	7.21**	0.25-1**	7.26*	0.50*
RQ05	25	8.28	0.60	8.35	0.31	7.75	0.35	8.38	0.77
RQ06	26	7.28	0.55	7.75	0.53	7.82	0.37	7.77	0.64
RQ07	34	7.54	0.47	7.52	0.54	7.29	0.43	7.67	0.64
RQ08	33	7.44	0.38	7.65	0.28	7.39	0.29	7.70	0.72
RQ09	21	7.56	0.58	7.52	0.39	7.23	0.57	7.88	0.50
RQ10	24	7.84*	0.44*	7.76	0.35	7.55	0.36	8.27	0.61
RQ11	22	6.47	0.25-1	6.27**	0.25-1**	6.40	0.25-1	6.06	0.25-1
RQ12	30	7.48	0.50	7.18	0.27	7.01	0.33	7.44	0.58
RQ13	35	7.11	0.34	7.28	0.50	6.85	0.29	7.36	0.41
RQ14	37	6.94*	0.28*	7.15**	0.25-1**	7.15**	0.25-1**	7.35*	0.25-1*
RQ15	39	6.49*	0.25-1*	6.63**	0.25-1**	6.63**	0.25-1**	6.77*	0.25-1*
RQ16	17	7.17	0.47	6.67	0.35	6.88	0.66	7.22	0.47

Table 3.2: Bandwidths: Values are taken from lab data unless noted with a ‘*’.

* Indicates the values came from site data for the modules which were not in the array during laboratory testing: RQ04, RQ11, RQ14, and RQ15 and one diode which was a loose cable connection and was fixed with new cables used on the telescope. Errors assigned for these diodes are either the systematic errors for the site measurement, or is set to 0.25-1GHz (this is assigned if there was a decent measurement for the diode on only one day, such that we could not compute a systematic error).

** Indicates the values are taken from the Q diode measurements, errors are discussed in the text.

3.2.4 Amplifier Bias

As discussed in section 2.3, the bandpasses of the modules are dependent on the properties of the low-noise amplifiers in the modules. The amplifier chip bias set-points are different between measurements performed in the laboratory and at the site, so one concern is whether the central frequencies and bandwidths measured in the lab can be used for site measurements and calibration observations. This could be a potential reason why the bandwidths computed from the site measurement, while consistent with the lab measurements, have a slightly lower average value for the Q diodes.

We investigated the relationship between central frequency and bias set-point and bandwidth and bias set-point for all amplification stages. We used data which we took for a different purpose as we didn’t anticipate this study, and therefore do not have

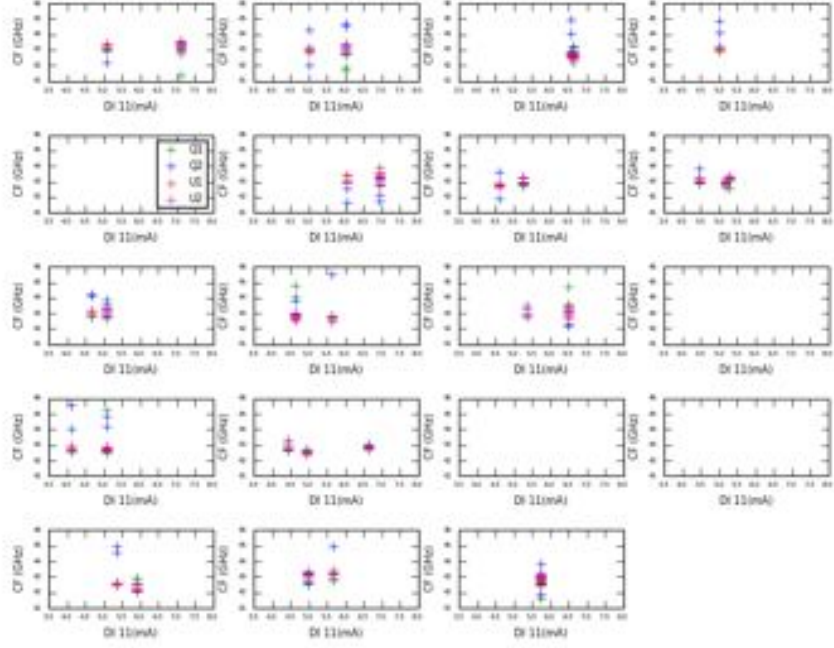
Site	Module	Q1		U1		U2		Q2	
-	-	Mean	σ	Mean	σ	Mean	σ	Mean	σ
-	-	(GHz)	(GHz)	(GHz)	(GHz)	(GHz)	(GHz)	(GHz)	(GHz)
RQ17	9	43.32	0.17	43.52	0.24	43.62	0.03	43.69	0.43
RQ18	23	43.38	0.34	43.09	0.22	43.32	0.23	43.53	0.40

Table 3.3: Central Frequencies: mean and standard deviations for eight laboratory measurements. RQ denotes current location in the receiver array during the observing season. Data is from laboratory measurements.

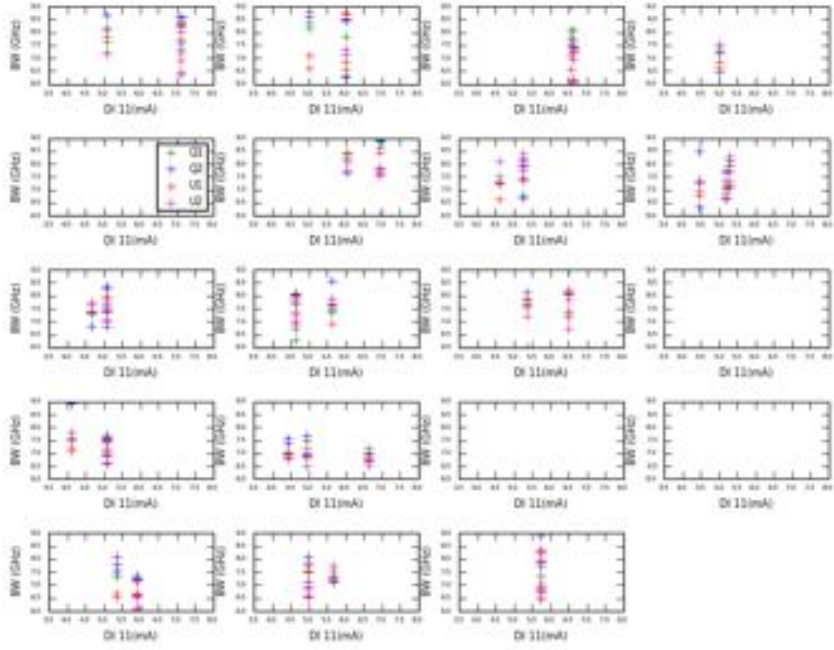
Site	Module	Q1		U1		U2		Q2	
-	-	Mean	σ	Mean	σ	Mean	σ	Mean	σ
-	-	(GHz)	(GHz)	(GHz)	(GHz)	(GHz)	(GHz)	(GHz)	(GHz)
RQ17	9	7.64	0.68	7.42	0.49	7.17	0.70	7.79	0.61
RQ18	23	8.22	0.47	7.69	0.84	7.45	0.66	8.18	0.54

Table 3.4: Bandwidths: mean and standard deviations for eight laboratory measurements. RQ denotes current location in the receiver array during the observing season. Data from laboratory measurements.

an optimal data set for doing so, for example the data set includes only 2-3 different amplifier biasing set points. Although the data are sparse (an example of central frequency against a first stage drain current is shown in Figure 3-4(a), and similarly for bandwidth in Figure 3-4(b), this stage was selected because it is expected to have the greatest potential impact on the bandpass) no evidence is found for a systematic dependence on drain current on the first stage amplifier or any other bias parameter. We therefore do not expect to bias our results by using laboratory and site data interchangeably as a result of different bias settings.



(a)



(b)

Figure 3-4: *a*: Central Frequency and *b*: Bandwidths as a function of amplifier drain current (mA) for the first stage amplifier drain current.

3.2.5 Central Frequencies and Bandwidths: Weighted by Source Spectrum

The central frequency and bandwidth calculations in sections 3.2.1 and 3.2.2 assumed a flat input spectrum across the bandpass. The values derived are appropriate for CMB observations, as a flat spectrum is consistent with a black-body source. However, the calibration and foreground sources will have a variety of spectral indices which will effect the source-weighted central frequency and bandwidth. The source-weighted equations were given in section 3.2 as equations 3.3 and 3.2. We use them to compute the source-weighted bandwidths and central frequencies with a variety of source spectral indices.

The spectrum for TauA is given by a polynomial fit of the form $\log(S(\text{Jy})) = a + b \log(\frac{\nu}{40\text{GHz}})$ (Ref. [90]). To convert it to thermodynamic units from S (the flux density in Janskys) to T_B (the equivalent temperature):

$$S = \frac{2k\nu^2}{c^2} T_B A_e \quad (3.6)$$

$$\log(S) = a + b \log\left(\frac{\nu}{\nu_0}\right) \rightarrow S = 10^a \left(\frac{\nu}{\nu_0}\right)^b \quad (3.7)$$

$$T_B = \frac{10^a c^2}{2k A_e \nu_0^b} \nu^{b-2} \quad (3.8)$$

The constant term $\frac{10^a c^2}{2k A_e \nu_0^b}$ will cancel in the both the bandwidth and central frequency calculations, leaving only the frequency dependence ν^{b-2} such that $\beta = b - 2$. With $b = -0.35$ (Ref. [90]), this gives a $\beta = -2.35$.

Table 3.5 summarizes the sources considered and their spectral indices. All other spectral indices are taken from literature (references given in the table) and are already given in terms of thermodynamic units, so they did not have to be converted. The spectral index of dust and synchrotron emission vary across the sky. We choose the same values WMAP fixed while fitting other components (Ref. [90]): $\beta_{dust} = 2.0$

and $\beta_{synch} = -3.2$. Atmospheric emission also depends on frequency; both the Q- and W-band frequency bands are near water absorption lines (Figure 4-1 in chapter 4), so the spectral profile is not a power law and also depends on the PWV. We use an atmospheric model (Ref. [72]) to produce the spectral dependence of the atmosphere for two extrema of PWV values (0.25mm and 5mm PWV) and computed the source-weighted bandwidth and central frequency in thermodynamic units.

We use the bandsweeps taken from site data to compute the source-weighted bandwidth and central frequency for each sweep in the set, and compute the average, systematic error (difference between the central frequency or bandwidth between the two days), and statistical error (statistical error within one day). Errors in the spectral index are not propagated primarily because of dominance of the systematic error. The results are given in Appendix B.2 in Tables B.1- B.10, most U diodes do not have values in this table because (as mentioned in section 3.2.2) the sweeper was malfunctioning during measurements to optimize the U diode signal. One can use the Q diode values with an estimated additional error of 0.25 GHz for the bandwidth and 0.15 GHz for the central frequency, although the errors should be taken as the systematic errors quoted above as 0.25-1 GHz.

Source	β	Reference	Tables
Dust	2.0	[30]	Table B.1, B.2
Soft Synchrotron	-3.2	[30]	Table B.3, B.4
Moon, Jupiter	0.0	[30]	Table 3.1, 3.2
Atmosphere (0.25 mm)	model*	[72]	B.7, B.8
Atmosphere (5 mm)	model*	[72]	B.9, B.10
Tau A	-2.35 ± 0.026	[90]	Table B.5, B.6

Table 3.5: Spectral indices at Q-band for various sources.

* Atmospheric emission is not a simple power law, instead we use a model to obtain sky temperature as a function of frequency.

3.3 Noise Temperature Measurements

Receiver noise can be computed via a ‘Y-factor’ measurement. This measurement uses two black-body thermal loads at two different temperatures (T_{hot} and T_{cold}) to isolate the contribution from receiver noise ($T_{receiver}$) to the power measured by the detector as:

$$T_{receiver} = \frac{T_{hot} - YT_{cold}}{Y - 1} \quad (3.9)$$

where

$$Y = \frac{P_{hot}}{P_{cold}} \quad (3.10)$$

P_{hot} is the average power (as discussed in section 2.3.2, the detector diode output of the QUIET modules in Volts is proportional to power, so in practice the average power will be the average voltage measured by a detector diode) detected while looking at a thermal load at temperature T_{hot} , and P_{cold} is the equivalent for a thermal load at temperature T_{cold} . We used three thermal loads, each consisting of a Zotefoam¹ (closed-cell expanded polypropylene foam) container with an absorber insert. One load was kept at room temperature (absorber temperature $\simeq 300$ K), the other two loads were filled with liquid cryogenics: one with liquid nitrogen (absorber temperature 77.5 K) and one with liquid oxygen (absorber temperature 90 K). The two cryogenic loads were placed on a cart (Figure 3-5) such that the window of the cryostat could ‘stare’ into the thermal load.

Zotefoam is >99% transparent at microwave frequencies (Ref. [15]) such that the modules observe a signal primarily from the absorber. With three load temperatures we obtain three Y-factor measurements of the receiver noise ($T_{hot}=300$ K, $T_{cold}=90$ K;

¹<http://zotefoams.com>



Figure 3-5: Two zotefoam cryogen buckets, supported by adjustable feet above a cart, which allows them to sit at the appropriate height for the receiver to see directly into the absorber insert. The cart allowed us to easily and quickly change between the two cryogenic loads for the Y-factor measurements. Measurements were performed such that we wheeled one load in front of the cryostat, integrated over 10 seconds to obtain the average power (voltage) for a given load, wheeled the cart out of the beam and rotated it such that the second load could be aligned with the beam. Each load weighs $\mathcal{O}(100 \text{ lbs})$.

$T_{hot}=300 \text{ K}$, $T_{cold}=77.5 \text{ K}$; and $T_{hot}=90 \text{ K}$, $T_{cold}=77.5 \text{ K}$). The absorber and zotefoam are unpolarized, so the noise temperature measurements are taken with the total power data stream. We will characterize the noise of the polarized data stream with a different measurement method (section 3.6).

To achieve adequate instrument sensitivity for the QUIET science goals, the noise temperatures for each module must be less than 35K. The distribution of noise temperatures from the Y-factor measurement for all diodes with $T_{hot}=90 \text{ K}$ and $T_{cold}=77.5 \text{ K}$ from five noise temperature measurements performed in Chile is given in Figure 3-6. The noise temperature distribution gives an average diode noise temperature of 26.5 K with standard deviation of 3.5 K, indicating we met our specification.

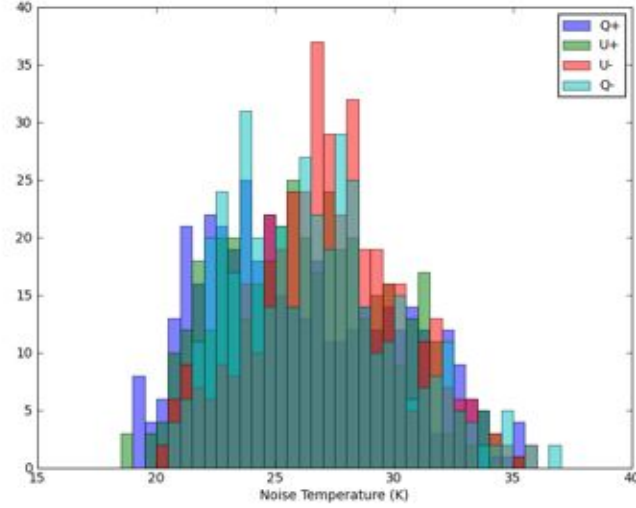


Figure 3-6: Distribution of noise temperatures for five measurements performed for all diodes just prior to integrating the receiver on the telescope mount, from Y-factor measurements taken with two cryogenic loads. The specification was that all modules had an average noise temperature less than 35K.

3.4 Responsivity

3.4.1 Total Power

The thermal loads can be used to measure the total power responsivity, the response of the measured total power stream to a given change in input temperature, via:

$$\text{Responsivity} = \frac{P_{hot} - P_{cold}}{T_{hot} - T_{cold}} \quad (3.11)$$

(variables are the same as in section 3.3 above). We measured the responsivities for each diode in the array in the laboratory prior to integration on the telescope mount with the two cryogenic thermal loads ($T_{hot}=90$ K, $T_{cold}=77.5$ K). The distribution of responsivities is shown in Figure 3-7. The polarized responsivities will be characterized using a separate method described below (Section 3.4.2).

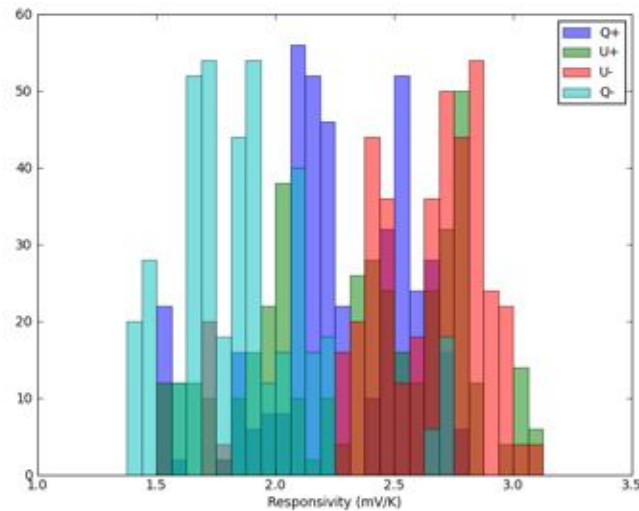


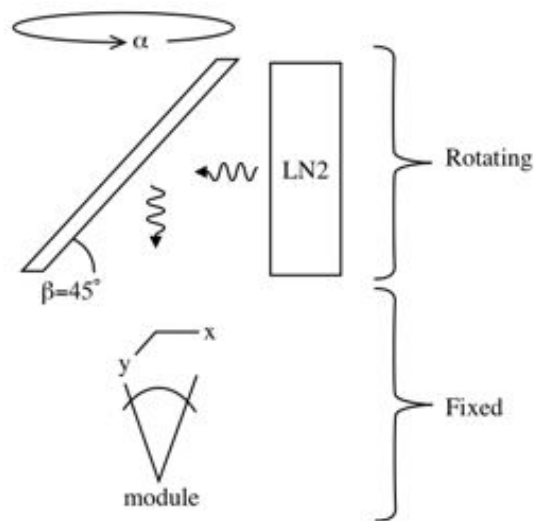
Figure 3-7: Distribution of diode responsivities from six measurements performed just prior to integrating the receiver on the telescope mount, from measurements taken with two cryogenic loads.

The responsivity of the modules depends on a variety of factors such that we do not necessarily expect that responsivities in the laboratory will exactly match those taken during observations. Thus these measurements are not values which should be used in analysis (we develop a responsivity model based from calibration sources for science observations and analysis, discussed further in Chapter 5), but are useful both as a sanity check for values obtained from calibration sources, and also because the values should be close enough that the testing performed in the laboratory to assess the receiver performance should reflect the expected performance during observations. The average responsivity from laboratory measurements is 2.23 mV/K with a standard deviation of 0.4 mV/K, where (as can be seen in Figure 3-7) most of the scatter comes from systematic differences between the diodes. These values are consistent with the equivalent values from the responsivity model from calibration observations of 2.29 mV/K with a standard deviation of 0.5 mV/K.

3.4.2 Polarized Response

We measured the polarized response of the receiver with the ‘optimizer’, a reflective plate and cryogenic load system that rotates around the boresight of the cryostat (schematic shown in Figure 3-8(a) and a picture in Figure 3-8(b)). The plate is oriented at angle β from the horizontal and reflects the light from the cryogenic load into the window of the cryostat with a small polarization defined by the resistivity and temperature of the plate, the plate angle β , and the temperature of the load. This entire apparatus rotates at a rate α such that the resulting polarized signal will rotate between the Stokes vectors at a rate of 2α . Polarization signals which do not rotate with the system (such as thermal emission from objects in the lab, which will also reflect from the plate and into the cryostat) will be detected at a rate of α , thus these effects can be removed. The loads were too small to fill the entire array beam, so the measurements are only used from the central polarimeter. This will still allow us to verify that the total power and polarized responsivities are similar, which will allow us to use total power gains when assessing polarized instrument sensitivity (see section 3.7).

Using the resistivity of a given reflector plate material and temperature of the thermal load, we can calculate the the magnitude of the polarized emission as equation 3.12 (derived in appendix C).



(a)



(b)

Figure 3-8: *a*: The optimizer consists of a reflective metal plate and a cryogenic load. The reflected signal is polarized (given by equation 3.12), as thermal load and plate are rotated around the cryostat window, the polarized signal will rotate. The stationary module will have a polarization axis, in this case noted as x and y in the figure. As the polarized signal rotates between x and y , the module will observe this as changing voltage levels on the Q and U diodes. Courtesy Keith Vanderlinde. *b*: A photograph of the optimizer setup on top of the Q-band cryostat. The cryogenic thermal load (white circular aperture) is one of the zotefoam buckets shown in Figure 3-5, the signal is reflected off of a metal plate (in profile) and into the window of the cryostat. Each load is 2 ft tall. Courtesy Ross Williamson.

$$I = \sqrt{4\pi\nu\rho\epsilon_0}(\cos(\beta) - \sec(\beta))(T_{plate} - T_{load}) \sin(2\alpha) \quad (3.12)$$

The predicted polarized emission and the measured voltage on the detector diodes give us the polarized reponsivity for the central polarimeter. We used multiple plate materials and two thermal loads to obtain multiple estimates of the responsivity. The theoretically predicted polarization for each plate and cryogenic load temperature are given in Table 3.6.

Cryogen	Material	Resistivity	Signal (mK)
LN ₂	Aluminum	2.9×10^{-8}	54
LN ₂	Stainless Steel	7.2×10^{-7}	267
LO ₂	Aluminum	2.9×10^{-8}	51
LO ₂	Stainless Steel	7.2×10^{-7}	250

Table 3.6: Expected polarized emission from the optimizer with different metal plates and cryogen loads. Assumed plate temperature is 289K and plate is at an angle $\beta = 45^\circ$ from the horizontal. Courtesy Ross Williamson.

An example of the measured signal from the optimizer for one of the diodes in the central module is given in Figure 3-9, the sinusoidal portion of the plot corresponds to rotation of the optimizer assembly around the cryostat boresight. The sinusoidal measurement was fit with equation 3.13:

$$f(t) = C_0 \sin(\omega t + c_0) + C_1 \sin(2\omega t + c_1) + C_2 \quad (3.13)$$

We extract the amplitude of the signal modulated at 2ω (coefficient C_1) and calculate the polarized responsivity from equation 3.12 given the known temperature of the load, the temperature and the resistivity of the metal plate. A comparison between the total power responsivity, measured with the two cryogenic thermal loads prior to setting up the optimizer, and the polarized responsivity measured with the

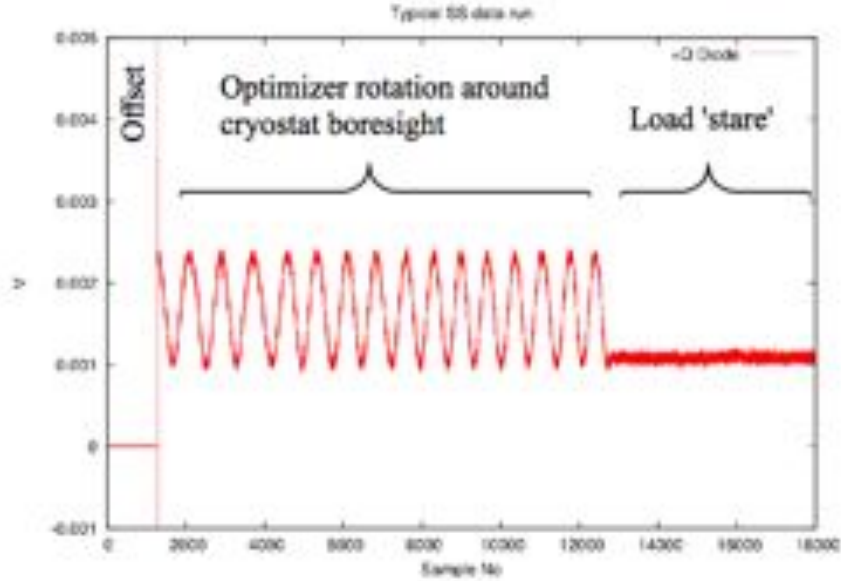


Figure 3-9: An example time stream of signal from an optimizer measurement for the Q+ diode (D1) with liquid nitrogen as the thermal load and the stainless steel plate as the metal reflector. The first section of data around 0V is taken with the phase switches biased down to give an offset measurement. The sinusoidal curve corresponds to rotating the plate and thermal load around the cryostat boresight, and the constant segment at the end was used to obtain the white noise. Courtesy Ross Williamson.

optimizer is shown in Figure 3-10. We show only measurements from the stainless steel plate because the signal-to-noise ratio for the aluminum plate measurement was too low to yield reliable results. The polarized responsivity is consistent with the total power responsivity for the central polarimeter. This is consistent with calibration measurements taken during observations in Chile (section 5.3), which found comparable responsivities between the total power and demodulated streams.

3.5 Compression

The responsivity calculation assumes that the power measured by the modules is linear across the range of input thermal loads. As discussed in Section 2.3, the third

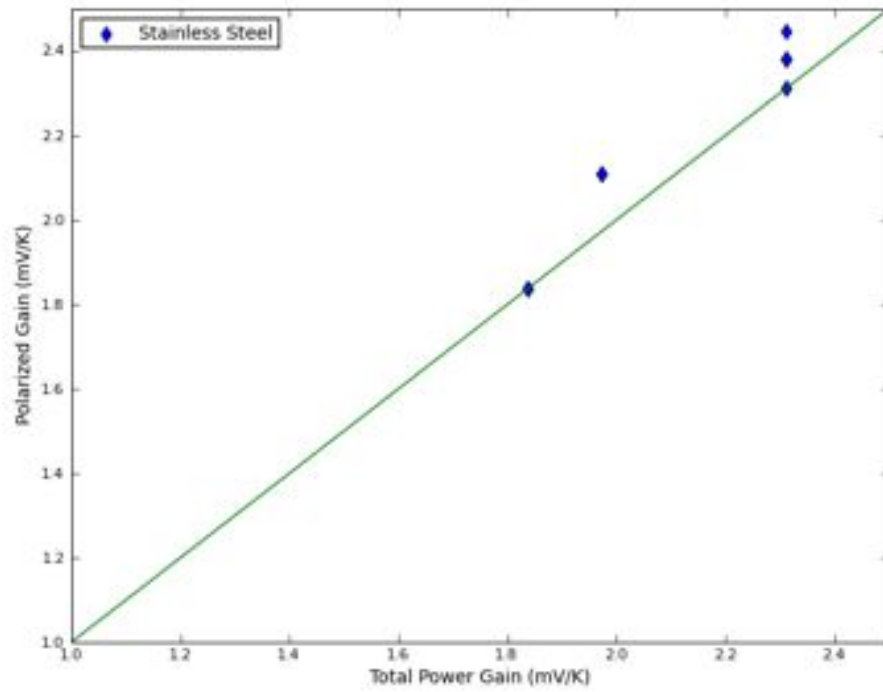


Figure 3-10: A comparison between the total power and polarized gains for the central polarimeter, all diodes. The green line indicates unity such that the total power and polarized gains are identical. The total power gain values used are the same for all loads and plate materials, as it was obtained from a previous measurement. We do not have estimates of error for this measurement. The responsivity of this module from analysis of calibration data taken during observations are consistent with these values (polarized responsivities of 1.7-2.9 mV/K).

stage amplifiers are likely to be uncompressed with input loads which are <90 K, however a 300K input load is expected to be compressed. Because the responsivities measured in the laboratory are comparable to those measured from calibration sources during observations, (section 3.4.1), we were not significantly compressed at cryogenic load temperatures.

3.6 Noise

In addition to the ‘Y-factor’ measurement, the receiver noise can be obtained using the noise power-spectrum. The noise-power spectrum is obtained from a Fourier-transform of the time-ordered data stream and is characterized by a $1/f$ function, defined as:

$$N(\nu) = \sigma_0 \left[1 + \left(\frac{\nu}{\nu_{knee}} \right)^\alpha \right] \quad (3.14)$$

Where $N(\nu)$ has units V/\sqrt{Hz} , σ_0 is the white noise level, α is the slope of the low frequency spectrum and ν_{knee} is the knee frequency. The high noise power at low frequencies represents signal variation on long time scales, such as offset and responsivity drifts with time. The knee frequency is determined by the intersection of the low frequency ‘red’ spectrum and the white noise level. The white noise floor is the minimum noise obtainable in the system. High frequency spikes tend to be electronic in origin (e.g. harmonics of common radio-frequency emission from power lines, switching and timing frequencies in the system, and occasionally radio stations). Typically both the low frequency spectrum and the high frequency spikes will be filtered, leaving only the white noise. This noise spectrum can be computed for either total power or demodulated data streams. Theoretically the white noise level in the two data streams should be identical, because we are interested primarily in the demodulated data stream we will consider the noise from the demodulated data time

stream in the following analysis.

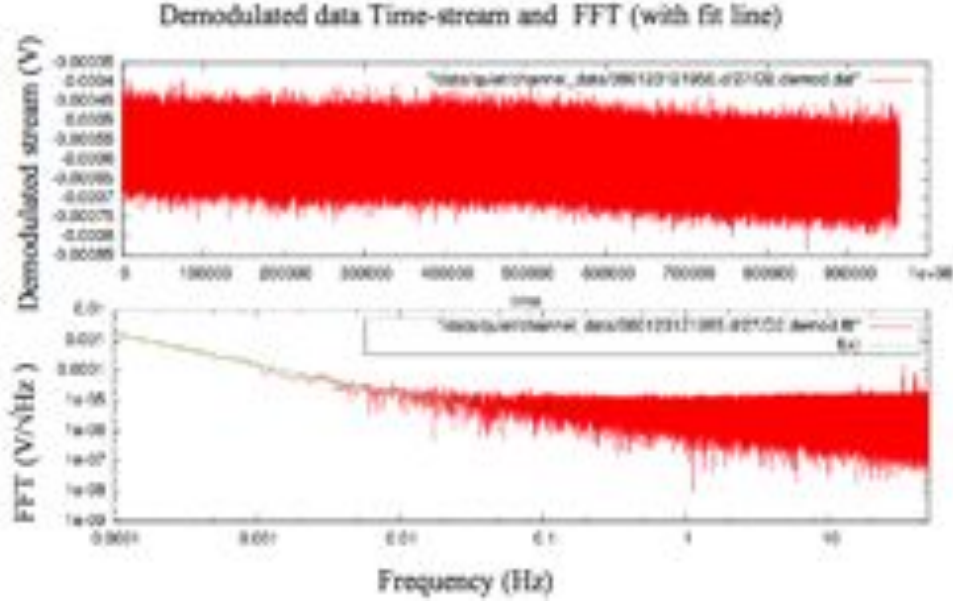


Figure 3-11: *Upper panel* The demodulated time stream for module 27, U1 diode taken over the course of 2.5 hours while looking at a liquid oxygen thermal load. *Lower panel* The resulting noise spectrum. The fit line is shown with parameters $\sigma_0 = 5.2 \mu\text{V}/\sqrt{\text{Hz}}$, $\alpha = -1.09$, and $\nu_{knee} = 23\text{mHz}$ for the noise model given by equation 3.14. Courtesy Robert Dumoulin.

We performed measurements using a cryogenic liquid nitrogen load, an example of a demodulated data stream and its noise spectrum taken from data in the laboratory with a $1/f$ fit is shown in Figure 3-11. The resulting distribution of white noise values for the demodulated stream for all diodes in the array is shown in Figure 3-12. The average noise floor was $2.7 \mu\text{V}/\sqrt{\text{Hz}}$. A variety of factors, particularly grounding conditions and sky temperature (the change in noise due to differences in input loading is calculable, this will be discussed in section 3.7), can contribute to the white noise level, so these are expected to be different from noise floors obtained during science observations.

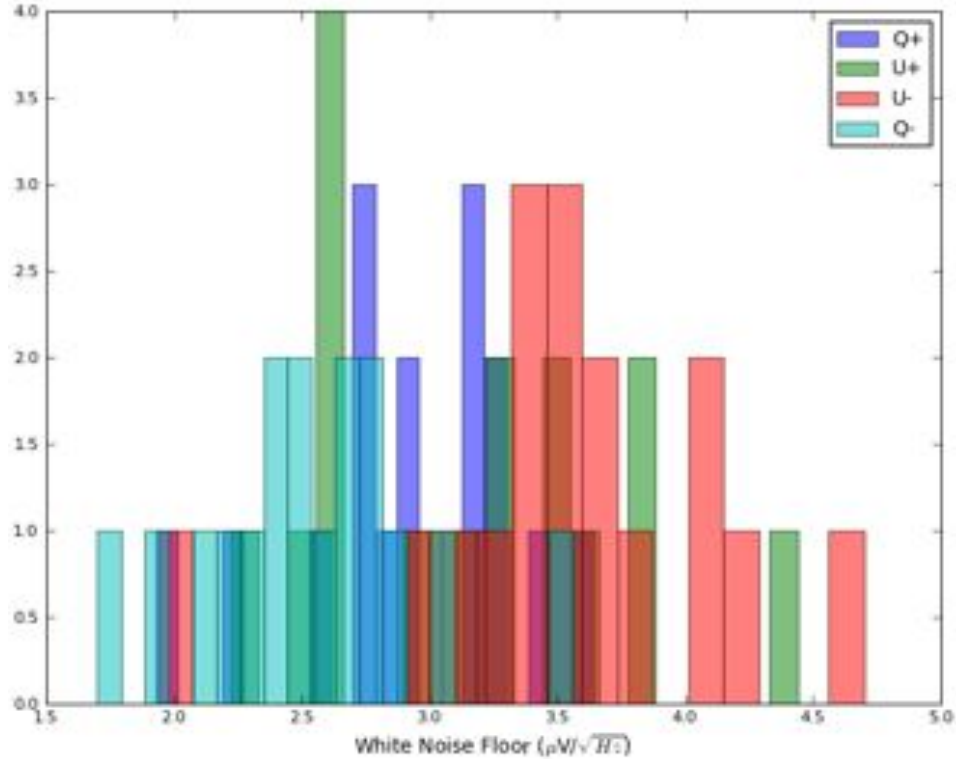


Figure 3-12: Distribution of white noise floor values for measurements just prior to integrating the receiver on the telescope mount, from a liquid-nitrogen stare over one hour with the demodulated stream.

3.7 Instrument Sensitivity

We chose the size of the pathfinder arrays to significantly improve E-mode measurements and B-mode constraints, and to prove the technology for future Phase II B-mode searches. Measurements were performed in the laboratory in Chile prior to science observations to verify that the receiver array would have an on-sky sensitivity better than $\simeq 60 \mu\text{Ks}^{1/2}$ (per-horn sensitivity of $300 \mu\text{Ks}^{1/2}$).

We compute polarimeter sensitivity with two different formulae. One method uses the noise temperatures calculated from a Y-factor measurement and receiver bandwidth to tabulate the sensitivity via:

$$\text{Sensitivity} \equiv \frac{T_{\text{receiver}} + T_{\text{input load}}}{\sqrt{\Delta\nu}} \quad [K s^{1/2}] \quad (3.15)$$

The second method uses a measurement of the white noise obtained while looking at a cryogenic load for $\simeq 1$ hour with the responsivity obtained from the two cryogenic loads to compute the sensitivity via:

$$\text{Sensitivity} \equiv \frac{\text{noise}}{\text{responsivity}} \quad \left[\frac{V s^{1/2}}{V/K} = K s^{1/2} \right] \quad (3.16)$$

The first method will yield a measurement of the sensitivity for the total power stream. The second method can be used as measurement of the polarized sensitivity under the assumption that the total power and demodulated responsivities are identical (verified by measurements given in section 3.4.2, and also shown to be true in the responsivity derived from calibration measurements during the observing season given in section 5). The distributions of the sensitivity for each diode for both calculations is given in Figure 3-13; the two methods of computing the sensitivity are comparable, indicating that the measurements of noise, gain, and bandwidth are consistent and also that the noise and gain between the demodulated and total power data streams are consistent.

The sensitivity for the entire array was computed as:

$$\text{Array sensitivity (K s}^{1/2}\text{)} = \frac{\sqrt{\sum_{\text{diode}} S_{\text{diode}}^2}}{N_{\text{diodes}}} \quad (3.17)$$

The array sensitivity values were obtained from both methodologies, and extrapolated to the Chilean sky temperature. This conversion is detailed thoroughly in appendix D, and includes the following:

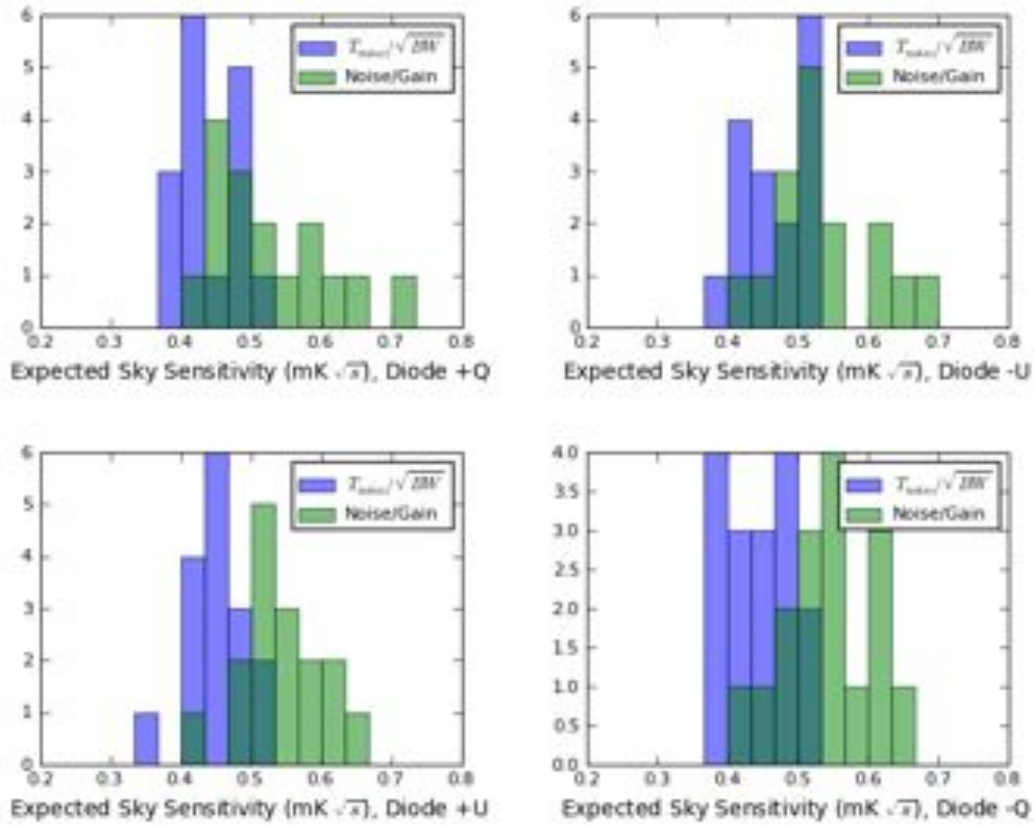


Figure 3-13: Distribution of polarimeter sensitivities for each of the four diodes, where the sensitivity has been computed twice from different sets of laboratory data; once according to equation 3.15, using noise temperatures and bandwidths, and again with equation 3.16 from noise and responsivity measurements. Here we extrapolated the results from both to show the expected sensitivity with a 14K Chilean sky load (scaling factor described in the text). These values are for individual diodes and so are larger than the array sensitivity values quoted in the text. The slight shift between the expected measurements could be due to bandwidth measurement errors or water vapor collection on the front face of the cryogenic thermal loads used for these measurements.

- Noise is a function of input thermal load, so we must include a scaling factor C_{sky} between the cryogenic loads used and the Chilean sky temperature. We do not have an exact measurement for the sky temperature, so it is not surprising if the extrapolated sensitivity from laboratory measurements do not exactly match those found from observations.
- As presented in appendix D, we must include a correction for the Rayleigh-Jeans approximation for the black-body loads, C_{RJ} .
- We mask data around the phase switch transition region, this removes 13% of the data, and this factor must be included in equation 3.15. This masking factor C_{mask} was first discussed in section 2.5, and is treated in appendix D.

The final result is:

$$\text{Sensitivity} = C_{RJ} C_{sky} \frac{T_{\text{receiver}} + T_{\text{sky}}}{\sqrt{\Delta\nu} * C_{mask}} \quad (3.18)$$

$$\text{Sensitivity} = C_{RJ} C_{sky} \frac{\text{noise}}{\text{gain}} \quad (3.19)$$

The atmospheric model we use for QUIET (Ref. [72]) predicts a zenith temperature of 8.5K, our range of observing elevations (70° to 43°) will yield atmospheric temperatures between 9K and 12.5K. I will assume a sky temperature of 11K, including the 3K CMB contribution, the total sky temperature is $\simeq 14\text{K}$. Accounting for the module which broke just prior to integration on the deck, the extrapolated array sensitivity values are $56 \mu\text{Ks}^{1/2}$ and $68 \mu\text{Ks}^{1/2}$ for equation 3.15 and equation 3.16, respectively. Taking the worst of the two values, we nearly achieved our sensitivity goal of $60 \mu\text{Ks}^{1/2}$. Values from science data from observations indicate an average array sensitivity value of $\simeq 60 \mu\text{Ks}^{1/2}$ (Chapter 5), computed via 3.16.

Chapter 4

Summary of Q-band Season: Observations and Data Reduction

This chapter addresses the QUIET observing site, observations with the Q-band receiver, data selection, and data reduction. QUIET observations are performed from the Chajnantor Test Facility (CTF). Between July and September 2008, the Q-band receiver was deployed to the CTF and calibration and commissioning observations were performed. Science data were collected between October 2008 and June 2009, during which time over 3000 hours of CMB data were logged. The Q-band receiver was removed from the telescope and replaced by the W-band receiver in June 2009. W-band observations are currently underway.

4.1 QUIET Observing Site

4.1.1 Observing Conditions

Microwave and sub-millimeter experiments select very dry observing sites to reduce signal absorption by atmospheric water vapor, and high altitude sites to reduce absorption from oxygen. The CTF is located at an altitude of 5080 m in the Atacama

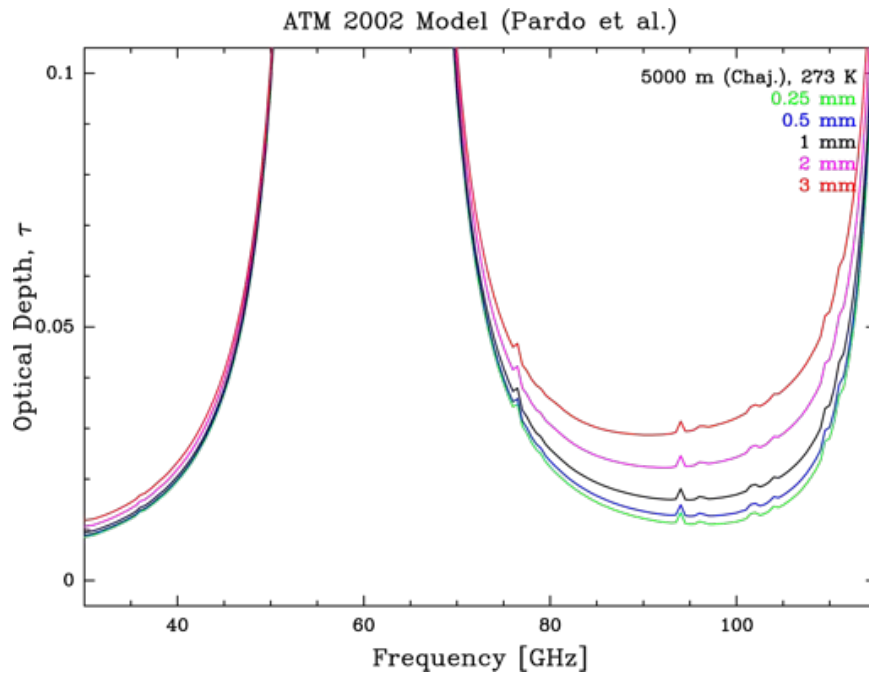


Figure 4-1: Atmospheric opacity near the two QUIET frequency bands (band centers are 40 and 90 GHz). Courtesy Simon Radford.

Desert in northern Chile: longitude $67^{\circ} 46'W$, latitude $23^{\circ} 02'S$. The atmospheric opacity at frequencies near the QUIET observing bands is shown in Figure 4-1. To minimize signal absorption, we chose 40 and 90 GHz as the central frequencies for the two receivers. The Atacama Desert is one of the driest places on Earth; a profile of the precipitable-water-vapor (PWV) from a weather station on a nearby telescope (APEX¹) during the Q-band season is shown in Figure 4-2, along with humidity, ambient temperature, and wind speed. The average PWV is $1.6\text{mm} \pm 1.3\text{ mm}$ for all scans (no data cuts). The Chilean summer (December-March) has a greater incidence of poor weather. This is apparent in the higher PWV values during those months.

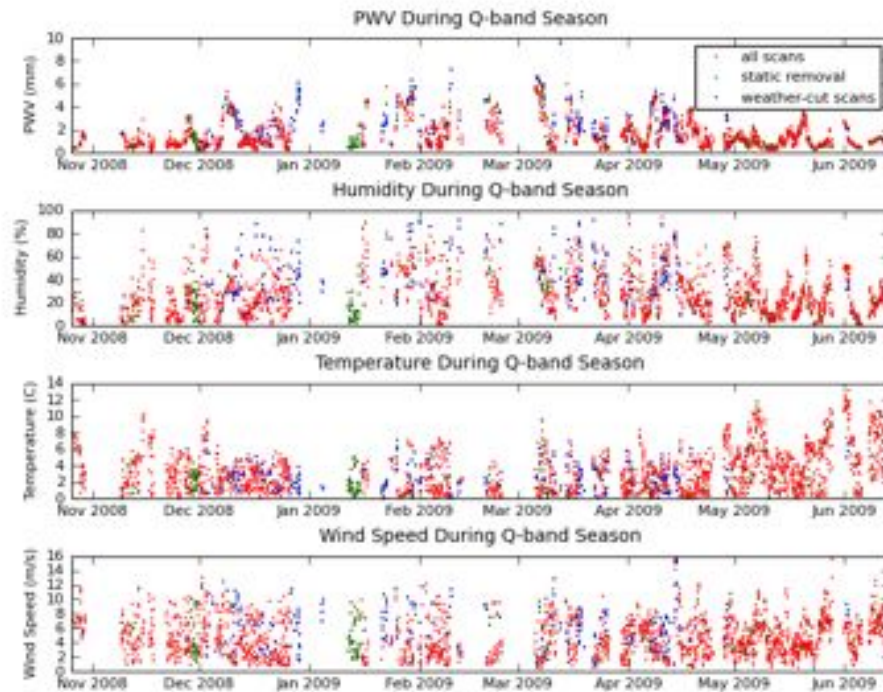


Figure 4-2: Weather variables, including PWV, humidity, ambient temperature, and wind speed for scans during the Q-band season. The green points denote scans which were removed for static cuts (section 4.4.2), and blue points denote scans which are removed by the weather cut (section 4.4.6), it should be emphasized that a high PWV does not necessarily indicate that the data quality will be poor. Typically we would not observe above 90% humidity. The weather station is taken off-line during very bad weather periods, as well as a one week period during QUIET observations, accounting for periods of missing data in the above plots. The PWV spikes are eye-catching but represent a small fraction of the data. Data courtesy APEX, Robert Dumoulin.

4.2 Patch Selection

We selected four CMB patches (2a, 4a, 6a, 7b) and two Galactic patches (Gb, Gc), each covering $15^\circ \times 15^\circ$, for observations. The QUIET patch coordinates are shown in Figure 4-3(a) and given in Table 4-3(b). QUIET patches were selected for their low synchrotron emission as measured by WMAP and because they remain at least 30° from the Sun and Moon during the year, allowing uninterrupted observations throughout the season. The two patches with the least expected foreground contamination are 4a and 6a. These patches were prioritized for scan time over the other patches.

4.3 Scan Strategy

QUIET primarily observes at four deck angles during the observing season: $\{30^\circ, 75^\circ, 120^\circ, 165^\circ\}$. Stepping the deck angle by 45° rotates the Stokes Q into Stokes U parameters.

We employ a fixed-elevation, azimuth-scanning technique: a patch is scanned in azimuth as it drifts through the beam, which generally takes $\simeq 1.5$ hours. The telescope then re-tracks the patch and begins another scan. By scanning at constant elevation for a given scan, we observe through a constant column density of atmosphere such that only weather variations within a scan contribute to atmospheric signal.

4.4 Data Selection and Reduction

Data reduction and analysis are performed on each patch using two independent pipelines, one employing maximum-likelihood map-making and power spectrum es-

¹The Atacama Patchfinder Experiment - a collaboration between the Max-Planck Institut für Radioastronomie of Bonn, the European Southern Observatory, and the Onsala Space Observatory

timation (Ref. [26]), and one a Pseudo- C_ℓ estimator (Ref. [82]). The data used in science analyses must be clean of artifacts such as weather, polarimeter malfunctions, and ground pickup. Selection criteria were developed independently for each pipeline from analysis of the time-ordered data stream, spectral information, and map-based tests. This chapter addresses data selection and reduction for the Maximum-likelihood pipeline, I will note which cuts are shared between the two pipelines.

4.4.1 Nomenclature

- **TOD: Time-ordered Data:** Polarimeter data in the time domain (polarimeter voltage as a function of time).
- **CES by scan and segment:** A segment is one full scan of a patch, performed at a constant elevation. Usually a given patch is within the elevation range of the telescope for longer than a single segment, so the telescope re-tracks to another elevation and performs another segment scan. Any segments of the same patch in series are labelled with the same scan number as the other scans, and is given a segment number to distinguish it from the scans at other elevations in the series. The scan and segment number together denote a Constant Elevation Scan (CES).

4.4.2 Standard and Static Cuts

The baseline data selection (removing dead detector diodes, testing procedures during the season) is common between the two pipelines. A description of these cuts and the effected scans is given in Table 4.1. I maintain the distinction between standard and static cuts for consistency with the notation used by the collaboration, there is no intrinsic difference.

Description	Modules Effected	CESes Effected
hybrid-Tee modules excluded*	RQ17 (all diodes), RQ18 (all diodes)	all
Phase switches not yet balanced*	all	≤ 125
Mislabelled*	all	377.6, 1302.1, 118.1, 1538.1, 1648.1, 783.1 829.1, 828.2, 897.1, 1335.1, 1468.1, 1468.2, 1786.4
Broken Diode*	RQ16 (all diodes), RQ08 U2	all
Poor noise spectrum*	RQ04 Q1	all
Non-stationary noise	RQ12 Q2	≤ 766
Preamplifier cables swapped	all	329-341
Ground-screen door open	all	398
Receiver off	all	529.2
Cable testing	all	563-596
Blown fuse	RQ07-RQ09, RQ12, RQ13, RQ16	632.5-636
Dome maintenance	all	759.1
Deck problem	all	937,951.1,953-955
Cryogenic temperatures stabilizing	all	980.1

Table 4.1: Description of static and standard cuts. These are common between the two pipelines, the CES numbering scheme is from the Maximum-likelihood pipeline. Cuts which are included in the ‘standard’ cuts are labelled with an *. A few of these occurred only once (for example, if the receiver was turned off during generator maintenance and the cryogenic temperatures needed to stabilize, generally we would not be taking data while they did so).

4.4.3 Scan Duration

Scans lasting fewer than 1000 seconds have poor noise fits due to paucity of data; these scans are removed.

4.4.4 Glitching Cut

As discussed in section 2.5.5, the ADC chips have a discontinuity in their output voltage at particular bit values. The resulting glitch effects both the demodulated

and total power streams at a total power level corresponding to the bit glitch location. We use a correction (Ref. [11], [83], [8]), applied identically in both pipelines, to correct and keep this data. Data was taken at 800kHz for each channel to measure the location of the glitch, the height of the discontinuity, and the range of bit values over which it effected the data. This data was used to correct the discontinuity in the demodulated data stream.

A cut was developed to remove scans which were not adequately corrected by this algorithm. After correcting the data, the binned total power and demodulated streams were plotted against each other and a straight line was fit. Any diode which has residuals to the fit of $\chi^2 > 10$ is removed (Ref. [11]). A successfully de-glitched plot of total power vs demodulated time stream is shown in Figure 4-4(a), the systematic effect from the residual glitching is 10% of the statistical uncertainty.

4.4.5 Phase Switch Cut

In the observing period Dec 2008 - Feb 2009, high humidity caused the phase switch circuits on the AIB boards to electrically short the PS21 phase switches on modules RQ11 and RQ12. This caused the phase switch current value to increase, as shown in Figures 4-5(a) and 4-5(c) for RQ11 and RQ12, respectively. PS21 was biased down on RQ12 for from Dec 27 - Jan 13 (these scans register a current near zero) after it shorted. This phase switch was biased normally again when we realized the shorting was dependent on the humidity and was not permanent. The distributions of the maximum phase switch currents for PS21 are shown in Figures 4-5(b) and 4-5(d), these yielded an upper limit for normal operation of 0.38 mA, and a lower limit of 0.2 mA, we used these at limits for cutting data with phase switch currents which were too high or biased down. We confirmed that periods when the phase switch current was high or low also had a reduced diode signal level for RQ11 and RQ12 by a factor of $\simeq 2$. This is expected if the phase switches are biased such that signal is allowed to propagate down only one module leg instead of both legs.

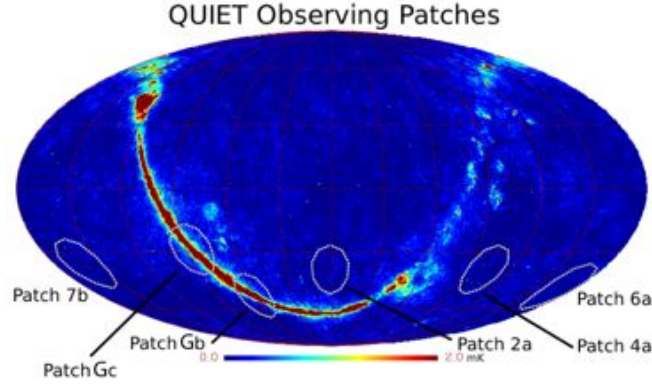
4.4.6 Weather Cut

Description and Design

We designed a cut to remove data taken during poor weather conditions. This section describes the development of the weather cut, the final product, and studies performed to ensure this cut did not bias the data set.

Contributions from weather are assessed with the double-demodulated time stream, downsampled to one second. We process the data first by binning the data into 10 second bins for one scan and one diode, and computing the standard deviation of each bin. We then compute the standard deviation of the distribution of standard deviation values. This yields a single value which encodes the variability of noise between 10 second time scales. We will call this the weather variable. We repeat this computation for all scans, giving a distribution of the weather variable for a particular diode over the observing season. We fit a Gaussian to the distribution of the weather variable for all scans of a given patch, and compute the gaussian width (σ) and mean (μ). We note any scans which have a weather variable greater than 5σ from the mean.

We repeat this for all diodes, and any scan for which 70% or more of the diodes lie outside of the 5σ limit is cut from the data set. We repeat this for a 30 second bin size, and for each patch, such that a scan can be cut by either the 10-second or 30-second bin size distributions. The distribution of the weather variable for module RQ09 (the central polarimeter) for all diodes is shown in Figure 4-6 for the 10-second bin size, the red vertical lines are the 5σ limit. We performed various studies to assess the accuracy of the weather cut and that we were not biasing the data set. Those studies are described in the following sections.



(a)

Patch	Coordinates		Time
	RA	DEC	Hours
6a	0h 48m	-48°	900
4a	5h 12m	-39°	768
2a	12h 4m	-39°	1002
7b	22h 44m	-36°	243
Gb (Galactic)	16h 0m	-53°	320
Gc (Galactic)	17h 46m	-29°	110
Calibration			142
Total CMB			2913

(b)

Figure 4-3: *a*: QUIET sky patches (circles), plotted over the WMAP Q-band temperature map (Ref. [36]) *b*: Hours spent on each QUIET patch with no data cuts imposed and coordinates in J2000. Because it is far from the other patches, Patch 2a was observed almost without interruption each day from the time it rose to the time it set and has the most integrated hours. Patch 7b, which had overlapping scan times with Patch 6a, was observed less frequently than the other CMB patches.

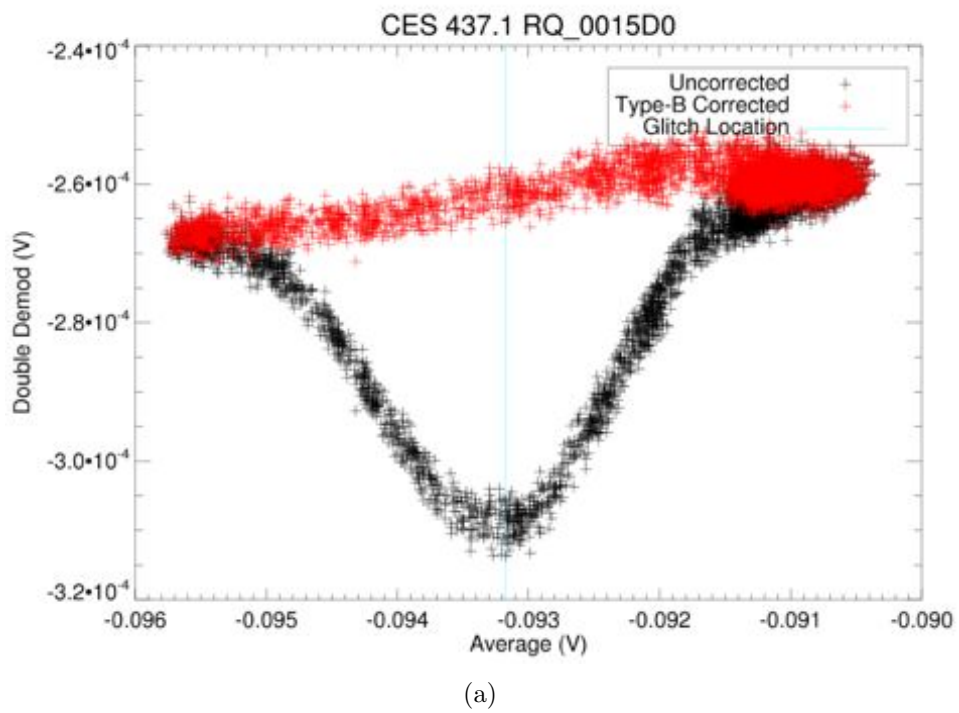
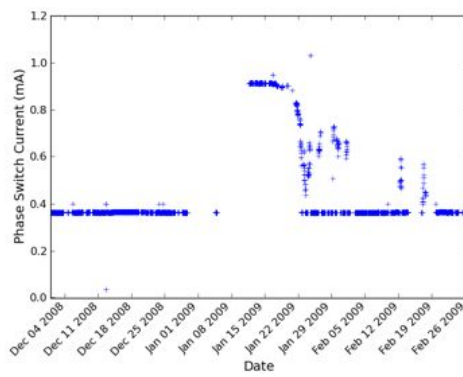
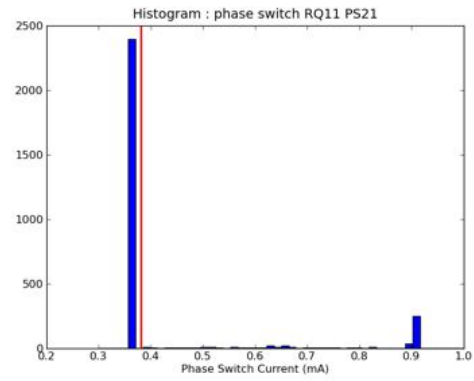


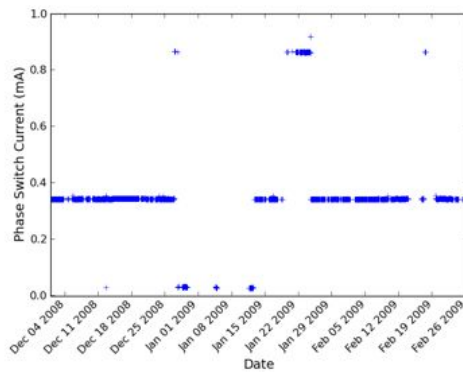
Figure 4-4: Total power vs. demodulated time stream before and after de-glitching for module RQ15, Q1 for scan 437.2. The cyan line shows the location of the glitch; the χ^2 was 49.2 before de-glitching, and 1.9 afterwards. Courtesy Immanuel Buder (Ref. [18]).



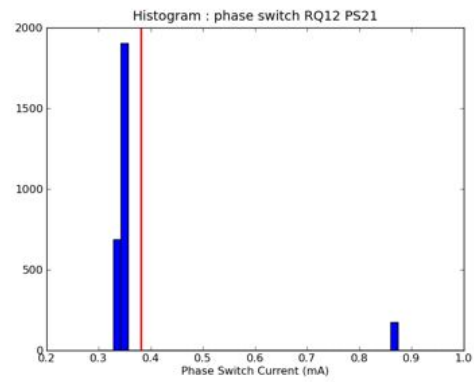
(a)



(b)



(c)



(d)

Figure 4-5: Maximum PS21 current for all scans for *a*: RQ11, as a function of time, *b*: RQ11, the distribution of currents, *c*: RQ12, as a function of time, and *d*: RQ12, the distribution of currents. The red vertical lines in the distributions denote the chosen maximum current value in mA for the phase-switch cut.

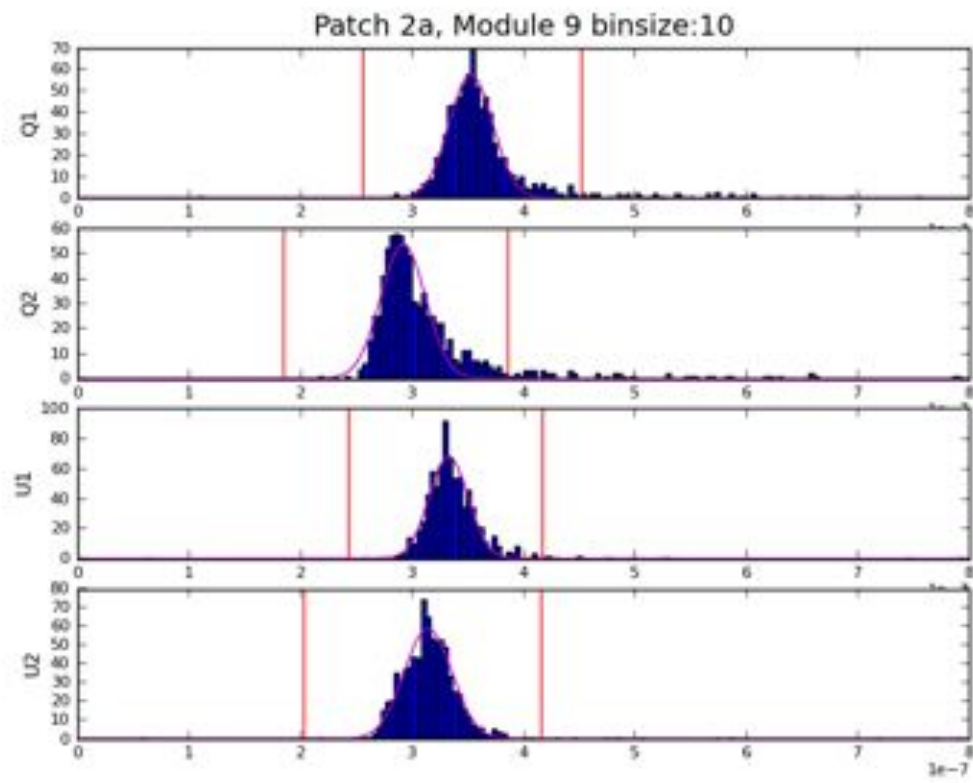


Figure 4-6: Histogram of standard deviation of standard deviation of binned data (10 second bins), Module 9. The red lines indicate 5σ of the distribution.

Studies

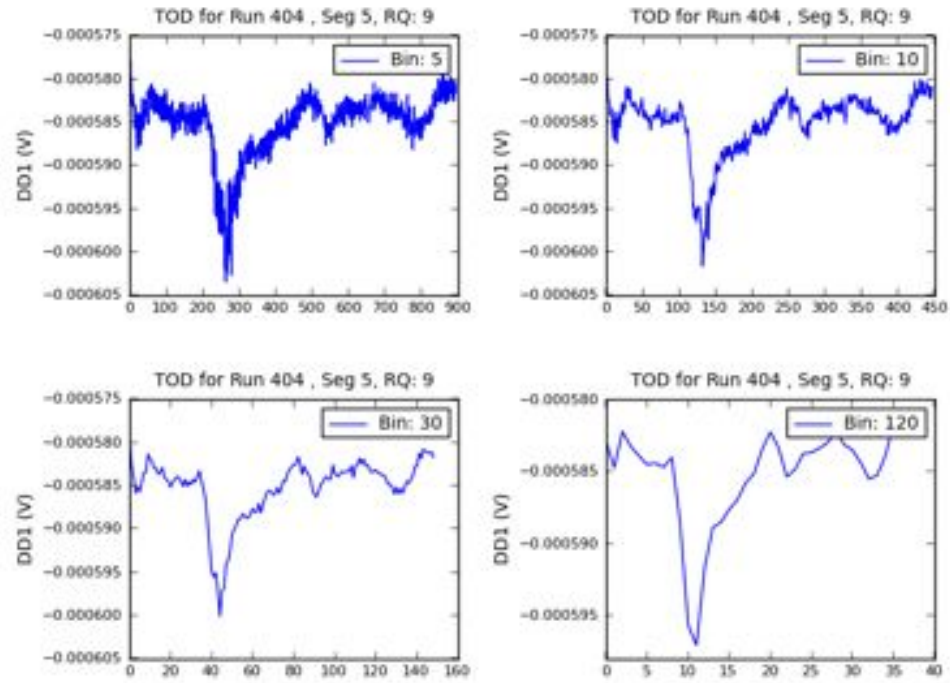
Time Scales for Weather Variable

The temperature of the enclosure drifts on a variety of time scales, and with it, the polarimeter data stream. This effect can be corrected in further analysis steps, and so we must choose a weather variable which selects only periods of bad weather, and does not flag data which is varying only from the enclosure temperature. The two effects are illustrated in Figures 4-7(a) and 4-7(b); these show the time-streams for scan 404, which has a clear spike originating from a cloud, and scan 1776, which has a signal envelope dependent only on the enclosure temperature and is not an example of bad weather.

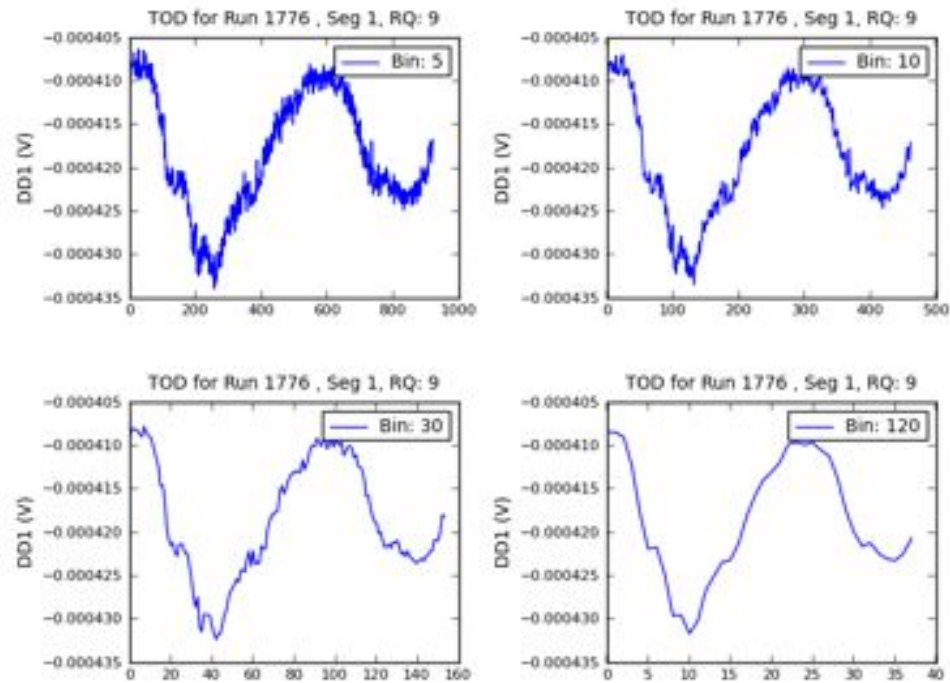
To isolate and cut scans which are affected by bad weather, we investigated a variety of binning time scales: 5 seconds, 10 seconds, 30 seconds, 60 seconds, and 120 seconds. The standard deviation of each bin for these bin sizes is shown for scan 404 (Figure 4-8(a)) and scan 1776 (Figure 4-8(b)). The significance of the weather variable for each of these bin sizes for both scans is given in Table 4.2. The spike from weather in scan 404 was detected at all bin sizes. Enclosure temperature variation was apparent by a bin size of 60 seconds as it includes the rise of the enclosure temperature in the RMS statistic. The 30 second bin size generally had the highest significance for weather. We included the 10 second time bin because it is near the scan frequency, and so will have sensitivity to stationary weather patterns. The overlap between the two bin-size cuts is $\simeq 80\%$, and is dominated by the Q-diodes (which have higher leakage and make up a larger percentage of the weather cut). A visual inspection of all scans which were cut by only one showed that both cuts were removing bad data, so both cuts were retained.

Bin size	CES 404.5	CES 1776.1
5	19σ	0.1σ
10	30σ	0.6σ
30	33σ	0.9σ
60	33σ	2.5σ
120	35σ	10.7σ

Table 4.2: The significance of the weather variable for a set of different bin sizes for scans 404 (bad weather) and 1776 (enclosure drift), RQ09 diode Q1 (DD1).

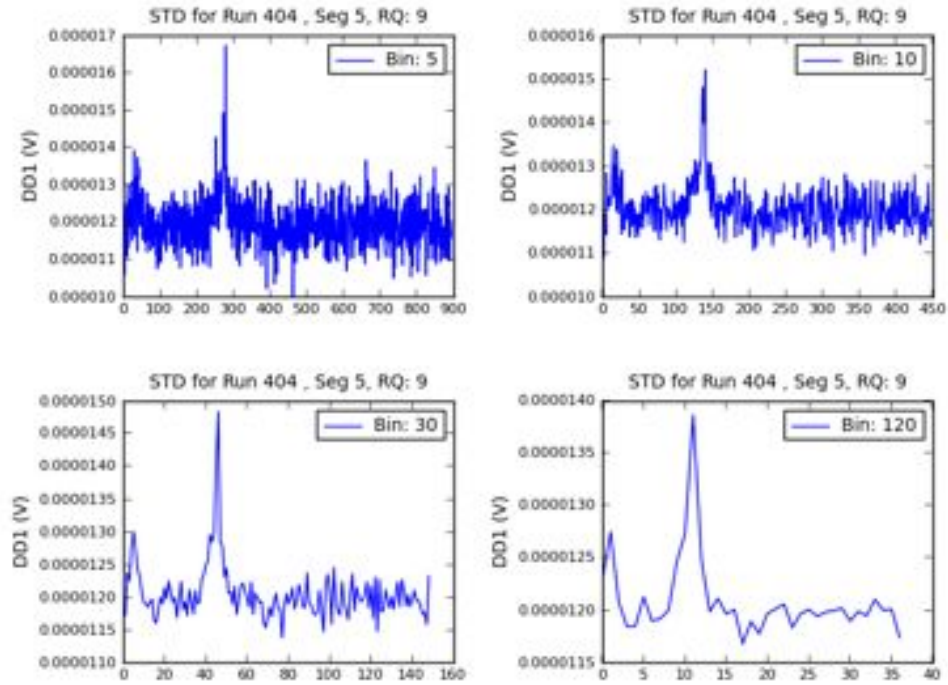


(a)

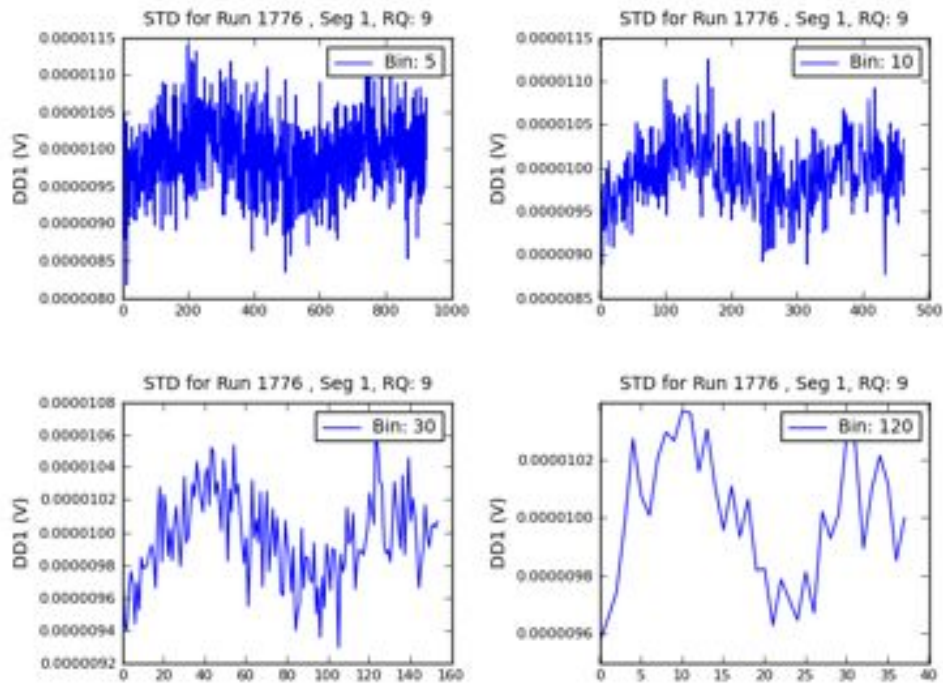


(b)

Figure 4-7: Demodulated stream for module RQ09 diode Q1 (DD1) binned into 5, 10, 30, and 120 second time bins for *a*: Scan 404, segment 5, which has a spike from weather in all bin sizes and *b*: Scan 1776, segment 1, which varies only with enclosure temperature.



(a)



(b)

Figure 4-8: *a*: Standard deviation per bin for module RQ09 diode Q1 (DD1) for scan 404 segment 5, for bin sizes of 5 seconds, 10 seconds, 30 seconds, and 120 seconds. The spike is from weather (likely a cloud). *b*: The same for scan 1776 segment 1. The envelope in the standard deviation comes from variation with enclosure temperature.

Bi-modal Distributions

We found many modules had distinctly different distributions in the weather variable between the two halves of the season, however there was nothing apparent in the data stream. We investigated whether this was due to enclosure temperature variation or differing weather conditions between the two halves of the season, however neither of these were contributing factors to the bimodal distributions. The underlying cause of the change in noise properties over the season was not resolved. We may be able to tailor the weather cut to each half of the season, this is currently under investigation.

Leakage

Water vapor is linearly polarized to only a small degree, $\ll 1\%$ (Ref.[34]), while the high-leakage modules have I \rightarrow Q leakage of order 1-2% (discussed in sections 2.2.4, 5.8), such that the polarization TODs are sensitive to water vapor and cloud-cover primarily through I \rightarrow Q/U leakage. Because the weather cut is based on the (unfiltered) demodulated stream, and hence is sensitive to only the linear polarization of the atmosphere and the leakage, the majority of the fluctuations present in the RMS statistic come from leakage from the total power weather-based fluctuations in the atmosphere into the polarized data stream. As a result, the majority of the diodes which comprise the 70% of diodes in the weather cut will tend to be those with relatively higher leakage. This is shown in Figure 4-9, which shows how frequently a diode was included in the 70% of modules contributing to cutting a particular scan as a function of leakage. Q-diodes have higher leakage and so are preferentially used in this statistic.

If we were cutting diode-by-diode or module-by-module, this would introduce a large systematic effect of only cutting modules or diodes with high leakage. However, the weather cut removes all diodes in a flagged scan, so we are not biasing the data set by cutting on a diode-by-diode basis. In addition, the weather cut requires at least 70% of the diodes to be cut such that it requires lower-leakage diodes to flare up as well for the scan to be removed.

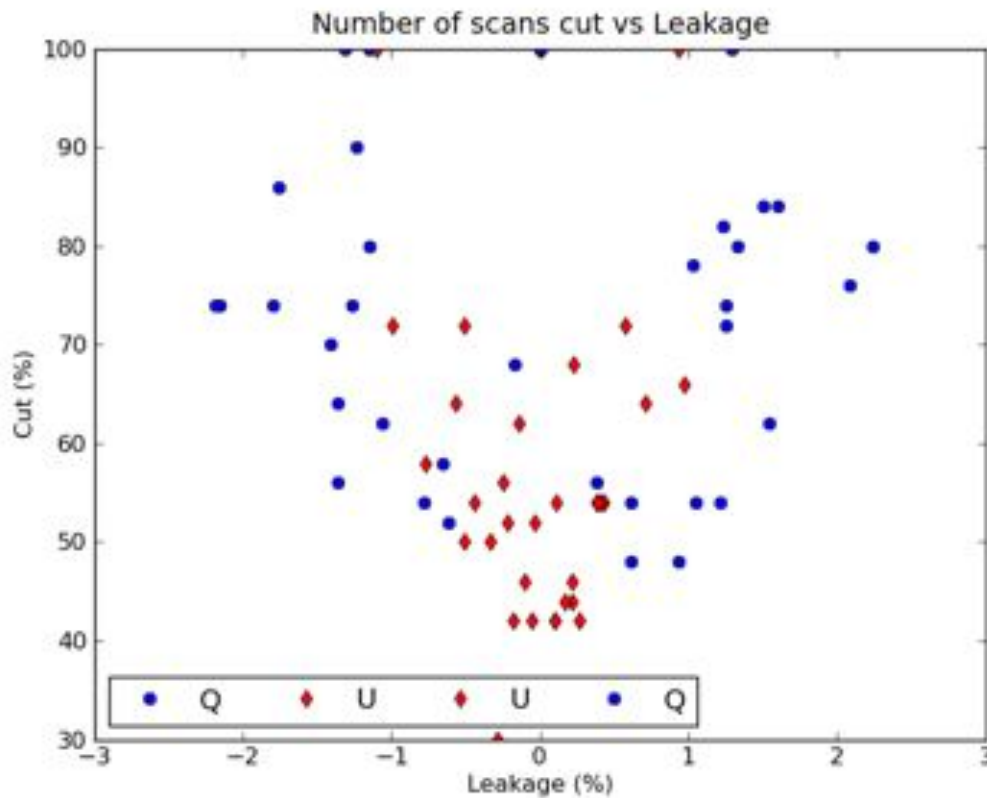


Figure 4-9: The weather cut requires that 70% of the diodes lie outside of a $5\text{-}\sigma$ threshold, this shows which diodes make up that 70% as a function of leakage. It is apparent that higher-leakage modules appear more frequently in the list of modules cut. Because weather effects both the demodulated and total power streams, and leakage is contamination from total power into the demodulated stream, this isn't unexpected. This study was done with patch 2a data only.

Bias

We created a set of simulated time-ordered-data with noise only (no signal) using the same simulation code we use in the Maximum-likelihood analysis pipeline for power spectrum analysis (section 6.4.3). The simulation code uses the pointing and calibration information for a set of selected scans (in our case 44, ideally we would draw a larger sample size but we have been limited by computation time), and uses the noise model (described below in section 4.4.7) and an input power spectrum to generate a set of TODs. In our case, the signal spectrum is null, allowing us to test

whether or not the weather monitor will bias the data set by removing scans which only contain noise. We used identical noise properties between the 44 scans, with $\nu_{knee} = 10\text{mHz}$, $\alpha = -2.0$, and $\sigma_0 = 1 \times 10^{-5}$. For each scan, an FFT was generated and then transformed back to TOD space. The resulting TOD for each scan and each diode were analyzed by the weather cutting program. If the weather cut had removed a scan, this would indicate it cuts on random noise, which would bias the data set. There were no cases where 70% of the diodes all had 5σ outliers for a given scan, so no data was cut, and the weather cut is not contributing to bias in the data set.

4.4.7 Fourier-Transform Based Cuts and Filtering

Fourier Transform Products

The maximum-likelihood pipeline generates fits to the noise-power spectra per diode for each scan with a noise model defined by a $1/f$ spectrum with a white noise floor:

$$N(\nu) = \sigma_0^2 \left[1 + \left(\frac{\nu}{\nu_{knee}} \right)^\alpha \right] \quad (4.1)$$

where $N(\nu)$ has units V^2/Hz . A Fourier transform of a typical data stream from one diode during a 1.5-hour scan of patch 6a is shown in Figure 4-10, with the noise model (black line), scan frequency (green dashed line) and knee frequency (solid blue line) marked. QUIET operates the telescope at its maximum slew rate of $6^\circ/\text{sec}$, resulting in scan frequencies $\simeq 0.1 \text{ Hz}$. These are significantly higher than typical instrument knee frequencies ($\simeq 0.01 \text{ Hz}$), such that we scan in the white-noise regime of the detector noise.

Filtering the FFT data

There is unwanted noise power in the noise spectrum both at low frequencies ($1/f$ – for the Q-band array this is generally below $\simeq 10 \text{ mHz}$) and at high frequencies (spikes around 6 Hz , and a forest of spikes above 15 Hz , as seen in the FFT spectrum

in Figure 4-10). The origin of the high frequency noise spikes is unclear, likely they are harmonics and noise aliasing of the power-line frequency (50Hz and 60Hz) and the switching and timing frequencies in the electronics system. To remove this noise, we filter the spectrum using:

$$F(\nu) = \frac{1}{1 + \left(\frac{\nu}{\nu_{\text{apod}}}\right)^{\alpha_{\text{apod}}}} \quad (4.2)$$

with two separate sets of filter parameters: the low-pass filter has $\nu_{\text{apod}}=4.5\text{Hz}$ and $\alpha_{\text{apod}} = 200$; the high-pass filter has $\nu_{\text{apod}} = 2.5\nu_{\text{scan}}$ and $\alpha_{\text{apod}} = -40$. The CMB signal is periodic in the Fourier domain at harmonics of the scan frequency, so the total integrated power in the first few harmonics is negligible compared to the power in the higher harmonics. Thus, filtering at low frequencies removes mostly noise and hardly any signal and so we chose the ν_{apod} for the high-pass filter to cut out noise below $2.5\times$ the scan frequency. The resolution of the beam begins to affect the signal-to-noise at higher harmonics thus we can filter high-frequency noise without incurring much data loss. A low-pass filter cut-off of 4.5 Hz removes $\simeq 25\%$ of the signal (Ref. [8]), we are currently investigating whether we can move the filter and retain more data. There are two reasons to filter this data: one is that there are spikes at high-frequencies which trigger a data cut. The second is that in the frequency range where the beam begins to roll off, the signal level is decreasing but the noise stays constant, decreasing your signal-to-noise. The noise spectrum before and after filtering is shown in Figure 4-10, it is apparent that both the high-frequency spiking and the low-frequency $1/f$ noise has been filtered out.

Data cutting with FFT data

We compute the χ^2 between the FFT of the data and noise model fit-line for each diode for each scan in the ranges: 0 - $2.5\nu_{\text{scan}}$ mHz, $2.5\nu_{\text{scan}}$ - 7Hz; we use only the range 200 mHz - 7 Hz for data cutting. The FFT χ^2 is defined as

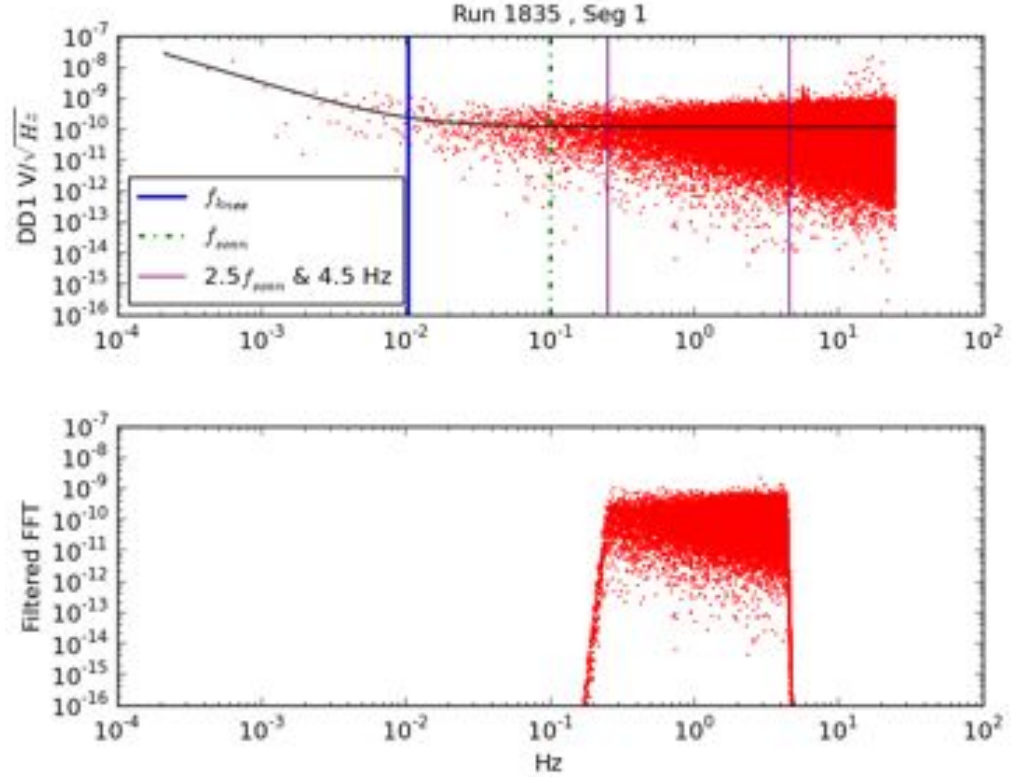


Figure 4-10: *Upper panel:* The Fourier transform of a typical (unfiltered) QUIET scan for a single detector diode of one polarimeter (Scan 1835, Segment 1), with noise model fit, scan and knee frequencies marked (module RQ09, diode Q1). Included are the high- and low-pass filter apodization frequencies. *Lower panel* After filtering.

$$\chi_{\text{FFT}}^2 = \sum_{\nu} \frac{F(\nu) \cdot |f_{\nu}|^2}{P(\nu)}, \quad (4.3)$$

where $P(\nu)$ is the expected noise spectrum, f_{ν} are the TOD Fourier coefficients, and $F(\nu)$ is the combined filter function. The mean of this distribution is given by:

$$\mu = \sum_{\nu} F(\nu) \quad (4.4)$$

the variance is given by:

$$\sigma^2 = \sum_{\nu} F(\nu)^2 \quad (4.5)$$

and the agreement between the fit and the data is quantified by

$$N_{\sigma} = \frac{\chi^2 - \mu}{\sigma} \quad (4.6)$$

The distribution of N_{σ} values for all scans and all diodes for the range $2.5\nu_{scan}$ -7Hz is shown in Figure 4-11, and compared to the distribution obtained from simulated data streams (noise only). If the average N_{σ} is greater than $4\text{-}\sigma$ between $2.5\nu_{scan}$ - 7Hz, the diode is cut for that CES segment. We also cut a diode from a scan if the diode knee frequency is higher than 50mHz. We are investigating whether we can shift this cutoff frequency higher given the high-pass filtering frequency of 200mHz.

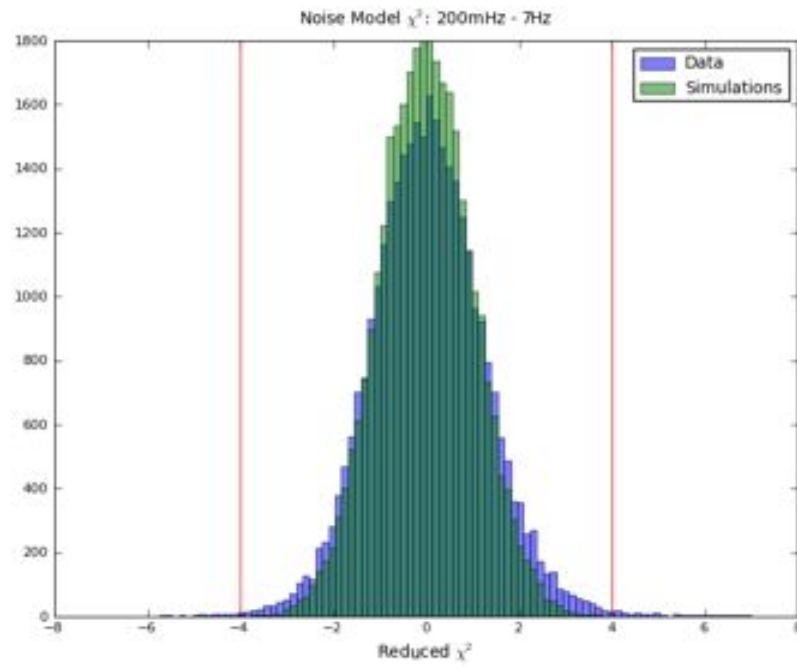


Figure 4-11: N_σ distribution for all diodes and all scans. A simulated data set was also generated directly from the noise model and the distribution N_{sigma} values for the simulated data set is also shown. The red vertical line denotes a $N_\sigma=4$, where we would cut the diode. We are investigating the differences between the simulated and data distributions. Data courtesy Robert Dumoulin.

4.4.8 Side-lobe Cut

As discussed in section 2.2, the optical design contains mirror-spillover which can cause power from astronomical sources such as the sun or the moon to leak into maps when the source intersects a sidelobe region. This section describes a cut which was developed to remove scans which have evidence of side-lobe contamination from the sun (Refs. [17], to appear in [18]). This cut is identical between the two pipelines.

4.4.9 Coordinate System

We use a coordinate system which is defined by the difference between the boresight pointing of the telescope and the location of the source (Ref. [8]). First, a horizontal coordinate system is defined from the boresight azimuth, elevation, and deck pointing (A,E,D) which rotates with the deck:

$$\vec{p}_0 = \begin{pmatrix} \cos(A) \cos E \\ -\sin(A) \cos(E) \\ \sin(E) \end{pmatrix} \quad (4.7)$$

$$\vec{s}_0 = \begin{pmatrix} -\cos(A) \sin E \cos(D) - \sin(A) \sin(D) \\ \sin(A) \sin(E) \cos(D) - \cos(A) \sin(D) \\ \cos(E) \cos(D) \end{pmatrix} \quad (4.8)$$

$$\vec{r}_0 = \vec{p}_0 \times \vec{s}_0 \quad (4.9)$$

\vec{p}_0 is the boresight pointing, \vec{s}_0 gives the orientation of the deck. The ephemeris location of the sun in azimuth and elevation coordinates can also be expressed as a pointing vector in the form of \vec{p}_0 , which we will denote as \vec{v} . Then the sun-boresight pointing can be expressed in spherical coordinates, θ and ϕ , such that θ defines the distance between the boresight pointing and the source, and ϕ will be the equivalent of a direction vector.

$$\theta = \arccos(\vec{v} \cdot \vec{p}_0) \quad (4.10)$$

$$\phi = \arctan\left(\frac{\vec{v} \cdot \vec{r}_0}{\vec{v} \cdot \vec{s}_0}\right) \quad (4.11)$$

θ and ϕ cover the ranges $0 < \theta < 180$ and $-180 < \phi < 180$. Regions above the deck in this coordinate system have $0 < \theta < 90$, regions below the deck have $90 > \theta > 180$.

For subsequent analysis, we will use a flat-projection of this coordinate system, defined as:

$$X = \theta \cos(\phi) \quad (4.12)$$

$$Y = \theta \sin(\phi) \quad (4.13)$$

The origin of the X,Y coordinate system is defined as the point when the boresight of the telescope is pointed directly at the sun.

4.4.10 Cut Development

All scans from all patches were co-added together in the X,Y coordinate system to identify which sun-boresight pointing locations have significantly more signal compared to the noise in the maps (Ref. [17]). An example map is shown in Figure 4-12(a). An X-Y map is produced for each module, and a box is drawn around regions with obvious sun contamination, as shown in Figure 4-12(b). This identifies module-dependent regions in X-Y space in which the sun has entered the sidelobe. The X-Y position for each module in each CES in the season is then evaluated (based on the boresight pointing and the sun's location for each scan) and if its X-Y position lies in the boxed region, the scan is cut for that module. A systematics study showed that the effect of the sun in the sidelobes was averaged over the season (the contamination from the sun through the sidelobes is fixed to the deck and so is not constant

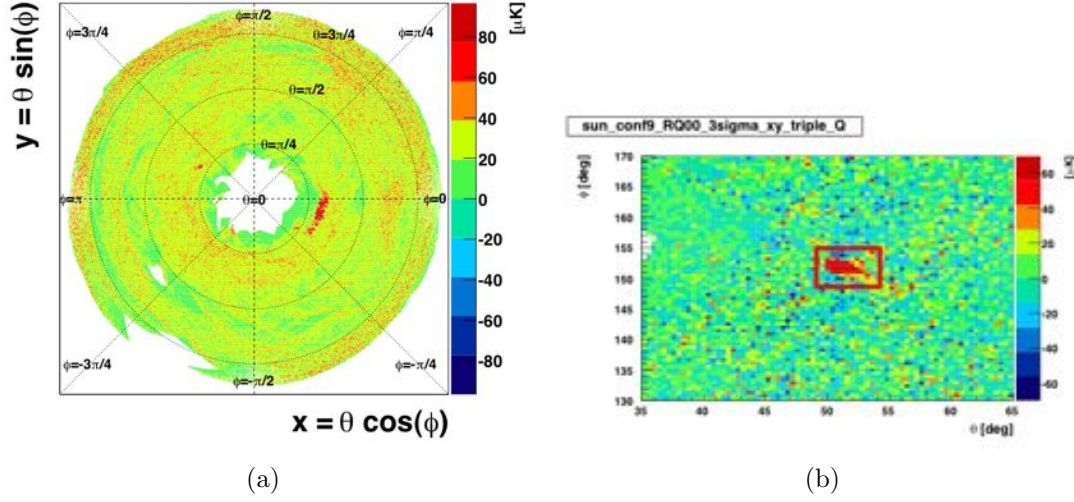


Figure 4-12: *a*: A co-added map for all CEs in a flat projection of the sun-boresight coordinates for RQ02 (all diodes). The sidelobe regions are located near a radius of $\theta = \pi/4$, one at a ϕ near zeros (large red swath), the other near ϕ of $3\pi/4$ (small red dot). *b*: Identification of a region with sun contamination, this is shown in θ, ϕ coordinates for RQ00 (all diodes), for the ‘triple reflection’ sidelobe, which is the small contamination seen on the left in *a*. Courtesy Yuji Chinone.

in celestial coordinates) that ultimately we could include these contaminated maps without impacting the science results (Refs. [17], [18]), although currently we remove them.

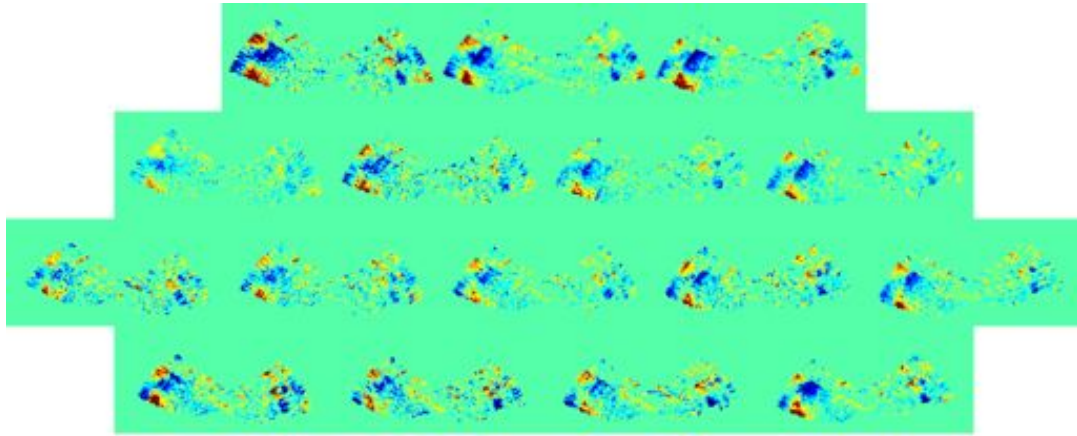
4.4.11 Ground Map

As noted above and in first discussed in section 2.2.6, the beam contains spillover which can contribute signal from astronomical sources when they intercept the sidelobe beam. This sidelobe structure can also point towards the ground, and contribute contamination from the ground into the data-stream. In an azimuth-elevation coordinate system at a given deck angle, the ground pickup should be constant (it intercepts structures such as mountains, nearby storage containers, generally things which are stationary on the ground). This raises the possibility of using the map-making formalism developed for the maximum-likelihood pipeline (discussed further in chapter 6)

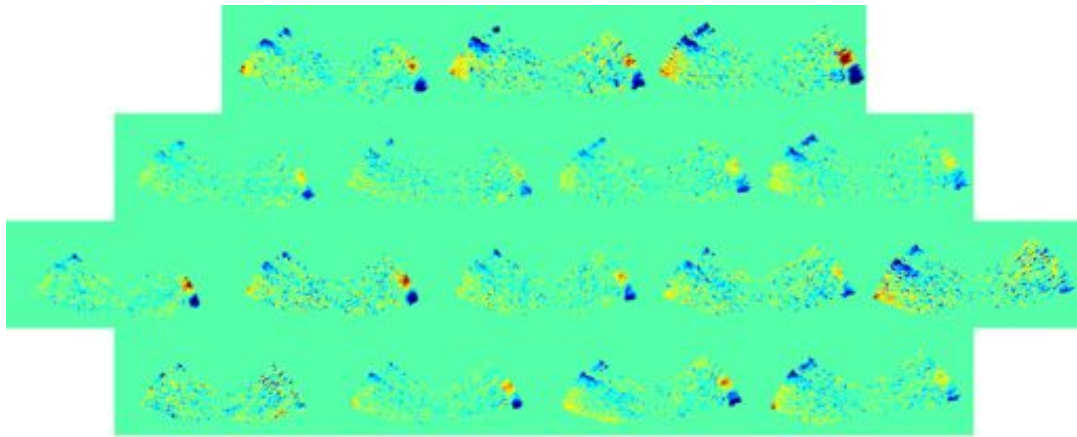
to create maps in azimuth and elevation coordinates. A summed map in azimuth and elevation coordinates composed of all CESes in the season at a particular deck angle should primarily be a map of ground contamination if there is significant contamination above the instrument noise. The underlying assumption is that the contribution from the ground is stationary through time.

For each module and for each deck angle, a co-added map (and noise per pixel) from the demodulated TODs of all scans is produced in azimuth-elevation coordinates. The CMB signal is not constant in the azimuth-elevation coordinate system, so the template map contains essentially no CMB signal. Template maps for each module at the four observation deck angles are given in Figures 4-13(a)- 4-14(b). The known sidelobe structure should produce more ground contamination around deck angles of 30° and 150° , this is consistent with the ground-maps. As noted in section 2.2.6, an upper ground-screen structure was designed to remove the two sidelobes generating this ground contamination, however it was not ready in time for Q-band observations.

With a template for each module and each observation deck angle, we correct each CES individually as follows. For a given CES and module we use the telescope pointing and the template map as a look-up table for the contribution from the ground to the data stream for each point in the TOD. This creates a second, parallel TOD which we can use to remove ground signal from the data stream (courtesy Sigurd Knaess, a detailed algorithmic description is to appear in Ref. [19]).

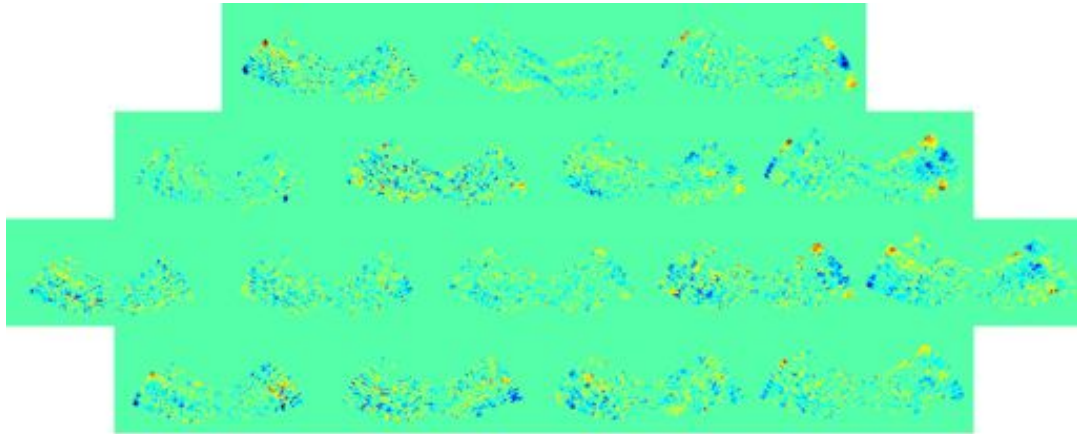


(a)

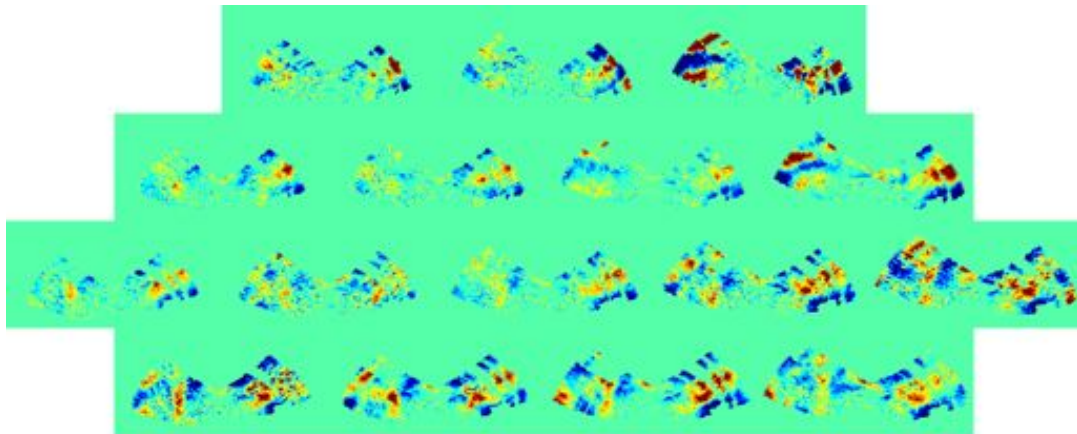


(b)

Figure 4-13: The ground map for deck angle a : 30° and b : 75° . Each module has two maps associated with it: one for the Q diodes (left map for each set) and one for the U diodes (right map for each set). RQ00 is the top left, RQ15 is lower right map. Coordinates are azimuth and elevation. Courtesy Sigurd Knaess.



(a)



(b)

Figure 4-14: The ground map for deck angle a : 120° and b : 165° . Each module has two maps associated with it: one for the Q diodes and one for the U diodes. RQ00 is the top left, RQ15 is lower right map. Coordinates are azimuth and elevation. Courtesy Sigurd Knaess.

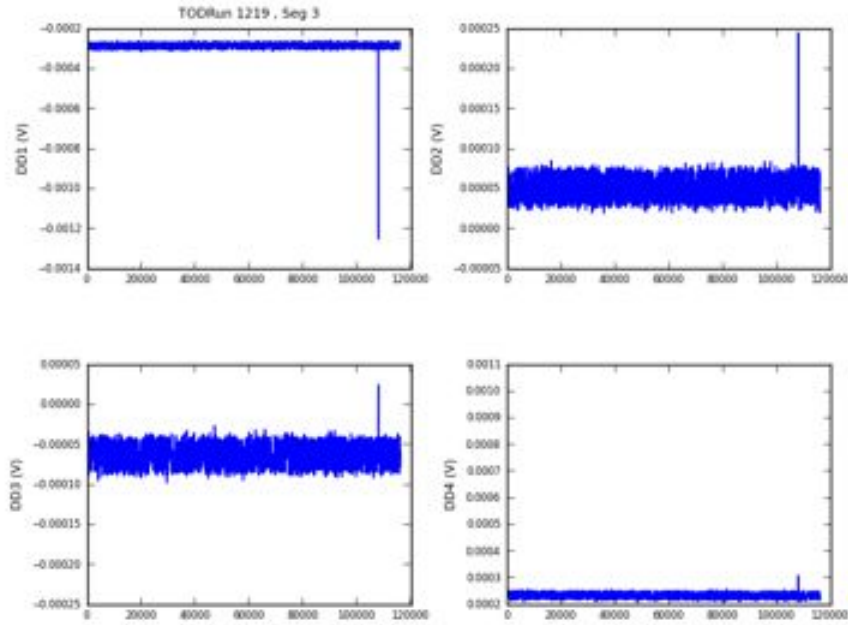


Figure 4-15: Spike in the demodulated stream for scan 1219, segment 3 for module RQ00. This was rejected with an outlier statistic of 41, 33, 30, 41 σ , for the Q1, U1, U2, and Q2 diodes respectively.

4.4.12 Max-Min Removal

We compute an outlier statistic to identify spikes in the time-ordered data stream. For each CES and each diode, the average and the root-mean-square of the data stream for the CES TOD is computed. The deviation from the mean is computed for each point in the TOD, and divided by the RMS to obtain an outlier statistic (equation 4.14, [19]). If the absolute value of the maximum outlier is greater than 7.0, the CES is removed from the scan for that diode. A TOD from one scan and module removed by this statistic is shown in Figure 4-15.

$$\text{Outlier} = \left| \text{MAX} \left(\frac{X - \bar{X}}{X_{RMS}} \right) \right| \quad (4.14)$$

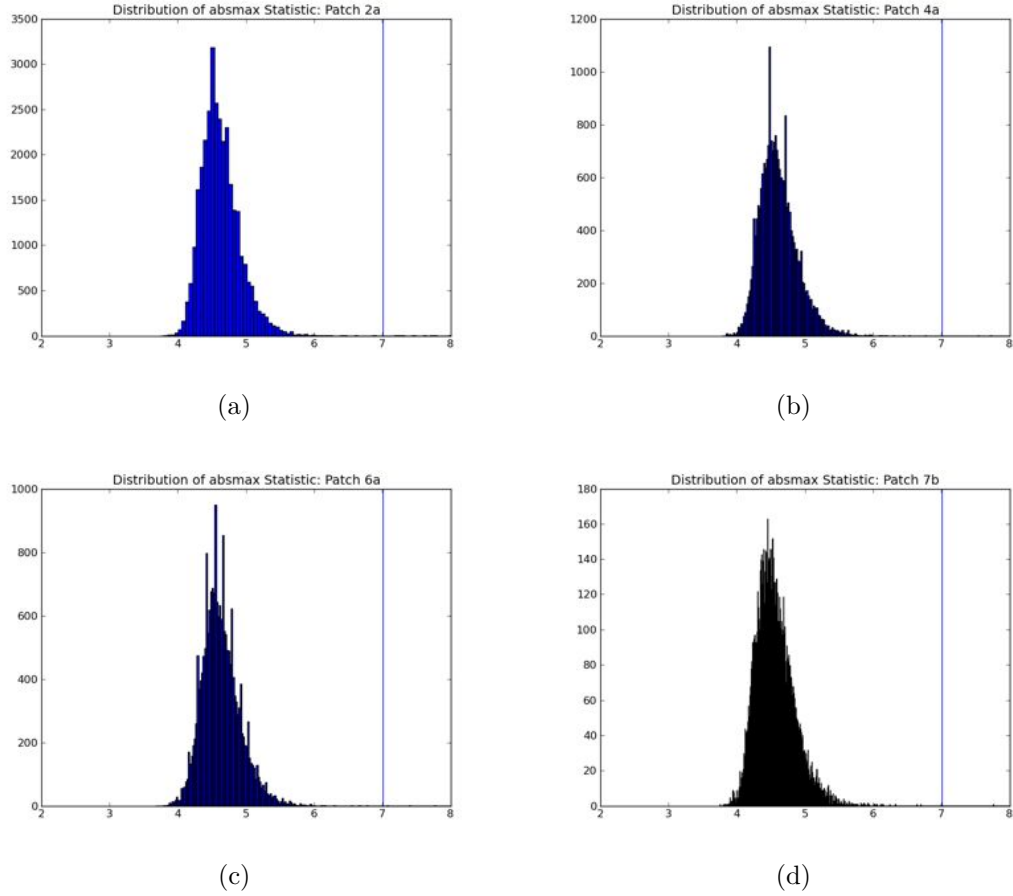


Figure 4-16: Distribution of the ‘absmax’ outlier statistics for all diodes and all CES’s for patch *a*: 2a, *b*: 4a, *c*: 6a, and *d*: 7b. The 7σ cut-off value is indicated by the blue vertical line.

The distribution of outlier statistics for each of the CMB patches is shown in Figures 4-16(a)- 4-16(d). These are distributions of the maximum outlier, which is why they do not peak at zero. A typical scan will have a max outlier of 4.5σ , so a 7σ cut seemed reasonable such that we do not cut into the bulk of the distribution. Outliers of this type are generally caused by glitching in the electronics chain, it is not necessarily true that there would only be one glitch per CES, this statistic will cut on the largest of them.

4.4.13 Source Removal and Edge-Masking

We use the WMAP point-source catalog (Ref. [91]) to mask point sources from the final summed maps prior to power spectrum analysis. We also mask the edge pixels if they have an RMS $3\times$ higher than the lowest RMS of the map.

4.4.14 Data Selected

These are preliminary, and a few values are currently being determined.

Cut	Patch 2a	Patch 4a	Patch 6a	Patch 7b
Standard removal*	20%	20%	20.7%	18.4%
RQ12, Q2*	0.5%	0.5%	0.5%	0.5%
Static*	2.8%	3.2%	3.1%	4.3%
Scan Duration*	4.6%	5%	4.2%	1.9%
Glitching*	2.0%	2.9%	5.5%	3.1%
Weather [†]	4.8%	9.9%	16.9%	13.5%
Sidelobe [†]	3.1%	11.3%	7.6%	2.8%
Phase Switch [†]	0.4%	0.2%	0%	0.1%
TOD Outlier [†]	1.1%	0.1%	0.2%	< 0.1%
FFT (χ^2 and f_{knee}) [†]	0.3%	0.2%	0.15%	0.08%
Total	35.2%	45.9%	51.3%	40.6%

Table 4.3: Percentage of data cut by each data cut. These are given as a fraction of CES-segment-diodes, not number of hours.

* Percentage taken from full data set.

[†] Percentage taken after the standard, RQ12Q2 cut, static, scan duration, and glitching cuts.

It should be noted that order is important here, we remove data from one criteria, and then the next, and then the next, in this order. As a result, any overlap between the cuts is not factored into the percentage value, and the values denote how much more data is removed with each successive cut.

Chapter 5

Instrument Calibration and Characterization

5.1 Introduction

We dedicate $\simeq 10\%$ of the QUIET observing season to instrument calibration observations. This chapter summarizes calibration procedures, products, uncertainties, and the resulting systematic errors from measurements of pointing, responsivity, polarimeter angle definitions, leakage, receiver bandpasses, beams, and correlated noise. QUIET has two independent data analysis pipelines (Maximum Likelihood and Pseudo- C_ℓ), I will describe the calibration for the Maximum Likelihood pipeline but they are similar. Instrument calibration analysis was performed by many collaborators, this is meant as a summary with final results to appear in Ref. [18].

5.1.1 Nomenclature

- Polarization modules - the 16 modules which are attached to the OMTs, these modules will measure the Q and U Stokes parameters in the differenced stream.
- hybrid-Tee modules - the two modules attached to the hybrid-Tee assembly,

these measure differential temperature between their two feedhorns.

- Drift Scan - A repetitive azimuth scan that uses the sky rotation to allow the source to drift through the beam. These allow us to scan through a constant column density of atmosphere.
- Raster Scan - A scan performed in which we slew in azimuth twice and re-track the source, generally changing the elevation of the telescope. Raster scans of calibration sources will typically need additional processing to remove the effects of changing atmospheric depth during the course of the scan.
- Constant Elevation Scan (CES) - this was described in Chapter 4.

5.2 Calibration Overview

5.2.1 Calibration Sources

Calibration sources are described below and the Q-band calibration scheme is summarized in Table 5.1.

- **Tau A**, or the Crab Nebula, is a supernova remnant with a polarized flux at Q-band known to an accuracy of $\pm 2.7\%$ from WMAP measurements (Ref. [90]). We perform measurements of Tau A with the central polarimeter every two nights, and with all other polarimeters at least once during the observing season. The maximum angle that Tau A rises above the horizon is usually within 5° of the lower elevation limit of the telescope, which is too low to use a drift scan for the central polarimeter. Instead, we employ a raster scan, observing at four deck angles $\{ 30, 75, 120, 165 \}$ such that we can use these measurements for polarization angle calibration. The polarized brightness of Tau A is 22.1 Jy (Ref [90]).

- **The Moon** We employ either a drift scan or a raster scan to observe the moon with each polarimeter during a single moon calibration measurement; this is performed once each week. A model of the moon (Ref. [8]) gives an expected polarization of $\simeq 1\text{K}$. We use a raster scan when the moon does not rise to a high enough elevation to drift through the entire beam.
- **Mini Sky-dips** We perform "mini sky-dips" once for each constant elevation scan (once per $\simeq 1.5$ hours). Each mini sky-dip consists of nodding the telescope in elevation by a few degrees (4° at the beginning of the season and 6.2° at the end, we changed the elevation range to increase signal-to-noise) causing the instrument to observe through different air masses. To use this as a calibrator we will need to use an atmospheric model to quantify the change in temperature during the dip, this will be discussed below in section 5.3.1. The total-power channels of the polarimeters and the demodulated channels of the hybrid-Tee modules will measure the resulting change in atmospheric temperature.
- **Sky-dips** Similar to a mini sky-dip, but refers to an elevation scan between an elevation of 43° - 87° . We performed this during final calibration measurements at the end of the season.
- **Wire grid polarizer** At the end of the Q-band season, we performed one measurement with a wire-grid polarizer. We placed the polarizer on the front face of the cryostat and rotated the grid around the boresight. The modulated polarized signal (on order of a few Kelvin) is then measured by the polarimeters.
- **Jupiter, RCW38, and Venus** are used as calibrators for the hybrid-Tee channels. We cannot use them as a polarization calibrators due to a combination of its low polarization flux, our beam size, and our sensitivity.

Source	Schedule	Calibration
Tau A, central polarimeter	Once/two days	Beam size and ellipticity, absolute polarimeter responsivity, absolute polarimeter angles
Tau A, off-center polarimeters	Once/season	Absolute polarimeter responsivity, absolute polarimeter angles
Moon (full array scan)	Once/week	Relative polarimeter responsivity between polarimeters, pointing, leakage, absolute polarimeter angles
Jupiter, Venus, RCW38 (hybrid-Tee channels)	Once/week	Absolute hybrid-Tee responsivity, pointing, beam size and beam ellipticity
Mini sky-dip	Once/scan	Relative hybrid-Tee and polarimeter responsivity, leakage monitoring
Polarized wire grid	Once/season	Relative polarimeter responsivity, relative polarimeter angles

Table 5.1: QUIET calibration scheme, including calibration sources and frequency of observation.

5.3 Responsivity

As discussed in chapter 3, the responsivity quantifies module diode response in voltage for a given input temperature. The responsivity of the hybrid-Tee modules are determined separately from the responsivity of the polarization modules. The total power channels and the demodulated channels of the polarization modules are also determined from different calibration sources. Calibration measurements are used to create a responsivity model for each of these streams: the hybrid-Tee demodulated stream, the total power streams of the polarization modules, and the demodulated streams of the polarization modules. Ultimately, the model for the total power streams of the polarized modules will only be used to quantify the effect of amplifier bias board temperature on the demodulated stream of the polarization modules. The responsivity models for the hybrid-Tee and the demodulated stream of the polarization modules are used by the data analysis pipelines to properly normalize the data streams to an absolute temperature scale.

5.3.1 Total Power Responsivity

As described in section 2.5.4, the responsivity of all data streams (demodulated and total power of the polarization and hybrid-Tee modules) depends on the amplifier bias, which is strongly dependent on the temperature of the bias boards, such that the dominant time-varying contribution to responsivity is the enclosure temperature. The responsivity model must account for this dependence.

During the course of a mini sky-dip measurement, the modules will observe a greater column density of atmosphere (and greater sky temperature) as the telescope ranges from high to low elevation. With an atmospheric model (Ref. [72]) to determine the sky temperature, the change in sky temperature during the mini sky-dip is used to obtain total power responsivity. We perform mini sky-dips prior to each CES, yielding a large statistical sample which can be used to probe the change in the responsivity with enclosure temperature. We do not rely on knowing the sky temperature for our absolute calibration.

We fit simultaneously for the zenith temperature from Jupiter measurements and obtain coefficients of gain variation with enclosure temperature for each diode from skydip measurements. The resulting model contains the fiducial responsivity value R_0 for each diode, which represents the responsivity of the diode at the typical regulating value of $T_{enc} = 25^\circ\text{C}$ whose magnitude is calibrated to Jupiter, and the parameter α which characterizes the dependence of the responsivity on enclosure temperature. The average value of R_0 for all diodes is 2.26 mV/K, typical uncertainties from the fitting are 0.1mV/K. This is consistent with laboratory measurements of module responsivity (section 3.4). The systematic error incurred from uncertainties in these quantities will be discussed below.

5.3.2 Polarization Responsivity

The atmosphere is nearly linearly unpolarized ($\ll 1\%$, Ref. [34]), such that the atmospheric temperature, PWV, and zenith temperature do not need to be considered in the polarized gain model. In the case where the responsivities in the two legs of the module are equal, we expect that the responsivity, and also the dependence of responsivity on T_{enc} (α), to be identical between the polarization and total power streams. Because we bias the modules so that the responsivities in each leg are balanced, we can use the α values measured for the total power stream for the demodulated stream as well. This approximation has also been confirmed from laboratory testing; we monitored the response of the total power and demodulated streams while varying the enclosure temperature and found the coefficients α were consistent between the two streams.

The absolute responsivity values for the polarized data stream are obtained from the polarized calibrator Tau A for the central polarimeter. We use the relative calibration measurements of all polarimeters of the Moon to obtain scaling factors between the central polarimeter and all other polarimeters, and hence obtain absolute responsivity values for the other polarimeters. This scaling factor was confirmed with the wire-grid measurement performed once at the end of the season. The average values of R_0 (the responsivity for the demodulated stream at an enclosure temperature of 25°C) for all diodes is 2.29 mV/K with similar fitting uncertainties as the total power responsivity values for R_0 . The R_0 values are consistent with the R_0 values for the total power stream for each diode.

5.3.3 Systematic Error Assessment

The primary science channel for QUIET is the demodulated stream, the total power responsivity model functioned primarily to solve for the coefficients α , the change in responsivity with respect to enclosure temperature. Thus systematic errors are

considered for the polarized responsivity model, these are tabulated for a variety of possible effects (Ref. [24]):

- The polarization fraction of Tau A is known to 3.2% (this uncertainty is higher than the WMAP accuracy of 2.7% because there is an error associated with the additional extrapolation factor from the WMAP 40.6 GHz measurement to the QUIET central frequency $\simeq 43$ GHz (the central frequency is diode-dependent). This will give an uncertainty in the amplitude of the Tau A signal, and hence the absolute amplitude of the power spectrum.
- The maximum difference in responsivity between values obtained from measurements of the absolute calibrators, the Moon, Tau A, and the wire grid is 2%. This gives an uncertainty in the absolute amplitude of the power spectrum.
- To assess the impact of uncertainties in the beam-size, we compute the responsivity model parameters allowing the beam size to change by $\pm 1\sigma$ from the nominal value (beams are discussed in section 5.9). This would primarily effect the measured Tau A value, leading to an additional uncertainty in the absolute amplitude of the power spectrum.
- To assess the impact of uncertainties in the measured central frequency of each polarimeter, we compute the responsivity model while allowing the central frequency to change by ± 0.5 GHz (these are typical uncertainties from measurements performed in the laboratory, see section 3.2). This effects the measured Tau A amplitude, and hence the absolute magnitude of the power spectrum.
- Offsets in the enclosure temperature (the thermistors are not absolutely calibrated, so while the change in enclosure temperature is well measured, the absolute temperature of the enclosure is not) could be a concern, however we scale the absolute responsivity to the absolute calibrators (Jupiter, Tau A), so the thermistor temperature offset will have no effect.

- There could also be offsets in measurements of the PWV, but again because we determine the absolute responsivity through absolute calibrators this will not impact the model.
- To assess the impact of improperly estimating the coefficients α (responsivity dependence on enclosure temperature), a set of TODs were simulated which were seeded with random enclosure temperature fluctuations. The resulting TODs were then analyzed with a responsivity model which had no correction for enclosure temperature, and one which corrected for enclosure temperature. The systematic error between them was negligible compared to the statistical error, this is likely due to heavy FFT-filtering (discussed in section 4.4.7), which removes long time-scale drifts such as enclosure temperature.

The results are presented in Table 5.2. Because the power spectrum scales as μK^2 , errors in the absolute scaling will contribute with a factor of two to the uncertainty in the power spectrum amplitude. Systematic errors from module dependent quantities (such as bandpasses) will be upper limits as the effects will generally average down, thus the systematic error is dominated by the uncertainties in the polarization fraction of Tau A.

Systematic	Value	Power Spectrum Amplitude (μK^2)
Polarization Fraction of Tau A	3.2%	6.4%
Difference between Moon, Tau A, and the wire grid	2%	4%
Beam size error	0.4%	0.8%
Bandpass error	1%	2%

Table 5.2: Systematic errors for the responsivity model used by the maximum likelihood pipeline. Courtesy Robert Dumoulin.

5.4 Sensitivity

We use equation 3.16 (section 3.7) to compute sensitivity for each constant elevation scan using the white noise floor, computed from a Fourier transform of the

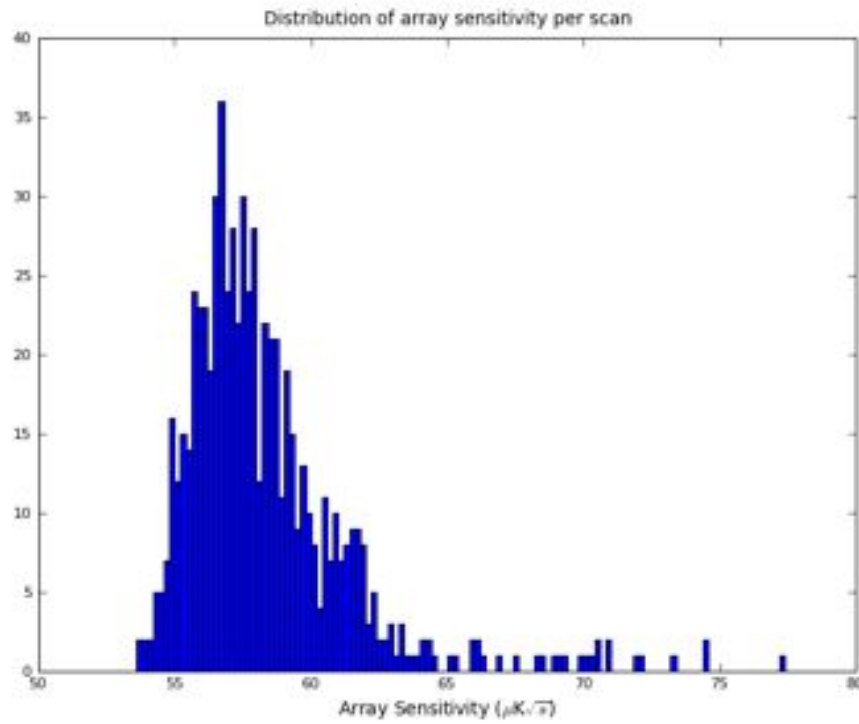


Figure 5-1: The distribution of array sensitivity for the polarization modules for all scans.

time-ordered data stream (this was first described in section 4.4.7, and an example FFT with the filtering was given in Figure 4-10) specifically from the region between 200mHz - 7.0 Hz, and the total power responsivity found from the mini sky-dip, corrected for the enclosure temperature, prior to the scan. A histogram of the array sensitivity for the polarization modules is shown in Figure 5-1. The average is $59\mu\text{K}\sqrt{s}$, as predicted from laboratory measurements in section 3.7

5.5 Pointing

The telescope mount can be slewed on three independent axes: elevation, deck rotation about boresight, and azimuth. Each axis has an encoder which measures how far the mount has slewed relative to an established zero point. To point at a source or

scan a patch, we obtain the ephemeris position of a source in azimuth and elevation, slew the telescope to that azimuth and elevation location, and the source should appear in the beam of the central polarimeter. Various non-idealities and offsets within the mount require that we create a pointing mount model to account for these offsets. These include flexure and tilting (k_f , ΔH_A , $\Delta\phi_A$, Θ_E); the offset between the boresight pointing of the receiver and the rotation axis of the telescope (Θ_c and Φ_c); and encoder offsets (E_0 , A_0 , and P_0 , ΔD) (Ref. [70]). These are described in more detail below. We do not present the full mount model here (details can be found in Ref. [8]), and just note that the mount model consists of a set of equations which use the above parameters to allow us to accurately point the boresight of the receiver beam at a target.

- k_f - Constant of flexure (degree per cosine of elevation).
- ΔH_A - The tilt of the azimuth axis in the direction of increasing hour angle.
- $\Delta\phi_A$ - The tilt of the azimuth axis in the direction of increasing latitude.
- Θ_E - The tilt of the elevation axis perpendicular to the azimuth tilt, measured clockwise around the direction of the azimuth vector.
- Θ_c - The magnitude of the collimation error, defined as the distance between the boresight of the telescope and the central polarimeter pointing.
- Φ_c - The deck angle at which the collimation error is directed radially outward.
- E_0 - The elevation encoder count at zero azimuth.
- A_0 - The azimuth encoder count at zero azimuth.
- P_0 - The deck encoder count that aligns the reference edge of the triangular platform to be horizontal. The reference edge should be chosen such that P_0 is close to zero.

- ΔD - The deck encoder offset between the deck angle and the orientation of the receiver array. This is not included in the real-time model.

We have a rough estimate of these parameters for real-time pointing of the telescope. These were obtained during commissioning specifically for the three largest contributions to the potential pointing offsets: the sag (encoded in k_f) and the collimation terms (encoded in Θ_c and Ψ_c). If the central polarimeter is not aligned with the rotation axis of the deck, the boresight of the receiver will trace a circle in the sky with radius Θ_c ('collimation offset') with a direction vector defined by Ψ_c (the angle between zenith and the central polarimeter when the deck angle is 0°) as the deck is rotated, shown in Figure 5-2. Because the pointing of the receiver changes with deck angle as a result of this pointing offset, the collimation terms are determined by the measurements at different deck angles. Deck flexure describes the elevation axis sag under gravity, which is defined such that the sag coefficient k_f is given by the difference between the encoded elevation and the receiver boresight elevation at the zenith. As a result the sag term is determined primarily by measurements at different elevations.

The rough estimate was obtained as follows: while tracking the moon we varied the real-pointing model parameters until the response of the central polarimeter was maximized, indicating the central polarimeter was centered on the moon. This resulted in the 'real-time' pointing model parameters of $\Theta_c=0.283^\circ$, $\Psi_c=-25^\circ$, and the sag coefficient is $k_f=-0.018$. Because this is clearly a rough method to determine the parameters for the live mount model, we verified this model with a set of calibration observations.

We performed 9 scans of the moon at a variety of different deck angles and elevations, creating a map of the moon with the central polarimeter for each scan. A two-dimensional gaussian function was used to fit this signal, producing the location of the center of the moon in encoder units for each scan. The difference between the encoded value where the center of the moon was detected and the ephemeris location

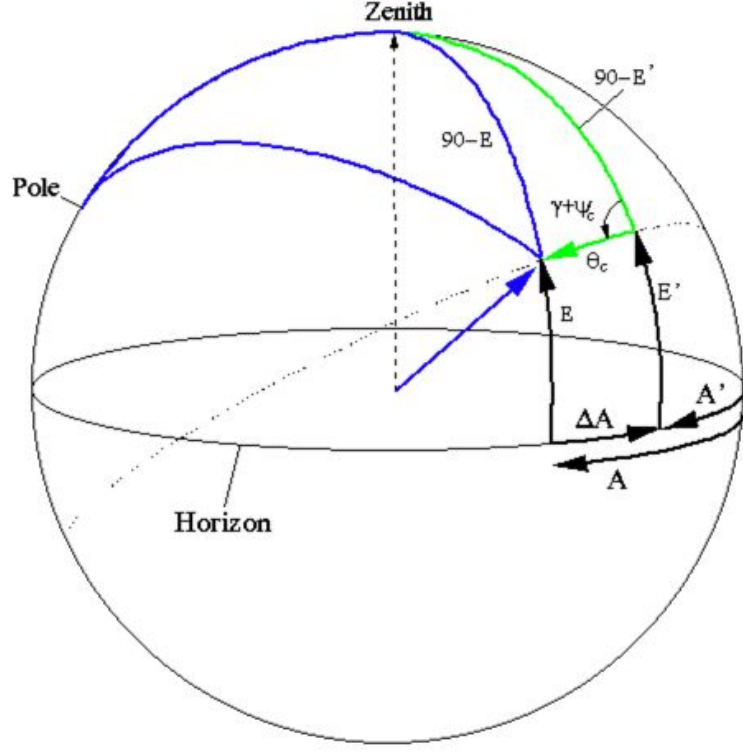


Figure 5-2: Illustration of the collimation offset parameters (Θ_c , Ψ_c). In this illustration, the mount is at the center of the sphere, the azimuth axis is denoted by A and is parallel with the horizon. The elevation axis is perpendicular to this and is denoted by E . The telescope is pointed to A' and E' at a deck angle given by γ . While the telescope is pointed at A' and E' , the source is observed by the receiver to be located at A and E . The collimation offset is then clearly seen to be the radial distance between the telescope pointing and the location where the source was observed by the receiver and the collimation angle is defined by the elevation axis. Courtesy Martin Shepherd.

of the moon gives the pointing offset.

We simultaneously fit the three mount-model parameters with nine measurements using a non-linear least squares fitting algorithm. The best-fit values are $\Theta_c = 0.268^\circ \pm 0.01^\circ$, $\Psi_c = -27.4^\circ \pm 1.8^\circ$, and $k_f = -1 \times 10^{-3} \pm 5.8 \times 10^{-4}$. The residuals between the real-time-pointing mount model used by the telescope and the best-fit values for the mount model parameters are 1.8 arcmin, less than 1/10 of our beamsize. The real-time model was deemed sufficient for use by the telescope for science observations.

Because we had started science observations slightly before the mount was verified, we kept using the mount model parameters from the rough fit, noting we incur an acceptable pointing error from doing so.

We refine the mount model parameters for the purposes of map-making, which will use the encoded values of azimuth, elevation, and deck to determine the pointing on the sky of each polarimeter in the array. The Maximum Likelihood pipeline uses Jupiter and Venus observations to fit for the mount model parameters throughout the season (the scans were described in section 5.2.1). The Jupiter observations are particularly useful for pointing because Jupiter is point-like at the Q-band beam resolution, and because the hybrid-Tee polarimeters used for Jupiter observations are located $\simeq 4^\circ$ away from the boresight, providing a larger lever arm for determining our pointing accuracy in certain mount model parameters. The current working mount model gives pointing residuals of 3.5 arcminutes, slightly larger than the pointing accuracy goal but not enough to compromise the Q-band Phase-I science goals.

Deck Encoder Slip

The deck-angle encoder was loose from the start of observations until January 28, 2009 when the situation was discovered and the encoder bolts were tightened. This caused the recorded deck position to vary such that there can be an error in the relationship between the encoder value and the true deck orientation. We quantified the magnitude of the encoder errors using moon measurements: because we scan over the moon with all polarimeters during the course of one moon calibration observations, the difference between the ephemeris position of the moon and the encoded position where each polarimeter saw the moon results in an absolute pointing for each polarimeter, and an absolute orientation of the array on the sky. This orientation can be compared to the encoded value of the deck angle. A similar analysis can be performed with the two hybrid-Tee modules using the calibration sources Venus, Jupiter, and RCW38. We found the deck angle encoder value jumped occasionally by $\lesssim 2^\circ$, as seen in Figure 5-

3, which shows the relative orientation between the array and the deck encoder. The deck angle offset between the encoded value and the position of the horns is included in the mount model as the fit parameter ΔD . The Maximum-likelihood analysis pipeline took this to be constant throughout the season, effectively ignoring the deck angle jumps. As described in the next section, systematic error assessment showed this did not bias the results.

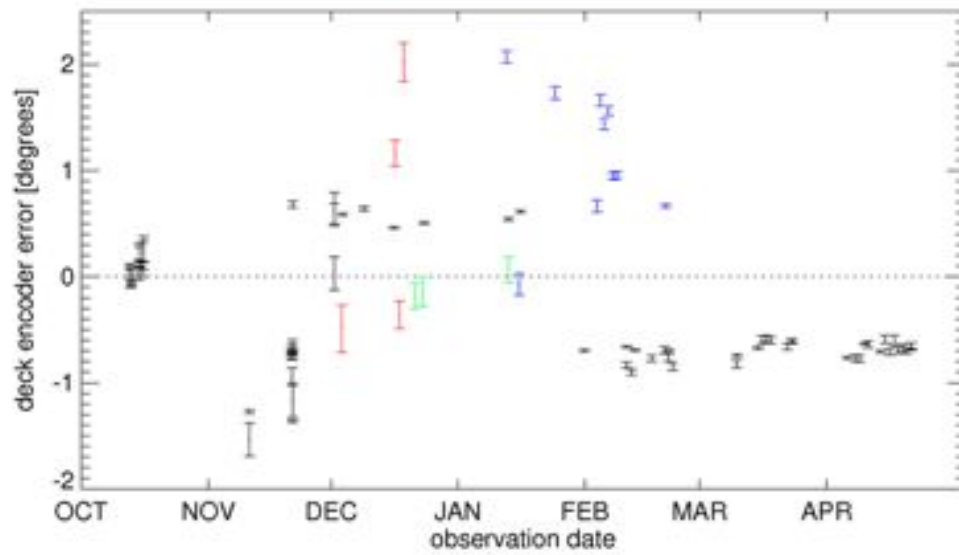


Figure 5-3: Difference between encoded deck angle and deck angle value obtained from the orientation of the outer polarimeters around the central polarimeter. The black points are from observations of the moon, red, blue and green are from observations of Jupiter, Venus, and RCW38, respectively. The deck-encoder slips can be seen from the difference between the deck angle encoder value and the array orientation (‘error’), which jump around zero until the end of January, when the problem was corrected. Courtesy Colin Bischoff.

5.5.1 Systematic Error Assessment

We assessed the systematic introduced from deck slippage by creating a simulated TOD which varies the deck angle randomly by 2° prior to January 28, and by 0.2° afterwards (Ref. [84]). We compute the angular power spectrum of the resulting

TODs, and compare it to a spectrum without these deck angle slips to quantify the effect on the final CMB angular power spectrum from the deck slippage. The QUIET noise level and scanning strategy are included in the simulated TODs. The results are included in Table 5.5; the systematic errors are 66% of the statistical errors. While this indicates the systematic is subdominant to the statistical error, additional investigations are being considered to assess whether this is a possible source of systematic bias.

5.6 Timing

The timing card in the receiver electronics enclosure obtains time-stamps from the telescope, and time stamps in the receiver data. However, the time-stamps are not necessarily aligned due to time lags from board processing. To measure the time lag between the receiver and telescope pointing, we performed azimuth slews across the moon: one a forward-going slew, the other a backward-going slew. We repeated these measurements at different slewing speeds: 1.5, 2.8, and 6 °/s; (6°/s is the slewing speed for CMB scans, the other two were chosen to be as different as possible because we were not sure of the origin of the timing lags). The methodology for this measurement is shown schematically in Figure 5-4, where $A_{Boresight}$ is the telescope azimuth encoder position at a given time, and A_{Moon} is the azimuth ephemeris position of the moon.

As the telescope performs a slew across the moon, the boresight pointing will correspond to the ephemeris location of the moon at some time stamp t . If the receiver time stamp is advanced from the telescope by Δt , then the receiver will register the moon at time stamp $t + \Delta t$. However, the telescope pointing $A_{Boresight}$ at time stamp $t + \Delta t$ will have already passed the moon, giving $A_{Boresight} - A_{Moon} > 0$ when the receiver registers the signal (this scenario is shown for a forward-going slew in the upper panel of Figure 5-4). The opposite will be true for the backward-going slew, shown in the lower panel of Figure 5-4. The difference in azimuth $A_{Boresight} - A_{Moon}$

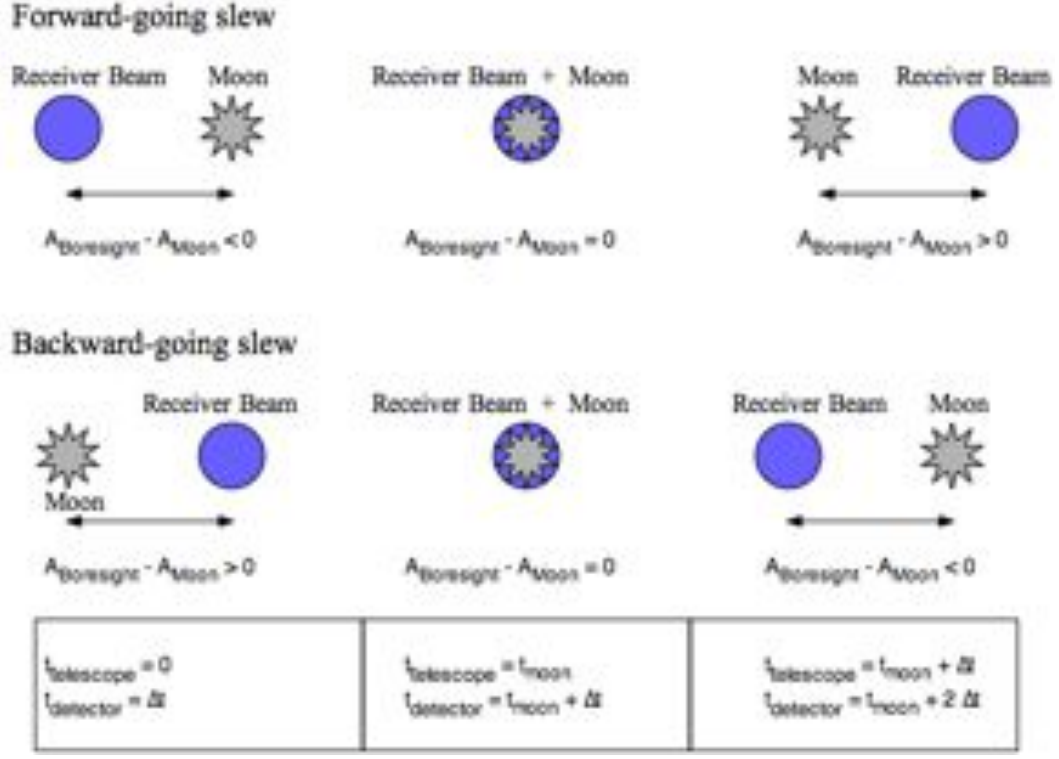


Figure 5-4: Illustration of the timing offset measurements. Shown is the receiver response for forward- and backward-going telescope slews. If the timing of the receiver is advanced relative to the telescope pointing for forward-going slews the detector diodes will observe the moon at $t_{\text{moon}} + \Delta t$; the same time stamp for the telescope encoder data will have passed the moon, giving a positive $A_{\text{Boresight}} - A_{\text{Moon}}$ pointing value. For backward-going slews, $A_{\text{Boresight}} - A_{\text{Moon}}$ will be negative.

depends on the speed of the telescope, the timing offset, and the collimation offset Θ_c , which can be expressed by equation 5.1:

$$\text{Timing Offset} = \frac{(A_{\text{Boresight}} - A_{\text{Moon}} + \Theta_c)_{\text{forward}} - (A_{\text{Boresight}} - A_{\text{Moon}} + \Theta_c)_{\text{backward}}}{\text{Telescope Slew Speed}} \quad (5.1)$$

We performed these azimuth measurements at three scanning speeds, the polarimeter response from the measurement with a slew rate of $6^\circ/\text{sec}$ is shown in

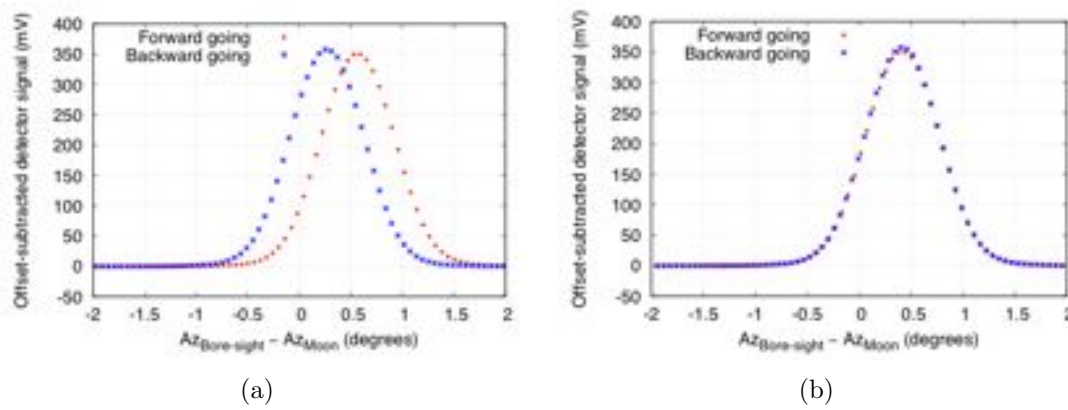


Figure 5-5: *a*: Signal measured by the central polarimeter for a scan of the moon with a scan speed of $6^\circ/\text{s}$, before timing correction, and *b*: after the timing correction. Courtesy Akito Kusaka.

Figure 5-5(a). The timing offset was measured to be $25 \text{ msec} \pm 1 \text{ msec}$. The response curve after correcting for this timing offset is shown in Figure 5-5(b). The peak of the corrected data stream is offset in azimuth from zero by about 0.5° , this is likely the effect of the collimation offset¹. We did not use this method to determine the collimation offset because measurements at many deck angles are far more accurate for this purpose.

5.7 Polarized Detector Angles

Polarized detector angles can be measured either relatively (the polarization angle relative to RQ09 diode Q1), or absolutely (their absolute value on the sky, with zenith at a deck angle of 0° as the reference axis). Polarized detector angles are measured absolutely for each diode from Moon and Tau A measurements. The wire-grid polarizer measurements can only measure the relative detector angles. We can align the average of the wiregrid angles to the average of the Tau A measurements

¹The scans were performed at an elevation of 60° , the collimation terms would offset the receiver beam from the telescope boresight by 0.52° , consistent with the observed offset of the corrected peak from zero.

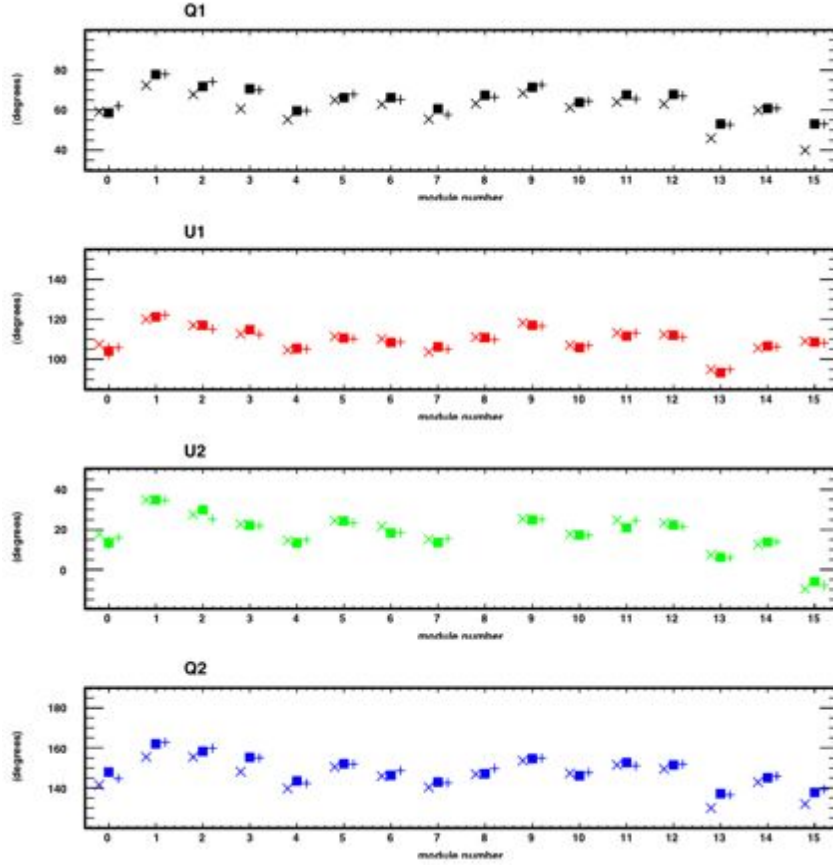


Figure 5-6: A comparison of detector angles computed from different calibration sources: the Moon (\times), Tau A (\blacksquare), and Wiregrid ($+$). Refs. [85], [18].

to use the polarized wiregrid measurements as an absolute calibration source. A comparison of the detector angles for the three calibrators is shown in Figure 5-6. There is a systematic difference in the detector angles for the Q diodes between the moon and Tau A measurements of $\simeq 4^\circ$. The statistical uncertainty in the Tau A measurements is 1° , comparable in magnitude to the accuracy to which we know the angle: 1.5° (Ref. [90]). Uncertainties in the polarization angle from the moon are 0.1° - 0.3° (Ref. [8]), thus the systematic difference between the moon and other calibration sources is larger than the statistical or systematic error of the individual measurements. This difference is not well understood but because it occurs for Q-diodes, is it likely due to leakage effects (section 5.8).

5.7.1 Systematic Error Assessment

Systematic errors were assessed between the different calibration sources by generating simulated TOD data using angles measured from Tau A and the wire grid polarizer, and then analyzing the TOD samples using the angles measured by the moon (Refs. [85], [18]). The QUIET noise level and scanning strategy are included in the simulated TODs. The resulting estimate of the effect on the power spectrum from the systematic differences in detector angles between calibration sources shows systematic errors which are 10% of the statistical errors for the EE and BB spectra at an ℓ of 300. This systematic will produce a minimum constraint QUIET can place on the tensor-to-scalar ratio of $r \simeq 0.1$.

5.8 Leakage

As discussed in section 2.2, the OMT-module system has leakage from total power to polarization; this will cause the CMB temperature signal to leak into the polarization maps. This leakage is mitigated by observing at multiple deck angles as the leakage signal will average down as the leakage map rotates with the deck. Leakage is measured for each diode with a variety of calibrators, and is expressed as a coefficient representing the amount of polarized emission a detector diode would measure from an unpolarized source.

- **The moon** We use a model developed within the collaboration (Ref. [8]) of the moon, which provides both an intensity and polarization template. Any polarization measured which is not predicted by the model is considered leakage, and from this a leakage coefficient is obtained.
- **Tau A** We adopt the WMAP (Ref. [90]) polarization fraction, angles, and the total power signal of Tau A; any additional measured polarized signal is classified as leakage.

- **Mini sky-dip** The atmosphere is nearly unpolarized ($\ll 1\%$, Ref. [34]), so any signal in the polarization channels which is modulated during the skydip is generated by leakage; the leakage value is the ratio of the polarized to total power amplitude of the skydip induced sin curve.

Because the leakage is thought to be dominated by a spike in the OMT bandpass, the contribution to the leakage from each source is likely to depend on the frequency spectrum of the source. We found that leakage coefficients measured from each calibration source are systematically different, and as shown in Figure 5-7, the leakage is in fact dependent on the spectral index of the source. The spectral index for the mini-sky dip was assumed to be dominated by the oxygen emission line, while the spectral index for the bad-weather period was assumed to be dominated by the water absorption; both spectral indices are obtained from a model. We do not use leakage obtained from bad weather in calibration, it was simply identified here for the purposes of studying the effect of spectral index on leakage. The moon is a black-body with spectral index 0, and Tau A has a falling spectrum with spectral index -2.35. Leakage values have been found to be constant over the season.

5.8.1 Systematic Error Assessment

We generated simulated TODs for each patch which are a combination of the Λ CDM power spectrum and a leakage signal. The leakage map is generated from the leakage coefficient for each diode used to leak signal from the CMB temperature anisotropy measured by WMAP (Ref. [44]). These simulations include the QUIET noise level and scan strategy. The angular power spectrum of the resulting map is computed, and compared to a power spectrum from simulated TODs without a leakage contribution. The difference between the two spectra is the systematic induced by leakage, the values were $\simeq 10\%$ and $\simeq 5\%$ of the statistical error at $\ell = 100$ for the EE and BB spectra, respectively.

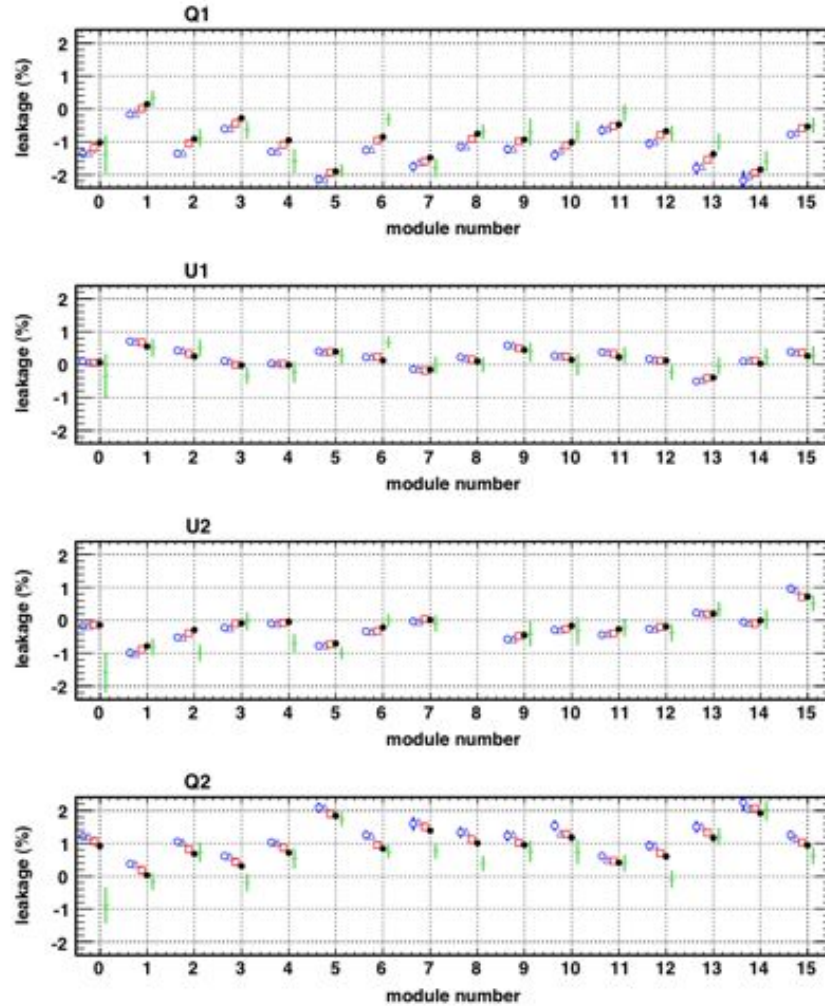


Figure 5-7: The upper panel shows a comparison of leakage coefficients as measured by a mini sky-dip (\circ), a sky-dip (\triangle), bad weather (\square), the Moon (\bullet), and Tau A ($+$), in order of spectral index for diode Q1. The other panels show the three diodes U1, U2, and Q2. The atmosphere has a spectral index which increases with frequency: $\beta > 0$. Bad weather will have a higher water vapor content, which has a gentler slope than the atmosphere. Courtesy Osamu Tajima, Ref. [18].

5.9 Beams

We use observations of Tau A and Jupiter to determine the beam profile of a given polarimeter. The beam profile gives the polarimeter response as a function of distance from the center of its beam. The radial profile is found by fitting for the center of the source and then performing a radial average in step sizes of 0.01 degrees. Tau A will yield an estimate of the polarized beam for the central polarimeter, and Jupiter will yield the same for the hybrid-Tee modules.

The beam profile creates a window function which defines the resolution of the instrument. This is transformed into spherical harmonics, and the resulting window function spectrum is convolved with the signal spectrum in the measured power spectrum, and so must be accounted for in the analysis pipelines.

5.9.1 Polarized Beams

We performed observations with the central polarimeter of Tau A every two days during the observing season (scans described in 5.2.1). The resulting $\simeq 80$ maps of Tau A can be combined (Figure 5-8) such that the final map is used to determine the beam profile of each of the four diodes in the central polarimeter. We fit a beam profile with a Hermite-polynomial, the polynomial order was explored and 18 was determined to be sufficient (for detailed description see Ref. [68]). The resulting beam profile is shown in Figure 5-9, and beam parameters are given in Table 5.3. The solid angle Ω is found by computing the Riemann sum over the 2D map (Ref. [67]). The beam profile for each diode was transformed into spherical harmonics to create a window function, shown in Figure 5-10(a). Uncertainties in the beam profile for each diode are propagated into spherical harmonics, and their comparison with the window function yields a percentage uncertainty in the window function, shown in 5-10(b).

We used the Hermite polynomial fit to create a simulated beam map, and sub-

	FWHM degrees	Solid Angle $\mu\text{Steradian}$	ellipticity %	Gain dBi	Calibrator
Q	0.448 ± 0.003	73.7	2.0 ± 0.6	52.3	Tau A
U	0.456 ± 0.004	70.4	1.0 ± 0.6	52.5	Tau A
m17/h17/Q1	0.460 ± 0.02	80.7	1.5 ± 0.3	51.9	Jupiter
m17/h17/Q2	0.456 ± 0.02	79.5	1.6 ± 0.3	52.0	Jupiter
m17/h18/Q1	0.457 ± 0.02	78.6	2.3 ± 0.3	52.0	Jupiter
m17/h18/Q2	0.457 ± 0.02	78.3	1.4 ± 0.3	52.1	Jupiter
m18/h17/Q1	0.450 ± 0.02	77.4	0.6 ± 0.3	52.1	Jupiter
m18/h17/Q2	0.453 ± 0.02	78.0	0.7 ± 0.3	52.1	Jupiter
m18/h18/Q1	0.460 ± 0.02	79.8	1.2 ± 0.3	52.0	Jupiter
m18/h18/Q2	0.460 ± 0.02	80.4	1.7 ± 0.3	51.9	Jupiter

Table 5.3: Beam parameters from Tau A and Jupiter measurements for RQ09 and RQ17,18 respectively. Jupiter measurements are denoted by module, horn, detector diode, this is described further in the text. Measurements of Jupiter use the hybrid Tee assembly, so when one horn is pointed at Jupiter, it will register in both modules attached to the hybrid Tee assembly (hence the module horn distinction). Values from Ref. [68]).

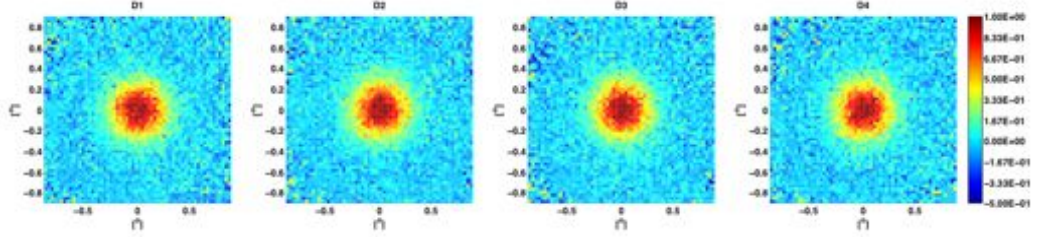


Figure 5-8: Normalized maps of Tau A for each of the four diodes in the central polarimeter with pixel size $0.03^\circ \times 0.03^\circ$. Courtesy Raul Monsalve (Ref. [67]).

tracted this from the combined map of Tau A. We found there is residual signal left in the maps which we express in low- ℓ spherical harmonics and obtain the dipole and quadrupole leakages. We discovered that the dominant leakage comes from our optics - an induced leakage of 0.31-0.35%. A full description of the methodology, including intermediate and final numbers, is given in Ref. [67]. We are currently evaluating the systematic impact this leakage has on our science goals.

We will likely use the beam profile of the central polarimeter for the beam profile of the other polarization modules; lower signal-to-noise beam maps of a few other

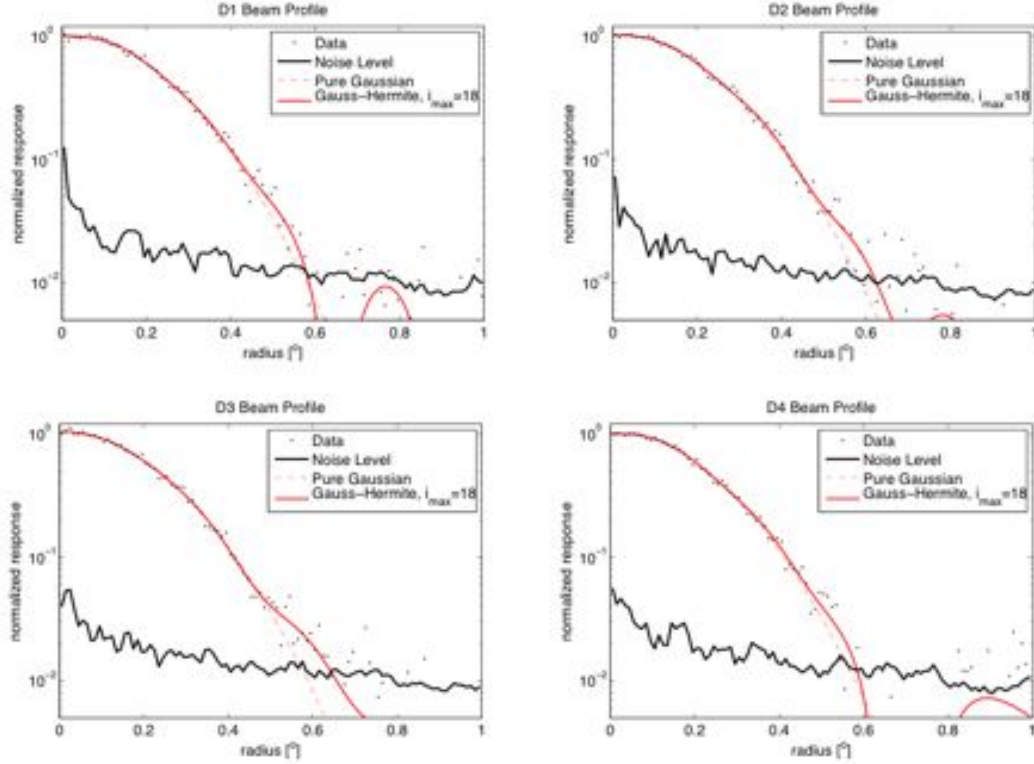


Figure 5-9: Radial beam profile for the central polarimeter, for diodes *Upper Left*: Q1, *Upper Right*: U1, *Lower Left*: U2, and *Lower Right*: Q2. This shows the comparison between the data, a purely Gaussian beam, and an 18-coefficient Hermite-polynomial fit from data with Tau A (Ref. [67]). The radial profile is computed as follows: the center of the source is fit assuming a Gaussian beam (as seen in the Gaussian fit in this figure, this is a good fit to angular distances of nearly 0.5 degrees), and a radial average is performed in steps of 0.01 degrees. The noise level is computed as the radial standard deviation: the radial average is the average of all points within a given annulus, and the noise is considered one standard deviation of these values (in practice the data is pixellated, so the average is a noise-weighted average and the standard deviation per-pixel is propagated into this radial noise). The χ^2 between the data and the polynomial fit is between 1.08-1.58, while for the Gaussian fit the χ^2 was between 1.36-1.74, depending on the diode.

polarimeters show that this is a valid approximation (Ref. [88]). Systematic errors resulting from using the beam map from the central polarimeter for all other polarimeters are currently being assessed.

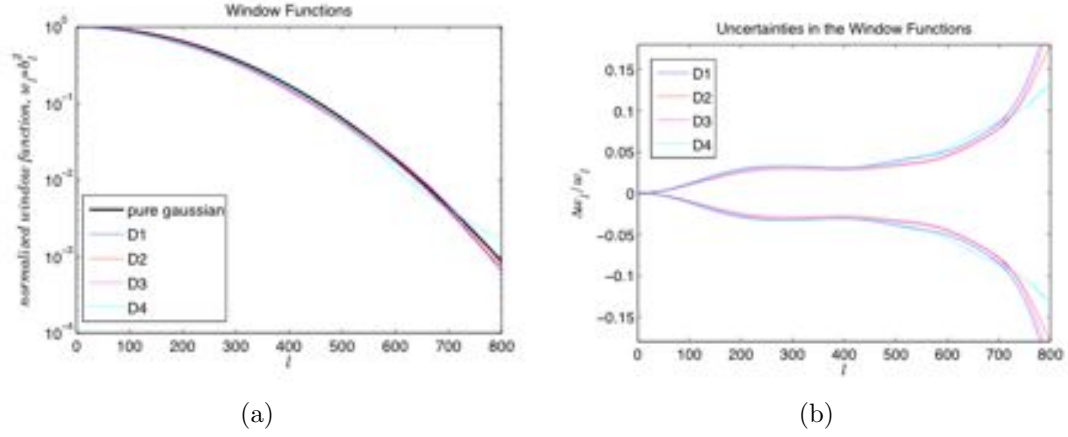


Figure 5-10: Window function in multipole moments of the four diodes in the central polarimeter from Tau A measurements of *a*: the beam and *b*: the errors in the window function from uncertainties in the beam (Ref [67]).

5.9.2 Total Power Beams

Maps of Jupiter with the hybrid-Tee modules yield beam profiles and window functions for the total power channels. Because the hybrid-Tee couples the input from two neighboring horns, observations of Jupiter with the hybrid-Tee modules yield a signal on all diodes whenever either horn is looking at Jupiter. Thus, a scan of Jupiter with both horns yields sixteen measurements: the four diodes in each module (eight diodes total) see Jupiter when one horn is observing Jupiter, and again when the second horn observes Jupiter. Because we are measuring the demodulated signal, the U diodes register null signal (as discussed in section 2.3), so the eight resulting measurements yield eight window functions. The resulting beam parameters for each of these eight combinations are given in Table 5.3, the Q diodes are consistent within a given horn and module combination, however the differences between the horns and modules are larger than the fitting errors. Because the beams measured by the hybrid-Tee modules are not used in calibration (except to determine the absolute scaling of Jupiter, which was a subdominant systematic, as discussed in section 5.3), the impact of the systematic differences between horns and modules is negligible. The eight window functions are shown in Figure 5-11(a), with uncertainties shown relative

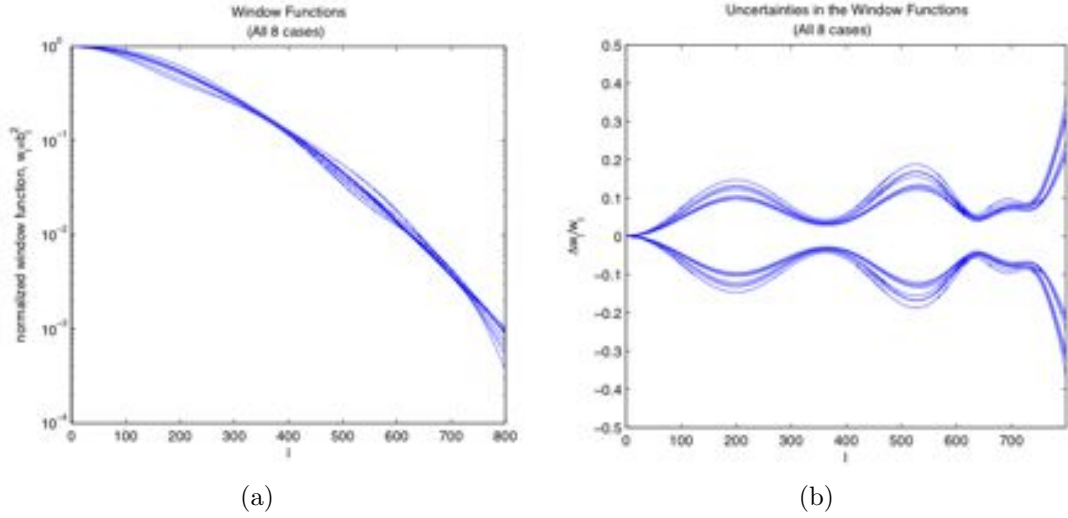


Figure 5-11: *a*: Window function of the eight diodes in the two hybrid-Tee polarimeters from Jupiter measurements from beam profile, and *b*: the uncertainties in the beam profile propagated into errors in the window function, and shown relative to the window function to give a percentage error (Ref [67]).

to the window function in Figure 5-11(b).

We expect the beam to vary across the focal plane, so the total power beam parameters as measured by the hybrid-Tees could potentially be used as beam parameters for the outer horns in the array, this is currently under discussion and has not been resolved yet.

5.9.3 Ghosting

Full-array scans of the moon showed ‘ghosting’: while one polarimeter was pointed at the moon, an adjacent polarimeter would also register a response (Figure 5-12). The magnitude of this feature was observed to be $\simeq 1\text{mK}$, which represents $\simeq 1\%$ of the polarized signal from the moon.

We believe the ghosting mechanism is the result of light from the moon reflecting off of the metal face in the feedhorn array, reflecting again off of the cryostat window, and into a nearby feedhorn. The attenuation factor for this optical path is expected

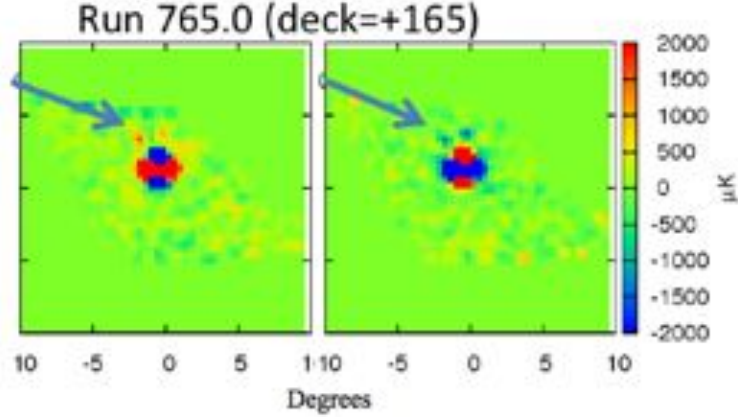


Figure 5-12: Map of the moon in RQ04. Left map is diode U1, right map is diode U2. The moon measurement is the bright spot in the center of each map, the ‘ghost’ moon is indicated by the arrow. Courtesy Akito Kusaka.

to be $\simeq 26$ dB below the main beam power (Ref. [18]), which includes the reflectivity of the window (section 2.6), and will be measured in the polarization stream through I \rightarrow Q leakage. With polarimeter leakage of $\simeq 1\%$, this gives an expected signal level of $\simeq 3$ mK, consistent with measurements of $\simeq 1$ mK.

5.9.4 Systematic Error Assessment for the Beams

The systematic error assessment for the beams includes effects from optics leakage, contamination from the sidelobes, and ghosting.

- The residual quadrupolar I \rightarrow Q leakage from the beams can create a signal which can couple to the CMB anisotropy and produce a false polarized signal. This effect is suppressed by $\mathcal{O}(\sin(2\phi))$ (where ϕ is the orientation of a given detector’s polarization axis on the sky), and an estimation of this effect (Ref. [18]) showed this to be negligibly small.
- As noted in section 2.2, we use an absorbing ground screen which absorbs radiation from the ground and other sources which could leak into the beam through sidelobe spillover. We have seen (Chapter 4) that there is some residual sidelobe

structure which has not been removed by the ground screen, causing contamination in the map when the sidelobe intercepted a bright source (the sun). An analysis of the systematic error from retaining this contaminated data was still a small fraction of the statistical error ($\simeq 0.5\%$ at ℓ of 150 and $\simeq 1\%$ at ℓ of 50 for the EE and BB spectra, respectively).

- We are currently estimating the effect of ground pick-up and ground-removal on the systematics.
- The systematic from ghosting is expected to be negligible, we plan to confirm by simulating a TOD which contains an offset ghosted polarization map.

5.10 Summary of Calibration and Systematics

5.10.1 Summary of Calibration Accuracy and Precision

The estimates for the accuracy to which we have currently characterized the instrument are summarized in Table 5.4. Refinements are underway and will appear in Ref. [18].

	Precision	Typical Value	Calibrators
Beam Size (FWHM) Ellipticity Optics I \rightarrow Q/U	<0.1 arcmin 0.6	27/12 arcmin (Q/W) <2% 0.31%-0.35%	Jupiter, Tau A
Pointing	3.5 arcmin	–	Jupiter, Venus, the Moon
Responsivity Polarization TT	7% 5%	2 mV/K 2 mV/K	Mini sky-dips, Tau A, the Moon, polarizing grid Jupiter, Venus, RCW38
Polarization Angle	$\pm 2^\circ$	–	The Moon, Tau A, polarization grid
I \leftrightarrow Q/U Leakage	$\pm 0.5\text{dB}$	-20dB / -27dB (Q/U)	Mini sky-dips, the Moon, Tau A

Table 5.4: Preliminary calibration precision for QUIET Phase I.

5.10.2 Systematics Summary

The estimates for the effect of the instrument systematics on power spectrum bias is summarized in Table 5.5.

Systematic	Value (EE) %	Value (BB) %	Reference
Deck Slippage	66 @ $\ell=350$	$\simeq 0.1$ @ $\ell=350$	Ref. [18]
Pointing Model	57 @ $\ell=350$	$\simeq 0.2$ @ $\ell=350$	Ref. [18]
Detector Angle	$\simeq 10$ @ $\ell = 300$	$\simeq 10$ @ $\ell = 300$	Ref. [18]
Leakage	$\simeq 10$ @ $\ell = 100$	$\simeq 5$ @ $\ell = 100$	Ref. [18]

Table 5.5: Maximum systematic errors, expressed as a percentage of the statistical error. Numbers are estimated from simulated power spectra. Ref. [18]. The ℓ value was chosen because it had the maximum systematic error compared to the statistical error.

Chapter 6

CMB Power Spectrum Analysis and Results With a Maximum Likelihood Pipeline

6.1 Introduction

We employ two independent analysis pipelines for CMB map-making and power spectrum estimation for the QUIET data set. This chapter addresses the Maximum-likelihood data analysis pipeline methodology, applications, and some preliminary results.

6.2 Maximum-Likelihood Method Background

The Maximum-likelihood method is a parameter-estimation algorithm based on Bayes theorem, which describes the probability distribution of a set of parameters Θ and assumptions I in a model given a data set D and an initial estimate for the likelihood of the model and parameters. This is described by the posterior, given by one form of Bayes' Theorem (see e.g Ref. [80]):

$$P(\Theta|D, I) \propto P(D|\Theta)P(\Theta|I) \quad (6.1)$$

Where $P(\Theta|D, I)$ is the posterior, $P(D|\Theta)$ is the ‘likelihood’, which describes the probability of the data given a set of parameters (generally this is what one measures), and $P(\Theta|I)$ is the ‘prior’, which encodes what one already knows about the parameters. If the prior is taken as uniform, then maximizing the likelihood will also maximize the posterior, yielding a distribution for each Θ from which one can find the most probable set of Θ to describe the data with the chosen model. The form of the likelihood depends on the model one is testing.

We use the Maximum-likelihood formalism in the Maximum-likelihood pipeline both for map-making and for power spectrum estimation.

6.3 Optimal Map Making

The Maximum-likelihood pipeline uses an “optimal” map-maker, defined by (Ref. [38]):

$$d_p = \left(P_{pt}^\dagger N_{tt'}^{-1} P_{t'p'} \right)^{-1} P_{pt}^\dagger N_{tt'}^{-1} d_{t'} \quad (6.2)$$

where $d_{t'}$ is a data point at a given time t' , d_p is the map pixel which that data point will map to, P is the pointing matrix, and $N_{tt'}^{-1}$ is the inverse of the noise-covariance matrix, which describes noise correlation between noise n at times t and t' : $N_{tt'} = \langle n(t)n(t') \rangle$. Functionally we compute the pixel-pixel covariance matrix, which is simply the first term in brackets: $N_{pp'}^{-1} = \left(P_{pt}^\dagger N_{tt'}^{-1} P_{t'p'} \right)^{-1}$. As was shown in Ref. [86], the mapmaking formalism described by equation 6.2 minimizes the residuals between the true map and the reconstructed map (known as minimum variance) and the map itself is lossless and unbiased. It is also the Maximum-likelihood estimate if

the noise is approximately Gaussian.

The pointing matrix P maps a point in the sky to a time and includes the pointing model, the polarimeter polarization angles for each detector diode, and the responsivity model. The inverse noise covariance matrix is formed from the noise model, discussed in section 4.4.7. It includes white noise diode-diode correlation coefficients (discussed in section 2.3.5), which are computed for each CES via:

$$\rho_{x,y} = \frac{\text{cov}(x,y)}{\sigma_x \sigma_y} \quad (6.3)$$

$$= \frac{\langle (x - \bar{x})(y - \bar{y}) \rangle}{\sigma_x \sigma_y} \quad (6.4)$$

$$= \frac{\langle xy \rangle - \langle x \rangle \langle y \rangle}{\sigma_x \sigma_y} \quad (6.5)$$

where x and y are the diode TODs, such that there is one correlation coefficient for each diode pair, per module, for each scan. The correlated noise between Q- and U- diodes in a single polarimeter can be in excess of 30% of the theoretical expectation. As long as this value is properly accounted for in the noise model this excess correlation has no effect on the data. The correlations do not extend to low frequencies in the $1/f$ portion of the noise power spectrum, so noise at frequencies lower than the knee frequency is modeled as uncorrelated, while noise in the white-noise regime is modeled as correlated. Implicit in the $1/f$ model is that the noise is stationary throughout one constant elevation scan such that we use one value to characterize the noise, we have found this to be a reasonable approximation in most cases. In theory, the noise covariance matrix should retain elements for all pairs of (t, t') over the entire observing season; in practice we use the noise power spectrum to determine the time interval necessary to achieve a desired accuracy in the noise matrix. We find that this is typically between 20–200 seconds.

Each CMB constant-elevation scan will produce two minimum variance maps and noise covariance matrices, one for the Stokes Q and another for the Stokes U parameters. The CES maps which pass data selection (discussed in chapter 4) are then

averaged together separately for the Q and U diodes, pixel-by-pixel, and the contribution to the final map is weighted by the noise per pixel of the submap. This yields two final maps, one for Stokes Q and one for Stokes U parameters.

Given the patch size, we are not sensitive to modes below $\ell < 25$. These modes add correlated noise to higher multipoles, but no signal, decreasing the signal-to-noise, so we remove them.

6.4 Maximum Likelihood Power Spectrum Estimation

6.4.1 Overview

The resulting map and noise covariance matrix from Maximum-likelihood map-making are used to estimate the angular power spectrum, itself using a Maximum-likelihood estimator. For the measured CMB map \mathbf{d} , we wish to solve for the true CMB signal \mathbf{s} and the signal power spectrum, encoded in a set of coefficients \mathbf{C}_ℓ . These coefficients are defined in spherical harmonics (Ref. [89], [55], discussed in Chapter 1)¹.

$$\mathbf{s} = \sum_{\ell m} a_{\ell m} Y_{\ell m} \quad (6.6)$$

$$\mathbf{a} \in \{a_{\ell m}^T, a_{\ell m}^E, a_{\ell m}^B\} \quad (6.7)$$

¹Following the notation from Chapter 1, the spin-2 nature of the polarization spherical harmonics $_{\pm 2}Y_{\ell m}$ has been absorbed into the definition of the coefficients $a_{\ell m}^E$ and $a_{\ell m}^B$.

$$C_{\ell m} C_{\ell' m'} = \langle \mathbf{a}_{\ell m} \mathbf{a}_{\ell' m'} \rangle = \mathbf{C}_\ell \delta_{\ell, \ell'} \delta_{m, m'} \quad (6.8)$$

$$\mathbf{C}_\ell = \begin{pmatrix} C_\ell^{TT} & C_\ell^{TE} & C_\ell^{TB} \\ C_\ell^{ET} & C_\ell^{EE} & C_\ell^{EB} \\ C_\ell^{BT} & C_\ell^{BE} & C_\ell^{BB} \end{pmatrix} \quad (6.9)$$

To measure the true CMB signal map \mathbf{s} and the power spectrum coefficients \mathbf{C}_ℓ , we must find:

$$P(\mathbf{s}, \mathbf{C}_\ell | \mathbf{d}) \propto P(\mathbf{d} | \mathbf{s}, \mathbf{C}_\ell) P(\mathbf{s} | \mathbf{C}_\ell) P(\mathbf{C}_\ell) \quad (6.10)$$

In this case the posterior is the first term and describes the distribution of \mathbf{s} and \mathbf{C}_ℓ given the map \mathbf{d} , the likelihood is given by the second term and describes the distribution of the data given the parameters for \mathbf{s} and \mathbf{C}_ℓ . The third term encodes the set of priors, which we take to be uniform for all parameters. The posterior takes the form (Ref. [26]):

$$P(\mathbf{s}, \mathbf{C}_\ell | \mathbf{d}) \propto e^{-\frac{1}{2}(\mathbf{d}-\mathbf{s})^\dagger N_{pp'}^{-1}(\mathbf{d}-\mathbf{s})} \prod_\ell \frac{e^{-\frac{2\ell+1}{2} \frac{\sigma_\ell}{\mathbf{C}_\ell}}}{\mathbf{C}_\ell^{\frac{2\ell+1}{2}}} \quad (6.11)$$

where $N_{pp'}^{-1}$ are elements of the pixel-pixel noise covariance matrix, and σ_ℓ is the CMB signal in harmonic space:

$$\sigma_\ell \equiv \frac{1}{2\ell+1} \sum_{m=-\ell}^{\ell} |\mathbf{a}_{\ell m}|^2 \quad (6.12)$$

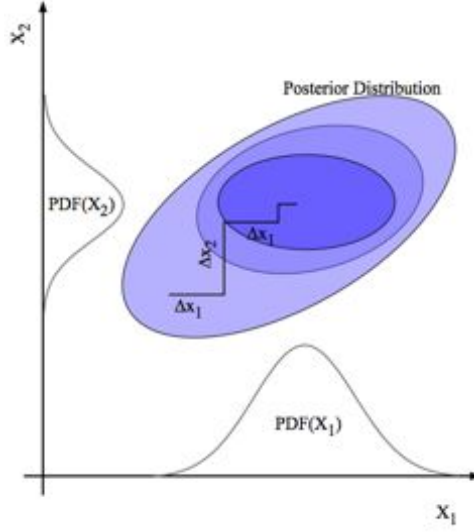


Figure 6-1: A schematic of a two-variable posterior. We sample from the probability distribution function for X_1 , and then of X_2 , iterating multiple times as the algorithm builds up the posterior for each variable.

6.4.2 Gibbs Sampling

To use the Maximum-likelihood theoretical framework for power spectrum analysis on a large data set with a complicated posterior such as the QUIET data set, we employ a Gibbs sampling routine to sample the joint signal and C_ℓ parameters (Ref. [29]). This reduces the algorithmic computation requirements from $\mathcal{O}(N_{pix}^3)$ to $\mathcal{O}(N_{pix}^2)$, where N_{pix} is the number of pixels in a map and is determined by the map resolution given by the parameter N_{side} (number of pixels per side of a map): $N_{pix} = N_{side}^2$. We use $N_{side} = 128$ when high resolution maps are not required, for example when we are testing differenced maps for consistency with null (described below, section 6.4.3) and do not need to probe power on the smallest scales. We use $N_{side}=256$ for the final power spectrum analysis.

The process of Gibbs sampling is illustrated schematically in Figure 6-1: for a joint posterior formed from two probability distribution functions of x_1 and x_2 , the likelihood is computed at an initial x_1^0 and x_2^0 value; one then chooses a new value x_1^1 for x_1 and computes the likelihood at the point (x_1^1, x_2^0) . Then a new value of the second

variable x_2 is chosen and the likelihood is computed at (x_1^1, x_2^1) , etc. A likelihood distribution is built from sampling the two different distributions iteratively. For the power spectrum estimation, we have a complicated posterior with distributions of the angular power spectrum coefficients C_ℓ and true CMB map \mathbf{s} . The sampling steps are (Ref. [26]):

$$\begin{aligned}\mathbf{s}^{i+1} &\leftarrow P(\mathbf{s}|\mathbf{C}_\ell^i, \mathbf{d}) \\ \mathbf{C}_\ell^{i+1} &\leftarrow P(\mathbf{C}_\ell|\mathbf{s}^{i+1}, \mathbf{d})\end{aligned}\tag{6.13}$$

where \leftarrow denotes sampling from a posterior, and iterates through a number of samples with index i , sampling jointly from the two distributions and computing the joint probability distribution of those parameters. There are standard techniques for defining the criteria both for choosing which points to sample next and also whether the sample is rejected or accepted (for more details see Ref. [26]). This creates a sampled distribution whose median is the Maximum-likelihood solution for \mathbf{C}_ℓ and \mathbf{s} given the data set \mathbf{d} . The width of the distribution is the error on the given parameter. Typically there is a burn-in period while the sampler algorithm probes less probable regions as it converges to sampling nearer to the center of the distribution. We only compute C_ℓ^{EE} and C_ℓ^{BB} in the matrix \mathbf{C}_ℓ .

6.4.3 Null Spectrum Testing

Before computing the angular power spectrum for the summed map, we must ensure that the data set we are using is cleaned of all artifacts such as ground pickup, weather, etc. To evaluate the quality of the data that survives the data selection criteria described in chapter 4, we split the data set in two halves based on a set of systematics which require investigation. These systematics and the resulting data splits are given in Table 6.1. From each of these data subsets, we create two maps, subtract one

map from the other to produce a ‘difference map’, and compute the power spectrum of the difference map using the same formalism used to create the angular power spectrum of the data. For example, if we are concerned about ground contamination, we can divide the data by the elevation of the sidelobe, as the maps with a low sidelobe elevations would be expected to have greater ground contamination. The signal should be removed in the difference map, leaving only noise, and the resulting power spectrum should be consistent with null power. If there are coherent artifacts which could bias the final result, they will appear as non-null bins in the power spectrum, and indicate that the data selection criteria will need to be improved. We run an extensive suite of null-tests, each designed to probe a different potential systematic error, and we do not compute the data power spectrum until all null-tests are consistent with null power.

The Maximum-likelihood power spectrum estimation algorithm is computationally intensive, so we selected a suite of 22 null tests to test the most critical systematic effects. These tests are summarized in Table 6.1, and we evaluate them for six angular-multipole bins: $25 < \ell < 75$, $75 < \ell < 125$, $125 < \ell < 175$, $175 < \ell < 225$, $225 < \ell < 275$, $275 < \ell < 325$ (with a higher N_{side} we will add an additional upper bin).

Null Test	Description	Systematic
Season	Difference First Half and Second Half of season	calibration changes with time
Tandem	Difference the first and last from the second and third quarter	calibration changes with weather
Quarter	Difference first and third from second and fourth quarters	–
Alternate	Difference alternating CESes	–
MAB 1 vs MAB 2+3	Difference Modules 0-6 from Modules 7-15	Bias and ADC Board
MAB 2 vs MAB 1+3	Difference Modules 10,11,14,15 from Modules 0-9, 12, 13	Bias and ADC Board
MAB 3 vs MAB 1+2	Difference Modules 7,8,9,12,13 from Modules 0-6, 10,11,14,15	Bias and ADC Board
Vert/Horiz Modules	Various module number splitting	–
Inner vs Outer	Difference Inner Modules (4,5,8,9,10,13,14) from Outer Modules (0-3, 6,7,11,12,15) in array	ground contamination and optics
Elevation	Difference scans above an elevation of 65° from scans below this elevation limit	ground contamination
Sidelobe	Difference scans with sidelobes pointed towards ground from sidelobes pointed at the sky	ground contamination
Sun-sidelobe distance	sun near or far from the sidelobe	sun contamination
Deck difference of 45°	deck angles 30° and 120° from 75° and 165°	detector angle calibration
Deck difference of 90°	deck angles 30° and 75° from 120° and 165°	detector angle calibration
PWV	High vs low water vapor	weather contamination
Humidity	High vs low humidity	weather contamination
Leakage	High vs low leakage modules	I→Q map contamination
Glitch1	Glitching in total power stream	glitching leakage into polarized data stream
Central Frequency	high vs low central frequency	may not be null
Enclosure Regulation	regulating vs non-regulating temperatures	Gain model
Cryogenic regulation	regulating vs non-regulating temperatures	cryogenic effects
Q/U	Q1-Q2 vs U1-U2	Noise model

Table 6.1: Maximum Likelihood null tests.

Prior to computing a null power spectrum, we can evaluate how likely a spectrum is to be null based on the characteristics of the differenced map. We compute a measure of our deviation from a signal-free, noise-dominated map as:

$$\sigma_{map} = \frac{\chi^2 - 1}{\sqrt{2N}} \quad (6.14)$$

$$(6.15)$$

where

$$\chi^2 = \frac{1}{N} \sum_p \frac{(d_p - model_p)^2}{\sigma_p^2} \quad (6.16)$$

and where d_p is the value of the map at pixel p , N is the number of degrees of freedom (N_{pix}), and σ_p is the noise computed for the p^{th} pixel from the noise model (chapter 4). $model_p$ gives a value for the pixel p from a data model; because we are testing a null hypothesis, in this case $model_p = 0$. The χ^2 is a reduced χ^2 such that a value of 1 would indicate that the variance of the difference between the data and the noise model consistent with the noise. We use the values of σ_{map} as an internal diagnostic to evaluate the properties of the differenced map, and hence how confident we are to begin the computationally intensive step of computing the angular power spectrum. Usually we choose a σ_{map} within 3σ as acceptable to proceed to angular power spectrum analysis.

Nullity Condition for the Power Spectrum

The Maximum-likelihood pipeline finds only non-negative solutions to the \mathbf{C}_ℓ spectrum. This will yield power spectra which are always positive, and yield a distribution width which does not trivially show that a given \mathbf{C}_ℓ is consistent with zero. To quantify the consistency with null power, we test the power spectrum against simulations

for each patch. The simulated data set are drawn from a null power distribution, so the data should fall within the simulation distribution to be null. The simulations are generated from the entire set of TODs for the season, removing the demodulated and total power timestreams, and using the parameters from the noise-model fit to generate a data set with identical pointing, gain, detector angles, and correlated noise as the true data set with an input CMB spectrum consistent with a Λ CDM. The resulting set of simulations should mimic the properties of the scan strategy exactly, and the differenced maps should be consistent with null. For a single CMB patch, we test consistency with null as follows:

1. For a given null test from Table 6.1, we obtain a differenced map and noise covariance matrix. We use 400 samples of the Gibbs sampler to build a \mathbf{C}_ℓ distribution for each ℓ -bin for both the EE and BB power spectra. We discard 100 samples during the burn-in period. The mean converges more quickly than the median, reliably within 400 samples, so we extract the mean and the distribution width from this distribution.
2. We repeat for the 100 simulated data sets, where the simulations contain $1/f$ noise, white noise, CMB signal, and correlated noise as described above. We then obtain a distribution of 100 mean values for each ℓ -bin representing the distribution from which our data should be drawn in the event that it is consistent with zero power.
3. The mean \mathbf{C}_ℓ value from the data is compared to the distribution mean \mathbf{C}_ℓ values from the 100 simulations via a P-test (Ref. [64]): the probability that we obtain a particular \mathbf{C}_ℓ value is given by the number of simulated data points that fall below the data \mathbf{C}_ℓ . This is shown schematically in Figure 6-2(a), where the distribution is composed of N samples and the number of samples which lie below the data \mathbf{C}_ℓ value is given by N_{below} . This creates one P value for each

ℓ -bin and each power spectrum type (EE and BB).

$$P = \frac{N_{below}}{N} \quad (6.17)$$

4. We test how consistent the data is with the simulations via a Kolmogorov-Smirnov test as follows:
 - (a) Create a cumulative histogram of P values for a single null test. Because each null test contains 6 ℓ -bins and two \mathbf{C}_ℓ spectra (EE, BB), this will be a cumulative distribution of 12 points for each null test.
 - (b) This cumulative distribution is compared against a uniform distribution. A cumulative histogram for a uniform distribution will be a line with unity slope. The largest discrepancy between the uniform cumulative histogram and the data cumulative histogram is designated a "D value". This is shown schematically in Figure 6-2(b). This gives one D value for each null test.
5. We repeat this exercise with each of the simulated data sets, so each simulation will also have a D value.
6. Then we form a distribution of the D values from the simulations, and compute a P-value test with the data, to say how probable it was that a particular D value was obtained. This is shown schematically in Figure 6-2(c). This final P-test gives us a set of probability-to-exceed (PTE) values for each null test. In this case we would like the PTE to be 50%, indicating that the distribution of data points lies in the center of the simulations.

To increase the speed of the analysis pipeline such that we can feasibly investigate the full suite of null tests, we reduced the number of pixels ($N_{side}=128$) and we chose to use a mean value estimate over the median value of the C_ℓ distribution for each

bin and null-test because it converges more quickly. For the final data analysis, the pixel numbers and the number of iterations can be changed.

6.5 Foreground Estimation

Each analysis pipeline will have to quantify and possibly remove foreground contamination. We chose the four QUIET CMB patches to have low foreground contamination based on an evaluation of the synchrotron flux from the Planck sky model in our frequency ranges (Ref. [57]) from the average RMS fluctuations within $3^\circ \times 3^\circ$ pixels for the QUIET scan strategy. The RMS values are given in Table 6.2 (Ref. [77]). This analysis was performed for patch selection only, and we used the Planck sky model instead of WMAP data because sensitive WMAP maps containing foreground emission estimates were not yet available. The two cleanest patches are expected to be 4a and 6a, followed by 2a and 7b.

Patch	Q-band (μK)		W-band (μK)	
	I	P	I	P
2a	14.19	1.05	5.48	0.1
4a	9.76	0.49	3.87	0.08
6a	4.71	0.68	1.03	0.07
7b	$\simeq 8.12$	$\simeq 1.33$	$\simeq 3.68$	$\simeq 0.14$

Table 6.2: Summary of patch foreground contamination. Values for foreground emission are taken from the Planck sky model (Ref. [57]). I is integrated (total intensity) power, and P is polarization fraction $P = \sqrt{Q^2 + U^2}$.

We can estimate the foreground contamination to our measured power spectrum with the Maximum-likelihood pipeline. To do so, we extrapolated power from measured polarized CMB maps in the K-band (Ref. [44]) to Q-band. The frequency dependence of this emission varies across the sky, so to evaluate the possible contribution from foreground emission to the angular power spectrum we will choose the range of spectral indices typically observed for synchrotron emission. Defining the power of foreground emission with frequency as $I = \nu^\beta$, the range of spectral indices

we consider are: $\beta = -2.8, -3.0, -3.2$. The power spectrum of the extrapolated foreground contamination was computed with the Maximum-likelihood pipeline, generating a distribution of C_ℓ and width. The C_ℓ value in the lowest ℓ -bin is given in Table 6.3; we present this for the lowest bin only because this is where we expect the foreground emission to peak. From this analysis, we expect to detect foreground power in patch 2a.

Spectrum	Patch	$\beta = -2.8$	$\beta = -3.0$	$\beta = -3.2$	EE amplitude
EE	2a	1.32 ± 0.37	1.01 ± 0.29	0.79 ± 0.22	8.75×10^{-2}
	4a	<0.71	<0.55	<0.43	8.75×10^{-2}
	6a	<0.29	<0.22	<0.17	8.75×10^{-2}
	7b	<0.37	<0.29	<0.22	8.75×10^{-2}
Spectrum	Patch	$\beta = -2.8$	$\beta = -3.0$	$\beta = -3.2$	BB constraint
BB	2a	0.35 ± 0.12	0.27 ± 0.09	0.21 ± 0.07	$< 1.33 \times 10^{-2}$
	4a	<0.41	<0.34	<0.26	$< 1.33 \times 10^{-2}$
	6a	<0.25	<0.20	<0.15	$< 1.33 \times 10^{-2}$
	7b	<0.41	<0.32	<0.24	$< 1.33 \times 10^{-2}$

Table 6.3: Summary of expected patch foreground contamination in the angular power spectrum for $26 < \ell < 75$ based on extrapolations from WMAP measurements in the Ka band. Units are $\frac{\ell(\ell+1)}{2\pi} C_\ell$ in μK^2 and the error is given by the width of the sampled distribution from the Maximum-likelihood pipeline angular power spectrum estimator. We expect to detect foreground power in Patch 2a. The other patches do not have contamination above the noise level of the WMAP map, and so the values given are 68% confidence limits. EE amplitude and BB constraint from Ref. [16]

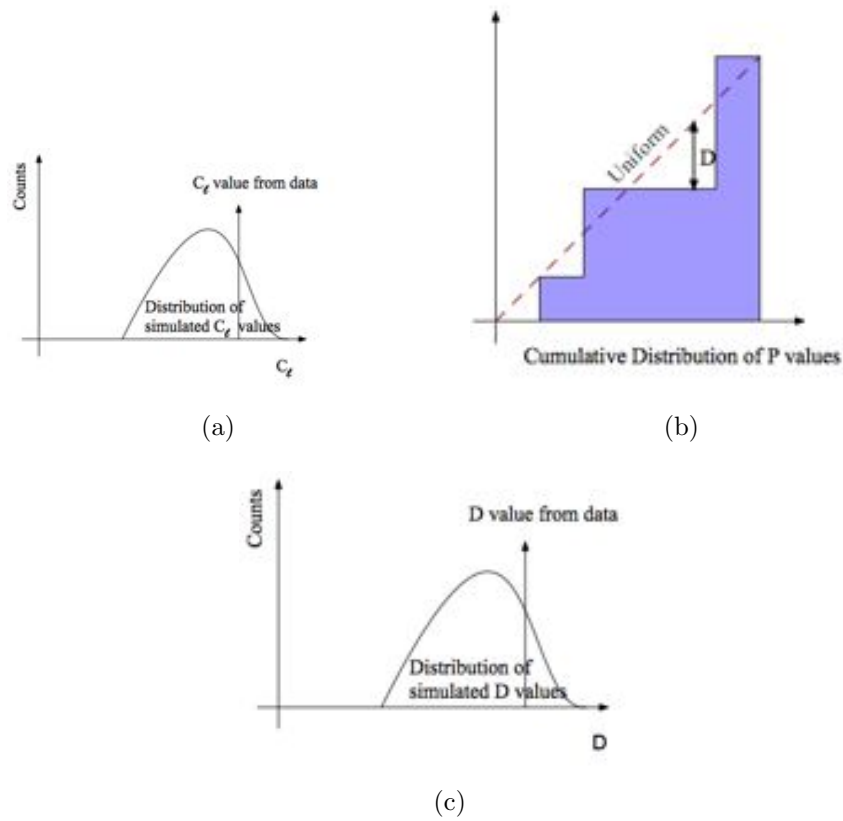


Figure 6-2: *a*: Schematic of a distribution of \mathbf{C}_ℓ values from the simulations, with the \mathbf{C}_ℓ from the data indicated. This defines a P value, which is the fraction of points below the data point. *b*: This shows the largest difference D between the cumulative distribution of P values for a null test compared to uniform. *c*: We test the D-values against simulations to quantify whether the data are consistent with null with another P-test.

6.6 Preliminary Results

6.6.1 Galactic Center

We compared polarization maps of the galactic center made from QUIET data with maps made from WMAP data (Ref. [44]), shown in Figures 6-3(a) and 6-3(b). The number of hours on the patch of sky is similar between the two maps, showing the higher quality polarization data from QUIET.

6.6.2 Null Tests

We use the Maximum-Likelihood algorithm to compute the null-maps and null-power spectra given in table 6.1. An example of a preliminary null map and power spectrum for the ‘pointel’ null test (differencing data when the elevation of the sidelobes are high from scans in which the sidelobes are at low elevations and possibly contaminated by emission from the ground) is given in Figures 6-4 and 6-5. As described in section 6.4.3, the C_ℓ value for each ℓ -bin (and for both the EE and BB spectra) is tested against a distribution of simulations, and a P-value is obtained. A cumulative histogram of these P-values for this null-test is given in Figure 6-6.

As discussed in section 6.4.3, each null-test will yield a probability to exceed. At the time of this writing, these values are not yet computed with a reliable set of simulations, we expect the results to appear in Ref. [18].

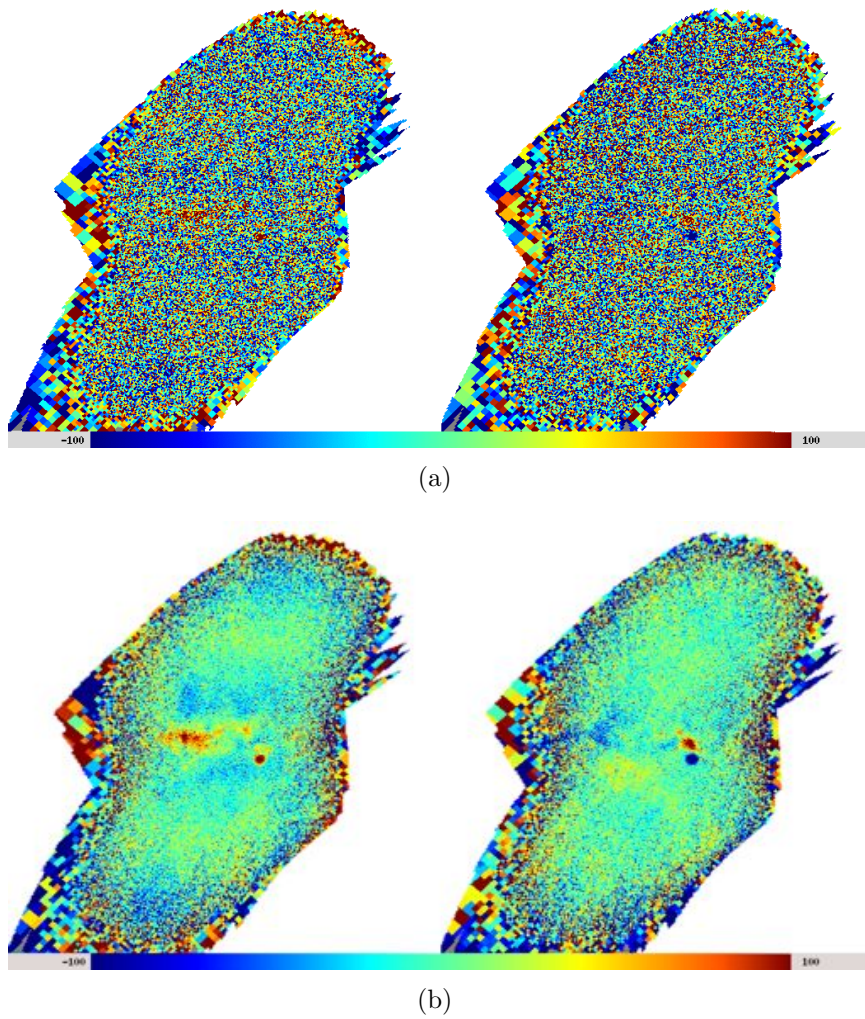


Figure 6-3: *a*: Polarized map of the Galactic center from WMAP data (Ref. [44]). *b*: The same region with QUIET Q-band data. The Stokes Q parameter map is on the left, and the Stokes U map is on the right. Units are μK , with a range of -100 to 100 μK . The pixel size is variable so that the map intensity scale is not dominated by the noise on the edges of the map.

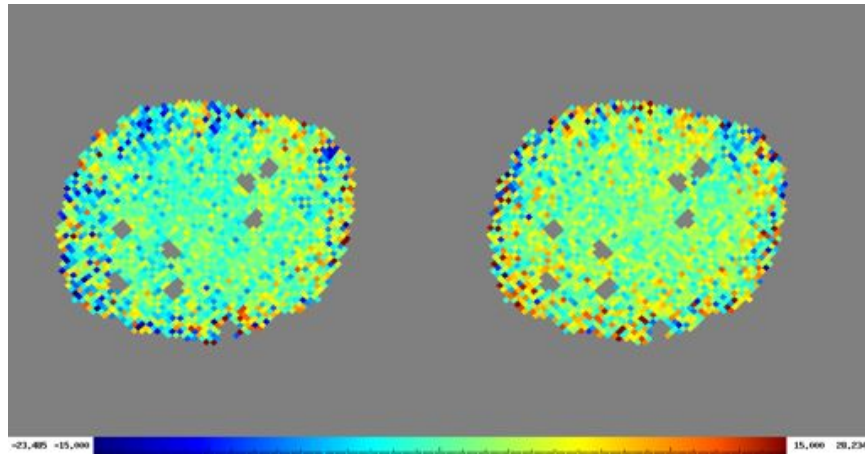


Figure 6-4: The null map of the ‘pointside’ null test for patch 2a. The map from the Q diodes is on the left and the U diodes map is on the right, with a scale of $\pm 15\mu\text{K}$. The map sigma for the combined Q and U map is 2.33σ (3σ is considered an outlier). Post-processing has removed multipoles less than 25, and the point-source mask has been applied (grey regions within the data map). The map was computed with $N_{side}=128$.

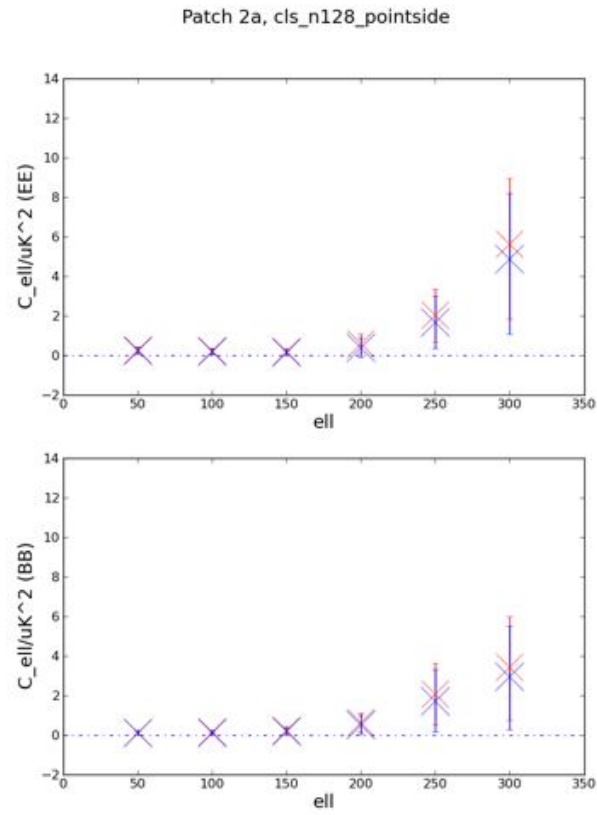


Figure 6-5: The EE and BB angular power spectrum of the ‘pointside’ null test for patch 2a. All values are within 2σ of null.

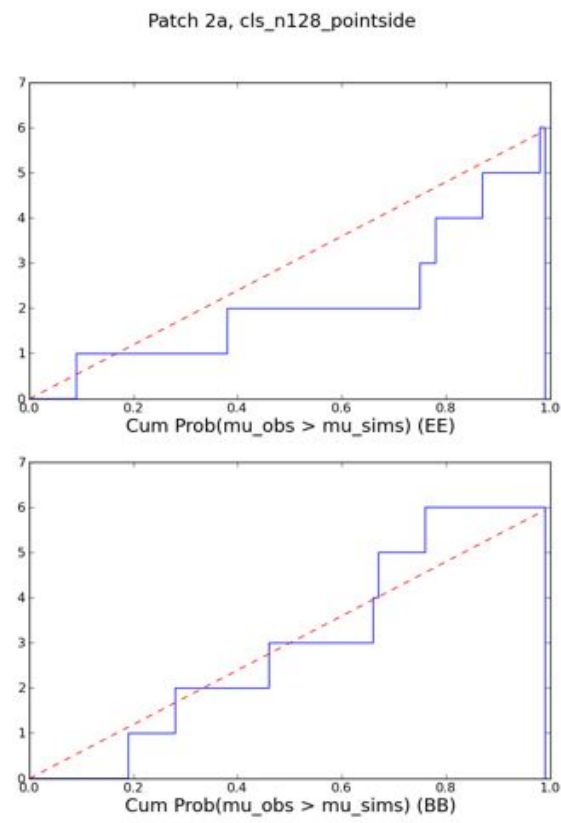


Figure 6-6: The P values for the ‘pointside’ null test.

Bibliography

- [1] P. Bannister, G. Nixon, and S. Staggs. Final Preproduction Memo for QUIET W-band OMTs. (internal memo), 2006.
- [2] D. Barkats et al. CMB Polarimetry using Correlation Receivers with the PIQUE and CAPMAP Experiments. 2005.
- [3] D. Baumann and L. McAllister. A Microscopic Limit on Gravitational Waves from D-brane Inflation. *Phys. Rev. D*, 75(12):123508–+, June 2007.
- [4] Daniel Baumann et al. CMBPol Mission Concept Study: Probing Inflation with CMB Polarization. *AIP Conf. Proc.*, 1141:10–120, 2009.
- [5] Dominic J. Benford, Michael C. Gaidis, and Jacob W. Kooi. Optical Properties of Zitex in the Infrared to Submillimeter. *Appl. Opt.*, 42(25):5118–5122, 2003.
- [6] C. L. Bennett, R. S. Hill, G. Hinshaw, M. R. Nolta, N. Odegard, L. Page, D. N. Spergel, J. L. Weiland, E. L. Wright, M. Halpern, N. Jarosik, A. Kogut, M. Limon, S. S. Meyer, G. S. Tucker, and E. Wollack. First-Year Wilkinson Microwave Anisotropy Probe (WMAP) Observations: Foreground Emission. *ApJS*, 148:97–117, 2003.
- [7] C. Bischoff, L. Hyatt, J. J. McMahon, G. W. Nixon, D. Samtleben, K. M. Smith, K. Vanderlinde, D. Barkats, P. Farese, T. Gaier, J. O. Gundersen, M. M. Hedman, S. T. Staggs, and B. Winstein. New Measurements of Fine-Scale CMB

- Polarization Power Spectra from CAPMAP at Both 40 and 90 GHz. *ArXiv e-prints*, 802, February 2008.
- [8] Colin Bischoff. Observing the Cosmic Microwave Background Polarization Anisotropy at 40 GHz with QUIET. Ph.D. Thesis, August 2010.
 - [9] S. P. Boughn, D. M. Fram, and R. B. Partridge. Isotropy of the Microwave Background at 8-millimeter Wavelength. *ApJ*, 165:439–+, May 1971.
 - [10] M. L. Brown, P. Ade, J. Bock, M. Bowden, G. Cahill, P. G. Castro, S. Church, T. Culverhouse, R. B. Friedman, K. Ganga, W. K. Gear, S. Gupta, J. Hinderks, J. Kovac, A. E. Lange, E. Leitch, S. J. Melhuish, Y. Memari, J. A. Murphy, A. Orlando, C. O’Sullivan, L. Piccirillo, C. Pryke, N. Rajguru, B. Rusholme, R. Schwarz, A. N. Taylor, K. L. Thompson, A. H. Turner, E. Y. S. Wu, M. Zemcov, and The QUaD collaboration. Improved Measurements of the Temperature and Polarization of the Cosmic Microwave Background from QUaD. *ApJ*, 705:978–999, November 2009.
 - [11] I. Buder. Type-B Glitch Correction. (internal memo), 2009.
 - [12] Immanuel Buder. Q/U Imaging Experiment (QUIET): a Ground-based Probe of Cosmic Microwave Background Polarization. volume 7741, page 77411D. SPIE, 2010.
 - [13] S. Chang and Jr. Prata, A. A Design Procedure for Classical Offset Dragonian Antennas with Circular Apertures. In *Antennas and Propagation Society International Symposium, 1999. IEEE*, volume 2, pages 1140 –1143 vol.2, aug 1999.
 - [14] Seunghyuk Chang and Jr. Prata, A. The Design of Classical Offset Dragonian Reflector Antennas with Circular Apertures. *Antennas and Propagation, IEEE Transactions on*, 52:12 – 19, 2004.

- [15] Ming-Tang Chen, Yuh-Jing Hwang, West M. Ho, Homing Jiang, Tah-Hsuing Chu, Li-Sien Wang, Sun-Nieng Hsieh, Johnson C. Han, and Malcolm M. Sinclair. Full-polarization W-band receiver for CMB detection. In Thomas G. Phillips and Jonas Zmuidzinas, editors, *Millimeter and Submillimeter Detectors for Astronomy*, volume 4855, pages 312–317. SPIE, 2003.
- [16] H. C. Chiang, P. A. R. Ade, D. Barkats, J. O. Battle, E. M. Bierman, J. J. Bock, C. D. Dowell, L. Duband, E. F. Hivon, W. L. Holzapfel, V. V. Hristov, W. C. Jones, B. G. Keating, J. M. Kovac, C. L. Kuo, A. E. Lange, E. M. Leitch, P. V. Mason, T. Matsumura, H. T. Nguyen, N. Ponthieu, C. Pryke, S. Richter, G. Rocha, C. Sheehy, Y. D. Takahashi, J. E. Tolan, and K. W. Yoon. Measurement of Cosmic Microwave Background Polarization Power Spectra from Two Years of BICEP Data. *ApJ*, 711:1123–1140, March 2010.
- [17] Yuji Chinone. Sun Side-lobe Cut. (internal memo), 2010.
- [18] QUIET Collaboration. First Results from QUIET. (In preparation).
- [19] QUIET Collaboration. First season QUIET results: Maximum Likelihood Analysis Methods. (In preparation).
- [20] QUIET Collaboration. The QUIET Instrument. (In preparation).
- [21] CTI-Cryogenics. Cryodyne Refrigeration System: Installation, Operation, and Servicing Instructions. CTI Fridge manual, —.
- [22] Clive Dickinson. Large Scale (1.4m) Beam Patterns. (internal memo), 2005.
- [23] Scott Dodelson. *Modern Cosmology*. 2003. In press.
- [24] Robert Dumoulin. (In preparation). Ph.D. Thesis, 2011.
- [25] J. Dunkley, A. Amblard, C. Baccigalupi, M. Betoule, D. Chuss, A. Cooray, J. Delabrouille, C. Dickinson, G. Dobler, J. Dotson, H. K. Eriksen, D. Finkbeiner,

- D. Fixsen, P. Fosalba, A. Fraisse, C. Hirata, A. Kogut, J. Kristiansen, C. Lawrence, A. M. Magalhães, M. A. Miville-Deschenes, S. Meyer, A. Miller, S. K. Naess, L. Page, H. V. Peiris, N. Phillips, E. Pierpaoli, G. Rocha, J. E. Vaillancourt, and L. Verde. Prospects for polarized foreground removal. In S. Dodelson, D. Baumann, A. Cooray, J. Dunkley, A. Fraisse, M. G. Jackson, A. Kogut, L. Krauss, M. Zaldarriaga, & K. Smith, editor, *American Institute of Physics Conference Series*, volume 1141 of *American Institute of Physics Conference Series*, pages 222–264, June 2009.
- [26] H. K. Eriksen, J. B. Jewell, C. Dickinson, A. J. Banday, K. M. Gorski, and C. R. Lawrence. Joint Bayesian Component Separation and CMB Power Spectrum Estimation. *ArXiv e-prints*, 709, September 2007.
- [27] J. W. Fowler et al. THE Atacama Cosmology Telescope: A First Measurement of the $600 < l < 8000$ Cosmic Microwave Background Power Spectrum at 148GHz. *ArXiv e-prints*, *arXiv:1001.2934*, January 2010.
- [28] Todd Gaier. W-band Module Document. (internal memo).
- [29] A. E. Gelfand and A. F. M. Smith. *Jour. Amer. Statist. Assn*, 85:398, 1990.
- [30] B. Gold, N. Odegard, J. L. Weiland, R. S. Hill, A. Kogut, C. L. Bennett, G. Hinshaw, X. Chen, J. Dunkley, M. Halpern, N. Jarosik, E. Komatsu, D. Larson, M. Limon, S. S. Meyer, M. R. Nolta, L. Page, K. M. Smith, D. N. Spergel, G. S. Tucker, E. Wollack, and E. L. Wright. Seven-Year Wilkinson Microwave Anisotropy Probe (WMAP) Observations: Galactic Foreground Emission. *ArXiv e-prints*, January 2010.
- [31] Paul. Goldsmith. *Quasioptical Systems: Gaussian Beam Quasioptical Propagation and Applications*. IEEE Press, 1998.
- [32] A. H. Guth. Inflationary universe: A Possible Solution to the Horizon and Flatness Problems. *Phys. Rev. D*, 23:347, 1981.

- [33] S. Hanany, P. Ade, A. Balbi, J. Bock, J. Borrill, A. Boscaleri, P. de Bernardis, P. G. Ferreira, V. V. Hristov, A. H. Jaffe, A. E. Lange, A. T. Lee, P. D. Mauskopf, C. B. Netterfield, S. Oh, E. Pascale, B. Rabii, P. L. Richards, G. F. Smoot, R. Stompor, C. D. Winant, and J. H. P. Wu. MAXIMA-1: A Measurement of the Cosmic Microwave Background Anisotropy on Angular Scales of $10'$ - 5° . *ApJ*, 545:L5–LL9, December 2000.
- [34] Shaul Hanany and Philip Rosenkranz. Polarization of the Atmosphere as a Foreground for Cosmic Microwave Background Polarization Experiments. *New Astronomy Reviews*, 47(11-12):1159 – 1165, 2003. Proceedings of the Workshop on The Cosmic Microwave Background Radiation and its Polarization.
- [35] Eugene. Hecht. *Optics, Fourth Edition*. Addison-Wesley, 2002.
- [36] G. Hinshaw, J. L. Weiland, R. S. Hill, N. Odegard, D. Larson, C. L. Bennett, J. Dunkley, B. Gold, M. R. Greason, N. Jarosik, E. Komatsu, M. R. Nolta, L. Page, D. N. Spergel, E. Wollack, M. Halpern, A. Kogut, M. Limon, S. S. Meyer, G. S. Tucker, and E. L. Wright. Five-Year Wilkinson Microwave Anisotropy Probe (WMAP) Observations: Data Processing, Sky Maps, and Basic Results. *ApJS*, 180:225–245, February 2009.
- [37] C. M. Hirata, N. Padmanabhan, U. Seljak, D. Schlegel, and J. Brinkmann. Cross-correlation of CMB with Large-Scale Structure: Weak Gravitational Lensing. *Phys. Rev. D*, 70(10):103501–+, November 2004.
- [38] E. Hivon, K. M. Górski, C. B. Netterfield, B. P. Crill, S. Prunet, and F. Hansen. MASTER of the Cosmic Microwave Background Anisotropy Power Spectrum: A Fast Method for Statistical Analysis of Large and Complex Cosmic Microwave Background Data Sets. *ApJ*, 567:2–17, March 2002.
- [39] Christian Holler. Inner Ground Screen Simulations. (internal memo), 2007.

- [40] Wayne Hu, Matthew M. Hedman, and Matias Zaldarriaga. Benchmark parameters for CMB polarization experiments. *Phys. Rev.*, D67:043004, 2003.
- [41] Wayne Hu and Martin J. White. A CMB Polarization Primer. *New Astron.*, 2:323, 1997.
- [42] W. Imbriale, C. Dickinson, and K. Thompson. QUIET: Large Scale (1.4m) W-band Optical Design. (internal memo), 2005.
- [43] John D. Jackson. *Classical Electrodynamics*. John Wiley and Son, Inc., 1999.
- [44] N. Jarosik, C. L. Bennett, J. Dunkley, B. Gold, M. R. Greason, M. Halpern, R. S. Hill, G. Hinshaw, A. Kogut, E. Komatsu, D. Larson, M. Limon, S. S. Meyer, M. R. Nolte, N. Odegard, L. Page, K. M. Smith, D. N. Spergel, G. S. Tucker, J. L. Weiland, E. Wollack, and E. L. Wright. Seven-Year Wilkinson Microwave Anisotropy Probe (WMAP) Observations: Sky Maps, Systematic Errors, and Basic Results. *ArXiv e-prints*, January 2010.
- [45] N. Jarosik, C. L. Bennett, M. Halpern, G. Hinshaw, A. Kogut, M. Limon, S. S. Meyer, L. Page, M. Pospieszalski, D. N. Spergel, G. S. Tucker, D. T. Wilkinson, E. Wollack, E. L. Wright, and Z. Zhang. Design, Implementation, and Testing of the Microwave Anisotropy Probe Radiometers. *ApJS*, 145:413–436, April 2003.
- [46] W. C. Jones, P. A. R. Ade, J. J. Bock, J. R. Bond, J. Borrill, A. Boscaleri, P. Cabella, C. R. Contaldi, B. P. Crill, P. de Bernardis, G. De Gasperis, A. de Oliveira-Costa, G. De Troia, G. di Stefano, E. Hivon, A. H. Jaffe, T. S. Kisner, A. E. Lange, C. J. MacTavish, S. Masi, P. D. Mauskopf, A. Melchiorri, T. E. Montroy, P. Natoli, C. B. Netterfield, E. Pascale, F. Piacentini, D. Pogosyan, G. Polenta, S. Prunet, S. Ricciardi, G. Romeo, J. E. Ruhl, P. Santini, M. Tegmark, M. Veneziani, and N. Vittorio. A Measurement of the Angular Power Spectrum of the CMB Temperature Anisotropy from the 2003 Flight of BOOMERANG. *ApJ*, 647:823–832, August 2006.

- [47] M. Kamionkowski, A. Kosowsky, and A. Stebbins. Statistics of Cosmic Microwave Background Polarization. *Phys. Rev. D*, 55:7368–7388, June 1997.
- [48] P. Kangaslahti, T. Gaier, M. Seiffert, S. Weinreb, D. Harding, D. Dawson, M. Soria, C. Lawrence, B. Hooberman, and A. Miller. Planar Polarimetry Receivers for Large Imaging Arrays at Q-band. In *Microwave Symposium Digest, 2006. IEEE MTT-S International*, pages 89 –92, 11-16 2006.
- [49] B Keating and E Wollack. Notes: Waveguide Hybrid Septum Polarizers. (internal memo).
- [50] Edward W. Kolb and Michael S. Turner. *The Early Universe*. Addison-Wesley, New York, NY, 1990.
- [51] E. Komatsu, K. M. Smith, J. Dunkley, C. L. Bennett, B. Gold, G. Hinshaw, N. Jarosik, D. Larson, M. R. Nolta, L. Page, D. N. Spergel, M. Halpern, R. S. Hill, A. Kogut, M. Limon, S. S. Meyer, N. Odegard, G. S. Tucker, J. L. Weiland, E. Wollack, and E. L. Wright. Seven-Year Wilkinson Microwave Anisotropy Probe (WMAP) Observations: Cosmological Interpretation. *ArXiv e-prints*, January 2010.
- [52] J. M. Kovac, E. M. Leitch, C. Pryke, J. E. Carlstrom, N. W. Halverson, and W. L. Holzapfel. Detection of polarization in the cosmic microwave background using DASI. *Nature*, 420:772–787, December 2002.
- [53] John D. Kraus. *Radio Astronomy*. Cygnus-Quasar Books, 2004.
- [54] J. Lamb. Miscellaneous Data on Material for Millimetre and Submillimetre Optics. ALMA internal memo, —.
- [55] D. L. Larson, H. K. Eriksen, B. D. Wandelt, K. M. Górski, G. Huey, J. B. Jewell, and I. J. O’Dwyer. Estimation of Polarized Power Spectra by Gibbs Sampling. *ApJ*, 656:653–660, February 2007.

- [56] C. R. Lawrence, T. C. Gaier, and M. Seiffert. Millimeter-wave MMIC cameras and the QUIET experiment. In C. M. Bradford, P. A. R. Ade, J. E. Aguirre, J. J. Bock, M. Dragovan, L. Duband, L. Earle, J. Glenn, H. Matsuhara, B. J. Naylor, H. T. Nguyen, M. Yun, & J. Zmuidzinas, editor, *Society of Photo-Optical Instrumentation Engineers (SPIE) Conference Series*, volume 5498 of *Society of Photo-Optical Instrumentation Engineers (SPIE) Conference Series*, pages 220–231, October 2004.
- [57] S. M. Leach, J. . Cardoso, C. Baccigalupi, R. B. Barreiro, M. Betoule, J. Bobin, A. Bonaldi, G. de Zotti, J. Delabrouille, C. Dickinson, H. K. Eriksen, J. González-Nuevo, F. K. Hansen, D. Herranz, M. LeJeune, M. López-Caniego, E. Martinez-González, M. Massardi, J. . Melin, M. . Miville-Deschênes, G. Patanchon, S. Prunet, S. Ricciardi, E. Salerno, J. L. Sanz, J. . Starck, F. Stivoli, V. Stolyarov, R. Stompor, and P. Vielva. Component Separation Methods for the Planck Mission. *ArXiv e-prints*, May 2008.
- [58] E. M. Leitch, J. M. Kovac, C. Pryke, J. E. Carlstrom, N. W. Halverson, W. L. Holzapfel, M. Dragovan, B. Reddall, and E. S. Sandberg. Measurement of Polarization with the Degree Angular Scale Interferometer. *Nature*, 420:763–771, December 2002.
- [59] A. R. Liddle and D. H. Lyth. *Cosmological Inflation and Large-Scale Structure*. Cambridge University Press, 2000.
- [60] Andrew R. Liddle and David H. Lyth. COBE, Gravitational Waves, Inflation and Extended Inflation. *Phys. Lett.*, B291:391–398, 1992.
- [61] Andrei D. Linde. A New Inflationary Universe Scenario: A Possible Solution of the Horizon, Flatness, Homogeneity, Isotropy and Primordial Monopole Problems. *Phys. Lett.*, B108:389–393, 1982.

- [62] M. Lueker, C. L. Reichardt, K. K. Schaffer, O. Zahn, P. A. R. Ade, K. A. Aird, B. A. Benson, L. E. Bleem, J. E. Carlstrom, C. L. Chang, H. M. Cho, T. M. Crawford, A. T. Crites, T. de Haan, M. A. Dobbs, E. M. George, N. R. Hall, N. W. Halverson, G. P. Holder, W. L. Holzapfel, J. D. Hrubes, M. Joy, R. Keisler, L. Knox, A. T. Lee, E. M. Leitch, J. J. McMahon, J. Mehl, S. S. Meyer, J. J. Mohr, T. E. Montroy, S. Padin, T. Plagge, C. Pryke, J. E. Ruhl, L. Shaw, E. Shirokoff, H. G. Spieler, Z. Staniszewski, A. A. Stark, K. Vanderlinde, J. D. Vieira, and R. Williamson. Measurements of Secondary Cosmic Microwave Background Anisotropies with the South Pole Telescope. *ArXiv e-prints*, *arXiv:0912.4317*, December 2009.
- [63] Louis. Lyons. *Statistics for Nuclear and Particle Physicists*. Cambridge University Press, 1992.
- [64] D. MacKay. *Information Theory, Inference, and Learning Algorithms*. Cambridge University Press, 2003.
- [65] J. C. Mather, E. S. Cheng, D. A. Cottingham, R. E. Eplee, D. J. Fixsen, T. Hewagama, R. B. Isaacman, K. A. Jensen, S. S. Meyer, P. D. Noerdlinger, S. M. Read, L. P. Rosen, R. A. Shafer, E. L. Wright, C. L. Bennett, N. W. Boggess, M. G. Hauser, T. Kelsall, S. H. Moseley, R. F. Silverberg, G. F. Smoot, R. Weiss, and D. T. Wilkinson. Measurement of the Cosmic Microwave Background Spectrum by the COBE FIRAS Instrument. *ApJ*, 420:439–444, January 1994.
- [66] A. D. Miller et al. A Measurement of the Angular Power Spectrum of the CMB from $\ell = 100$ to 400. *ApJ*, 524:L1, 1999.
- [67] Raul Monsalve. (In preparation). Ph.D. Thesis, 2012.

- [68] Raul A. Monsalve. Beam characterization for the QUIET Q-Band Instrument using Polarized and Unpolarized Astronomical Sources. volume 7741, page 77412M. SPIE, 2010.
- [69] Glen Nixon. OMT Measurements. (internal memo), 2008.
- [70] S. Padin, M. C. Shepherd, J. K. Cartwright, R. G. Keeney, B. S. Mason, T. J. Pearson, A. C. S. Readhead, W. A. Schaal, J. Sievers, P. S. Udomprasert, J. K. Yamasaki, W. L. Holzapfel, J. E. Carlstrom, M. Joy, S. T. Myers, and A. Otarola. The Cosmic Background Imager. *PASP*, 114:83–97, January 2002.
- [71] L. Page, C. Jackson, C. Barnes, C. Bennett, M. Halpern, G. Hinshaw, N. Jarosik, A. Kogut, M. Limon, S. S. Meyer, D. N. Spergel, G. S. Tucker, D. T. Wilkinson, E. Wollack, and E. L. Wright. The Optical Design and Characterization of the Microwave Anisotropy Probe. *ApJ*, 585:566–586, March 2003.
- [72] J. Pardo, J. Cernicharo, and E. Serabyn. Atmospheric Transmission at Microwaves (ATM): An Improved Model for Millimeter/Submillimeter Applications. In *Transactions on Antennas and Propagation, 2001. IEEE*, volume 49, pages 1683–1694, dec 2001.
- [73] David M. Pozar. *Microwave Engineering*. Addison-Wesley Publishing Company, Inc., 1993.
- [74] C. Pryke, P. Ade, J. Bock, M. Bowden, M. L. Brown, G. Cahill, P. G. Castro, S. Church, T. Culverhouse, R. Friedman, K. Ganga, W. K. Gear, S. Gupta, J. Hinderks, J. Kovac, A. E. Lange, E. Leitch, S. J. Melhuish, Y. Memari, J. A. Murphy, A. Orlando, R. Schwarz, C. O. Sullivan, L. Piccirillo, N. Rajguru, B. Rusholme, A. N. Taylor, K. L. Thompson, A. H. Turner, E. Y. S. Wu, and M. Zemcov. Second and Third Season QUaD Cosmic Microwave Background Temperature and Polarization Power Spectra. *ApJ*, 692:1247–1270, February 2009.

- [75] Britt Reichborn-Kjennerud. Building and Flying the E and B Experiment to Measure the Polarization of the Cosmic Microwave Background. Ph.D. Thesis, May 2010.
- [76] J. Ruze. Antenna Tolerance Theory—A Review. *Proc of the IEEE*, 54:633–640, 1966.
- [77] Dorothea Samtleben. Summary of Patch Selection. (internal memo), 2008.
- [78] J. L. Sievers, C. Achermann, J. R. Bond, L. Bronfman, R. Bustos, C. R. Contaldi, C. Dickinson, P. G. Ferreira, M. E. Jones, A. M. Lewis, B. S. Mason, J. May, S. T. Myers, N. Oyarce, S. Padin, T. J. Pearson, M. Pospieszalski, A. C. S. Readhead, R. Reeves, A. C. Taylor, and S. Torres. Implications of the Cosmic Background Imager Polarization Data. *ApJ*, 660:976–987, May 2007.
- [79] J. L. Sievers, B. S. Mason, L. Weintraub, C. Achermann, P. Altamirano, J. R. Bond, L. Bronfman, R. Bustos, C. Contaldi, C. Dickinson, M. E. Jones, J. May, S. T. Myers, N. Oyarce, S. Padin, T. J. Pearson, M. Pospieszalski, A. C. S. Readhead, R. Reeves, M. C. Shepherd, A. C. Taylor, and S. Torres. Cosmological Results from Five Years of 30 GHz CMB Intensity Measurements with the Cosmic Background Imager. *ArXiv e-prints*, January 2009.
- [80] D.S. Sivia. *Data Analysis: A Bayesian Tutorial (2nd Ed.)*. Oxford University Press, 2006.
- [81] Kendrick M. Smith et al. CMBPol Mission Concept Study: Gravitational Lensing. 2008.
- [82] Kendrick M. Smith and Matias Zaldarriaga. A General Solution to the E-B Mixing Problem. *Phys. Rev.*, D76:043001, 2007.
- [83] O. Tajima. Type-B Glitch Correction. (internal memo), 2009.

- [84] Osamu Tajima. Systematic Error Estimation about Deck-Encoder Slip. (internal memo), 2010.
- [85] Osamu Tajima, Colin Bischoff, and Yuji Chinone. Q-band Detector Angle Summary and Systematic Error. (internal memo), 2010.
- [86] M. Tegmark. How to Make Maps from Cosmic Microwave Background Data Without Losing Information. *ApJ*, 480:87–90, May 1997.
- [87] M. Tristram, G. Patanchon, J. F. Macías-Pérez, P. Ade, A. Amblard, R. Ansari, É. Aubourg, A. Benoît, J.-P. Bernard, A. Blanchard, J. J. Bock, F. R. Bouchet, A. Bourrachot, P. Camus, J.-F. Cardoso, F. Couchot, P. de Bernardis, J. Delabrouille, F.-X. Désert, M. Douspis, L. Dumoulin, P. Filliatre, P. Fosalba, M. Girard, Y. Giraud-Héraud, R. Gispert, L. Guglielmi, J.-C. Hamilton, S. Hanany, S. Henrot-Versillé, J. Kaplan, G. Lagache, J.-M. Lamarre, A. E. Lange, K. Madet, B. Maffei, C. Magneville, S. Masi, F. Mayet, F. Nati, O. Perdereau, S. Plaszczyński, M. Piat, N. Ponthieu, S. Prunet, C. Renault, C. Rosset, D. Santos, D. Vibert, and D. Yvon. The CMB Temperature Power Spectrum from an Improved Analysis of the Archeops Data. *A&A*, 436:785–797, June 2005.
- [88] Department of Physics University of Miami. Q-Band Central Horn Beam Analysis using Tau A. (internal memo), 2010.
- [89] B. D. Wandelt, D. L. Larson, and A. Lakshminarayanan. Global, Exact Cosmic Microwave Background Data Analysis Using Gibbs Sampling. *Phys. Rev. D*, 70(8):083511–+, October 2004.
- [90] J. L. Weiland, N. Odegard, R. S. Hill, E. Wollack, G. Hinshaw, M. R. Greason, N. Jarosik, L. Page, C. L. Bennett, J. Dunkley, B. Gold, M. Halpern, A. Kogut, E. Komatsu, D. Larson, M. Limon, S. S. Meyer, M. R. Nolte, K. M. Smith, D. N. Spergel, G. S. Tucker, and E. L. Wright. Seven-Year Wilkinson

Microwave Anisotropy Probe (WMAP) Observations: Planets and Celestial Calibration Sources. *ArXiv e-prints*, January 2010.

- [91] E. L. Wright, X. Chen, N. Odegard, C. L. Bennett, R. S. Hill, G. Hinshaw, N. Jarosik, E. Komatsu, M. R. Nolta, L. Page, D. N. Spergel, J. L. Weiland, E. Wollack, J. Dunkley, B. Gold, M. Halpern, A. Kogut, D. Larson, M. Limon, S. S. Meyer, and G. S. Tucker. Five-Year Wilkinson Microwave Anisotropy Probe (WMAP) Observations: Source Catalog. *ApJS*, 180:283–295, February 2009.
- [92] M. Zaldarriaga and U. Seljak. All-sky Analysis of Polarization in the Microwave Background. *Phys. Rev. D*, 55:1830–1840, February 1997.
- [93] Matias Zaldarriaga and Uros Seljak. Gravitational Lensing Effect on Cosmic Microwave Background Polarization. *Phys. Rev.*, D58:023003, 1998.

Appendix A

Module Signal Processing

A.1 Phase Switch Transmission Imbalance

Here we consider the action of phase switching both legs, and include the possibility that the transmission coefficient in one phase switch state is not identical to the transmission coefficient in the other state. The results are presented in section 2.3.5, the following is a derivation of those results. The phase switching Jones matrix we consider will be:

$$\begin{pmatrix} e^{i\phi_A} & 0 \\ 0 & e^{i\phi_B} \end{pmatrix} \rightarrow \begin{pmatrix} +1 & 0 \\ -\beta_A & 0 \\ 0 & +1 \\ 0 & -\beta_B \end{pmatrix} \quad (\text{A.1})$$

Before, we considered $e^{i\phi_A} = 1$ and $e^{i\phi_B} = \pm 1$. With this new expression for the phase switching matrix, we have added the following elements:

- We can phase-switch both legs, such that $e^{i\phi_A}$ has two possible states, and similarly for $e^{i\phi_B}$.
- The two phase switch states for each phase switch can have unequal transmission coefficients. Here we assume the transmission is normalized such that in one

state, a phase switch will transmit with a coefficient of 1, while in the other state it transmits with a reduced coefficient of $\beta_{A,B}$.

Thus, we have four possible combination states corresponding to: $((1,1),(1,-\beta_B),(-\beta_A,1),(-\beta_A,-\beta_B))$. Using this new Jones matrix, each diode will have one output for each of these phase switch combinations, such that the expression for the electric field on each diode (prior to rectification) is:

$$\begin{aligned}
 \begin{pmatrix} (1,1) \\ (1,-\beta_B) \\ (-\beta_A,1) \\ (-\beta_A,-\beta_B) \end{pmatrix}^{Q1} &= \frac{1}{8} \begin{pmatrix} g_Q E_L + g_B E_R \\ g_A E_L - \beta_B g_B E_R \\ \beta_A g_A E_L + g_B E_R \\ \beta_A g_A E_L - \beta_B g_B E_R \end{pmatrix} \\
 \begin{pmatrix} (1,1) \\ (1,-\beta_B) \\ (-\beta_A,1) \\ (-\beta_A,-\beta_B) \end{pmatrix}^{Q2} &= \frac{1}{8} \begin{pmatrix} g_Q E_L - g_B E_R \\ g_A E_L + \beta_B g_B E_R \\ \beta_A g_A E_L - g_B E_R \\ \beta_A g_A E_L + \beta_B g_B E_R \end{pmatrix} \\
 \begin{pmatrix} (1,1) \\ (1,-\beta_B) \\ (-\beta_A,1) \\ (-\beta_A,-\beta_B) \end{pmatrix}^{U1} &= \frac{1}{8} \begin{pmatrix} (1+i)g_Q E_L + (1-i)g_B E_R \\ (1+i)g_A E_L - (1-i)\beta_B g_B E_R \\ (1+i)\beta_A g_A E_L + (1-i)g_B E_R \\ (1+i)\beta_A g_A E_L - (1-i)\beta_B g_B E_R \end{pmatrix} \\
 \begin{pmatrix} (1,1) \\ (1,-\beta_B) \\ (-\beta_A,1) \\ (-\beta_A,-\beta_B) \end{pmatrix}^{U2} &= \frac{1}{8} \begin{pmatrix} (1+i)g_Q E_L - (1-i)g_B E_R \\ (1+i)g_A E_L + (1-i)\beta_B g_B E_R \\ (1+i)\beta_A g_A E_L - (1-i)g_B E_R \\ (1+i)\beta_A g_A E_L + (1-i)\beta_B g_B E_R \end{pmatrix}
 \end{aligned}$$

We will consider the Q1 and U1 diodes only because the final results for Q2 and U2 are identical but with opposite sign. The diodes will rectify the signal, and so for each phase switch combination state, we find:

$$\begin{pmatrix} (1, 1) \\ (1, -\beta_B) \\ (-\beta_A, 1) \\ (-\beta_A, -\beta_B) \end{pmatrix}^{Q1} = \frac{1}{8} \begin{pmatrix} g_A^2 E_L E_L^* + g_B^2 E_R E_R^* + g_A g_B (E_L E_R^* + E_R E_L^*) \\ g_A^2 E_L E_L^* + \beta_B^2 g_B^2 E_R E_R^* - \beta_B g_A g_B (E_L E_R^* + E_R E_L^*) \\ \beta_A^2 g_A^2 E_L E_L^* + g_B^2 E_R E_R^* - \beta_A g_A g_B (E_L E_R^* + E_R E_L^*) \\ \beta_A^2 g_A^2 E_L E_L^* + \beta_B^2 g_B^2 E_R E_R^* + \beta_A \beta_B g_A g_B (E_L E_R^* + E_R E_L^*) \end{pmatrix}$$

$$\begin{pmatrix} (1, 1) \\ (1, -\beta_B) \\ (-\beta_A, 1) \\ (-\beta_A, -\beta_B) \end{pmatrix}^{U1} = \frac{1}{8} \begin{pmatrix} g_A^2 E_L E_L^* + g_B^2 E_R E_R^* + i g_A g_B (E_L E_R^* - E_R E_L^*) \\ g_A^2 E_L E_L^* + \beta_B^2 g_B^2 E_R E_R^* - i \beta_B g_A g_B (E_L E_R^* - E_R E_L^*) \\ \beta_A^2 g_A^2 E_L E_L^* + g_B^2 E_R E_R^* - i \beta_A g_A g_B (E_L E_R^* - E_R E_L^*) \\ \beta_A^2 g_A^2 E_L E_L^* + \beta_B^2 g_B^2 E_R E_R^* + i \beta_A \beta_B g_A g_B (E_L E_R^* - E_R E_L^*) \end{pmatrix}$$

As discussed and outlined in section 2.3.5, we phase switch one leg at 4kHz, and difference the signals to form a demodulated stream. For an ideal module, this will produce a signal proportional to the Stokes Q parameter on the Q diodes, and Stokes U parameter on the U diodes. In that simple case, the transmission in leg A was simply 1 (so $-\beta_A = 1$) and the phase switching occurred only on leg B, specifically with $-\beta_B = -1$, and the two possible states from phase switching leg B were differenced. A similar differencing operation for this more complicated case will first hold leg A to be constant at 1, and difference the two phase switch states on leg B: $(1, 1) - (1, -\beta_B)$. Then we will hold leg A to be fixed at $-\beta_A$ and difference the two phase switch states on leg B: $(-\beta_A, 1) - (-\beta_A, -\beta_B)$. This will yield two demodulated streams (again, for simplicity we are considering only two diodes):

$$\begin{pmatrix} (1, 1) - (1, -\beta_B) \\ (-\beta_A, 1) - (-\beta_A, -\beta_B) \end{pmatrix}^{Q1} = \frac{1}{4} \begin{pmatrix} g_B^2 (1 - \beta_B^2) E_R E_R^* + g_A g_B (E_L E_R^* + E_R E_L^*) \\ g_B^2 (1 - \beta_B^2) E_R E_R^* + \beta_A g_A g_B (E_L E_R^* + E_R E_L^*) \end{pmatrix}$$

$$\begin{pmatrix} (1, 1) - (1, -\beta_B) \\ (-\beta_A, 1) - (-\beta_A, -\beta_B) \end{pmatrix}^{U1} = \frac{1}{4} \begin{pmatrix} g_B^2(1 - \beta_B^2)E_R E_R^* + i g_A g_B (E_L E_R^* - E_R E_L^*) \\ g_B^2(1 - \beta_B^2)E_R E_R^* - i \beta_A g_A g_B (E_L E_R^* - E_R E_L^*) \end{pmatrix}$$

We see that the phase switch transmission imbalance introduces leakage from total power I into polarization ($E_R E_R^*$ is proportional to I and V) in either of the A leg phase switching states (1 or β_A), and the signal we measure on the Q and U diodes is no longer simply the Stokes Q and U parameters. However, the leakage factor is identical between the two phase switch states for leg A. So if we switch the phase-switch on leg A, and difference again, we find (after substituting expressions for E_R, E_L from section 2.3.5):

$$\begin{pmatrix} Q1 : [(1, 1) - (1, -\beta_B)] - [(-\beta_A, 1) - (-\beta_A, -\beta_B)] \\ U1 : [(1, 1) - (1, -\beta_B)] - [(-\beta_A, 1) - (-\beta_A, -\beta_B)] \end{pmatrix} = \frac{1}{4} \begin{pmatrix} g_A g_B (1 + \beta_A)(1 + \beta_B)Q \\ -g_A g_B (1 + \beta_A)(1 + \beta_B)U \end{pmatrix}$$

For the full set of diodes:

$$\begin{pmatrix} Q1 \\ Q2 \\ U1 \\ U2 \end{pmatrix} = \frac{1}{4} \begin{pmatrix} g_A g_B (1 + \beta_A)(1 + \beta_B)Q \\ -g_A g_B (1 + \beta_A)(1 + \beta_B)Q \\ -g_A g_B (1 + \beta_A)(1 + \beta_B)U \\ g_A g_B (1 + \beta_A)(1 + \beta_B)U \end{pmatrix}$$

So if we switch leg A at a slower rate than leg B and difference the demodulated streams, we remove leakage terms and are left with signals proportional to the Stokes Q and U parameters measured on the Q and U diodes, respectively.

A.2 Module Systematics

Here we consider the signal resulting from a variety of imperfections in the module: complex gain and phase lags in the 180° coupler.

A.3 Signal Processing including systematics

A.3.1 No Systematics: OMT input

This was treated in the text (Section 2.3.5).

A.3.2 No Systematics: hybrid-Tee input

This was treated in the text (Section 2.3.5).

A.3.3 Complex gain: OMT input

It is typical of transistors and amplifiers to introduce phase terms to the signal, so we investigate the effects on the measured signal here. The Jones matrix incorporating complex gain is:

$$S^{amplifier} = \begin{pmatrix} g_A & 0 \\ 0 & g_B \end{pmatrix} \rightarrow \begin{pmatrix} g_A e^{i\theta_A} & 0 \\ 0 & g_B e^{i\theta_B} \end{pmatrix} = e^{i\theta_A} \begin{pmatrix} g_A & 0 \\ 0 & g_B e^{i(\theta_B - \theta_A)} \end{pmatrix} \equiv \begin{pmatrix} g_A & 0 \\ 0 & g_B e^{i\theta} \end{pmatrix}$$

Substituting this expression for the amplification Jones matrix in section 2.3.5 gives the signal prior to rectification by the diodes of the form (for each diode):

$$\begin{pmatrix} E_{Q1} \\ E_{Q2} \end{pmatrix} = \frac{1}{2\sqrt{2}} \begin{pmatrix} g_A E_L \pm g_B e^{i\theta} E_R \\ g_A E_L \mp g_B e^{i\theta} E_R \end{pmatrix}$$

$$\begin{pmatrix} E_{U1} \\ E_{U2} \end{pmatrix} = \frac{1}{4} \begin{pmatrix} (1+i)g_A E_L \pm (1-i)g_B e^{i\theta} E_R \\ (1+i)g_A E_L \pm (1-i)g_B e^{i\theta} E_R \end{pmatrix}$$

The diodes measure the rectified signal, which will have the form:

$$\begin{pmatrix} Q1 \\ Q2 \\ U1 \\ U2 \end{pmatrix} = \frac{1}{8} \begin{pmatrix} g_A^2 E_L E_L^* + g_B^2 E_R E_R^* \pm g_A g_B (E_L E_R^* e^{-i\theta} + E_R E_L^* e^{i\theta}) \\ g_A^2 E_L E_L^* + g_B^2 E_R E_R^* \mp g_A g_B (E_L E_R^* e^{-i\theta} + E_R E_L^* e^{i\theta}) \\ g_A^2 E_L E_L^* + g_B^2 E_R E_R^* \pm i g_A g_B (E_L E_R^* e^{-i\theta} - E_R E_L^* e^{i\theta}) \\ g_A^2 E_L E_L^* + g_B^2 E_R E_R^* \mp i g_A g_B (E_L E_R^* e^{-i\theta} - E_R E_L^* e^{i\theta}) \end{pmatrix}$$

Substituting values for E_R, E_L (these were given in section 2.3.5) gives:

$$\begin{pmatrix} Q1 \\ Q2 \\ U1 \\ U2 \end{pmatrix} = \frac{1}{8} \begin{pmatrix} g_A^2 \frac{I+V}{2} + g_B^2 \frac{I-V}{2} \pm g_A g_B [e^{-i\theta} (\frac{Q}{2} + i\frac{U}{2}) + e^{i\theta} (\frac{Q}{2} - i\frac{U}{2})] \\ g_A^2 \frac{I+V}{2} + g_B^2 \frac{I-V}{2} \mp g_A g_B [e^{-i\theta} (\frac{Q}{2} + i\frac{U}{2}) + e^{i\theta} (\frac{Q}{2} - i\frac{U}{2})] \\ g_A^2 \frac{I+V}{2} + g_B^2 \frac{I-V}{2} \pm i g_A g_B [e^{-i\theta} (\frac{Q}{2} + i\frac{U}{2}) - e^{i\theta} (\frac{Q}{2} - i\frac{U}{2})] \\ g_A^2 \frac{I+V}{2} + g_B^2 \frac{I-V}{2} \mp i g_A g_B [e^{-i\theta} (\frac{Q}{2} + i\frac{U}{2}) - e^{i\theta} (\frac{Q}{2} - i\frac{U}{2})] \end{pmatrix}$$

and simple substitution to trigonometric terms yields:

$$\begin{pmatrix} Q1 \\ Q2 \\ U1 \\ U2 \end{pmatrix} = \frac{1}{8} \begin{pmatrix} g_A^2 \frac{I+V}{2} + g_B^2 \frac{I-V}{2} \pm g_A g_B [Q \cos(\theta) + U \sin(\theta)] \\ g_A^2 \frac{I+V}{2} + g_B^2 \frac{I-V}{2} \mp g_A g_B [Q \cos(\theta) + U \sin(\theta)] \\ g_A^2 \frac{I+V}{2} + g_B^2 \frac{I-V}{2} \pm g_A g_B [-U \cos(\theta) + Q \sin(\theta)] \\ g_A^2 \frac{I+V}{2} + g_B^2 \frac{I-V}{2} \mp g_A g_B [-U \cos(\theta) + Q \sin(\theta)] \end{pmatrix}$$

The \pm which appears in front of terms $\propto g_A g_B$ originated from the phase switching action, where we had set $\phi = 0, 180$. When we phase switch, the signal on a given diode will change from $+$ to $-$ and back again. During signal processing, we can either add the phase switched stages together ('total power' stream), or difference them ('demodulated' stream). Averaging the two phase switch states will remove

components which change sign with the phase switch state:

$$\begin{pmatrix} Q1 \\ Q2 \end{pmatrix}^{total-power} = \begin{pmatrix} U1 \\ U2 \end{pmatrix}^{total-power} = \frac{1}{4} \begin{pmatrix} (g_A^2 + g_B^2)\frac{I}{2} + (g_A^2 - g_B^2)\frac{V}{2} \\ (g_A^2 + g_B^2)\frac{I}{2} + (g_A^2 - g_B^2)\frac{V}{2} \end{pmatrix}$$

Differencing ('demodulating') instead removes terms which are constant between the two phase switch states:

$$\begin{pmatrix} Q1 \\ Q2 \\ U1 \\ U2 \end{pmatrix}^{demodulated} = \frac{1}{4} \begin{pmatrix} g_A g_B (Q \cos(\theta) + U \sin(\theta)) \\ -g_A g_B (Q \cos(\theta) + U \sin(\theta)) \\ -g_A g_B (U \cos(\theta) - Q \sin(\theta)) \\ g_A g_B (U \cos(\theta) - Q \sin(\theta)) \end{pmatrix}$$

The effects of complex gain, where the induced phase lag is parametrized by θ , can be summarized as:

- The total power (averaged) signal is unchanged from the nominal case with only real gain.
- The demodulated (differenced) signal contains a contribution from leakage between Q and U which is proportional to $\sin(\theta)$.

A.3.4 Complex gain: Hybrid-Tee input

A complex gain will effect the measurements of the hybrid-Tee as well. Because this effect comes from the module, the only difference from the treatment in section A.3.3 is in the input from the hybrid-Tee. The Jones matrices for complex gain are:

$$\begin{pmatrix} E_{Q1} \\ E_{Q2} \end{pmatrix} = \frac{1}{2\sqrt{2}} \begin{pmatrix} g_A E_A \pm g_B e^{i\theta} E_B \\ g_A E_A \mp g_B e^{i\theta} E_B \end{pmatrix}$$

$$\begin{pmatrix} E_{U1} \\ E_{U2} \end{pmatrix} = \frac{1}{4} \begin{pmatrix} (1+i)g_A E_A \pm (1-i)g_B e^{i\theta} E_B \\ (1+i)g_A E_A \pm (1-i)g_B e^{i\theta} E_B \end{pmatrix}$$

The E_A and E_B are now inputs from the hybrid-Tees (these were given in section 2.3.5), and the coefficients are real and we are considering the phases equal between the two states, so we will anticipate that the exponential terms which denote wave propagation will be removed when we rectify the signal, so:

$$E_A = E_A^* = E_{y,1} + E_{x,2} \quad (\text{A.2})$$

$$E_B = E_B^* = E_{y,1} - E_{x,2} \quad (\text{A.3})$$

$$(\text{A.4})$$

Substituting the complex gain Jones matrix into the expression given in section 2.3.5, the input from the hybrid-Tee, and rectifying the signal (squaring it) yields:

$$\begin{pmatrix} Q1 \\ Q2 \\ U1 \\ U2 \end{pmatrix} \stackrel{\text{hybrid-Tee}}{=} \frac{1}{4} \begin{pmatrix} (g_A^2 + g_B^2)(|E_{y,1}|^2 + |E_{x,2}|^2) \pm g_A g_B (|E_{y,1}|^2 - |E_{x,2}|^2) \cos(\theta) \\ (g_A^2 + g_B^2)(|E_{y,1}|^2 + |E_{x,2}|^2) \mp g_A g_B (|E_{y,1}|^2 - |E_{x,2}|^2) \cos(\theta) \\ (g_A^2 + g_B^2)(|E_{y,1}|^2 + |E_{x,2}|^2) \pm g_A g_B (|E_{y,1}|^2 - |E_{x,2}|^2) \sin(\theta) \\ (g_A^2 + g_B^2)(|E_{y,1}|^2 + |E_{x,2}|^2) \mp g_A g_B (|E_{y,1}|^2 - |E_{x,2}|^2) \sin(\theta) \end{pmatrix}$$

The \pm which appears in front of terms like $g_A g_B$ originated from the phase switching action, where we had set $\phi = 0, 180$. When we phase switch, the signal on a given diode will change from $+$ to $-$ and back again. During signal processing, we can either add the phase switched stages together ('total power' stream), or difference them ('demodulated' stream). Averaging the two phase-switch states will remove components which change sign with the phase switch state:

$$\begin{pmatrix} Q1 \\ Q2 \\ U1 \\ U2 \end{pmatrix}^{total-power, hybrid-Tee} = \frac{1}{4} \begin{pmatrix} (g_A^2 + g_B^2)(|E_{y,1}|^2 + |E_{x,2}|^2) \\ (g_A^2 + g_B^2)(|E_{y,1}|^2 + |E_{x,2}|^2) \\ (g_A^2 + g_B^2)(|E_{y,1}|^2 + |E_{x,2}|^2) \\ (g_A^2 + g_B^2)(|E_{y,1}|^2 + |E_{x,2}|^2) \end{pmatrix} \quad (A.5)$$

Differencing (‘demodulating’) instead removes terms which are constant between the two phase-switch states:

$$\begin{pmatrix} Q1 \\ Q2 \\ U1 \\ U2 \end{pmatrix}^{demodulated, hybrid-Tee} = \frac{1}{4} \begin{pmatrix} g_A g_B (|E_{y,1}|^2 - |E_{x,2}|^2) \cos(\theta) \\ -g_A g_B (|E_{y,1}|^2 - |E_{x,2}|^2) \cos(\theta) \\ g_A g_B (|E_{y,1}|^2 - |E_{x,2}|^2) \sin(\theta) \\ -g_A g_B (|E_{y,1}|^2 - |E_{x,2}|^2) \sin(\theta) \end{pmatrix} \quad (A.6)$$

The total power signal is the same as though there was no complex gain, but introduces an additional term to the Q-diodes in the demodulated signal, and causes a non-zero demodulated signal to be measured on the U-diodes. The phase introduced by the amplifiers could be computed via: $\tan \theta = \frac{U}{Q}$.

A.3.5 Imperfect coupling within the Hybrid-Tee

The hybrid-Tee could introduce a phase lag between the coupled legs (recall: its two output ports are the sum and difference of the two horns). The module is assumed to have no systematics (no complex gain, etc), and the only effect is to add a phase lag on the $E_{x,1}$ polarization state.

The E_A and E_B are now inputs from the hybrid-Tees (these were given in section 2.3.5):

$$E_A = E_{y,1} + E_{x,2}e^{i\theta} \quad (\text{A.7})$$

$$E_A^* = E_{y,1}^* + E_{x,2}e^{-i\theta} \quad (\text{A.8})$$

$$E_B = E_{y,1} - E_{x,2}e^{i\theta} \quad (\text{A.9})$$

$$E_B^* = E_{y,1}^* - E_{x,2}e^{-i\theta} \quad (\text{A.10})$$

$$(\text{A.11})$$

Using the Jones matrices defined in section 2.3.5 and the new input from the hybrid-Tee, and rectifying the signal (squaring it) yields:

$$\begin{pmatrix} Q1 \\ Q2 \\ U1 \\ U2 \end{pmatrix}^{hybrid-Tee} = \frac{1}{8} \begin{pmatrix} g_A^2 E_L E_L^* + g_B^2 E_R E_R^* \pm g_A g_B (E_L E_R^* + E_R E_L^*) \\ g_A^2 E_L E_L^* + g_B^2 E_R E_R^* \mp g_A g_B (E_L E_R^* + E_R E_L^*) \\ g_A^2 E_L E_L^* + g_B^2 E_R E_R^* \pm 2i g_A g_B (E_L E_R^* - E_R E_L^*) \\ g_A^2 E_L E_L^* + g_B^2 E_R E_R^* \mp 2i g_A g_B (E_L E_R^* - E_R E_L^*) \end{pmatrix}$$

$E_L E_L^* = E_R E_R^* = |E_x|^2 + |E_y|^2$, $E_L E_R^* = |E_y|^2 - |E_x|^2 + E_x E_y (e^{i\theta} - e^{-i\theta})$, and $E_L^* E_R = |E_y|^2 - |E_x|^2 + E_x E_y (-e^{i\theta} + e^{-i\theta})$. Thus, the final expression for the hybrid-Tee with a phase lag on one of the input polarization states is:

$$\begin{pmatrix} Q1 \\ Q2 \\ U1 \\ U2 \end{pmatrix}^{hybrid-Tee} = \frac{1}{4} \begin{pmatrix} (g_A^2 + g_B^2)(|E_{y,1}|^2 + |E_{x,2}|^2) \pm g_A g_B (|E_{y,1}|^2 - |E_{x,2}|^2) \\ (g_A^2 + g_B^2)(|E_{y,1}|^2 + |E_{x,2}|^2) \mp g_A g_B (|E_{y,1}|^2 - |E_{x,2}|^2) \\ (g_A^2 + g_B^2)(|E_{y,1}|^2 + |E_{x,2}|^2) \mp g_A g_B (E_{y,1} E_{x,2}) \sin(\theta) \\ (g_A^2 + g_B^2)(|E_{y,1}|^2 + |E_{x,2}|^2) \pm g_A g_B (E_{y,1} E_{x,2}) \sin(\theta) \end{pmatrix}$$

The \pm which appears in front of terms $\propto g_A g_B$ originated from the phase switching action, where we had set $\phi = 0, 180$. When we phase switch, the signal on a given

diode will change from $+$ to $-$ and back again. During signal processing, we can either add the phase switched stages together (‘total power’ stream), or difference them (‘demodulated’ stream). Averaging the two phase switch states will remove components which change sign with the phase switch state:

$$\begin{pmatrix} Q1 \\ Q2 \\ U1 \\ U2 \end{pmatrix}^{total-power, hybrid-Tee} = \frac{1}{4} \begin{pmatrix} (g_A^2 + g_B^2)(|E_{y,1}|^2 + |E_{x,2}|^2) \\ (g_A^2 + g_B^2)(|E_{y,1}|^2 + |E_{x,2}|^2) \\ (g_A^2 + g_B^2)(|E_{y,1}|^2 + |E_{x,2}|^2) \\ (g_A^2 + g_B^2)(|E_{y,1}|^2 + |E_{x,2}|^2) \end{pmatrix} \quad (\text{A.12})$$

Differencing (‘demodulating’) instead removes terms which are constant between the two phase switch states:

$$\begin{pmatrix} Q1 \\ Q2 \\ U1 \\ U2 \end{pmatrix}^{demodulated, hybrid-Tee} = \frac{1}{4} \begin{pmatrix} g_A g_B (|E_{x,2}|^2 - |E_{y,1}|^2) \\ -g_A g_B (|E_{x,2}|^2 - |E_{y,1}|^2) \\ -g_A g_B (E_{y,1} E_{x,2}) \sin(\theta) \\ g_A g_B (E_{y,1} E_{x,2}) \sin(\theta) \end{pmatrix} \quad (\text{A.13})$$

- The total power signal is unchanged relative to the no-lag case
- The demodulated signal will have an identical Q diode signal as a no-lag case
- It adds a small signal on the U diodes.

A.3.6 Phase lag in 180° coupler at *input*: OMT input

This is identical to the case of complex gain (section A.3.3), as it introduces a phase factor on both legs. This can be seen directly from the pre-rectified output matrix of Jones vectors for this phase lag:

$$\begin{pmatrix} E_{Q1} \\ E_{Q2} \end{pmatrix} = \frac{1}{2\sqrt{2}} \begin{pmatrix} g_A E_L \pm g_B e^{i\theta} E_R \\ g_A E_L \mp g_B e^{i\theta} E_R \end{pmatrix}$$

$$\begin{pmatrix} E_{U1} \\ E_{U2} \end{pmatrix} = \frac{1}{4} \begin{pmatrix} (1+i)g_A E_L \pm (1-i)g_B e^{i\theta} E_R \\ (1+i)g_A E_L \pm (1-i)g_B e^{i\theta} E_R \end{pmatrix}$$

Which is identical to the complex gain case.

A.3.7 Phase lag in 180° coupler at input: Hybrid-Tee input

This would be introduced by (for example) one of the Schiffman phase delay lines having a slightly longer or shorter delay structure than is ideal. Formally this is identical to the case of complex gain (section A.3.4), as it introduces a phase factor on only one leg (this was demonstrated above for the OMT case in section A.3.6).

A.3.8 Phase lag in the branchline coupler of the 180° coupler: OMT input

The coupler could also add a phase lag to (for example) only the portion of the signal which traverses the additional leg in the branchline coupler (described in section 2.3.2). The Jones matrix for this lag is given by:

$$S^{180^\circ} = \frac{1}{\sqrt{2}} \begin{pmatrix} 1 & 1 \\ 1 & -1 \end{pmatrix} \rightarrow \frac{1}{\sqrt{2}} \begin{pmatrix} e^{i\theta} & 1 \\ 1 & -e^{i\theta} \end{pmatrix} \quad (\text{A.14})$$

Substituting this expression for the 180° coupler Jones matrix in section 2.3.5 gives the signal prior to rectification by the diodes with the form:

$$\begin{pmatrix} E_{Q1} \\ E_{Q2} \end{pmatrix} = \frac{1}{2\sqrt{2}} \begin{pmatrix} g_A e^{i\theta} & \pm g_B \\ g_A & \mp g_B e^{i\theta} \end{pmatrix} \begin{pmatrix} E_A \\ E_B \end{pmatrix}^{in}$$

$$\begin{pmatrix} E_{U1} \\ E_{U2} \end{pmatrix} = \frac{1}{4} \begin{pmatrix} g_A e^{i\theta}(1+i) & \pm g_B(1-i) \\ g_A(1+i) & \mp g_B e^{i\theta}(1-i) \end{pmatrix} \begin{pmatrix} E_A \\ E_B \end{pmatrix}^{in}$$

The diodes measure the rectified signal, which will have the form:

$$\begin{pmatrix} Q1 \\ Q2 \\ U1 \\ U2 \end{pmatrix} = \frac{1}{8} \begin{pmatrix} g_A^2 E_L E_L^* + g_B^2 E_R E_R^* \pm g_A g_B (E_L E_R^* e^{i\theta} + E_R E_L^* e^{-i\theta}) \\ g_A^2 E_L E_L^* + g_B^2 E_R E_R^* \mp g_A g_B (E_L E_R^* e^{i\theta} + E_R E_L^* e^{-i\theta}) \\ g_A^2 E_L E_L^* + g_B^2 E_R E_R^* \pm i g_A g_B (E_L E_R^* e^{i\theta} - E_R E_L^* e^{-i\theta}) \\ g_A^2 E_L E_L^* + g_B^2 E_R E_R^* \mp i g_A g_B (E_L E_R^* e^{i\theta} - E_R E_L^* e^{-i\theta}) \end{pmatrix}$$

Substituting E_L and E_R (given in section 2.3.5)

$$\begin{pmatrix} Q1 \\ Q2 \\ U1 \\ U2 \end{pmatrix} = \frac{1}{8} \begin{pmatrix} g_A^2 \frac{I+V}{2} + g_B^2 \frac{I-V}{2} \pm \frac{g_A g_B}{2} [Q(e^{i\theta} + e^{-i\theta}) + iU(e^{i\theta} - e^{-i\theta})] \\ g_A^2 \frac{I+V}{2} + g_B^2 \frac{I-V}{2} \mp \frac{g_A g_B}{2} [Q(e^{i\theta} + e^{-i\theta}) + iU(e^{i\theta} - e^{-i\theta})] \\ g_A^2 \frac{I+V}{2} + g_B^2 \frac{I-V}{2} \pm i \frac{g_A g_B}{2} [Q(e^{i\theta} - e^{-i\theta}) + iU(e^{i\theta} + e^{-i\theta})] \\ g_A^2 \frac{I+V}{2} + g_B^2 \frac{I-V}{2} \mp i \frac{g_A g_B}{2} [Q(e^{i\theta} - e^{-i\theta}) + iU(e^{i\theta} + e^{-i\theta})] \end{pmatrix}$$

And minor simplification to write this in trigonometric terms yields:

$$\begin{pmatrix} Q1 \\ Q2 \\ U1 \\ U2 \end{pmatrix} = \frac{1}{8} \begin{pmatrix} g_A^2 \frac{I+V}{2} + g_B^2 \frac{I-V}{2} \pm g_A g_B [Q \cos(\theta) - U \sin(\theta)] \\ g_A^2 \frac{I+V}{2} + g_B^2 \frac{I-V}{2} \mp g_A g_B [Q \cos(\theta) - U \sin(\theta)] \\ g_A^2 \frac{I+V}{2} + g_B^2 \frac{I-V}{2} \pm g_A g_B [-U \cos(\theta) - Q \sin(\theta)] \\ g_A^2 \frac{I+V}{2} + g_B^2 \frac{I-V}{2} \mp g_A g_B [-U \cos(\theta) - Q \sin(\theta)] \end{pmatrix}$$

The \pm which appears in front of terms like $g_A g_B$ originated from the phase switching action, where we had set $\phi = 0, 180$. When we phase switch, the signal on a given diode will change from $+$ to $-$ and back again. During signal processing, we can either add the phase switched stages together ('total power' stream), or difference them ('demodulated' stream). Averaging the two phase switch states will remove

components which change sign with the phase switch state:

$$\begin{pmatrix} Q1 \\ Q2 \end{pmatrix}^{total-power} = \begin{pmatrix} U1 \\ U2 \end{pmatrix}^{total-power} = \frac{1}{4} \begin{pmatrix} (g_A^2 + g_B^2)\frac{I}{2} + (g_A^2 - g_B^2)\frac{V}{2} \\ (g_A^2 + g_B^2)\frac{I}{2} + (g_A^2 - g_B^2)\frac{V}{2} \end{pmatrix}$$

Differencing (‘demodulating’) instead removes terms which are constant between the two phase switch states:

$$\begin{pmatrix} Q1 \\ Q2 \\ U1 \\ U2 \end{pmatrix}^{demodulated} = \frac{1}{4} \begin{pmatrix} g_A g_B (Q \cos(\theta) - U \sin(\theta)) \\ -g_A g_B (Q \cos(\theta) - U \sin(\theta)) \\ -g_A g_B (U \cos(\theta) + Q \sin(\theta)) \\ g_A g_B (U \cos(\theta) + Q \sin(\theta)) \end{pmatrix}$$

The effects of this phase lag can be summarized by:

- The total power (averaged) signal is unaffected
- The demodulated (differenced) signal has leakage between the Stokes parameters, where the leakage has opposite sign from the first case.

A.3.9 Phase lag at the output the 180° coupler: OMT input

Now consider the case where the phase lag occurred at the output of the 180° coupler, on only one leg. The Jones matrix for the 180° coupler will now take the form:

$$S^{180^\circ} = \frac{1}{\sqrt{2}} \begin{pmatrix} 1 & 1 \\ 1 & -1 \end{pmatrix} \rightarrow \frac{1}{\sqrt{2}} \begin{pmatrix} 1 & 1 \\ 1 & -e^{i\theta} \end{pmatrix} \quad (\text{A.15})$$

Substituting this expression for the 180° coupler Jones matrix in section 2.3.5 gives the signal prior to rectification by the diodes with the form:

$$\begin{pmatrix} E_{Q1} \\ E_{Q2} \end{pmatrix} = \frac{1}{2\sqrt{2}} \begin{pmatrix} g_A & \pm g_B \\ g_A & \mp g_B e^{i\theta} \end{pmatrix} \begin{pmatrix} E_A \\ E_B \end{pmatrix}^{in}$$

$$\begin{pmatrix} E_{U1} \\ E_{U2} \end{pmatrix} = \frac{1}{4} \begin{pmatrix} g_A(1+i) & \pm g_B(1-ie^{i\theta}) \\ g_A(1+i) & \mp g_B(e^{i\theta}-i) \end{pmatrix} \begin{pmatrix} E_A \\ E_B \end{pmatrix}^{in}$$

The diodes measure the rectified signal, which will have the form:

$$\begin{pmatrix} Q1 \\ Q2 \\ U1 \\ U2 \end{pmatrix} = \frac{1}{8} \begin{pmatrix} g_A^2 E_L E_L^* + g_B^2 E_R E_R^* \pm g_A g_B (E_L E_R^* + E_R E_L^*) \\ g_A^2 E_L E_L^* + g_B^2 E_R E_R^* \mp g_A g_B (E_L E_R^* e^{-i\theta} + E_R E_L^* e^{i\theta}) \\ g_A^2 E_L E_L^* + g_B^2 (1 + \sin(\theta)) E_R E_R^* \pm \\ \frac{g_A g_B}{2} [E_L E_R^* (1 + ie^{-i\theta} + i - e^{-i\theta}) + E_L^* E_R (1 - ie^{i\theta} - i - e^{i\theta})] \\ g_A^2 E_L E_L^* + g_B^2 (1 + \sin(\theta)) E_R E_R^* \mp \\ \frac{g_A g_B}{2} [E_L E_R^* (1 + ie^{-i\theta} + i - e^{-i\theta}) + E_L^* E_R (1 - ie^{i\theta} - i - e^{i\theta})] \end{pmatrix}$$

Substituting E_L and E_R (given in section 2.3.5)

$$\begin{pmatrix} Q1 \\ Q2 \\ U1 \\ U2 \end{pmatrix} = \frac{1}{8} \begin{pmatrix} g_A^2 \frac{I+V}{2} + g_B^2 \frac{I-V}{2} \pm g_A g_B Q \\ g_A^2 \frac{I+V}{2} + g_B^2 \frac{I-V}{2} \mp g_A g_B (Q \cos(\theta) + U \sin(\theta)) \\ g_A^2 \frac{I+V}{2} + g_B^2 (1 + \sin(\theta)) \frac{I-V}{2} \pm \frac{g_A g_B}{2} [\\ (\frac{Q}{2} + \frac{iU}{2})(1 + ie^{-i\theta} + i - e^{-i\theta}) + (\frac{Q}{2} - \frac{iU}{2})(1 - ie^{i\theta} - i - e^{i\theta})] \\ g_A^2 \frac{I+V}{2} + g_B^2 (1 + \sin(\theta)) \frac{I-V}{2} \mp \frac{g_A g_B}{2} [\\ (\frac{Q}{2} + \frac{iU}{2})(1 + ie^{-i\theta} + i - e^{-i\theta}) + (\frac{Q}{2} - \frac{iU}{2})(1 - ie^{i\theta} - i - e^{i\theta})] \end{pmatrix}$$

And minor simplification to transform to trigonometric variables yields:

$$\begin{pmatrix} Q1 \\ Q2 \\ U1 \\ U2 \end{pmatrix} = \frac{1}{8} \begin{pmatrix} g_A^2 \frac{I+V}{2} + g_B^2 \frac{I-V}{2} \pm g_A g_B Q \\ g_A^2 \frac{I+V}{2} + g_B^2 \frac{I-V}{2} \mp g_A g_B (Q \cos(\theta) + U \sin(\theta)) \\ g_A^2 \frac{I+V}{2} + g_B^2 (1 + \sin(\theta)) \frac{I-V}{2} \mp \\ \frac{g_A g_B}{2} [U(1 + \cos(\theta) + \sin(\theta)) - Q(1 - \cos(\theta) + \sin(\theta))] \\ g_A^2 \frac{I+V}{2} + g_B^2 (1 + \sin(\theta)) \frac{I-V}{2} \pm \\ \frac{g_A g_B}{2} [U(1 + \cos(\theta) + \sin(\theta)) - Q(1 - \cos(\theta) + \sin(\theta))] \end{pmatrix}$$

The \pm which appears in front of terms like $g_A g_B$ originated from the phase switching action, where we had set $\phi = 0, 180$. When we phase switch, the signal on a given diode will change from $+$ to $-$ and back again. During signal processing, we can either add the phase switched stages together ('total power' stream), or difference them ('demodulated' stream). Averaging the two phase switch states will remove components which change sign with the phase switch state:

$$\begin{pmatrix} Q1 \\ Q2 \\ U1 \\ U2 \end{pmatrix}^{total-power} = \frac{1}{4} \begin{pmatrix} (g_A^2 + g_B^2) \frac{I}{2} + (g_A^2 - g_B^2) \frac{V}{2} \\ (g_A^2 + g_B^2) \frac{I}{2} + (g_A^2 - g_B^2) \frac{V}{2} \\ (g_A^2 + g_B^2 [1 + \sin(\theta)]) \frac{I}{2} + (g_A^2 - g_B^2 [1 + \sin(\theta)]) \frac{V}{2} \\ (g_A^2 + g_B^2 [1 + \sin(\theta)]) \frac{I}{2} + (g_A^2 - g_B^2 [1 + \sin(\theta)]) \frac{V}{2} \end{pmatrix}$$

Differencing ('demodulating') instead removes terms which are constant between the two phase switch states:

$$\begin{pmatrix} Q1 \\ Q2 \\ U1 \\ U2 \end{pmatrix}^{demodulated} = \frac{1}{4} \begin{pmatrix} g_A g_B Q \\ -g_A g_B [Q \cos(\theta) + U \sin(\theta)] \\ -\frac{g_A g_B}{2} [U(1 + \cos(\theta) + \sin(\theta)) - Q(1 - \cos(\theta) + \sin(\theta))] \\ \frac{g_A g_B}{2} [U(1 + \cos(\theta) + \sin(\theta)) - Q(1 - \cos(\theta) + \sin(\theta))] \end{pmatrix}$$

The effects of this phase lag are:

- The total power (averaged) signal on the U diodes is changed from the non-lagged case, and will be different by a factor of $(1 - \sin(\theta))$ relative to the total power signal measured on the Q diodes.
- The demodulated (differenced) signal contains cross-polarization terms which leak signal between Q and U. For $\theta \simeq 0$, both reduce to the usual case.

A.4 Correlated Noise

We investigate the correlated noise between diodes in the case with no systematics, in the case with complex gain, and in the case of a phase lag within the coupling structure of the 180° coupler. The equation defining this correlation coefficient (equation 2.42) and variable definitions are given in Section 2.3.5, also the portions of the following analysis was described in Ref. [8]. We assume the noise in each amplifier is gaussian random such that the following statistics describe the variance of the noise:

$$\begin{aligned}
\langle a_0^2 \rangle &= \langle a_1^2 \rangle = \sigma_a^2 \\
\langle b_0^2 \rangle &= \langle b_1^2 \rangle = \sigma_b^2 \\
\langle a_0^4 \rangle &= \langle a_1^4 \rangle = 3\sigma_a^4 \\
\langle b_0^4 \rangle &= \langle b_1^4 \rangle = 3\sigma_b^4 \\
\langle a_0^2 a_1^2 \rangle &= \sigma_a^4 \\
\langle b_0^2 b_1^2 \rangle &= \sigma_b^4 \\
\langle a_0^2 b_0^2 \rangle &= \langle a_0^2 b_1^2 \rangle = \langle a_1^2 b_0^2 \rangle = \langle a_1^2 b_1^2 \rangle = \sigma_a^2 \sigma_b^2 \\
\langle a_0 b_0 \rangle &= \langle a_0 b_1 \rangle = \langle a_1 b_0 \rangle = \langle a_1 b_1 \rangle = 0
\end{aligned} \tag{A.16}$$

Given the definitions of E_L and E_R 2.3.5, the following expressions can be de-

rived which represent the variance between left- and right- polarized states assuming gaussian noise (this is general and not specific to the modules):

$$\begin{aligned}
\langle E_L E_L^* \rangle &= \langle a_0^2 + a_1^2 \rangle = 2\sigma_a^2 \\
\langle E_R E_R^* \rangle &= \langle b_0^2 + b_1^2 \rangle = 2\sigma_b^2 \\
\langle E_L E_R^* + E_L^* E_R \rangle &= \langle a_0 b_0 + a_1 b_1 \rangle = 0 \\
\langle E_L E_R^* - E_L^* E_R \rangle &= \langle 2i(a_1 b_0 - a_0 b_1) \rangle = 0 \\
\langle (E_R E_R^*)^2 \rangle &= \langle b_0^4 \rangle + \langle b_1^4 \rangle + 2 \langle b_0^2 b_1^2 \rangle = 8\sigma_b^4 \\
\langle (E_L E_L^*)^2 \rangle &= \langle a_0^4 \rangle + \langle a_1^4 \rangle + 2 \langle a_0^2 a_1^2 \rangle = 8\sigma_a^4 \\
\langle E_R^* E_R E_L^* E_L \rangle &= \langle (a_0^2 + a_1^2)(b_0^2 + b_1^2) \rangle = 4\sigma_a^2 \sigma_b^2 \\
\langle E_R E_R E_L^* E_L^* \rangle &= \langle E_R^* E_R^* E_L E_L \rangle = 0 \\
\langle E_R E_R E_R E_L^* \rangle &= \langle E_R^* E_R^* E_R E_L \rangle = 0 \\
\langle E_R E_L E_L^* E_L^* \rangle &= \langle E_R^* E_L E_L E_L^* \rangle = 0
\end{aligned} \tag{A.17}$$

The variance between the Stokes Q, U, I, and V can be derived with the expressions above and the definitions of the Stokes parameters in terms of E_L and E_R (given in section 2.3.5), again these are general and not specific to QUIET but do assume the noise is gaussian distributed. These will use used to find the variance and co-variance for the QUIET module diodes, whose signal we have in terms of I, V, Q and U.

$$\begin{aligned}
\langle Q \rangle &= \langle E_L E_R^* + E_L^* E_R \rangle = 0 \\
\langle U \rangle &= \langle E_L E_R^* - E_L^* E_R \rangle = 0 \\
\langle II^* \rangle &= \langle (E_L E_L^* + E_R E_R^*)(E_L E_L^* + E_R E_R^*) \rangle = 8(\sigma_a^4 + \sigma_b^4 + \sigma_a^2 \sigma_b^2) \\
\langle VV^* \rangle &= \langle (E_L E_L^* - E_R E_R^*)(E_L E_L^* - E_R E_R^*) \rangle = 8(\sigma_a^4 + \sigma_b^4 - \sigma_a^2 \sigma_b^2) \\
\langle QQ^* \rangle &= \langle (E_L E_R^* + E_R E_L^*)(E_L^* E_R + E_R^* E_L) \rangle = 8\sigma_a^2 \sigma_b^2 \\
\langle UU^* \rangle &= \langle (E_L E_R^* - E_R E_L^*)(E_L^* E_R - E_R^* E_L) \rangle = 8\sigma_a^2 \sigma_b^2 \\
\langle IV^* \rangle \quad \langle I^* V \rangle &= \langle (E_L E_L^* + E_R E_R^*)(E_L E_L^* - E_R E_R^*) \rangle = 8(\sigma_a^4 - \sigma_b^4) \\
\langle IQ^* \rangle &= \langle I^* Q \rangle = \langle (E_L E_L^* + E_R E_R^*)(E_L^* E_R + E_R^* E_L) \rangle = 0 \\
\langle IU^* \rangle &= \langle I^* U \rangle = \langle (E_L E_L^* + E_R E_R^*)(E_L^* E_R - E_R^* E_L) \rangle = 0 \\
\langle VQ^* \rangle &= \langle V^* Q \rangle = \langle (E_L E_L^* - E_R E_R^*)(E_L^* E_R + E_R^* E_L) \rangle = 0 \\
\langle VU^* \rangle &= \langle V^* U \rangle = \langle (E_L E_L^* - E_R E_R^*)(E_L^* E_R - E_R^* E_L) \rangle = 0 \\
\langle QU^* \rangle &= \langle Q^* U \rangle = (-i) \langle (E_L E_R^* + E_R E_L^*)(E_L^* E_R - E_R^* E_L) \rangle = 0 \quad (\text{A.18})
\end{aligned}$$

A.4.1 No Systematics

We will use the correlation coefficient given in equation 2.42 in section 2.3.5. For the case with no systematics, the correlation coefficients between the Q diodes, and between the Q and U diodes, are expressed as:

$$\begin{aligned}
C_{Q1,Q2} &= \frac{\langle Q1Q2 \rangle - \langle Q1 \rangle \langle Q2 \rangle}{\sqrt{(\langle Q1^2 \rangle - \langle Q1 \rangle^2)(\langle Q2^2 \rangle - \langle Q2 \rangle^2)}} = \frac{2(g_A^2 \sigma_a^2 - g_B^2 \sigma_b^2)^2}{2(g_A^2 \sigma_a^2 + g_B^2 \sigma_b^2)^2} \\
C_{Q1,U1} &= \frac{\langle Q1U1 \rangle - \langle Q1 \rangle \langle U1 \rangle}{\sqrt{(\langle Q1^2 \rangle - \langle Q1 \rangle^2)(\langle U1^2 \rangle - \langle U1 \rangle^2)}} = \frac{2(g_A^4 \sigma_a^4 + g_B^4 \sigma_b^4)}{2(g_A^2 \sigma_a^2 + g_B^2 \sigma_b^2)^2} \quad (\text{A.19}) \\
&\quad (\text{A.20})
\end{aligned}$$

To evaluate these correlation coefficients, we will use the following prescription:

1. We extract the expression for the signal on each diode (Q1, Q2, U1, U2) prior to demodulation or averaging (because noise is correlated noise within the module, the post-processing will not effect the correlation) in terms of the Stokes parameters I, V, Q, and U (we found these in section A.2).
2. Compute the terms necessary for the correlation expression for the diode sets we are interested in (Q1-Q2, U1-U2, and Q1-U1, noting that all correlations between Q and U diodes will be identical).
3. Substitute these terms into equation 2.42. For example, to evaluate the correlation between the Q and U diodes without systematics, to solve the coefficients given in equation A.19, we will need the following expressions:

$$\begin{aligned}
\langle Q1 \rangle &= \langle (g_A^2 + g_B^2) \frac{I}{2} + (g_B^2 - g_A^2) \frac{V}{2} + g_A g_B Q \rangle \\
\langle U1 \rangle &= \langle (g_A^2 + g_B^2) \frac{I}{2} + (g_B^2 - g_A^2) \frac{V}{2} + g_A g_B U \rangle \\
&= \langle (g_A^2 + g_B^2) \frac{E_L E_L^* + E_R E_R^*}{2} \rangle + \langle (g_B^2 - g_A^2) \frac{E_L E_L^* - E_R E_R^*}{2} \rangle \\
&\quad + \langle g_A g_B (E_L E_R^* + E_R E_L^*) \rangle \\
&= (g_A^2 + g_B^2)(\sigma_a^2 + \sigma_b^2) + (g_A^2 - g_B^2)(\sigma_a^2 - \sigma_b^2) + (g_B^2 - g_A^2)(0) \\
&= 2(g_A^2 \sigma_a^2 + g_B^2 \sigma_b^2) \xrightarrow{g_A = g_B = 1} 2(\sigma_a^2 + \sigma_b^2)
\end{aligned} \tag{A.21}$$

$$\begin{aligned}
\langle Q1Q1^* \rangle &= \langle |(g_A^2 + g_B^2)\frac{I}{2} + (g_B^2 - g_A^2)\frac{V}{2} + g_A g_B Q|^2 \rangle \\
&= (g_A^2 + g_B^2)^2 \frac{\langle II^* \rangle}{4} + (g_A^2 + g_B^2)(g_B^2 - g_A^2) \frac{\langle IV^* \rangle}{4} \\
&\quad + (g_B^2 - g_A^2)^2 \frac{\langle VV^* \rangle}{4} + (g_A g_B)^2 \langle QQ^* \rangle \\
&= 2(g_A^2 + g_B^2)^2(\sigma_a^4 + \sigma_b^4 + \sigma_a^2 \sigma_b^2) + 2(g_A^2 + g_B^2)(g_A^2 - g_B^2)(\sigma_a^4 - \sigma_b^4) \\
&\quad + 2(g_A^2 - g_B^2)^2(\sigma_a^4 + \sigma_b^4 - \sigma_a^2 \sigma_b^2) + 8(g_A g_B)^2(\sigma_a^2 \sigma_b^2) \\
&\quad \xrightarrow{g_A=g_B=1} 8(\sigma_a^4 + \sigma_b^4 + 2\sigma_a^2 \sigma_b^2) = 8(\sigma_a^2 + \sigma_b^2)^2 \\
\langle Q1Q2^* \rangle &= 2(g_A^2 + g_B^2)^2(\sigma_a^4 + \sigma_b^4 + \sigma_a^2 \sigma_b^2) + 2(g_A^2 + g_B^2)(g_B^2 - g_A^2)(\sigma_a^4 - \sigma_b^4) \\
&\quad + 2(g_A^2 - g_B^2)^2(\sigma_a^4 + \sigma_b^4 - \sigma_a^2 \sigma_b^2) - 8(g_A g_B)^2(\sigma_a^2 \sigma_b^2) \\
\langle Q1U1 \rangle &= 2(g_A^2 + g_B^2)^2(\sigma_a^4 + \sigma_b^4 + \sigma_a^2 \sigma_b^2) + 2(g_A^2 + g_B^2)(g_A^2 - g_B^2)(\sigma_a^4 - \sigma_b^4) \\
&\quad + 2(g_A^2 - g_B^2)^2(\sigma_a^4 + \sigma_b^4 - \sigma_a^2 \sigma_b^2) \tag{A.22}
\end{aligned}$$

The numerator and denominator of equation A.19 contain the following quantities, which we evaluate here:

$$\begin{aligned}
\langle Q1^2 \rangle - \langle Q1 \rangle^2 &= [2(g_A^2 + g_B^2)^2(\sigma_a^4 + \sigma_b^4 + \sigma_a^2 \sigma_b^2) + 2(g_A^2 + g_B^2)(g_B^2 - g_A^2)(\sigma_a^4 - \sigma_b^4) \\
&\quad + 2(g_B^2 - g_A^2)^2(\sigma_a^4 + \sigma_b^4 - \sigma_a^2 \sigma_b^2) + 8g_A^2 g_B^2 \sigma_a^2 \sigma_b^2] - [4(g_A^2 \sigma_a^2 + g_B^2 \sigma_b^2)^2] \\
&= (g_A^4 + g_B^4)(\sigma_a^4 + \sigma_b^4) + (g_A^4 - g_B^4)(\sigma_a^4 - \sigma_b^4) + 4g_A^2 g_B^2 \sigma_a^2 \sigma_b^2 \\
&= 2(g_A^2 \sigma_a^2 + g_B^2 \sigma_b^2)^2 \xrightarrow{g_A=g_B=1} 2(\sigma_a^2 + \sigma_b^2)^2 \\
\langle Q1Q2^* \rangle - \langle Q1 \rangle \langle Q2 \rangle &= (g_A^4 + g_B^4)(\sigma_a^4 + \sigma_b^4) + (g_A^4 - g_B^4)(\sigma_a^4 - \sigma_b^4) - 4g_A^2 g_B^2 \sigma_a^2 \sigma_b^2 \\
&= 2(g_A^2 \sigma_a^2 - g_B^2 \sigma_b^2)^2 \xrightarrow{g_A=g_B=1} 2(\sigma_a^2 - \sigma_b^2)^2 \\
\langle Q1U1^* \rangle - \langle Q1 \rangle \langle U1 \rangle &= (g_A^4 + g_B^4)(\sigma_a^4 + \sigma_b^4) + (g_A^4 - g_B^4)(\sigma_a^4 - \sigma_b^4) \\
&= 2(g_A^4 \sigma_a^4 + g_B^4 \sigma_b^4) \xrightarrow{g_A=g_B=1} 2(\sigma_a^4 + \sigma_b^4) \tag{A.23}
\end{aligned}$$

We will also need the following:

$$\begin{aligned}
\langle Q2^2 \rangle - \langle Q2 \rangle^2 &= \langle Q1^2 \rangle - \langle Q1 \rangle^2 = \langle U1^2 \rangle - \langle U1 \rangle^2 = \langle U2^2 \rangle - \langle U2 \rangle^2 \\
\langle Q2 \rangle &= \langle Q1 \rangle = \langle U1 \rangle = \langle U2 \rangle
\end{aligned}
\tag{A.24}$$

Substituting these into equation A.19 gives the following correlation expressions for the correlation between the two Q diodes, and between the Q and U diodes:

$$\begin{aligned}
C_{Q1,Q2} &= \frac{\langle Q1Q2 \rangle - \langle Q1 \rangle \langle Q2 \rangle}{\sqrt{(\langle Q1^2 \rangle - \langle Q1 \rangle^2)(\langle Q2^2 \rangle - \langle Q2 \rangle^2)}} = \frac{2(g_A^2 \sigma_a^2 - g_B^2 \sigma_b^2)^2}{2(g_A^2 \sigma_a^2 + g_B^2 \sigma_b^2)^2} \\
C_{Q1,U1} &= \frac{\langle Q1U1 \rangle - \langle Q1 \rangle \langle U1 \rangle}{\sqrt{(\langle Q1^2 \rangle - \langle Q1 \rangle^2)(\langle U1^2 \rangle - \langle U1 \rangle^2)}} = \frac{2(g_A^4 \sigma_a^4 + g_B^4 \sigma_b^4)}{2(g_A^2 \sigma_a^2 + g_B^2 \sigma_b^2)^2}
\end{aligned}
\tag{A.25}$$

We can simplify this by assuming that the noise σ already contains the gain from the amplifiers in the relevant leg, such that we can absorb g_A into σ_A and g_B into σ_B :

$$\begin{aligned}
C(Q1, Q2) &= \frac{(\sigma_a^2 - \sigma_b^2)^2}{(\sigma_a^2 + \sigma_b^2)^2} \xrightarrow{\sigma_a = \sigma_b} 0 \\
C(Q1, U1) &= \frac{\sigma_a^4 + \sigma_b^4}{(\sigma_a^2 + \sigma_b^2)^2} \xrightarrow{\sigma_a = \sigma_b} \frac{1}{2}
\end{aligned}
\tag{A.26}$$

It can be shown that $C(U1, U2) = C(Q1, Q2)$ (Ref. [8]). If the noise is identical between the two legs, $C(Q1, Q2) \rightarrow 0$ and $C(Q1, U2) \rightarrow 0.5$.

A.4.2 Complex Gain

We repeat the prescription outlined above in section A.4.1, however this time instead of using the expressions for the diode measurement from a no-systematics case, we will use the expression for the diode measurement derived assuming complex gain (section A.3.3). In this case, the inputs to the correlation expression given by equation 2.42.

$$\begin{aligned}
\langle Q1 \rangle_{\text{imperf}} &= \langle (g_A^2 + g_B^2) \frac{I}{2} + (g_A^2 - g_B^2) \frac{V}{2} + g_A g_B (Q \cos(\theta) + U \sin(\theta)) \rangle = \langle Q1 \rangle \\
\langle Q1Q2^* \rangle_{\text{imperf}} &= \langle [(g_A^2 + g_B^2) \frac{I}{2} + (g_A^2 - g_B^2) \frac{V}{2} + g_A g_B (Q \cos(\theta) + U \sin(\theta))] \times \\
&\quad [(g_A^2 + g_B^2) \frac{I}{2} + (g_A^2 - g_B^2) \frac{V}{2} - g_A g_B (Q \cos(\theta) + U \sin(\theta))]^* \rangle \\
&= 2(g_A^2 + g_B^2)^2 (\sigma_a^4 + \sigma_b^4 + \sigma_a^2 \sigma_b^2) + 2(g_A^2 + g_B^2)(g_A^2 - g_B^2)(\sigma_a^4 - \sigma_b^4) \\
&\quad + 2(g_A^2 - g_B^2)^2 (\sigma_a^4 + \sigma_b^4 - \sigma_a^2 \sigma_b^2) - 8(g_A g_B)^2 (\sigma_a^2 \sigma_b^2) \\
\langle Q1U1^* \rangle_{\text{imperf}} &= \langle [(g_A^2 + g_B^2) \frac{I}{2} + (g_A^2 - g_B^2) \frac{V}{2} + g_A g_B (Q \cos(\theta) + U \sin(\theta))] \times \\
&\quad [(g_A^2 + g_B^2) \frac{I}{2} + (g_A^2 - g_B^2) \frac{V}{2} + g_A g_B (U \cos(\theta) - Q \sin(\theta))] \rangle \\
&= 2(g_A^2 + g_B^2)^2 (\sigma_a^4 + \sigma_b^4 + \sigma_a^2 \sigma_b^2) + 2(g_A^2 + g_B^2)(g_A^2 - g_B^2)(\sigma_a^4 - \sigma_b^4) \\
&\quad + 2(g_A^2 - g_B^2)^2 (\sigma_a^4 + \sigma_b^4 - \sigma_a^2 \sigma_b^2)
\end{aligned} \tag{A.27}$$

These expressions are identical to the non-phase lagged version, hence complex gain does not affect correlated noise.

A.4.3 Phase Lag at the Input to the 180° Coupler

As we noted in section A.3.6, the expression for the diode signal for this case is identical to the complex gain diode signal, hence the correlation coefficient will also be the same. Hence, this systematic also has no effect on correlated noise.

A.4.4 Phase Lag in the Branchline Coupler

We repeat the prescription outlined above in section A.4.1, however this time instead of using the expressions for the diode measurement from a no-systematics case, we will use the expression for the diode measurement derived assuming that the 180° coupler added a phase lag to the portion of the signal which was delayed by the extra $\lambda/4$ section of the branchline coupler (section A.3.9). We find the expressions for Q1, Q2, U1, and U2 in terms of Stokes Q, U, I, and V parameters from equations presented in section A.3.8. We will use these to derive an expression for the terms for equation 2.42 with the diode signal:

$$\begin{aligned}
\langle Q1Q2^* \rangle_{\text{imperf}} &= \langle [(g_A^2 + g_B^2)\frac{I}{2} + (g_A^2 - g_B^2)\frac{V}{2} + g_A g_B(Q \cos(\theta) - U \sin(\theta))] \times \\
&\quad [(g_A^2 + g_B^2)\frac{I}{2} + (g_A^2 - g_B^2)\frac{V}{2} - g_A g_B(Q \cos(\theta) - U \sin(\theta))]^* \rangle \\
&= 2(g_A^2 + g_B^2)^2(\sigma_a^4 + \sigma_b^4 + \sigma_a^2 \sigma_b^2) + 2(g_A^2 + g_B^2)(g_A^2 - g_B^2)(\sigma_a^4 - \sigma_b^4) \\
&\quad + 2(g_A^2 - g_B^2)^2(\sigma_a^4 + \sigma_b^4 - \sigma_a^2 \sigma_b^2) - 8(g_A g_B)^2(\sigma_a^2 \sigma_b^2) \\
\langle Q1U1^* \rangle_{\text{imperf}} &= \langle [(g_A^2 + g_B^2)\frac{I}{2} + (g_A^2 - g_B^2)\frac{V}{2} + g_A g_B(Q \cos(\theta) - U \sin(\theta))] \times \\
&\quad [(g_A^2 + g_B^2)\frac{I}{2} + (g_A^2 - g_B^2)\frac{V}{2} + g_A g_B(U \cos(\theta) + Q \sin(\theta))] \rangle \\
&= 2(g_A^2 + g_B^2)^2(\sigma_a^4 + \sigma_b^4 + \sigma_a^2 \sigma_b^2) + 2(g_A^2 + g_B^2)(g_A^2 - g_B^2)(\sigma_a^4 - \sigma_b^4) \\
&\quad + 2(g_A^2 - g_B^2)^2(\sigma_a^4 + \sigma_b^4 - \sigma_a^2 \sigma_b^2) \tag{A.28}
\end{aligned}$$

These terms are identical to those derived for no systematics (section A.4.1), so although the diode signal has a slightly different expression from the cases considered above, this case also does not change the correlated noise in the module.

A.4.5 Phase Lag at the Output of the Coupler

This case assumes that the output of the 180° coupler has a phase lag on only one of the legs. This does produce an additional term in the correlated noise. These expressions were evaluated in Ref. [8], and have the following form:

$$C(U1, U2) = \frac{(\sigma_a^2 - \sigma_b^2 \cos(\theta))^2}{(\sigma_a^4 + 2\sigma_a^2\sigma_b^2 + \sigma_b^4 \cos^2(\theta))} \xrightarrow{\sigma_a=\sigma_b} 0 \quad (\text{A.29})$$

Appendix B

Bandpasses: Site measurements

B.1 Bandpasses from Site Measurements

During the course of bandpass measurements at the site, we took 35 separate bandsweeps over two days. As mentioned in section 3.2.2, the U diodes were not well measured by site data, so I present only data from the Q-diodes. Figures B-1- B-2 show the Q1 and Q2 diode bandpasses for all modules, where each bandpass has been normalized by the area under the bandpass to bring them to a common scale. A bandsweep is only included if the computed bandwidth is between 6-9 GHz and if there were no drop-outs (portions where the signal drops dramatically due to interference between metal components in the testing setup).

Figures B-3- B-4 show the averaged bandpasses for the Q1 and Q2 diodes for all modules from the normalized bandpasses which passed the criteria given above. The average is computed frequency point by frequency point, and the errors are computed from the standard deviation, also per frequency point. The given error bars are treated as statistical, although they contain the systematic error from the differences between the two days. If a module had only one day of data which passed the criteria, the errors quoted are 4×10^{-4} , which is the mean of the error values for modules which had valid sweeps taken on both days.

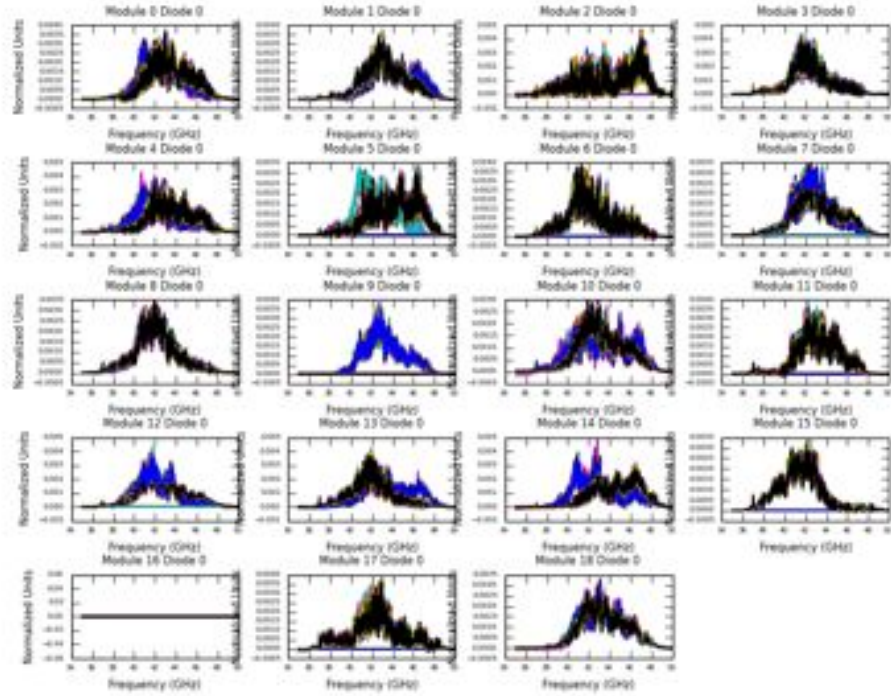


Figure B-1: Q1 diode bandpasses measured by site data. All sweeps which meet the criteria given in the beginning of this section are included, and the data has been normalized by the area under the bandpass. If a bandpass did not meet the criteria it is plotted as a straight line and does not enter into any computations. The bandpasses were not always consistent between the two days of testing, for example the distinctly different set of bandpasses for Modules 4, 5, and 12 stem from differences in the reflection conditions between the two days. Module 9 had few bandpasses which passed the criteria on the second day.

B.2 Bandwidths and Central Frequencies for Source Weighted Bandpasses

This section gives tables of source-weighted central frequencies and bandpasses for all modules in the array, from data taken at the site. The organization of the tables, with references and spectral indices, is listed in section 3.2.5 in Table 3.5. The U diodes were not measured well at the site, so most of those columns are null, however it is possible to use the values from the Q diodes with an additional uncertainty of

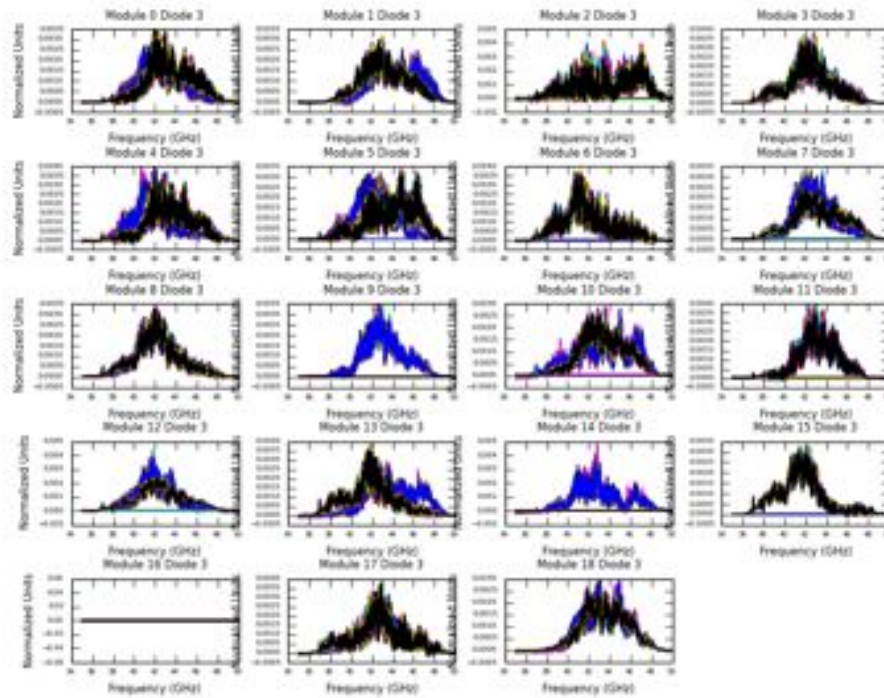


Figure B-2: Q2 diode bandpasses measured by site data. All sweeps which meet the criteria given in the beginning of this section are included, and the data has been normalized by the area under the bandpass. If a bandpass did not meet the criteria it is plotted as a straight line and does not enter into any computations. The bandpasses were not always consistent between the two days of testing, for example the distinctly different set of bandpasses for Modules 4, 5, and 12 stem from differences in the reflection conditions between the two days. Module 9 had few bandpasses which passed the criteria on the second day.

0.25-1GHz.

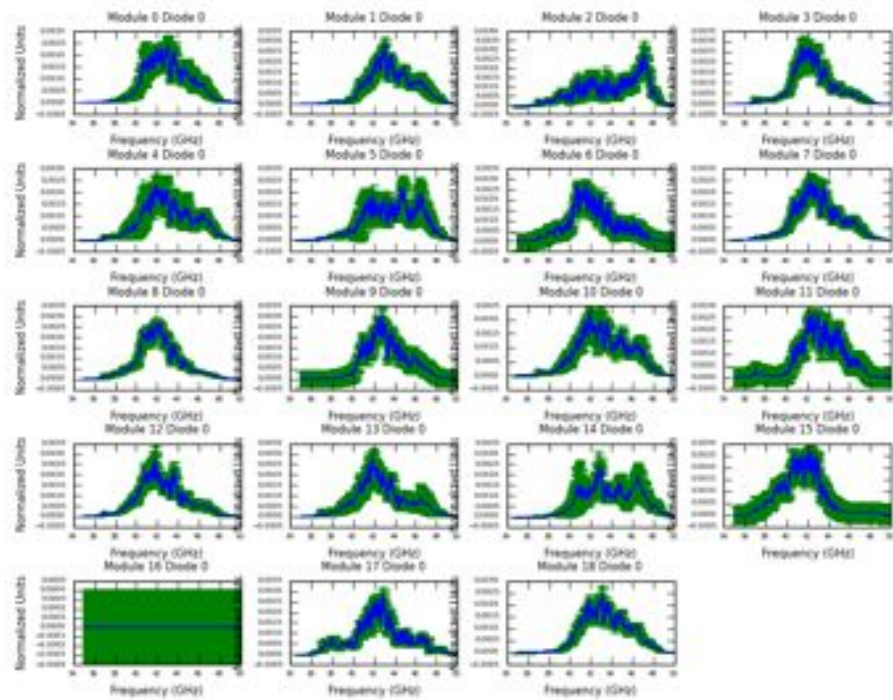


Figure B-3: Q1 diode bandpasses, normalized by the area under the bandpass and averaged together. Errors shown are statistical, or $4\text{E-}4$ for diodes which have good data on only one of the days (discussed in the text).

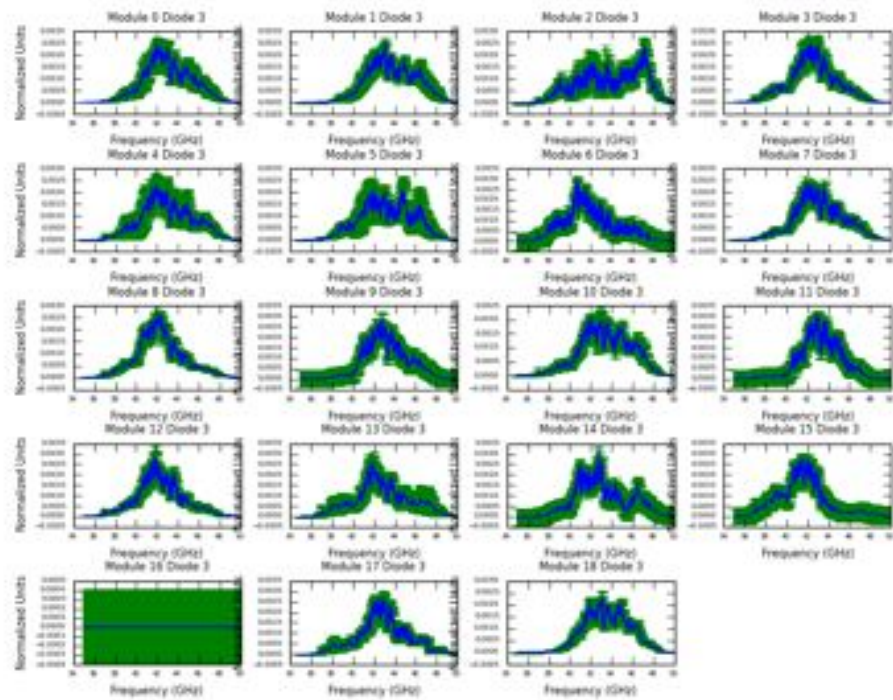


Figure B-4: Q2 diode bandpasses, normalized by the area under the bandpass and averaged together. Errors shown are statistical, or $4\text{E-}4$ for diodes which have good data on only one of the days (discussed in the text).

Site	Module	Q1			U1			U2			Q2		
		Mean (GHz)	σ_{stat} (GHz)	σ_{sys} (GHz)	Mean (GHz)	σ_{stat} (GHz)	σ_{sys} (GHz)	Mean (GHz)	σ_{stat} (GHz)	σ_{sys} (GHz)	Mean (GHz)	σ_{stat} (GHz)	σ_{sys} (GHz)
-	-												
-	-												
RQ00	27	43.14	0.040	0.56	-	-	-	-	-	-	43.18	0.040	0.61
RQ01	28	43.91	0.050	0.47	43.58	0.080	0.25-1	43.63	0.082	0.25-1	44.01	0.046	0.56
RQ02	29	44.64	0.083	0.08	-	-	-	-	-	-	44.36	0.079	0.12
RQ03	10	42.75	0.047	0.19	-	-	-	43.00	-	0.25-1	42.76	0.050	0.24
RQ04	36	43.24	0.056	0.61	-	-	-	-	-	-	43.15	0.060	0.65
RQ05	25	43.37	0.056	1.08	-	-	-	-	-	-	43.29	0.055	1.05
RQ06	26	42.50	0.106	0.25-1	-	-	-	-	-	-	42.23	0.114	0.25-1
RQ07	34	43.23	0.057	0.12	-	-	-	-	-	-	43.33	0.061	0.12
RQ08	33	42.37	0.050	0.08	-	-	-	-	-	-	42.55	0.055	0.11
RQ09	21	43.45	0.083	0.25-1	-	-	-	-	-	-	43.40	0.074	0.25-1
RQ10	24	43.55	0.065	0.08	-	-	-	-	-	-	43.70	0.067	0.05
RQ11	22	43.53	0.089	0.25-1	-	-	-	43.78	0.102	0.25-1	43.45	0.083	0.25-1
RQ12	30	42.69	0.062	0.35	-	-	-	-	-	-	42.50	0.057	0.29
RQ13	35	43.13	0.056	0.98	43.53	0.121	0.25-1	43.76	0.135	0.25-1	43.25	0.061	1.16
RQ14	37	44.07	0.054	1.03	-	-	-	-	-	-	43.36	0.104	0.25-1
RQ15	39	41.72	0.087	0.25-1	-	-	-	-	-	-	41.79	0.085	0.25-1
RQ16	17	-	-	-	-	-	-	-	-	-	-	-	-
RQ17	9	42.97	0.049	0.18	43.20	-	0.25-1	43.62	0.089	0.25-1	43.15	0.045	0.16
RQ18	23	43.69	0.052	0.07	-	-	-	-	-	-	43.82	0.051	0.03

Table B.1: Central Frequencies: $\beta=2.0$ (appropriate for dust emission).

Site	Module	Q1			U1			U2			Q2		
		Mean (GHz)	σ_{stat} (GHz)	σ_{sys} (GHz)	Mean (GHz)	σ_{stat} (GHz)	σ_{sys} (GHz)	Mean (GHz)	σ_{stat} (GHz)	σ_{sys} (GHz)	Mean (GHz)	σ_{stat} (GHz)	σ_{sys} (GHz)
-	-												
-	-												
RQ00	27	6.71	0.065	0.19	-	-	-	-	-	-	7.12	0.075	0.10
RQ01	28	7.01	0.077	0.13	8.28	0.100	0.25-1	7.83	0.120	0.25-1	7.44	0.071	0.10
RQ02	29	7.11	0.156	0.29	-	-	-	-	-	-	8.00	0.152	0.21
RQ03	10	6.41	0.070	0.22	-	-	-	7.05	-	0.25-1	7.25	0.076	0.10
RQ04	36	7.37	0.106	0.53	-	-	-	-	-	-	7.48	0.110	0.64
RQ05	25	6.78	0.093	0.73	-	-	-	-	-	-	7.00	0.091	0.50
RQ06	26	7.33	0.206	0.25-1	-	-	-	-	-	-	7.92	0.216	0.25-1
RQ07	34	7.15	0.068	0.58	-	-	-	-	-	-	7.55	0.071	0.50
RQ08	33	6.49	0.074	0.23	-	-	-	-	-	-	7.02	0.084	0.18
RQ09	21	6.58	0.126	0.25-1	-	-	-	-	-	-	6.73	0.118	0.25-1
RQ10	24	7.97	0.080	0.65	-	-	-	-	-	-	8.10	0.083	0.56
RQ11	22	6.50	0.139	0.25-1	-	-	-	6.18	0.166	0.25-1	6.06	0.116	0.25-1
RQ12	30	7.16	0.052	1.08	-	-	-	-	-	-	6.99	0.051	0.76
RQ13	35	7.10	0.081	0.68	7.53	0.212	0.25-1	7.67	0.233	0.25-1	7.55	0.100	0.40
RQ14	37	7.00	0.074	0.07	-	-	-	-	-	-	7.55	0.206	0.25-1
RQ15	39	6.49	0.111	0.25-1	-	-	-	-	-	-	6.82	0.122	0.25-1
RQ16	17	-	-	-	-	-	-	-	-	-	-	-	-
RQ17	9	7.05	0.125	0.95	6.64	-	0.25-1	6.88	0.135	0.25-1	7.23	0.124	0.91
RQ18	23	7.34	0.063	0.32	-	-	-	-	-	-	7.21	0.060	0.08

Table B.2: Bandwidths: $\beta=2.0$ (appropriate for dust emission).

Site	Module	Q1			U1			U2			Q2		
		Mean (GHz)	σ_{stat} (GHz)	σ_{sys} (GHz)	Mean (GHz)	σ_{stat} (GHz)	σ_{sys} (GHz)	Mean (GHz)	σ_{stat} (GHz)	σ_{sys} (GHz)	Mean (GHz)	σ_{stat} (GHz)	σ_{sys} (GHz)
-	-												
-	-												
RQ00	27	42.67	0.044	0.56	-	-	-	-	-	-	42.65	0.044	0.62
RQ01	28	43.40	0.060	0.46	42.92	0.087	0.25-1	42.95	0.095	0.25-1	43.47	0.053	0.58
RQ02	29	43.67	0.097	0.03	-	-	-	-	-	-	43.37	0.085	0.07
RQ03	10	42.25	0.047	0.20	-	-	-	42.25	-	0.25-1	42.17	0.054	0.27
RQ04	36	42.62	0.066	0.73	-	-	-	-	-	-	42.51	0.071	0.78
RQ05	25	43.76	0.117	0.25-1	-	-	-	-	-	-	42.72	0.066	0.95
RQ06	26	41.86	0.101	0.25-1	-	-	-	-	-	-	41.50	0.092	0.25-1
RQ07	34	42.68	0.049	0.06	-	-	-	-	-	-	42.73	0.063	0.06
RQ08	33	41.84	-	0.08	-	-	-	-	-	-	41.99	0.054	0.15
RQ09	21	43.00	0.098	0.25-1	-	-	-	-	-	-	42.93	0.083	0.25-1
RQ10	24	42.87	0.071	0.12	-	-	-	-	-	-	43.08	-	0.07
RQ11	22	43.01	0.105	0.25-1	-	-	-	43.12	0.129	0.25-1	43.01	0.091	0.25-1
RQ12	30	42.13	0.057	0.26	-	-	-	-	-	-	41.94	0.051	0.22
RQ13	35	42.58	0.061	0.94	42.91	0.081	0.25-1	43.07	0.069	0.25-1	42.61	0.067	1.17
RQ14	37	43.49	0.041	1.12	-	-	-	-	-	-	42.67	0.131	0.25-1
RQ15	39	41.21	0.081	0.25-1	-	-	-	-	-	-	41.18	0.079	0.25-1
RQ16	17	-	-	-	-	-	-	-	-	-	-	-	-
RQ17	9	42.20	-	0.34	42.72	-	0.25-1	43.10	0.116	0.25-1	42.51	-	0.33
RQ18	23	43.18	0.053	0.05	-	-	-	-	-	-	43.32	0.051	0.03

Table B.3: Central Frequencies: $\beta=3.2$ (appropriate for soft synchrotron emission).

Site	Module	Q1			U1			U2			Q2		
		Mean (GHz)	σ_{stat} (GHz)	σ_{sys} (GHz)	Mean (GHz)	σ_{stat} (GHz)	σ_{sys} (GHz)	Mean (GHz)	σ_{stat} (GHz)	σ_{sys} (GHz)	Mean (GHz)	σ_{stat} (GHz)	σ_{sys} (GHz)
-	-												
-	-												
RQ00	27	6.43	0.075	0.25	-	-	-	-	-	-	6.89	0.077	0.10
RQ01	28	6.83	0.085	0.09	8.16	0.109	0.25-1	8.48	0.123	0.25-1	7.29	0.076	0.02
RQ02	29	8.50	0.176	0.11	-	-	-	-	-	-	8.79	0.158	0.05
RQ03	10	6.11	0.072	0.07	-	-	-	7.23	-	0.25-1	7.23	0.087	0.05
RQ04	36	6.83	0.119	0.21	-	-	-	-	-	-	6.92	0.123	0.32
RQ05	25	8.07	0.187	0.25-1	-	-	-	-	-	-	7.28	0.109	0.90
RQ06	26	6.87	0.221	0.25-1	-	-	-	-	-	-	7.26	0.219	0.25-1
RQ07	34	6.86	0.074	0.65	-	-	-	-	-	-	7.32	0.074	0.58
RQ08	33	6.39	-	0.31	-	-	-	-	-	-	6.73	0.082	0.35
RQ09	21	6.17	0.161	0.25-1	-	-	-	-	-	-	6.41	0.147	0.25-1
RQ10	24	7.77	0.089	0.88	-	-	-	-	-	-	7.87	-	0.67
RQ11	22	6.45	0.159	0.25-1	-	-	-	6.84	0.190	0.25-1	6.08	0.122	0.25-1
RQ12	30	6.86	0.059	1.07	-	-	-	-	-	-	6.85	0.050	0.74
RQ13	35	6.89	0.087	0.52	6.67	0.258	0.25-1	7.08	0.290	0.25-1	7.46	0.106	0.28
RQ14	37	6.81	0.084	0.55	-	-	-	-	-	-	6.98	0.233	0.25-1
RQ15	39	6.53	0.108	0.25-1	-	-	-	-	-	-	6.74	0.108	0.25-1
RQ16	17	-	-	-	-	-	-	-	-	-	-	-	-
RQ17	9	7.33	-	0.97	6.28	-	0.25-1	6.64	0.148	0.25-1	7.17	-	1.03
RQ18	23	7.02	0.066	0.40	-	-	-	-	-	-	7.10	0.065	0.11

Table B.4: Bandwidths: $\beta=-3.2$ (appropriate for soft synchrotron emission).

Site	Module	Q1			U1			U2			Q2		
		Mean (GHz)	σ_{stat} (GHz)	σ_{sys} (GHz)	Mean (GHz)	σ_{stat} (GHz)	σ_{sys} (GHz)	Mean (GHz)	σ_{stat} (GHz)	σ_{sys} (GHz)	Mean (GHz)	σ_{stat} (GHz)	σ_{sys} (GHz)
-	-												
-	-												
RQ00	27	42.75	0.043	0.56	-	-	-	-	-	-	42.74	0.043	0.62
RQ01	28	43.48	0.058	0.46	43.03	0.086	0.25-1	43.07	0.093	0.25-1	43.56	0.051	0.57
RQ02	29	43.83	0.098	0.03	-	-	-	-	-	-	43.54	0.082	0.08
RQ03	10	42.33	0.047	0.20	-	-	-	42.38	-	0.25-1	42.27	0.053	0.26
RQ04	36	42.72	0.064	0.71	-	-	-	-	-	-	42.61	0.069	0.76
RQ05	25	43.88	0.112	0.25-1	-	-	-	-	-	-	42.81	0.063	0.97
RQ06	26	41.96	0.101	0.25-1	-	-	-	-	-	-	41.61	0.094	0.25-1
RQ07	34	42.77	0.052	0.07	-	-	-	-	-	-	42.83	0.062	0.07
RQ08	33	41.92	0.062	0.07	-	-	-	-	-	-	42.08	0.054	0.14
RQ09	21	43.07	0.094	0.25-1	-	-	-	-	-	-	43.01	0.080	0.25-1
RQ10	24	42.98	0.070	0.09	-	-	-	-	-	-	43.19	-	0.04
RQ11	22	43.10	0.102	0.25-1	-	-	-	43.24	0.125	0.25-1	43.08	0.088	0.25-1
RQ12	30	42.22	0.065	0.28	-	-	-	-	-	-	42.03	0.051	0.23
RQ13	35	42.67	0.060	0.95	43.00	0.096	0.25-1	43.18	0.064	0.25-1	42.71	0.066	1.16
RQ14	37	43.60	0.056	1.09	-	-	-	-	-	-	42.78	0.126	0.25-1
RQ15	39	41.29	0.081	0.25-1	-	-	-	-	-	-	41.28	0.080	0.25-1
RQ16	17	-	-	-	-	-	-	-	-	-	-	-	-
RQ17	9	42.32	-	0.32	42.79	-	0.25-1	43.18	0.111	0.25-1	42.63	0.080	0.31
RQ18	23	43.26	0.053	0.05	-	-	-	-	-	-	43.40	0.051	0.03

Table B.5: Central Frequencies: Tau A ($\beta=2.35$)

Site	Module	Q1			U1			U2			Q2		
		Mean (GHz)	σ_{stat} (GHz)	σ_{sys} (GHz)	Mean (GHz)	σ_{stat} (GHz)	σ_{sys} (GHz)	Mean (GHz)	σ_{stat} (GHz)	σ_{sys} (GHz)	Mean (GHz)	σ_{stat} (GHz)	σ_{sys} (GHz)
-	-												
-	-												
RQ00	27	6.48	0.072	0.24	-	-	-	-	-	-	6.93	0.076	0.10
RQ01	28	6.87	0.083	0.10	8.21	0.105	0.25-1	8.40	0.123	0.25-1	7.33	0.075	0.02
RQ02	29	8.34	0.180	0.16	-	-	-	-	-	-	8.75	0.155	0.02
RQ03	10	6.15	0.074	0.10	-	-	-	7.20	-	0.25-1	7.23	0.085	0.03
RQ04	36	6.91	0.116	0.25	-	-	-	-	-	-	7.01	0.121	0.37
RQ05	25	7.99	0.177	0.25-1	-	-	-	-	-	-	7.24	0.105	0.84
RQ06	26	6.94	0.218	0.25-1	-	-	-	-	-	-	7.36	0.219	0.25-1
RQ07	34	6.91	0.073	0.64	-	-	-	-	-	-	7.36	0.073	0.57
RQ08	33	6.40	0.080	0.29	-	-	-	-	-	-	6.76	0.082	0.32
RQ09	21	6.23	0.156	0.25-1	-	-	-	-	-	-	6.46	0.142	0.25-1
RQ10	24	7.83	0.088	0.86	-	-	-	-	-	-	7.88	-	0.64
RQ11	22	6.46	0.154	0.25-1	-	-	-	6.71	0.186	0.25-1	6.07	0.119	0.25-1
RQ12	30	6.91	0.059	1.08	-	-	-	-	-	-	6.86	0.050	0.74
RQ13	35	6.93	0.086	0.56	6.82	0.251	0.25-1	7.20	0.280	0.25-1	7.49	0.105	0.32
RQ14	37	6.84	0.084	0.50	-	-	-	-	-	-	7.08	0.229	0.25-1
RQ15	39	6.52	0.107	0.25-1	-	-	-	-	-	-	6.74	0.110	0.25-1
RQ16	17	-	-	-	-	-	-	-	-	-	-	-	-
RQ17	9	7.34	-	0.94	6.33	-	0.25-1	6.70	0.144	0.25-1	7.14	0.148	1.07
RQ18	23	7.08	0.065	0.39	-	-	-	-	-	-	7.13	0.064	0.10

Table B.6: Bandwidths: Tau A ($\beta=2.35$)

Site	Module	Q1			U1			U2			Q2		
		Mean (GHz)	σ_{stat} (GHz)	σ_{sys} (GHz)	Mean (GHz)	σ_{stat} (GHz)	σ_{sys} (GHz)	Mean (GHz)	σ_{stat} (GHz)	σ_{sys} (GHz)	Mean (GHz)	σ_{stat} (GHz)	σ_{sys} (GHz)
-	-												
-	-												
RQ00	27	6.93	0.065	0.16	-	-	-	-	-	-	7.34	0.074	0.07
RQ01	28	7.18	0.076	0.09	8.30	0.103	0.25-1	7.57	0.124	0.25-1	7.53	0.071	0.23
RQ02	29	6.35	0.128	0.29	-	-	-	-	-	-	7.36	0.143	0.29
RQ03	10	6.73	0.074	0.26	-	-	-	7.17	-	0.25-1	7.48	0.078	0.11
RQ04	36	7.73	0.107	0.73	-	-	-	-	-	-	7.87	0.112	0.84
RQ05	25	6.76	0.095	0.50	-	-	-	-	-	-	6.97	0.089	0.29
RQ06	26	7.73	0.209	0.25-1	-	-	-	-	-	-	8.40	0.220	0.25-1
RQ07	34	7.44	0.066	0.55	-	-	-	-	-	-	7.81	0.075	0.46
RQ08	33	6.81	0.078	0.19	-	-	-	-	-	-	7.39	0.088	0.14
RQ09	21	6.89	0.119	0.25-1	-	-	-	-	-	-	7.00	0.111	0.25-1
RQ10	24	8.04	0.079	0.45	-	-	-	-	-	-	8.00	0.084	0.31
RQ11	22	6.66	0.142	0.25-1	-	-	-	6.14	0.157	0.25-1	6.18	0.133	0.25-1
RQ12	30	7.45	0.053	1.07	-	-	-	-	-	-	7.27	0.054	0.81
RQ13	35	7.27	0.079	0.61	7.88	0.203	0.25-1	6.92	-	0.94	7.69	0.099	0.26
RQ14	37	7.12	0.071	0.38	-	-	-	-	-	-	7.89	0.199	0.25-1
RQ15	39	6.72	0.123	0.25-1	-	-	-	-	-	-	7.18	0.134	0.25-1
RQ16	17	-	-	-	-	-	-	-	-	-	-	-	-
RQ17	9	7.38	0.127	0.96	6.92	-	0.25-1	6.93	0.152	0.25-1	7.51	0.125	0.92
RQ18	23	7.55	0.063	0.27	-	-	-	-	-	-	7.33	0.061	0.09

Table B.7: Bandwidths: Atmosphere at 250 mm PWV

Site	Module	Q1			U1			U2			Q2		
		Mean (GHz)	σ_{stat} (GHz)	σ_{sys} (GHz)	Mean (GHz)	σ_{stat} (GHz)	σ_{sys} (GHz)	Mean (GHz)	σ_{stat} (GHz)	σ_{sys} (GHz)	Mean (GHz)	σ_{stat} (GHz)	σ_{sys} (GHz)
-	-												
-	-												
RQ00	27	43.35	0.041	0.57	-	-	-	-	-	-	43.42	0.041	0.63
RQ01	28	44.16	0.049	0.50	43.88	0.080	0.25-1	43.90	0.079	0.25-1	44.28	0.046	0.58
RQ02	29	45.05	0.072	0.09	-	-	-	-	-	-	44.80	0.074	0.14
RQ03	10	42.96	0.050	0.20	-	-	-	43.28	-	0.25-1	42.99	0.051	0.25
RQ04	36	43.55	0.056	0.56	-	-	-	-	-	-	43.46	0.060	0.59
RQ05	25	43.61	0.053	1.15	-	-	-	-	-	-	43.52	0.055	1.12
RQ06	26	42.77	0.115	0.25-1	-	-	-	-	-	-	42.54	0.126	0.25-1
RQ07	34	43.48	0.060	0.14	-	-	-	-	-	-	43.61	0.063	0.14
RQ08	33	42.58	0.051	0.09	-	-	-	-	-	-	42.79	0.056	0.11
RQ09	21	43.68	0.085	0.25-1	-	-	-	-	-	-	43.63	0.076	0.25-1
RQ10	24	43.86	0.064	0.13	-	-	-	-	-	-	44.02	0.067	0.11
RQ11	22	43.74	0.089	0.25-1	-	-	-	43.99	0.086	0.25-1	43.63	0.086	0.25-1
RQ12	30	42.93	0.064	0.40	-	-	-	-	-	-	42.73	0.061	0.32
RQ13	35	43.40	0.055	1.05	43.86	0.125	0.25-1	43.29	-	0.87	43.54	0.060	1.21
RQ14	37	44.37	0.055	1.01	-	-	-	-	-	-	43.72	0.102	0.25-1
RQ15	39	41.93	0.094	0.25-1	-	-	-	-	-	-	42.05	0.091	0.25-1
RQ16	17	-	-	-	-	-	-	-	-	-	-	-	-
RQ17	9	43.25	0.068	0.12	43.43	-	0.25-1	43.87	0.082	0.25-1	43.43	0.064	0.09
RQ18	23	43.95	0.053	0.07	-	-	-	-	-	-	44.06	0.052	0.03

Table B.8: Central Frequency: Atmosphere at 250 mm PWV

Site	Module	Q1			U1			U2			Q2		
		Mean (GHz)	σ_{stat} (GHz)	σ_{sys} (GHz)	Mean (GHz)	σ_{stat} (GHz)	σ_{sys} (GHz)	Mean (GHz)	σ_{stat} (GHz)	σ_{sys} (GHz)	Mean (GHz)	σ_{stat} (GHz)	σ_{sys} (GHz)
-	-												
-	-												
RQ00	27	6.90	0.065	0.17	-	-	-	-	-	-	7.32	0.074	0.08
RQ01	28	7.17	0.076	0.09	8.32	0.102	0.25-1	7.63	0.124	0.25-1	7.53	0.071	0.21
RQ02	29	6.46	0.148	0.31	-	-	-	-	-	-	7.48	0.145	0.28
RQ03	10	6.68	0.073	0.25	-	-	-	7.17	-	0.25-1	7.46	0.078	0.11
RQ04	36	7.69	0.107	0.70	-	-	-	-	-	-	7.82	0.112	0.81
RQ05	25	6.78	0.095	0.54	-	-	-	-	-	-	6.99	0.090	0.33
RQ06	26	7.68	0.210	0.25-1	-	-	-	-	-	-	8.33	0.221	0.25-1
RQ07	34	7.41	0.067	0.56	-	-	-	-	-	-	7.78	0.074	0.47
RQ08	33	6.76	0.077	0.20	-	-	-	-	-	-	7.34	0.087	0.15
RQ09	21	6.85	0.120	0.25-1	-	-	-	-	-	-	6.97	0.113	0.25-1
RQ10	24	8.05	0.079	0.49	-	-	-	-	-	-	8.04	0.084	0.36
RQ11	22	6.65	0.142	0.25-1	-	-	-	6.16	0.166	0.25-1	6.17	0.132	0.25-1
RQ12	30	7.41	0.053	1.08	-	-	-	-	-	-	7.24	0.054	0.81
RQ13	35	7.26	0.079	0.63	7.84	0.206	0.25-1	6.91	-	0.96	7.69	0.099	0.29
RQ14	37	7.11	0.072	0.32	-	-	-	-	-	-	7.86	0.201	0.25-1
RQ15	39	6.69	0.121	0.25-1	-	-	-	-	-	-	7.13	0.132	0.25-1
RQ16	17	-	-	-	-	-	-	-	-	-	-	-	-
RQ17	9	7.34	0.127	0.97	6.88	-	0.25-1	6.94	0.150	0.25-1	7.48	0.126	0.93
RQ18	23	7.53	0.063	0.28	-	-	-	-	-	-	7.32	0.061	0.08

Table B.9: Bandwidths: Atmosphere at 5000 mm PWV

Site	Module	Q1			U1			U2			Q2		
		Mean (GHz)	σ_{stat} (GHz)	σ_{sys} (GHz)	Mean (GHz)	σ_{stat} (GHz)	σ_{sys} (GHz)	Mean (GHz)	σ_{stat} (GHz)	σ_{sys} (GHz)	Mean (GHz)	σ_{stat} (GHz)	σ_{sys} (GHz)
-	-												
-	-												
RQ00	27	43.31	0.041	0.57	-	-	-	-	-	-	43.38	0.041	0.63
RQ01	28	44.12	0.049	0.50	43.82	0.080	0.25-1	43.86	0.080	0.25-1	44.24	0.046	0.58
RQ02	29	44.99	0.080	0.10	-	-	-	-	-	-	44.73	0.075	0.13
RQ03	10	42.92	0.049	0.20	-	-	-	43.23	-	0.25-1	42.95	0.051	0.25
RQ04	36	43.49	0.056	0.57	-	-	-	-	-	-	43.41	0.060	0.60
RQ05	25	43.57	0.053	1.14	-	-	-	-	-	-	43.48	0.055	1.11
RQ06	26	42.72	0.113	0.25-1	-	-	-	-	-	-	42.48	0.124	0.25-1
RQ07	34	43.44	0.059	0.13	-	-	-	-	-	-	43.56	0.063	0.14
RQ08	33	42.54	0.051	0.09	-	-	-	-	-	-	42.75	0.056	0.11
RQ09	21	43.64	0.085	0.25-1	-	-	-	-	-	-	43.59	0.076	0.25-1
RQ10	24	43.80	0.065	0.12	-	-	-	-	-	-	43.97	0.067	0.10
RQ11	22	43.70	0.089	0.25-1	-	-	-	43.95	0.089	0.25-1	43.60	0.087	0.25-1
RQ12	30	42.89	0.064	0.39	-	-	-	-	-	-	42.69	0.060	0.32
RQ13	35	43.35	0.056	1.04	43.80	0.125	0.25-1	43.24	-	0.86	43.49	0.060	1.21
RQ14	37	44.32	0.055	1.02	-	-	-	-	-	-	43.66	0.102	0.25-1
RQ15	39	41.89	0.093	0.25-1	-	-	-	-	-	-	42.00	0.090	0.25-1
RQ16	17	-	-	-	-	-	-	-	-	-	-	-	-
RQ17	9	43.20	0.067	0.13	43.39	-	0.25-1	43.83	0.084	0.25-1	43.38	0.062	0.10
RQ18	23	43.91	0.053	0.07	-	-	-	-	-	-	44.02	0.052	0.03

Table B.10: Bandwidths: Atmosphere at 5000 mm PWV

Appendix C

Optimizer Signal Derivation

Light is polarized as it is reflected off of a plate, this is given by (Ref. [31]):

$$R_{\parallel} = 1 - \sqrt{16\pi\nu\rho\epsilon_0} \sec(\beta) \quad (\text{C.1})$$

$$R_{\perp} = 1 - \sqrt{16\pi\nu\rho\epsilon_0} \cos(\beta) \quad (\text{C.2})$$

Where ν is the frequency of observation, ρ is the bulk resistivity of the metal, and β is the angle of incidence between the plate and the load. The signal we measure is proportional to Stokes U, as:

$$Q = \frac{E_x^2 - E_y^2}{2} \quad (\text{C.3})$$

We will choose E_x and E_y such that:

$$E_x^2 = T_{load} * R_{\parallel} \quad (\text{C.4})$$

$$E_y^2 = T_{load} * R_{\perp} \quad (\text{C.5})$$

Thus:

$$Q_{load} = \frac{1}{2} T_{load} (R_{\parallel} - R_{\perp}) \quad (C.6)$$

$$= T_{load} \sqrt{4\pi\nu\rho\epsilon_0} (\sec\beta - \cos\beta) \quad (C.7)$$

The plate transmits instead of reflects, where $T \equiv 1 - R$, such that

$$E_x^2 = T_{plate} * (1 - R_{\parallel}) \quad (C.8)$$

$$E_y^2 = T_{plate} * (1 - R_{\perp}) \quad (C.9)$$

Thus:

$$Q_{plate} = \frac{1}{2} T_{plate} (R_{\perp} - R_{\parallel}) \quad (C.10)$$

$$= \frac{1}{2} T_{load} \sqrt{16\pi\nu\rho\epsilon_0} (\cos\beta - \sec\beta) \quad (C.11)$$

The final signal is then given by:

$$Q_{tot} = Q_{plate} + Q_{load} \quad (C.12)$$

$$= \sqrt{4\pi\nu\rho\epsilon_0} (\sec\beta - \cos\beta) (T_{load} - T_{plate}) \quad (C.13)$$

This signal is modulated by the rotation angle given by α . Because the Stokes vectors are defined such that they double-cover a circle, the polarization modulation frequency will be 2α .

$$I = \sqrt{4\pi\nu\rho\epsilon_0} (\sec\beta - \cos\beta) (T_{load} - T_{plate}) \sin(2\alpha) \quad (C.14)$$

Appendix D

Sensitivity Calculation

D.1 Array Sensitivity Computation

The RMS noise of a diode with intrinsic noise T_{rec} , bandwidth $\Delta\nu$, integration time τ , and target load temperature T_{load} is given by ([53]):

$$\Delta T_{RMS} = \frac{T_{rec} + T_{load}}{\sqrt{\tau \Delta\nu}} \quad (D.1)$$

The sensitivity is given by:

$$S = \frac{T_{rec} + T_{load}}{\sqrt{\Delta\nu}} \left[\frac{K}{\sqrt{Hz}} \right] \quad (D.2)$$

This is also equivalent to the white noise floor σ (discussed in section 3.6) in units of V/\sqrt{Hz} given the responsivity R (units of V/K):

$$S = \frac{\sigma}{R} \left[\frac{K}{\sqrt{Hz}} \right] \quad (D.3)$$

Typically these quantities are computed in units of seconds, the conversion is $Hz/2 = 1/s$.

D.1.1 Masking Factor

We mask the phase-switch transition region, masking 13% of the data. This results in a masking factor of 0.87, which must be explicitly inserted into equation D.2 as a factor which decreases τ . This factor is implicit in equation D.3 through the Fourier transform of the noise (which is used to obtain the noise floor).

Typical values for diode sensitivity after including the masking factor are $1\text{mK}\sqrt{s}$.

D.1.2 Combining Diodes to Find Array Sensitivity

$$S_{array} = \frac{\sqrt{\sum_{diode} S_{diode}^2}}{N} \quad (\text{D.4})$$

If all diodes have equal sensitivity, the sensitivity of the array will be $S_{array} = \frac{S_{diode}}{\sqrt{N}}$. The array sensitivity while looking at a cryogenic load is $110\mu\text{K}\sqrt{s}$ and $119\mu\text{K}\sqrt{s}$ for equation D.2 and D.3, respectively.

D.1.3 Extrapolation for the Chilean Sky

We measure both T_{rec} and σ while looking at a cryogenic load, however noise scales with input load, so the noise measured while looking at the Chilean sky will be larger than we would measure while looking at the cryogenic load. To extrapolate the sensitivity values computed from cryogenic loads to the Chilean sky, we correct the sensitivity by:

$$\frac{T_{rec} + T_{sky}}{T_{rec} + T_{cryogenic}} \quad (\text{D.5})$$

for both equation D.2 and D.3. We will assume a sky temperature of 11K with a CMB temperature of 3K, giving a total sky temperature of 14K.

D.1.4 Rayleigh-Jeans Correction

The computation of noise (above) assumed that the power measured by the polarimeter is directly proportional to temperature. This approximation is valid at long wavelengths, however it begins to break down when $\lambda < 1$ cm.

The expression for the brightness of a thermal source is given by:

$$B_{Planck}(\nu, T) = \frac{2h\nu^3}{c^2} \frac{1}{e^{h\nu/kT} - 1} \quad (D.6)$$

where h is Planck's constant, k is the Boltzmann constant, and c is the speed of light. The linear approximation to this ($h\nu \ll kT$) is known as the Rayleigh-Jeans law and has the form:

$$B_{RJ}(\nu, T) = \frac{2\nu^3 kT}{c^3} \quad (D.7)$$

Such that the brightness temperature in the Rayleigh-Jeans approximation is given by:

$$T_B = \frac{B_{RJ}(\nu, T)c^3}{2\nu^3 k} \quad (D.8)$$

Antenna noise temperature is defined in the Rayleigh-Jeans approximation. To express noise temperature in terms of thermodynamic units, we compare the brightness B_{Planck} with B_{RJ} , and make a distinction between the temperature in thermodynamic units (T_θ) and in antenna noise temperature T_A :

$$B_{Planck} = B_{RJ} \quad (D.9)$$

$$\frac{2h\nu^3}{c^2} \frac{1}{e^{h\nu/kT_\theta} - 1} = \frac{2\nu^3 kT_A}{c^3} \quad (D.10)$$

$$T_A = \frac{h\nu/k}{e^{h\nu/kT} - 1} \quad (D.11)$$

The correction from antenna noise temperature into thermodynamic units is then given by:

$$\frac{T_\theta}{T_A} = \frac{e^{h\nu/kT_\theta} - 1}{h\nu/kT_\theta} \quad (\text{D.12})$$

This is noted in a variety of references, including Ref. [9]. The Q-band (40 GHz) will have a correction factor of 1.45, the W-band (90 GHz) will have a correction factor of 2.44 for a thermodynamic temperature $T_\theta = T_{CMB} = 2.73\text{K}$.

These corrections together give us an extrapolation for expected sensitivity to the CMB given the Chilean sky temperature of 14K: $56\mu\text{K}\sqrt{s}$ and $68\mu\text{K}\sqrt{s}$ for equation D.2 and D.3, respectively.